



HAL
open science

In situ nanotomography investigation of cavity nucleation and growth in light alloys during high temperature deformation

Richi Kumar

► **To cite this version:**

Richi Kumar. In situ nanotomography investigation of cavity nucleation and growth in light alloys during high temperature deformation. Mechanics of materials [physics.class-ph]. Université Grenoble Alpes, 2019. English. NNT : 2019GREAI065 . tel-02528824

HAL Id: tel-02528824

<https://theses.hal.science/tel-02528824>

Submitted on 2 Apr 2020

HAL is a multi-disciplinary open access archive for the deposit and dissemination of scientific research documents, whether they are published or not. The documents may come from teaching and research institutions in France or abroad, or from public or private research centers.

L'archive ouverte pluridisciplinaire **HAL**, est destinée au dépôt et à la diffusion de documents scientifiques de niveau recherche, publiés ou non, émanant des établissements d'enseignement et de recherche français ou étrangers, des laboratoires publics ou privés.

THÈSE

Pour obtenir le grade de

DOCTEUR DE LA COMMUNAUTE UNIVERSITE GRENOBLE ALPES

Spécialité: 2MGE Matériaux, Mécanique, Génie civil, Electrochimie

Arrêté ministériel : 25 mai 2016

Présentée par

Richi KUMAR

Thèse dirigée par **M. Luc SALVO**
co-encadré par **M. Pierre LHUISSIER**
co-encadré par **Mme. Julie VILLANOVA**

préparée au sein du **Laboratoire SIMaP**
dans **l'École Doctorale I-MEP2**

***In situ* nanotomography investigation of cavity nucleation and growth in light alloys during high temperature deformation**

Etude par nanotomographie *in situ* de la germination et de la croissance de cavités lors de la déformation à chaud d'alliages légers

Thèse soutenue publiquement le **29/10/2019**

devant le jury composé de :

M. Guillermo REQUENA

Professeur, German Aerospace Center (DLR), RWTH-Aachen University, Président

M. Andras BORBELY

Directeur de recherche, Ecole des mines de Saint Etienne, Rapporteur

M. Jean Yves BUFFIERE

Professeur, INSA de Lyon, Rapporteur

Mme. Martine BLAT-YRIEIX

Ingénieurs de recherche, EDF, Examineur

M. Luc SALVO

Directeur de recherche, SIMaP, Directeur de thèse

M. Pierre LHUISSIER

Chargé de Recherches CNRS, SIMaP, co-encadrant

Mme. Julie VILLANOVA

Beamline scientifique, ESRF, co-encadrant

M. Remi TUCOULOU

Beamline Operation Manager, ESRF, Invité

M. Jean SUSINI

Directeur de recherche, ESRF, Invité



Summary

High temperature deformation proceeds in nucleation, growth and coalescence of voids or creep cavities. Hence investigation of damage in form of cavities during high temperature deformation has been a subject of great interest for researchers over the years. Several theoretical models have been proposed to predict cavity nucleation and growth. However despite significant progresses with theoretical models, the experimental validations of these models have been handful. The main reason for this has been a lack of suitable characterization tools that allows *in situ* investigation of nucleation and growth of cavities at high spatial resolution (smaller than 1 μm).

In the present work a technique for *in situ* nanotomography investigation during high temperature deformation has been developed. This involved development of two mechanical devices that could fit in a furnace in order to perform 4D *in situ* damage analysis at high temperature (below 1073 K). Additionally multi resolution data acquisition routines were developed which allowed imaging at high (100 nm) and low resolution (645 nm) periodically. These developments allowed 4D imaging of damage nucleation and growth in form of creep cavities at 100 nm pixel size and scan time of 7 seconds. Thanks to this nucleation and volumetric growth of individual cavities could be tracked during deformation which could in turn be compared to theoretical models.

This technique has been used to study nucleation and growth of damage during high temperature deformation (7.9 MPa, 698 K), in Al -3.6 wt% Cu alloy. This model alloy allows controlled generation of second phase particles to promote cavity nucleation and has hence been chosen for the study. Changes in shape of cavities with straining has been examined. Also, the change of volumetric cavity growth rate versus equivalent radius of individual cavities has been compared to existing models of cavity growth by diffusion and plasticity. It was seen that several pre-existing porosities were present in the alloy, while very few cavity nucleations were observed. The experimental data of growth rate matched well with the studied models and it was concluded that cavities initially grew by diffusion, while the growth mechanism changed to plasticity near failure.

Further the use of *in situ* nanotomography has been extended to studying nucleation and growth during creep deformation (3.2 MPa, 673 K) in commercial AZ31 alloy. Evolution of small and nearly spherical cavities into complex cavities has been studied, by analysing changes in shape during growth. Volumetric cavity growth rate has also been computed and compared to diffusion and grain boundary sliding models. In a specific case grain boundary sliding was calculated by tracking the displacements of intermetallics which acted as markers. Influence of this on a cavity present on the sliding boundary has been studied.

Few cavity nucleations were seen during deformation while most of the damage proceeded in growth of pre-existing cavities. Examination of cavity shape indicated diffusion and grain boundary sliding as the dominant mechanisms driving growth. Diffusion dominating growth in early stages (strain below 0.3) of deformation while later an interplay of the two mechanism caused growth. On comparing volumetric growth data with experimental results, it was seen that conventional grain boundary diffusion model over predicted growth rate, while constrained diffusion models were successful in predicting growth rate in the correct order of magnitude as seen experimentally. A direct proportionality was observed between grain boundary displacement and cavity length in a cavity where growth dominated by grain boundary sliding. Additionally apart from growth considerable proportion of cavities showed a decrease in volume during deformation. This was attributed to sintering of cavities under the effect of diffusion.

Resumé

La déformation à haute température induit la germination, la croissance et la coalescence de cavités, domaine très étudié en science des matériaux. Plusieurs modèles théoriques ont été proposés pour prédire la nucléation et la croissance de la cavité mais la comparaison avec l'expérience est limitée. La principale raison en est le manque d'outils de caractérisation appropriés permettant d'étudier *in situ* la nucléation et la croissance des cavités à haute résolution spatiale (inférieure à 1 μm).

Dans le cadre de ce travail, la nanotomographie *in situ* aux RX a été mise au point pour l'étude des déformations à haute température. Deux dispositifs mécaniques pouvant s'adapter dans un four ont été développés : ceci permet de réaliser une analyse 4D *in situ* des dommages à haute température (inférieure à 1073 K). De plus, des routines d'acquisition de données à résolutions multiples ont été mises au point, ce qui a permis d'obtenir alternativement des images à haute résolution (100 nm) et à basse résolution (645 nm). Ces développements ont permis l'imagerie 4D de la germination et de la croissance de l'endommagement avec une taille de pixels de 100 nm et un temps de balayage de 7 secondes. Ces données expérimentales ont été comparées aux modèles théoriques.

Cette technique a été utilisée pour étudier la germination et la croissance des dommages lors de déformations à haute température (7,9 MPa, 698 K), dans un alliage d'Al -3,6% en poids de Cu. Cet alliage modèle permet la génération contrôlée de particules de seconde phase pour favoriser la germination des cavités. Les changements de forme des cavités avec la déformation ont été étudiés. De plus, l'évolution avec la déformation du taux de croissance volumétrique de la cavité par rapport au rayon équivalent des cavités individuelles a été comparé aux modèles existants de croissance de la cavité par diffusion et plasticité. On a constaté la présence de plusieurs porosités préexistantes dans l'alliage, alors que très peu de germination de cavité ont été observées. Les données expérimentales sur le taux de croissance correspondent bien aux modèles étudiés et il a été conclu que les cavités se développaient initialement par diffusion suivi par une croissance par plasticité.

L'utilisation de la nanotomographie *in situ* a été étendue à l'étude de la nucléation et de la croissance pendant la déformation à haute température (3,2 MPa, 673 K) dans l'alliage commercial AZ31. L'évolution de petites cavités presque sphériques en cavités complexes a été étudiée, en analysant les changements de forme pendant la croissance. Le taux de croissance volumétrique de la cavité a également été calculé et comparé aux modèles de diffusion et de glissement aux joints de grain. Dans un cas particulier, le glissement aux joints de grain a été estimé en suivant les déplacements des intermétalliques qui servaient de marqueurs.

Peu de germination de cavité ont été observées au cours de la déformation, par contre les cavités préexistantes, issues du laminage, ont évolué en taille avec la déformation. L'examen des formes des cavités a révélé que la diffusion et le glissement aux joints de grain sont les mécanismes principaux de la croissance. La diffusion dominant la croissance dans les premiers stades (déformation inférieure à 0,3) puis une combinaison des deux mécanismes gouverne la croissance. Le modèle de croissance par diffusion surestime les données expérimentales tandis que les modèles de diffusion restreinte s'ajustent mieux aux évolutions de volume des cavités. Une proportionnalité directe a été observée entre le glissement au joint de grain et la longueur de la cavité dans une cavité où la croissance est dominée par le glissement aux joints de grain. De plus, outre la croissance, une proportion importante de cavités a montré une diminution du volume pendant la déformation. Ceci a été attribué au frittage des cavités sous l'effet de la diffusion.

Acknowledgements

First and foremost, I would like to thank Prof. Luc Salvo, Dr. Pierre Lhuissier (University Grenoble Alpes, CNRS, SIMaP) and Dr. Julie Villanova (Beamline scientist ID16B, ESRF) for their supervision and guidance during the thesis. Without their inputs and persistent encouragement, this thesis would not have been possible. I also extend my gratitude to Dr. Remi Tucoulou, beamline operational manager, for his guidance and continuous support during the thesis.

I am deeply grateful to ESRF and CEMAM for giving me the required financial support in the form of PhD grant and the allocated beamtimes.

I sincerely acknowledge the efforts of Mr. Xavier Bataillon and Mr. Charles Josserond of GPM2 laboratory, University Grenoble Alpes for their contributions in developing the mechanical devices. I am also grateful to Sylvain Laboure, technician at ID16B, ESRF for his help with the furnace installations during the beamtimes.

I extend my gratitude to Prof. Jean Jacques Blandin for his theoretical insights which allowed me to analyse my results and write an informative thesis. I would also like to express my gratitude to the staff and technicians of ESRF and SIMaP for assisting me in various academic and professional activities.

I want to thank my friends and colleagues Vanessa, Sara, Ines and JP for being such wonderful companions and for making my time at ESRF immensely enjoyable. Special thanks to my fellow researchers Shrey, Prasanta and Jayant for being such amazing friends.

I owe my deepest gratitude to my parents for their belief in my goals and abilities, Archie bhaiya and Pooja bhabi for always having my back and Yuvan for being the cutest baby ever. Last but not the least, I would thank with all my heart my best buddy, Atin for helping me out with my work, being my editor and proof reader. And for being with me through thick and thin, encouraging me and keeping me sane. It would have been impossible without him.

Thank you all for making this happen!

Contents

| | |
|---|-----------|
| Introduction | 25 |
| Chapter 1. State of the art..... | 29 |
| 1.1 High temperature deformation..... | 29 |
| 1.1.1 Diffusion creep..... | 33 |
| 1.1.2 Dislocation creep..... | 35 |
| 1.1.3 Superplasticity | 37 |
| 1.1.4 Deformation mechanism map | 41 |
| 1.2 Creep cavities | 42 |
| 1.2.1 Nucleation of creep cavities | 42 |
| 1.2.2 Growth of creep cavities..... | 45 |
| 1.3 Characterization of creep cavities..... | 54 |
| 1.3.1 Density change measurements..... | 54 |
| 1.3.2 2D imaging techniques: OM, SEM, TEM | 55 |
| 1.3.3 3D imaging techniques: FIB-SEM, XMT | 58 |
| 1.4 X-ray Computed Tomography (X-ray CT)..... | 60 |
| 1.4.1 Physics of interaction of X-rays with matter and different contrast modes | 60 |
| 1.4.2 X-ray source | 63 |
| 1.4.3 X-ray tomography for imaging cavities..... | 64 |
| 1.5 Summary | 69 |
| 1.6 Objectives | 70 |
| Chapter 2. Materials and Method | 74 |
| 2.1 Materials..... | 74 |
| 2.1.1 Al-Cu alloy | 74 |
| 2.1.2 AZ31 | 75 |
| 2.2 In situ nanotomography setup..... | 78 |
| 2.2.1 The European Synchrotron Radiation Facility (ESRF) | 79 |
| 2.2.2 The ID16B beamline..... | 80 |
| 2.2.3 Furnace (improvement of temperature calibration)..... | 82 |
| 2.2.4 Mechanical devices | 85 |
| 2.3 Data acquisition..... | 88 |
| 2.4 Data Processing | 94 |

| | | |
|-------------------|--|------------|
| 2.4.1 | Phase retrieval and reconstruction..... | 95 |
| 2.5 | 3D volume analysis | 103 |
| 2.5.1 | Analysis | 103 |
| 2.5.2 | Digital Volume Correlation: Tracking features..... | 105 |
| 2.5.3 | Segmentation | 109 |
| 2.5.4 | Sphericity and volume estimation..... | 114 |
| 2.6 | Determination of mechanical parameters..... | 114 |
| 2.6.1 | Stress, strain and strain rate: notch area | 115 |
| 2.6.2 | Strain and strain rate: DVC | 115 |
| 2.6.3 | Stress: ex situ high temperature deformation tests..... | 115 |
| 2.6.4 | Triaxiality | 117 |
| Chapter 3. | High temperature deformation of Al-Cu alloy | 119 |
| 3.1 | Second phase particles..... | 119 |
| 3.1.1 | Generation of second phase particles..... | 120 |
| 3.1.2 | Characteristics of second phase particles..... | 121 |
| 3.1.3 | Pre-existing cavities | 123 |
| 3.1.4 | Summary | 125 |
| 3.2 | Cavity nucleation and growth during high temperature deformation..... | 126 |
| 3.2.1 | <i>In situ</i> high temperature deformation nanotomography setup | 126 |
| 3.2.2 | Data analysis | 127 |
| 3.2.3 | High temperature deformation parameters | 128 |
| 3.2.4 | 3D tomography results | 129 |
| 3.2.5 | Nucleation of cavities | 130 |
| 3.2.6 | Growth of cavities | 131 |
| 3.2.7 | Discussion | 134 |
| 3.3 | Constant strain rate high temperature deformation..... | 141 |
| 3.3.1 | Sample preparation and acquisition parameters..... | 141 |
| 3.3.2 | Mechanical parameters | 141 |
| 3.4 | Conclusions..... | 143 |
| Chapter 4. | High temperature deformation of Mg alloy (AZ31)..... | 144 |
| 4.1 | Initial microstructure | 144 |
| 4.2 | Technical details..... | 146 |
| 4.2.1 | <i>In situ</i> high temperature deformation nanotomography setup and acquisition | 147 |
| 4.2.2 | Data analysis | 148 |

| | | |
|------------|--|------------|
| 4.2.3 | Mechanical parameters | 148 |
| 4.3 | Nucleation of cavities | 150 |
| 4.3.1 | Results | 150 |
| 4.3.2 | Discussion | 151 |
| 4.4 | Growth of cavities: average measurements | 152 |
| 4.5 | Growth of cavities: individually tracked cavity measurements..... | 155 |
| 4.5.1 | Growth classifications and mechanism | 155 |
| 4.5.2 | Predominant evolution type..... | 169 |
| 4.5.3 | Volumetric growth rate: comparison with models..... | 171 |
| 4.6 | Conclusions | 194 |
| | <i>Conclusions</i>..... | 197 |
| | <i>Perspectives</i> | 201 |
| | <i>Appendix A</i> | 208 |
| | <i>Appendix B</i> | 216 |
| | <i>Appendix C</i> | 224 |
| | <i>Appendix D</i> | 225 |

List of figures

| | |
|--|----|
| Figure 1.1 Constant (a) true stress (strain as a function of time) and (b) strain rate creep (stress as a function of strain) behaviour in pure metals [22] | 31 |
| Figure 1.2 The steady-state creep-rate ($\dot{\epsilon}_{min}$) versus time-to-rupture t_f for dispersion strengthened cast aluminium deformed. Note: the $\dot{\epsilon}_{min}$ and t_f are same as $\dot{\epsilon}_{ss}$ and t_r of equation (1.2) [7]. | 32 |
| Figure 1.3 Schematic illustration showing the mechanism of Nabarro-Herring creep (via lattice diffusion of vacancies) and Coble creep (via grain boundary diffusion of vacancies) in a grain, under the effect of a tensile stress: σ . The dotted lines indicate vacancy flux. | 34 |
| Figure 1.4 Schematic illustration of dislocation based grain boundary sliding accommodation mechanism proposed by Ball and Hutchinson [41]. | 38 |
| Figure 1.5 Schematic illustration of diffusion based accommodating mechanism during grain boundary sliding as proposed by Ashby and Verral in (a) initial (b) intermediate and (c) final state. (d-e) Illustration showing the possible diffusion paths of matter (in dotted lines) during the transition from initial to final state. A and B indicate diffusion paths that were not accounted in this model [42]. | 39 |
| Figure 1.6 Schematic illustration of diffusion based accommodating mechanism during grain boundary sliding as proposed by Lee [43]. | 39 |
| Figure 1.7 Deformation mechanism map for pure aluminium with (a) grain size $10 \mu\text{m}$ and (b) grain size 1mm [47]. | 41 |
| Figure 1.8 The formation of a cavity from (a) particle-obstacle during grain boundary sliding (GBS) [7] and (b) at grain boundary triple points due to stress concentration during grain boundary sliding (σ_n is the normal stress on the transverse grain boundary and σ_s is the shear stress on sliding boundary) [53]. | 44 |
| Figure 1.9 (a, b) Stress induced by boundary sliding at jogs. (c) Formation of void as a result of tensile stress on a jog [8]. | 44 |
| Figure 1.10 (a) Grain boundary sliding along a transverse grain boundary. (b) Formation of jog as a result of slip in grain B. (c) Decohesion along the jog as a result of further boundary sliding resulting in nucleation of cavity indicated in a circle marked c [55]. | 45 |
| Figure 1.11 Schematic illustration of an array of cavities of radius r on a grain boundary, growing via diffusion under the effect of a stress. | 46 |
| Figure 1.12 Cavity growth due to grain boundary sliding [64]. | 48 |
| Figure 1.13 Cavity growth by grain boundary sliding at a tensile ledge [65]. | 48 |

| | |
|--|----|
| Figure 1.14 Schematic illustration of a cavity (represented by circle) in (a) high temperature creep when grain size greater than 50 μm (b) superplastic deformation when grain size nearly 5 μm [66]. | 49 |
| Figure 1.15 (a) Schematic illustration of an isolated cavitated grain boundary facet. (b) Zoomed view of one of the cavity [67]. | 50 |
| Figure 1.16 Schematic illustration showing trend of cavity growth rate obtained (a) diffusion, superplastic diffusion and power law (plasticity) models in term of $dr/d\epsilon$ versus r [66] (b) diffusion, superplastic diffusion and plasticity model in terms in dV/dt versus r . | 53 |
| Figure 1.17 Plot showing evolution of cavity volume per unit weight with $\epsilon\sigma^{2.3}$ in copper at constant temperature and different loads (mentioned in figure) [73]. | 54 |
| Figure 1.18 Optical micrograph of gauge section of copper pulled to fracture in superplastic regime at 823K with initial strain rate of (a) $3.33 \times 10^{-2} \text{ s}^{-1}$ and (b) $1.67 \times 10^{-5} \text{ s}^{-1}$ The tensile axis is vertical [75]. | 56 |
| Figure 1.19 (a) SEM micrograph of Ti Al alloy subjected to creep deformation at 1073 K, 270 MPa, showing cavities with a spherical cap shape along grain boundaries of grains indicated by number 1 to 5 [76]. (b) Evolution of cavity density with strain in 12 % Cr ferritic steel, crept at 923 K and 80 MPa, [77]. | 57 |
| Figure 1.20 Creep cavities in AISI type 316 stainless steel from a power station steam header showing reheat cracking was studied using TEM. High Angle Annular Dark Field – Scanning Transmission Electron Microscopy Imaging (HAADF-STEM) image from grain boundary showing a faceted cavity in contact with different second phase particles and matrix. (b) Schematic diagram overlaid onto HAADF image showing different phases identified by composition and selected area electron diffraction (SAED). V is cavity, α is ferrite, γ is austenite matrix and 's', 'm' and 'l' indicated small, medium and large M_{23}C_6 phase particles respectively [80]. | 58 |
| Figure 1.21 Schematic illustration of basic principle of X-ray microtomography acquisition and reconstruction into 3D volumes [81]. | 60 |
| Figure 1.22 Schematic illustration of two primary contrast mechanisms employed in X-ray imaging (a) absorption contrast (b) phase contrast [83]. | 62 |
| Figure 1.23 Schematic illustration of setup for holotomography [84]. | 63 |
| Figure 1.24 Schematic illustration of (fan beam geometry (b) cone beam geometry (c) parallel beam geometry. Here CCD camera is used as a 2D detector [78]. | 63 |
| Figure 1.25 Slice of the brass sample after (a) 348 min creep and (b) 431 min creep. One voxel is about $4 \mu\text{m}^3$. Creep performed at 25 MPa and 648 K [16]. | 65 |
| Figure 1.26 (a) Number of cavities per unit area N_a and per unit volume N_v as a function of strain. [78] (b) Average growth rate of voids as a function of volume [15] (c) 3D rendered image obtained by in situ X-ray microtomography of AZ31 alloy, | |

showing an example of a coalescence event: several cavities are detected for the lowest strain and the cavities progressively connect together via a coalescence process. The largest cavity is in yellow whereas the others are in blue, voxel size $(1.2 \mu\text{m})^3$ [12]. 66

Figure 1.27 (a) A 2D surface view of a random area of the 3D volume of AZ61 at $\epsilon = 1.05$. A, B and C cavity regions are identified not to be connected with any particle. (b) Same view transformed into a 3D by extending the depth below the surface. Particles are found to be attached to the cavity regions of A and B. Cavity region C is still observed to be not connected with any particle, [90]. The limit to resolution is $1.8 \mu\text{m}$. Deformation was performed at 623 K and strain rate $5 \times 10^{-4} \text{ s}^{-1}$. (c) 3-D perspective views of pores/cavities (both are shown in red) and particles (green) captured at the final loading step in Al-Mg alloy deformed at 923 K. A grain boundary image (grey) has been superposed on (c) in (d), resolution is nearly $1 \mu\text{m}$ [11]..... 67

Figure 1.28 State of the art of in situ X-ray tomography: Pixel size versus scan time illustrating the state of the art for in situ X-ray laboratory and synchrotron tomography. Scan times of about 10 min are usually necessary to operate with nanometer pixel size ($\leq 100 \text{ nm}$). Similarly, ultra-fast tomography ($\leq 10 \text{ s}$ time scan) is only attainable with micrometer resolution [94]. 68

Figure 1.29 Schematic illustration of plot showing volumetric growth rates of cavities governed by different growth mechanisms..... 71

Figure 1.30 Scan time versus pixel size map showing, imaging parameters employed for tomographic investigations of creep cavities. Note that a scan time of 120 minutes was assigned to studies when no scan time was reported.[15,91,98–113] 72

Figure 2.1 (a) Schematic illustration of ingot cast for Al – 3.6 wt% Cu sample, from which cylindrical rods (highlighted in grey) were machined. (b) Drawing of sample used for compact mechanical device (machined from the rod). (c) Drawing of sample used for motorised mechanical device (machined from, the rod). All measurements in mm. 75

Figure 2.2 (a) Schematic illustration of AZ31 sheet of 2 mm thickness (RD: Rolling direction, TD: Transverse direction, ND: Normal direction), from which cylindrical rods were machined (highlighted in grey). (b) Drawing of sample used for compact mechanical device (machined from the rod), a small piece of alumina tube (2 mm length) was glued to the top of this, which has been marked (c) Drawing of sample used for motorised mechanical device (machined from the rod). All measurements in mm. 76

Figure 2.3 (a) Optical micrograph (b) Histogram of grain sizes observed using EBSD map (c) EBSD map (d) Inverse pole figure in the normal direction of a AZ31 sample, Work of T. Dessolier [114]. This sample was obtained from the same AZ31 sheet that was used for machining the samples for this thesis. 77

Figure 2.4 Transverse 2D slice from high resolution (pixel size 100nm) tomography of a AZ31 sample. Two types of intermetallics seen in the sample have been

| | |
|--|----|
| encircled. Yellow circle: grey intermetallic, Red circle: black Intermetallic (cavity in white)..... | 78 |
| Figure 2.5 (a) Schematic illustration of the main components of the ESRF. (b) Schematic illustration of the main components of the storage ring. Source: www.esrf.eu | 79 |
| Figure 2.6 Schematic illustration of in situ nanotomography setup at the ID16B beamline of ESRF, showing a compact mechanical device that fits inside the beamline furnace [118]..... | 81 |
| Figure 2.7 Radiograph of Al -6.1wt% Ni eutectic alloy obtained as a part of a calibration regime (a) before melting, showing solid eutectic phase, (b) after melting showing molten alloy..... | 83 |
| Figure 2.8 Calibration curve for furnace using different eutectics, showing the sample and furnace temperature corresponding to percentage the power supplied. Red markers indicate calibration with mechanical device (M). ΔT indicates constant difference in temperature of furnace and sample in 697 ± 50 K temperature regime. A fit to the power and corresponding sample temperature is also indicated with the defining equation mentioned on the top of the plot, where P is Power and T is Temperature..... | 84 |
| Figure 2.9 Schematic illustration of the compact mechanical device (a) front view (b) section view, used for high temperature in situ nanotomography experiment at ID16B beamline of ESRF [118]. (c) Plot showing variation of force with displacement, for the spring used in the compact mechanical device measured using a compression testing machine..... | 86 |
| Figure 2.10 (a) Schematic depiction of the motorised mechanical device. (b) Detailed view of the top part of the device (c) Photo of device placed on the rotating stage of the beamline. Measurements are in mm. | 87 |
| Figure 2.11 Schematic illustration of positions of furnace and sample with respect to the focussed beam at (a) High Resolution (HR pixel size is 100 nm) (b) Low Resolution acquisition (LR pixel size is 645 nm). | 88 |
| Figure 2.12 A transverse 2D slice from LR volume depicting the scheme of acquisition where 4 HR volumes are acquired as indicated by HR1 to HR4, the offset between the centres of successive HR scans is 90 μm . Remember that the HR3 volume stands in the middle of the LR field of view..... | 90 |
| Figure 2.13 Flowchart showing steps involved in obtaining 3D volumes using X-ray tomography. | 95 |
| Figure 2.14 A horizontal slice from 3D HR volume of AZ31 sample for which phase retrieval was done using (a) Paganin method (b) iterative non-linear conjugate gradient method. No ring artefact correction done for both volumes the grey level profile along the red line shown below each slice (intermetallics are in black, cavities are in white and matrix is in grey)..... | 97 |

| | |
|--|-----|
| Figure 2.15 A horizontal slice from 3D HR volume of AZ31 sample reconstructed (a) without ring correction (b) with ring correction using post processing of volume [126]. The grey level profile along the red line is shown below each slice. (intermetallics are in black, cavities are in white and matrix is in grey)..... | 99 |
| Figure 2.16 A horizontal slice from 3D HR volume of AZ31 sample reconstructed (a) without ring correction (b) with ring correction (using parameters listed in Table 2.7), the grey level profile along the red line is shown below each slice. Note that the grey levels in this slice is different from Figure 2.15 A horizontal slice from 3D HR volume of AZ31 sample because the two figures have been converted from 32 to 8 bit using different grey level range. (intermetallics are in black, cavities are in white and matrix is in grey)..... | 101 |
| Figure 2.17 A cropped horizontal slice from HR 3D volume of AZ31 sample that has been reconstructed (a) with 721 projections acquired during full 0 to 360° rotation (b) with 360 projections acquired during half 0 to 180° rotation, the grey level profile along the red line is shown below each slice (intermetallics are in black, cavities are in white and matrix is in grey)..... | 103 |
| Figure 2.18 Flowchart followed for LR volume analysis. | 104 |
| Figure 2.19 Flowchart followed for HR volume analysis..... | 105 |
| Figure 2.20 A transverse slice from 3D LR volume of AZ31 sample with intermetallics in black, which act as guiding points that are tracked between the (a) reference state and (b) and deformed state in order to estimate the displacement field. (c) Displacement of features between state (a) and (b) (intermetallics are in black, cavities are in white and matrix is in grey)..... | 106 |
| Figure 2.21 A horizontal slice from 3D HR of (a) Al-Cu sample where the second phase particles are seen in black, cavity in white and matrix in grey (b) AZ31 sample where the intermetallic particles are seen in black, cavity in white and matrix in grey. | 109 |
| Figure 2.22 (a) Transverse cross section view of a LR 3D volume, where a threshold has been applied to separate the notch and air (b) Plot of mean grey value for different slices, where a slice 0 corresponds to top of the notch and slice 1080 to the bottom. The dotted line indicates the minimum in the grey value, which corresponds to minimum notch area (sample is in white and air is in black)..... | 110 |
| Figure 2.23 A horizontal slice from 3D HR Al-Cu volume (a) before applying filter (b) after applying a mean shift filter, along with a grey level plot along the red line for the two slices. (c) A segmented image of the filtered slice. | 111 |
| Figure 2.24 Example of segmentation of cavity in Al-Cu sample by 2 different methods. The region indicated by black box in (a1) was cropped and threshold using iterative intermeans threshold which is shown in (b). The slice in (a1) was subjected to edge detection and is shown in (c1) the corresponding plot profile grey level along the red lines are shown in (a2) and (c2). (d) is a cropped segmented slice based on the average threshold of 195..... | 113 |

| | |
|---|-----|
| Figure 2.25 Plot of stress versus strain from a strain rate jump test on AC5 sample (698 K). Each number marked in red corresponds to a different strain rate. The strain rate and stress corresponding to each number is listed in Table 2.9 | 116 |
| Figure 2.26 Schematic of the notched sample showing definitions for r_{section} and r_{notch} | 117 |
| Figure 2.27 Plot showing change in triaxiality during sample deformation. | 118 |
| Figure 3.1 Schematic illustration of a portion of the Al-Cu equilibrium phase diagram (x axis: Cu in weight %, y axis: Temperature in Kelvin). The different phases are single phase solid solution of Al and Cu (α), the liquid (L) and semi-solid region ($\alpha + L$) (indicated in grey)..... | 120 |
| Figure 3.2 Horizontal 2D slice showing second phase particle and pre-existing cavities in an Al-Cu solutionised sample heat treated at 893 K for 5 minutes. | 121 |
| Figure 3.3 Probability of (a) equivalent radius and (b) sphericity of second phase particles produced by heat treatment for 3 (AC3) and 5 minutes (AC5)..... | 122 |
| Figure 3.4 Histogram showing probability of second phase particles produced by 5 minutes heat treatment (blue histogram), among these the particles associated with pre-existing cavities are separately plotted (white histogram). | 123 |
| Figure 3.5 Probability of equivalent radius of pre-existing cavities produced by heat treatment for 3 (AC3) and 5 (AC5) minutes..... | 124 |
| Figure 3.6 Plot showing radius of pre-existing cavities versus radius of the particles they were associated with. | 125 |
| Figure 3.7 Evolution of mechanical parameters of the AC5 sample with time (a) strain versus time (b) strain rate versus time (c) stress versus time. The 3 stages of creep: primary (I), secondary (II) and tertiary (III) are marked in (b)..... | 128 |
| Figure 3.8 2D slices (a) of top view (XY) and (b) side view (YZ) from low resolution volume of AC5 sample at the start of deformation, the second phase particles are indicated in black and they are seen to line up along the grain boundary. Also, the region of interest is indicated, which is probed in the high resolution scans. The position of the two slices with respect to each other are indicated by the blue line. (c) High resolution 3D rendering of AC5 sample at start of deformation, with second phase particles (green) and pre-existing cavities (red)..... | 129 |
| Figure 3.9 3D rendered view of growth of cavity (red) alongside a second phase particle (green) as the AC5 sample strains (ϵ) with time (t, in minutes) | 130 |
| Figure 3.10 3D rendered view of nucleation and growth of cavity (red) alongside a second phase particle (green) as the AC5 sample strains (ϵ) with time (t, in minutes)..... | 131 |
| Figure 3.11 Volume of pre-existing and newly nucleated cavities with time, as seen in AC5 sample on subjecting it to high temperature deformation. The uncertain zone indicates the limit to resolution. The pre-existing cavity which was visible in the | |

| | |
|---|-----|
| uncertain zone, but could not be segmented is marked separately. The two cavities that were not visible in the uncertain zone are marked as newly nucleated. The error bar (in blue) has been calculated as per technique mentioned in section: 2.5.3.3 and is shown for only two cavities to maintain clarity in the plot..... | 132 |
| Figure 3.12 Shape change of pre-existing and newly nucleated cavities as a function of time in direction (a), (b) Perpendicular to tensile axis X and Y respectively and (c) Parallel to the tensile axis: Z (refer to Figure 3.8 for coordinate axis). The experimental transition time (T_t) for the various cavities is indicated by the grey region, average transition time is indicated by dotted line. | 133 |
| Figure 3.13 Plot of cavity growth rate (dV/dt) versus equivalent radius showing experimental cavity growth rate data for pre-existing and newly nucleated cavities, seen in AC5 sample on subjecting it to high temperature deformation..... | 134 |
| Figure 3.14 Plot of cavity growth rate (dV/dt) versus equivalent radius, showing comparison of experimental cavity growth data with diffusion and plasticity based cavity growth models in AC5 sample for 4 different cavities. The inter cavity spacing ($2l$) used in calculation has also been indicated for each cavity. The error bar (in blue, in (a)) has been calculated as per technique mentioned in section: 2.5.3.3. The transition radius (T_r) for the various cavities is indicated by dotted line. | 137 |
| Figure 3.15 (a) Plot showing change in transition radius obtained from model with time of sample deformation (b) Transition radius obtained experimentally versus transition radius from model, for AC5 sample. The red line is a straight line with a slope of 1..... | 140 |
| Figure 3.16 Plot showing (a) strain versus time and (b) strain rate versus time with applied strain rate indicated by red line..... | 142 |
| Figure 3.17 (a) LR Transverse 2D slice for Al-Cu sample after deformation at 250 min with region of 1 HR scan indicated by red box (b) HR Transverse 2D slice for Al-Cu sample after deformation at 250 min. (c) Volume versus time plot showing growth of cavities between 200 and 260 minutes. (cavities are in white and second phase particles in black) | 142 |
| Figure 4.1 (a) 3D rendered volume (combination of 4 HR volumes pixel size 100 nm) of sample at the start of deformation (cavities in red and Intermetallics in green). (b) Histogram showing probability of (b1) radius and (b2) sphericity of intermetallic. (c) Histogram showing probability of (c1) equivalent radius and (b2) sphericity of pre-existing cavity. Rolling direction is parallel to tensile direction..... | 145 |
| Figure 4.2 Plot showing evolution of (a) strain with time and (b) strain rate with time in sample..... | 149 |
| Figure 4.3 (a) Strain rate jump test for AZ31 sample at 673 K. The data relevant for the current work has been marked in red. Work of R. Boissière [144] .NOTE comma represent decimal point..... | 150 |

| | |
|--|-----|
| Figure 4.4 3D rendered volumes showing nucleation and growth of a cavity with strain, (marked at the bottom of each box) in sample. A different view of the cavity at the last scan is also shown, highlighted by a box for better comprehension of the 3 dimensional shape of the cavity (cavities are in red and intermetallics in green). | 151 |
| Figure 4.5 Transverse 2D slice of three cavity (a1) (b1) and (c1) at the time of nucleation and after growth (a2), (b2) and (c2). The relevant cavities have been encircled and the strains have been marked at the bottom left corner. (a3), (b3) and (c3) is 3D rendered image of cavities at strains corresponding 0.89, 0.92 and 0.92 respectively. | 152 |
| Figure 4.6 Average evolution of cavity statistics with strain (a) number density (b) volume fraction (c) total cavity volume. | 153 |
| Figure 4.7 (a) Transverse 2D slice from LR volume (pixel size 645 nm) at strain of 0.9. The red box presents the approximate dimension which is probed in a single HR volume (pixel size 100 nm, cavities are in white and intermetallics in black). (b) 3D rendered volume showing cavities and intermetallics in one high resolution (HR) volume imaged at strain of 0.9 (cavities are in red and intermetallics in green). | 154 |
| Figure 4.8 Schematic showing typical examples of evolution of cavity shape for (a) type 1A (b) type 1B (c) type 2 (d) type 3 (e) type 4 along with assigned symbols. Accompanied by a corresponding plot showing evolution of lengths with strain, along the principle growth directions. Orientation of the 3 directions is on the basis of coordinate system shown on top right corner of (a). | 156 |
| Figure 4.9 3D rendered volumes showing evolution of a cavity with strain (marked at the bottom of each box) in sample. Type of evolution has been marked using symbols at top left corner (see Table 4.1 for reference). A different view of the cavity at the last scan is also shown, highlighted by a box for better comprehension of the 3 dimensional shape of the cavity (cavities are in red and intermetallics in green). | 159 |
| Figure 4.10 Evolution of length of cavity (shown in Figure 4.9) along L, W, D dimension (represented by bounding box in right bottom) with strain. The type of evolutions have also been marked along with 3D rendered view of cavities in different evolution regimes. | 160 |
| Figure 4.11 Schematic illustration showing evolution of cavities during high temperature deformation, affected by grain boundary sliding..... | 161 |
| Figure 4.12 3D rendered volumes showing evolution of a cavity with strain, (marked at the bottom of each box) in sample. Type of evolution has been marked using symbols at top left corner (see Table 4.1 for reference). A different view of the cavity at the last scan has been also shown, highlighted by a box for better comprehension of the 3 dimensional shape of the cavity (cavities are in red). | 163 |
| Figure 4.13 Evolution of length of cavity (shown in Figure 4.12) along L, W, D dimension (represented by bounding box in right bottom) with strain. The type of evolutions have also been marked along with 3D rendered view of cavities in different evolution regimes. | 164 |

| | |
|---|-----|
| Figure 4.14 3D rendered volumes showing evolution of a cavity with strain, (marked at the bottom of each box) in sample. Type of evolution has been marked using symbols at top left corner see Table 4.1 for reference. A different view of the cavity at the last scan has been also shown, highlighted by a box better comprehension of the 3 dimensional shape of the cavity. (cavities are in red and intermetallics in green). | 165 |
| Figure 4.15 Evolution of length of cavity (shown in Figure 4.14) along L, W, D dimension (represented by bounding box in right bottom) with strain. The type of evolutions have also been marked along with 3D rendered view of cavities in different evolution regimes. | 166 |
| Figure 4.16 3D rendered volumes showing evolution of a cavity with strain, (marked at the bottom of each box) in sample. Type of evolution has been marked using symbols at top left corner see Table 4.1 for reference. A different view of the cavity at the last scan has been also shown, highlighted by a box for better comprehension of the 3 dimensional shape of the cavity (cavities are in red and intermetallics in green). | 167 |
| Figure 4.17 Evolution of length of cavity (shown in Figure 4.16) along L, W, D dimension (represented by bounding box in right bottom) with strain. The type of evolutions have also been marked along with 3D rendered view of cavities in different evolution regimes. | 168 |
| Figure 4.18 Normalized deformation fields or $\epsilon_{eq} / \langle \epsilon_{eq} \rangle$ strain component at 573 K at $\langle \epsilon_{eqe} \rangle = 0.15$. (b) Equivalent normalised deformation distribution function at 573 K and for different states of deformation. Work of T. Dessolier [114] | 169 |
| Figure 4.19 Plot showing probability of different type of evolution mechanisms with strain. | 170 |
| Figure 4.20 Plot showing pathway of different types of evolution, shown for the 30 tracked cavities with strain. | 171 |
| Figure 4.21 (a) SEM micrograph of a AZ31 sample with an imposed micro grid (b) a cropped 2D slice showing cavity in a matrix , work of T. Dessolier [114]. The red box in (a) indicates the size of the cropped slice shown in (b). | 173 |
| Figure 4.22 Schematic illustration of geometry of cavity (a) geometry for classical model. Geometry modifications used while applying (a) grain boundary diffusion model (b) lattice diffusion model..... | 173 |
| Figure 4.23 Plot showing volumetric growth rate as per grain boundary diffusion, lattice diffusion and diffusion superplasticity, along with experimental data (cyan markers)..... | 175 |
| Figure 4.24 Effect of (a) r/l (b) stress (c) grain boundary diffusivity on volumetric growth rate based on grain boundary diffusion, lattice diffusion and diffusion superplasticity models. The parameters variations relevant to the plots are listed in Table 4.3. | 176 |

| | |
|--|-----|
| Figure 4.25 Plot showing volumetric growth rate as per constrained grain boundary diffusion model (red), along with experimental data (cyan markers) | 178 |
| Figure 4.26 Schematic showing a cylindrical cavity of cross section area A_c and length $2r$ lying on a grain boundary, sliding at a rate of u_b (a) in 2D [65] (b) in 3D | 178 |
| Figure 4.27 Plot showing volumetric growth rate as per grain boundary sliding model corresponding to different cross section, transvers to sliding direction, along with experimental data (cyan markers)..... | 179 |
| Figure 4.28 Plots showing volumetric growth rate for three cavities in (a) (b1) and (c1) growing by type 1A mechanism. Experimental data shown by red markers. Cyan markers in the background are experimental data from all cavities. (b2) and (c2) are plots with constrained growth model with adjusted stress values corresponding to (b1) and (c1) respectively..... | 181 |
| Figure 4.29 Plots showing volumetric growth rate for four cavities in (a) (b) (c) and (d) growing by type 1B mechanism. Experimental data shown by black markers. Cyan markers in the background are experimental data from all cavities. A 3D rendered view of the cavity corresponding to each plot is provided on the bottom right corner for reference..... | 182 |
| Figure 4.30 Plots showing volumetric growth rate of two cavities in (a) and (b) growing by type 2 mechanism. Experimental data shown by green markers. Cyan markers in the background are experimental data from all cavities. A 3D rendered view of the cavity corresponding to each plot is provided on the bottom right corner for reference..... | 184 |
| Figure 4.31 Schematic illustration (a) showing indication of grain boundary sliding seen through superimposed 3D rendering of position of intermetallic in a low (grey) and a high strain state (green) (cavity in red) (b) of definition of different vectors and directions used in quantifying grain boundary sliding. | 185 |
| Figure 4.32 Plots showing displacement of intermetallics in (a) X1 and X2 direction (from 0 to 0.9 strain) (b) NGB direction with strain. | 187 |
| Figure 4.33 Plot showing net length of cavity along (a) S1 direction versus displacement of grain boundary in this direction (b) S2 direction versus displacement of grain boundary. Red lines are straight lines with slope one, shown to indicate a direct proportionality..... | 188 |
| Figure 4.34 Plot showing volumetric growth rate of a cavity shown by magenta (type 3) and black (type 1B) markers. The growth rate by grain boundary sliding (GBS) model corresponding to sliding along S1 shown by green line, (A1 is cross section transverse to S1) and corresponding to sliding along S2 shown by red line, (A2 is cross section transverse to S2). 3D rendered view of cavity growing under S1 and S2 sliding have also been shown for reference. (See Figure 4.14 for growth montage of this cavity) | 189 |

Figure 4.35 Plot showing a comparison of volumetric rate predicted from grain boundary sliding model using u_b estimated from macro strain rate (dashed blue line) and that measured locally (dashed blue line)..... 190

Figure 4.36 Plot showing $2\gamma/r$ versus strain for different cavities that evolved by type 4 mechanism during deformation of the sample,..... 191

Figure 4.37 (a,b,c1) Plots showing comparison of experimental data from 3 cavities (red markers) of shrinkage of cavity compared with diffusion based sintering (in black). (c2) Plot showing data from cavity in (c1) compared with shrinkage rate due grain boundary diffusivity. Data for remaining cavities showing type 4 evolution is indicated by cyan markers in the background. 192

Figure 4.38 (a) Plot showing normalised cavity growth versus time for cavities evolving by type 4 mechanism. (b) 3D rendered view showing the evolution of a cavity with strain..... 193

List of symbols and abbreviations

Symbols

| | | |
|-----------------------|--|----------------------------------|
| \dot{u}_b | Grain boundary sliding rate | $\text{m} \cdot \text{s}^{-1}$ |
| $\dot{\epsilon}_{CO}$ | Coble steady state creep rate | s^{-1} |
| $\dot{\epsilon}_{NH}$ | Nabarro-Herring steady state creep rate | s^{-1} |
| A_{CO} | Constant (Coble creep) | |
| A_{NH} | Constant (Nabarro-Herring creep) | |
| A_{gb} | Surface area of displaced grain boundary | m^2 |
| A_v | Surface area of cavity | m^2 |
| Q_{gb} | Activation energy for grain boundary diffusion | $\text{J} \cdot \text{mol}^{-1}$ |
| Q_L | Activation energy for lattice diffusion | $\text{J} \cdot \text{mol}^{-1}$ |
| r_c | Critical radius | m |
| γ_{gb} | Interfacial energy of grain boundary | $\text{J} \cdot \text{m}^{-2}$ |
| A_c | Cross section of cavity | m^2 |
| C_{MMG} | Monkman-Grant constant | |
| D_0 | Diffusion frequency factor | $\text{m}^2 \cdot \text{s}^{-1}$ |
| D_{gb} | Grain boundary diffusivity | $\text{m}^2 \cdot \text{s}^{-1}$ |
| D_l | Lattice diffusivity | $\text{m}^2 \cdot \text{s}^{-1}$ |
| T_r | Transition radius | m |
| T_t | Transition time | s |
| V_t | Normalised crack tip velocity | |
| d_{sg} | Subgrain size | m |
| f_s | Facet size | m |
| t_r | Time to rupture | s |
| α_r | Constant (Constrained diffusion) | |
| $\dot{\epsilon}$ | Strain rate | s^{-1} |
| $\dot{\epsilon}_{ss}$ | Steady state strain rate | s^{-1} |
| σ_{ss} | Steady state stress | MPa |
| ΔG | Change in free energy | $\text{J} \cdot \text{mol}^{-1}$ |

| | | |
|----------------|---|----------------------|
| ΔP | Internal gas pressure | Pa |
| Σ | Normalised stress | |
| A | Dimensionless constant (Mukherjee Bird Dorn equation) | |
| A' | Constant (sub grain size effect) | |
| B | Constant (power law creep) | |
| d | Grain size | m |
| E | Elastic modulus | Pa |
| k | Boltzmann constant | J. K ⁻¹ |
| L | Diffusion length | m |
| n | Stress exponent | |
| q | Subgrain size exponent | J. mol ⁻¹ |
| r | Radius | m |
| T | Temperature | K |
| t | Time | s |
| T _m | Melting temperature | K |
| V | Volume | m ³ |
| γ | Surface energy | J. m ⁻² |
| Ω | Atomic volume | m ³ |
| G | Shear modulus | Pa |
| Q | Activation energy | J. mol ⁻¹ |
| b | Burgers vector | m |
| l | Half of inter cavity spacing | m |
| p | Inverse grain size exponent | |
| δ | Grain boundary width | m |
| ϵ | Strain | |
| σ | Applied stress | Pa |
| $\omega = r/l$ | Ratio of cavity radius and half of inter cavity spacing | |

Symbols: tomography related

| | | |
|--------------------|----------------------------|-----------------|
| \mathcal{F} | Fourier transform | |
| \mathcal{F}^{-1} | Inverse Fourier transform | |
| $I_{\theta,D}$ | Intensity | |
| T_{θ} | Transmittance function | |
| δ_r | Refractive index decrement | |
| k | Wave number | m^{-1} |
| β | Absorption index | |
| η | Refractive index | |
| λ | Wavelength | m |

Abbreviations

| | |
|------------|---|
| SAXS | Small Angle X-ray Scattering |
| SANS | Small Angle Neutron Scattering |
| OM | Optical Microscopy |
| SEM | Scanning Electron Microscopy |
| TEM | Transmission Electron Microscopy |
| FIB-SEM | Focused Ion Beam Scanning Electron Microscopy |
| XMT | X-ray Micro tomography |
| SAED | Selected area electron diffraction |
| HAADF-STEM | High Angle Annular Dark Field – Scanning Transmission Electron Microscopy |
| 2D | Two dimensional |
| 3D | Three dimensional |
| PID | Proportional Integral Derivative |
| HR | High Resolution |
| LR | Low Resolution |
| ROI | Region of Interest |
| FBP | Filtered Back Projection |
| DVC | Digital Volume Correlation |

Introduction

In the context of fossil fuel depletion and environmental challenges for reducing greenhouse emissions, finding solutions for saving energy in particular in the automotive sector has become vital. This driving force for lightening the structures pushes for the use of light alloys such as magnesium or aluminium based alloys [1,2]. Structural weight saving has in fact been a key axis of research of The Centre of Excellence of Multifunctional Architected Materials (CEMAM), that has partly funded this thesis.

While light alloys are highly desirable, forming of such alloys is hugely dependent on the crystallographic structure, on the micro-structure and on the loading conditions (temperature, strain rate, stress) [3]. Hot and warm metal forming is commonly employed to process and shape such alloys [4]. Many aluminium and magnesium alloys have also been known to show super plastic deformation when deformed under specific temperature (generally high) and strain rates, Figure. 1 (a) shows an example of a Mg alloy (AZ91) showing nearly 1000% elongation prior to failure. Commercialisation of this ability to show such exceptional deformation, into viable metal forming processes, has been keenly pursued over the past few decades. Figure. 1 (b) shows prototype of an auto part developed by forming a magnesium alloy (AZ31B) under superplastic conditions [5]. This is especially true for commercial magnesium based alloys, owing to their poor deformability at room temperature.

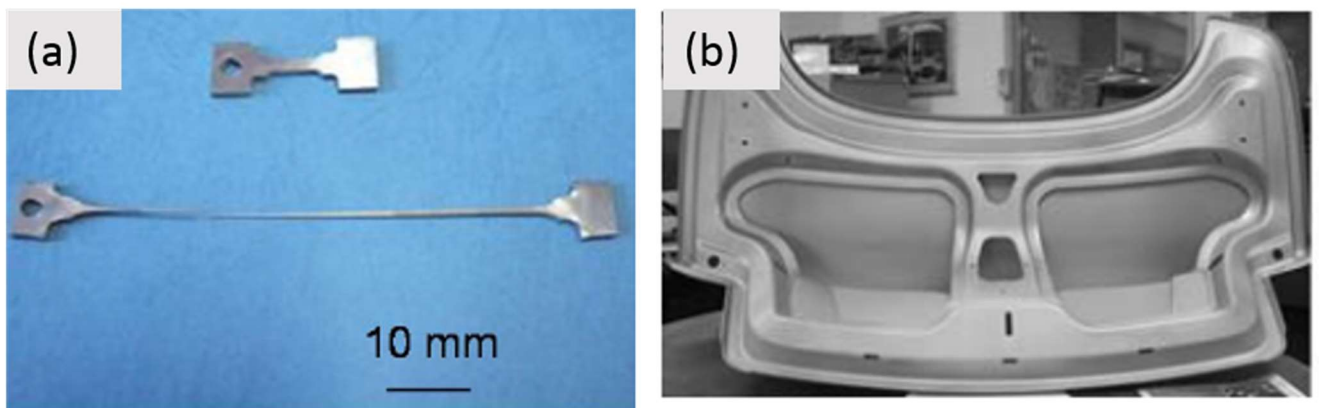


Figure. 1 (a) Tensile sample of an AZ91 alloy processed by ECAE showing superplastic deformation [6] (b) Prototype auto parts superformed from Magnesium Alloy (AZ31B) [5]

While deformation at high temperature eases metal forming, the required high temperature can induce damage of material. This damage during high temperature deformation (at temperature greater than $0.5 T_m$: Melting temperature) often involves formation of voids or creep cavities [7,8]. Hence nucleation and growth of cavities during high temperature deformation has been a subject of great interest for researchers over the years.

Nucleation of cavities has been generally linked to stress concentrations on second phase particles, grain boundaries, and triple junctions [7,9]. Growth of cavities on the other hand is attributed to diffusion, plasticity or superplasticity.

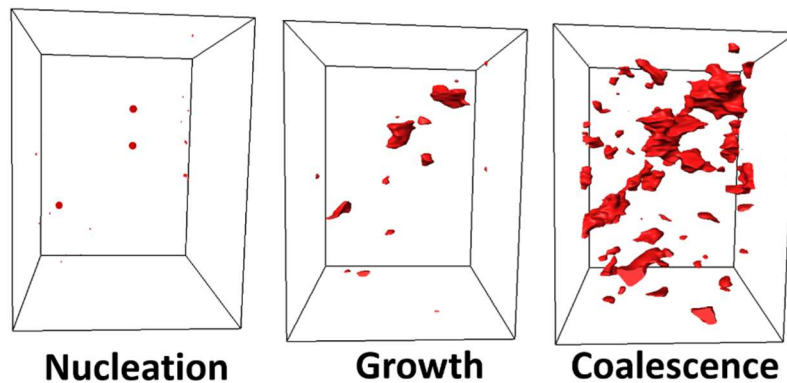


Figure. 2 Schematic illustration showing nucleation, growth and coalescence of cavities (red).

In spite of significant theoretical analysis of cavity growth driven by diffusion, plasticity and superplasticity, experimental investigations of these theories has been thread bare. This is especially true for mechanisms operating during early stages of growth. One reason for this has been the lack of suitable characterisation tool. The study of early stages of deformation requires good resolution (less than $1 \mu\text{m}$) hence has been pursued mainly by post mortem technique like electron microscopy [10]. But post mortem studies are not always convenient to study the dynamics of nucleation and growth. Over the past few years *in situ* investigations on creep cavities have also been done using microtomography [11–14]. However owing to its limited resolution (coarser than $2 \mu\text{m}$) studies have been limited to investigating cavity growth driven by plasticity (operating during late stages of growth) [11,15,16].

In the present study, *in situ* 3D imaging has been combined with nano scale pixel size (100 nm) to provide new insights into the high temperature deformation process. The study was first initiated on model Al-Cu alloys. Heat treatment of this alloy

allowed by controlled generation of copper rich second phase particles of desired size. These particles were expected to act as sites for cavity nucleation. Using the technique nucleation and growth of cavities due to diffusion and plasticity have been explored. This was followed by investigating creep cavity growth in commercial magnesium alloy: AZ31.

AZ31 is a commercially viable magnesium alloy (typical composition: Al 3 wt %, Zn 1 wt %, Mg balance) thanks to its unique properties like low density and high specific strength and low price [3]. The alloy is known to exhibit superplastic deformation when deformed at specific strain rates and elevated temperatures [17–21]. In this study *in situ* nanotomography was used to explore cavity nucleation and growth during deformation of AZ31 alloys in super plastic regime. Effect of grain boundary sliding on cavity growth was explored and applicability of available models during such growth was examined.

Layout of the thesis

- **Chapter 1** introduces the readers to the basic scientific concept used in the thesis. This includes sections on: high temperature deformation in materials, creep cavity nucleation and growth models and techniques for creep cavity characterization. The objective for the thesis are laid out at the end of this chapter.
- **Chapter 2** deals with the materials and methods used in this thesis. The chapters begins with a description of sample preparations for the two: Al-Cu and AZ31 magnesium alloy that were investigated in this work. Followed by a detailed description of the *in situ* high temperature deformation nanotomography setup that has been developed as a part of this thesis. This is followed by a section on data acquisition, data processing and image analysis techniques used / developed for this work.
- **Chapter 3** is dedicated to the presenting results and discussions on investigation of creep cavity nucleation and growth on the Al-Cu alloy.
- **Chapter 4** caters to studying the nucleation and growth of creep cavities in commercial AZ31 magnesium alloy, while it deforms in a superplastic regime.
- **Conclusions** sums up the key outcomes of this thesis.

- **Perspectives** lists the further improvements that can be made to the present study and suggests new studies that can be undertaken using the technique developed.

Chapter 1. State of the art

The purpose of this chapter is to introduce the readers to the basic scientific concepts used in this thesis. The chapter begins with an introduction to high temperature deformation in materials. This section describes in brief the various mechanisms, which govern deformation at high temperature in crystalline metals. It is known that at high temperature, damage occurs by nucleation, growth and coalescence of cavities. Investigation of nucleation and growth of these cavities is the primary focus of this thesis. Hence the second section presents the state of art of the various creep cavity nucleation and growth models. The following section focuses on the various techniques that have been historically used for characterising creep cavities. The last section is dedicated to describing X-ray tomography, since this is the technique chosen for creep cavity characterisation in this thesis.

1.1 High temperature deformation

When materials are subjected to high temperature ($T > 0.5 T_m$, where T_m is melting point), they tend to deform at a stress, much lower than their yield strength (at conventional strain rate). Such time dependent plasticity at high temperature is referred to as creep.

Plasticity under creep conditions can be tested by heating materials at a high temperature ($T > 0.5 T_m$) under two types of loading conditions:

- Constant load: by applying a dead weight on the sample to cause it to deform under constant load. The true stress of the sample essentially changes because as the sample strains, there is a change in the cross section, accompanied by a change in stress. This is how conventional creep tests are performed.
- Constant strain rate: by pulling or compressing the sample at a controlled speed causing it to deform at a constant rate. Here again, to maintain a constant true strain rate, the ram speed must be adjusted to compensate for the change in length of the sample during straining. Such tests can be done either in tension or compression.

Such studies are generally performed under uniaxial loading conditions.

Creep in pure metals is generally known to proceed in three stages (see Figure 1.1):

- Stage I: Primary creep, is a transient regime in which dislocation structure evolves.

In constant load condition this is characterized by a decrease in strain rate (Figure 1.1 a)

In constant strain rate conditions, work hardening in this regime leads to an increase in stress (Figure 1.1 b).

- Stage II: In secondary creep the work hardening is balanced by the recovery and consequently a steady creep rate is achieved.

In constant load condition this is characterized by a constant strain rate called the steady state strain rate ($\dot{\epsilon}_{ss}$) (Figure 1.1 a).

In constant strain rate conditions, the stress becomes constant in this regime, this stress is referred to as steady state stress (σ_{ss}) (Figure 1.1 b).

- Stage III: Tertiary creep is marked by the onset of various instabilities like void coalescence, onset of necking, recrystallization etc. This leads to an eventual failure.

In constant load condition this is characterized by an increase in strain rate (Figure 1.1 a).

In constant strain rate conditions, the stress begins to decrease in this regime (Figure 1.1 b).

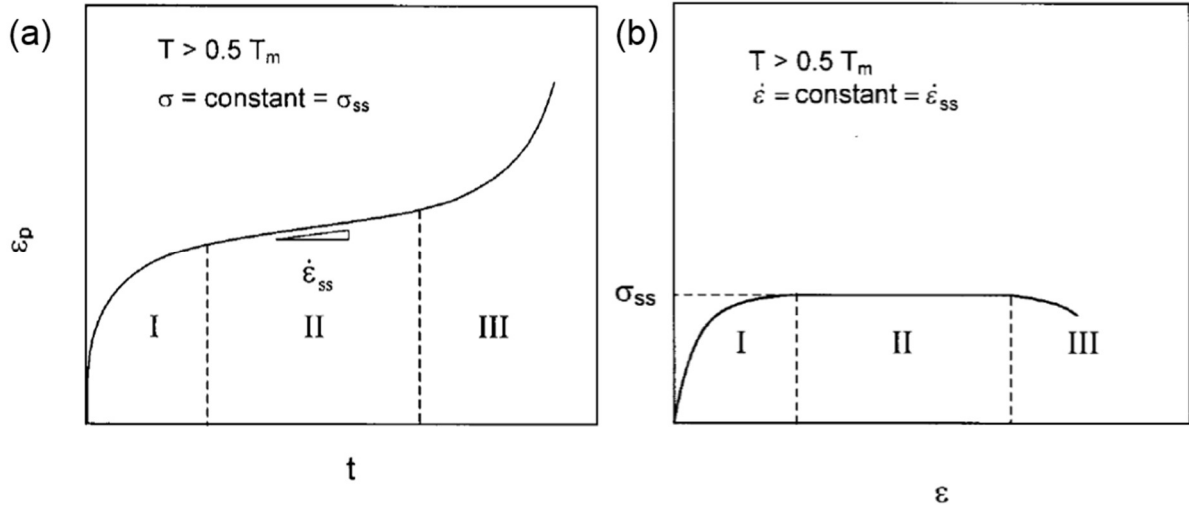


Figure 1.1 Constant (a) true stress (strain as a function of time) and (b) strain rate creep (stress as a function of strain) behaviour in pure metals [22]

Bird, Mukherjee, and Dorn [23] formulated the creep strain rate for steady state as a function of stress, temperature and grain size given by:

$$\dot{\epsilon}_{ss} = A \frac{D_0 G b}{kT} \left(\frac{\sigma}{G}\right)^n \left(\frac{b}{d}\right)^p \exp\left(\frac{-Q}{kT}\right) \quad (1.1)$$

where A is a dimensionless constant D_0 is the diffusion frequency factor, G is shear modulus, b is burgers vector, σ is the applied stress, n is the stress exponent, p is inverse grain size exponent, Q is the activation energy, k is Boltzmann constant, T is the temperature, d is grain size.

It is of importance to predict the steady state strain rate because it in turn allows to estimate the time to rupture (t_r) using the Monkman-Grant relationship [24].

$$\dot{\epsilon}_{ss} t_r = C_{MMG} \quad (1.2)$$

where C_{MMG} is the Monkman-Grant constant, such that the strain to failure is often a fixed multiple of this constant. This is a phenomenological relationship, Figure 1.2 shows a plot of data from dispersion strengthened cast aluminium [25] where such a relationship has been observed.

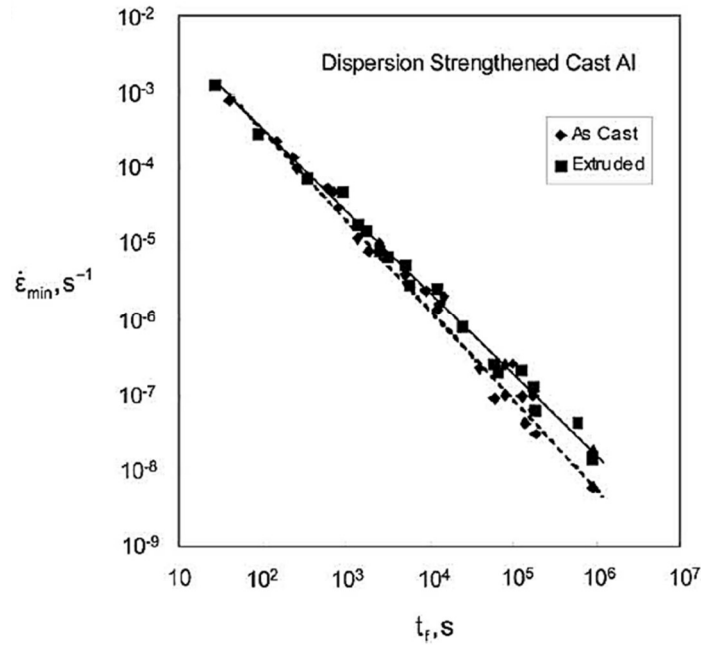


Figure 1.2 The steady-state creep-rate ($\dot{\epsilon}_{min}$) versus time-to-rupture t_f for dispersion strengthened cast aluminium deformed. Note: the $\dot{\epsilon}_{min}$ and t_f are same as $\dot{\epsilon}_{ss}$ and t_r of equation (1.2) [7].

Creep tests are carried out to determine the stress exponent, activation energy values and inverse grain size exponent. These parameters in turn indicate the active creep mechanism during steady state. Stress exponent can be obtained by a battery of tests at constant temperature and different stress levels or strain rate jump tests. Activation energy is obtained from series of tests carried out at constant stress and varying temperatures. Similarly carrying out creep tests for materials with different grain sizes at a constant temperature and stress is used to estimate the inverse grain size exponent.

It should be noted that the stress exponent may vary during deformation with change in mechanical parameter (stress and strain rate) a material is subjected to. Further deformation at high temperature may also assist grain growth in a material.

Deformation in materials is driven by the various defects present in the material: vacancy, dislocations and grain boundaries. Depending on the defects driving the deformation, the mechanism of deformation differs.

In the following section the three major types of creep, will be described along with a prelude on the corresponding defects which participate in each of these mechanisms:

1. Diffusion creep
2. Dislocation creep
3. Grain boundary sliding

Different deformation modes that contribute to the creep strain are diffusion, slip or grain boundary sliding. It should be noted that the process that controls the creep rate, is not necessarily the same as the one that produces strain [26].

1.1.1 Diffusion creep

At any temperature there is an equilibrium concentration of vacancies present in a material. Depending on the stress state, a gradient of vacancy in a system may occur. Vacancies then flow down the concentration gradient, resulting in an opposite flow of matter [26]. Hence under the effect of stress, vacancies can induce material strain by transport of matter.

Nabarro-Herring [27,28] proposed a mechanism of deformation in which excess vacancies are created on the grain boundary perpendicular to the tensile axis. This gradient of vacancy concentration between grain boundaries perpendicular and parallel to the tensile axis, results in a flow of matter. The vacancies move from grain boundary normal to tensile axis, to the grain boundary along tensile axis through the lattice, causing a net elongation of the grain, see Figure 1.3.

For such a mechanism to be active it is imperative that:

- There are enough sources of vacancies, which mean large grain boundary area or small grains.
- The temperature is high enough to cause sufficient vacancy flow.
- The stress is low enough, for dislocation motion to be difficult.

In case of lattice diffusion, the steady state strain rate $\dot{\epsilon}_{NH}$ is given by Nabarro-Herring creep [22]:

$$\dot{\epsilon}_{NH} = A_{NH} \frac{D_l \sigma \Omega}{kT d^2} \quad (1.3)$$

where A_{NH} is a constant D_l is the lattice self-diffusion coefficient and Ω is the atomic volume.

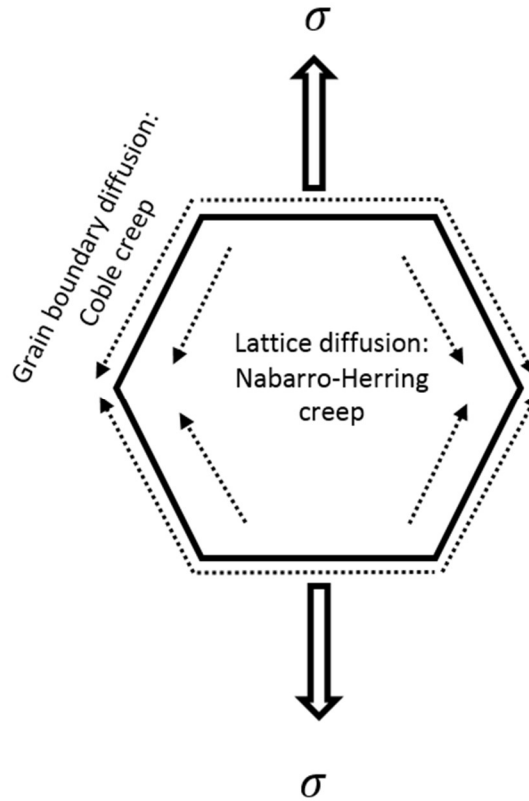


Figure 1.3 Schematic illustration showing the mechanism of Nabarro-Herring creep (via lattice diffusion of vacancies) and Coble creep (via grain boundary diffusion of vacancies) in a grain, under the effect of a tensile stress: σ . The dotted lines indicate vacancy flux.

Coble [29] later proposed a mechanism for creep for polycrystals in which grain boundary diffusion was more overwhelming as compared to lattice diffusion, see Figure 1.3. Hence transport of matter occurred via grain boundary instead of the lattice. This mechanism could be dominant at lower temperatures, where owing to its lower activation energy, grain boundary diffusion is more prominent.

The steady state Coble creep rate $\dot{\epsilon}_{CO}$ is:

$$\dot{\epsilon}_{CO} = A_{CO} \frac{\delta D_{gb} \Omega \sigma}{kT d^3} \quad (1.4)$$

where, A_{co} is a constant, δ is the grain boundary width and D_{gb} is the grain boundary diffusion coefficient.

For both Nabarro-Herring and Coble creep the stress exponent (n) is equal to 1, but the grain size exponent (p) increases from 2 in Nabarro Herring creep to 3 in Coble creep.

1.1.2 Dislocation creep

Dislocations are line defects that are a boundary between the slipped and unslipped region in a material. There is a strain field associated with the dislocations, thanks to which they react to the applied stress, which causes them to move. This movement in turn results in plastic deformation of materials. Dislocation creep is comprised of such deformation.

Depending on the obstacle to dislocation motion, dislocation creep can be divided into: climb controlled and glide controlled.

1.1.2.1 Climb controlled creep:

In this mechanism, big obstacles hinder dislocation motion, and hence diffusion assisted recovery is needed to abet dislocation motion. Here climb is the rate controlling mechanism. A stress exponent of 5 is attributed to such deformation while the activation energy is that of self-diffusion. Climb control is commonly observed in pure metals but also seen in some alloys, and is commonly referred to as Class M (M for pure metal) behaviour. The steady state strain rate would be:

$$\dot{\epsilon}_{ss} \propto \sigma^n, n \cong 5 \quad (1.5)$$

Weertman [30] proposed one of the first dislocation models in which glide occurs over large distances till dislocations are held up at barriers such as dipoles. Recovery occurs through climb leading to dislocation annihilation. Such deformations often leads to formation of grain substructures during primary creep which stabilises into sub grain boundaries during steady state creep [31]. The subsequent macroscopic deformation during the steady state is due to the migration of these subgrain boundaries [32].

Sherby et al [33] sought to define the effect of subgrain size on the steady state creep rate. The relationship between subgrain size and stress [34] was established as:

$$d_{sg} \cong Sb \left(\frac{\sigma}{E} \right)^{-1} \quad (1.6)$$

where d_{sg} is the subgrain size, S a constant and E elastic modulus. At high stresses ($\frac{\sigma}{E} > 10^{-2}$) a stronger dependence on stress was seen:

$$d_{sg} \propto \left(\frac{\sigma}{E} \right)^{-2} \quad (1.7)$$

To determine the effect of the subgrain size on creep strain rate, constant structure (hence constant subgrain size) creep tests were conducted on a metal undergoing subgrain formation during creep. It was found that the dependence of stress on instantaneous creep rate was different from that of the steady state creep rate and rightly so, owing to variation in subgrain size. The instantaneous strain rate was defined by:

$$\dot{\epsilon}_i \propto A' d_{sg}^q \sigma^n \quad (n \cong 8, q \cong 3) \quad (1.8)$$

where A' is a constant and q the subgrain size exponent. A number of investigators performed stress drop tests on high purity polycrystalline aluminium [35–37], where the stress exponent was found to be an average of 8. Similarly creep rate dependence on metastable subgrain size from similar tests have revealed the subgrain size exponent to be 3 [33,35,38]. Note that when subgrain size is free to adjust to stress, a stress exponent of $\cong 5$ is obtained.

1.1.2.2 Glide controlled creep

When obstacles to the dislocations are on the scale of the dislocation core they can be overcome by thermal agitation. In such cases, both rate controlling and strain producing mechanism is glide. For example interaction of dislocation with solutes can manifest as solute segregation around dislocations or chemical interaction of solutes [39] with dislocation (Suzuki effect). Such interactions often hinder dislocation motion making glide of dislocation difficult. As a result of hindered glide, glide rates can be slower than climb, hence glide becomes the rate controlling

mechanism. In glide controlled creep, no subgrains are observed and this is commonly referred to as Class A (A for alloys) behaviour. Class A behaviour is not observed in pure metals, but Class M behaviour is sometimes observed in alloys too. A stress exponent of 3 is attributed to such deformations. The steady state strain rate is given by:

$$\dot{\epsilon}_{ss} \propto \sigma^n, n \cong 3 \quad (1.9)$$

At very high stresses and intermediate temperatures, an exponential dependence of strain rate on stress appears, also referred to as 'power law breakdown'. The steady state strain rate under such conditions is given by:

$$\dot{\epsilon}_{ss} \propto \exp(B\sigma) \quad (1.10)$$

where B is a constant.

1.1.3 Superplasticity

A grain boundary is a two dimensional crystal defect which introduces misorientation in a crystal. Superplasticity is comprised of sliding of grain boundaries. It is defined as the ability of polycrystalline materials to exhibit in a generally isotropic manner, very high elongations prior to failure [40]. Such behaviour has two main prerequisites: small and stable grain size (less than 10 μm) and high temperature of deformation (T greater than 0.5 T_m). Conventionally superplasticity is associated with low strain rates from 10^{-5} to 10^{-3} s^{-1} .

A strain rate sensitivity between 0.33 and 1 (strain rate sensitivity is the inverse of stress exponent) and a stress exponent between 1 and 3, in equation (1.1) generally defines the steady state strain rate for deformation governed by this mechanism.

Grain boundary sliding is accepted as the predominant mechanism responsible for superplasticity. The cavities that would form as a result of extensive sliding of grains must be accommodated by a complementary mechanism. The two major accommodating mechanisms proposed are those involving: diffusion and dislocations.

The dislocation based model was first proposed by Ball and Hutchinson [41]. It said that grains in favorable position undergo grain boundary sliding, this would produce

stress concentrations at obstacles like triple points. These stress concentrations are accommodated by generation of dislocations which pile up at the next grain boundary. The rate controlling step here is the removal of dislocations by climb in or along grain boundary, see Figure 1.4. Such models predicts $n = 2$, $p = 2$ or $p = 3$ and diffusion coefficient D can be D_{gb} or D_l depending on whether dislocation moves along grain boundary or within the grain respectively.

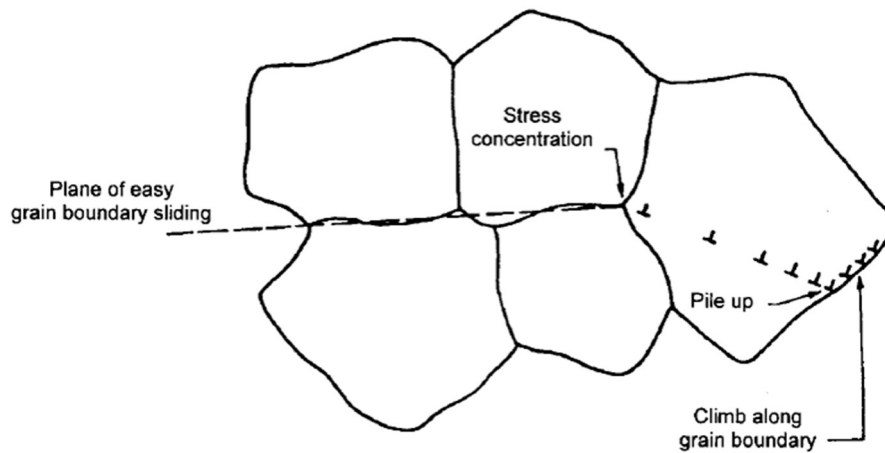


Figure 1.4 Schematic illustration of dislocation based grain boundary sliding accommodation mechanism proposed by Ball and Hutchinson [41].

The diffusion based accommodation mechanism was first suggested by Ashby and Verral [42]. It runs on a topological argument based on the fact the net shape of the grains remains unchanged during the deformation, see Figure 1.5 (a) and (c). There is a transport of matter along the grain boundary (Figure 1.5 d-e), which temporarily changes the shape of the grain and causes a switch in the neighboring grain, as can be seen in Figure 1.5 (a-c). Further diffusion helps in restoring the original grain shape. It was however pointed out that this model does not consider the long diffusion paths, indicated as A and B in Figure 1.5 (e) [43].

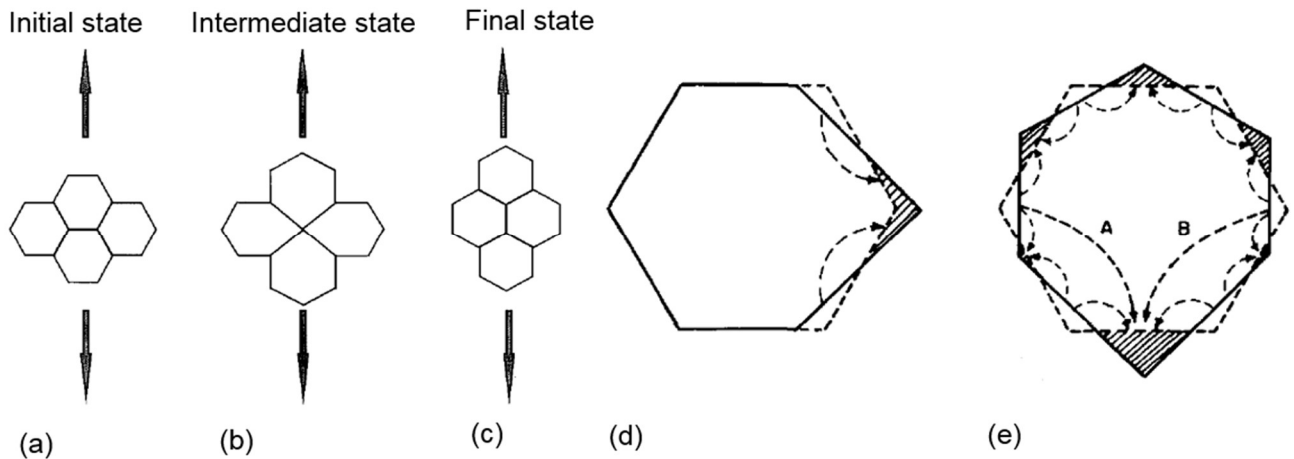


Figure 1.5 Schematic illustration of diffusion based accommodating mechanism during grain boundary sliding as proposed by Ashby and Verral in (a) initial (b) intermediate and (c) final state. (d-e) Illustration showing the possible diffusion paths of matter (in dotted lines) during the transition from initial to final state. A and B indicate diffusion paths that were not accounted in this model [42].

Taking these diffusion paths into consideration, another mechanism based on diffusion was proposed [43]. This is schematically depicted in Figure 1.6. As per this mechanism, the diffusion brings the grain into elongated shape, as seen in Figure 1.5 (c). The subsequent change in shape as seen in in Figure 1.5 (d-e) is attributed to reduction in free energy by reducing the overall grain boundary area. This change brings back the grains to the original shape hence the mechanism is shape preserving.

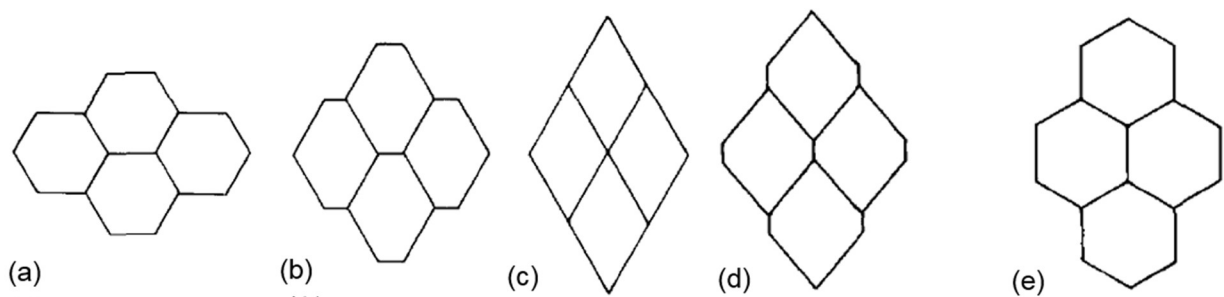


Figure 1.6 Schematic illustration of diffusion based accommodating mechanism during grain boundary sliding as proposed by Lee [43].

It should be noted that unlike plasticity and diffusion based creep deformation, the shape of grains remains unchanged during superplastic deformation.

Table 1.1 summarizes the various creep mechanisms that were described in this section along with a few others. This table lists the n , p and Q parameter for each of

them, and the temperature and stress where such mechanisms are likely to active. Here Q_L stands for activation energy for diffusion via lattice and Q_{gb} stands for activation energy for diffusion via grain boundary.

Table 1.1 Summary of various creep mechanisms, the temperature and stress range are indicative, for precise values, deformation mechanisms maps must be consulted.

| Creep mechanism | n / stress dependence | p | Q | Stress range | Temperature range |
|--|--|----------|---------------|---------------------|--------------------------|
| Diffusion (Nabarro-Herring) [27,28] | 1 | 2 | Q_l | Low | High |
| Diffusion (Coble) [29] | 1 | 3 | Q_{gb} | Low | Low |
| Diffusion (Harper-Dorn) [44] | 1 | 0 | Q_l | Low | Near melting point |
| Dislocation (Climb controlled) [45] | 5 | 0 | Q_l | Intermediate | Intermediate |
| Dislocation (Glide controlled) [30] | 3 | 0 | Q_l | | |
| Dislocation (Power law breakdown) | $\dot{\epsilon}_{ss} \propto \exp(B\sigma)$ B is a constant | 0 | $\sim Q_l$ | High | Intermediate |
| Grain boundary sliding [41] | 2 | 2-3 | Q_l, Q_{gb} | Low | Intermediate-high |

1.1.4 Deformation mechanism map

From the previous sections it is clear that there are several possible mechanisms which govern deformation in materials during high temperature deformation. It is often interesting to know which deformation mechanism is dominant in a material, this obviously depends on the various mechanical parameters (stress and strain rate), temperature and structure (grain size, dislocation density of the material etc). Deformation mechanism maps or Ashby maps present a very convenient way to map out the dominant deformation mechanism under a given mechanical condition [46,47].

The two axis of the maps are normalized stress (σ/G), and temperature (T/T_m) with iso strain rate superimposed on it, showing the strain rate expected by applying a combination of stress and temperature. The map indicates the regions in which different deformation mechanisms are active. There are two other ways of presenting this map: normalized strain rate versus normalized stress and normalized strain rate versus normalized temperature.

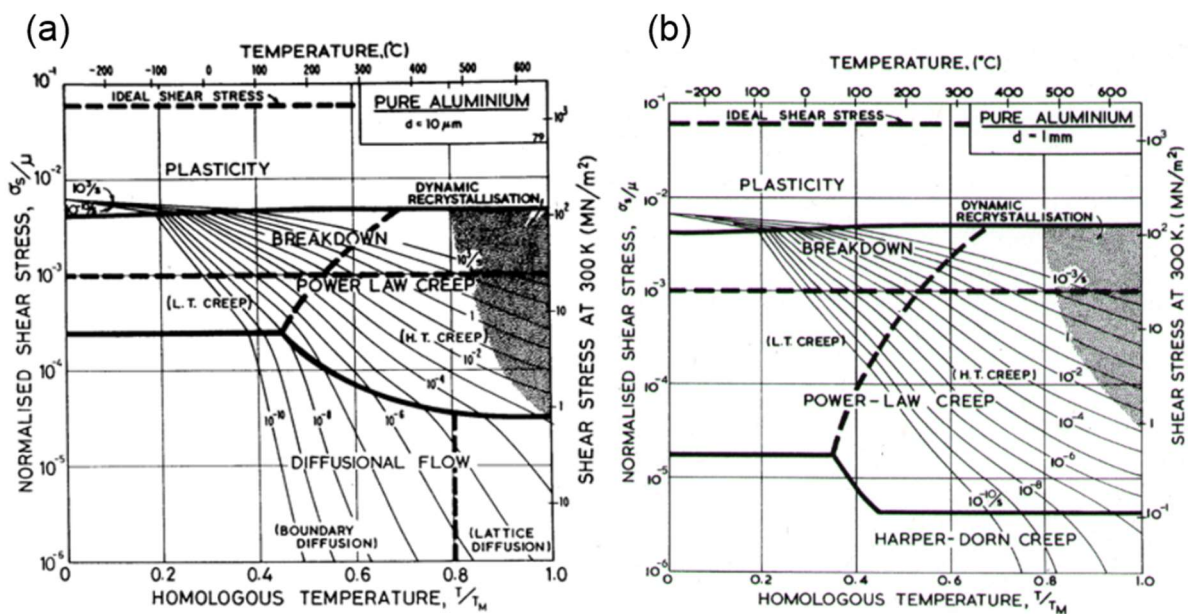


Figure 1.7 Deformation mechanism map for pure aluminium with (a) grain size $10 \mu\text{m}$ and (b) grain size 1mm [47]

Figure 1.7 shows an example of one such map for pure aluminium at two different grain sizes. Comparative examination of the two map reveals information like Harper Dorn creep [44] replaces diffusional flow at large grain sizes.

1.2 Creep cavities

During high temperature deformation, formation, growth and coalescence of cavities (R type voids) or grain boundary triple point cracks (W type cracks) leads to reduction in ductility and eventual failure. R type voids or creep cavities generally form at low stresses while cracks are often associated with high stress creep [8]. This thesis focusses on study nucleation and growth of creep cavities and the following sections would serve as a brief, non-exhaustive summary of studies made in this field.

1.2.1 Nucleation of creep cavities

Nucleation of creep cavities has been a subject of study for several decades, still the cause of nucleation has not been well established. Cavities have however generally been observed to nucleate at grain boundaries, especially those transverse to the tensile direction. Second phase particles lying on grain boundary have also been observed to be preferential sites of cavity nucleation [48]. Based on the various models proposed in literature, there are primarily the following three mechanisms operating during creep cavity nucleation:

1.2.1.1 Vacancy condensation

Raj and Ashby [49] proposed a cavity nucleation theory, where stress concentration along a grain boundary leads to vacancy condensation, resulting in nucleation of cavities. For a grain boundary with a tensile stress of σ acting across it, the free energy change would be contributed by work done by the tensile stress and change in interface energy.

$$\Delta G = -\sigma\Omega + A_v\gamma - A_{gb}\gamma_{gb} \quad (1.11)$$

where, Ω is the atomic volume A_v and A_{gb} are the surface area of cavity and displaced grain boundary area respectively, γ and γ_{gb} are the surface and interfacial energy of metal and grain boundary respectively.

The critical radius r_c at which ΔG reaches maximum results in:

$$r_c = \left(\frac{2\gamma}{\sigma} \right) \quad (1.12)$$

This gives the minimum radius above which a nucleated cavity is stable. For example for pure aluminum with a surface energy of 0.98 J/m^2 [50] at a stress of 10 MPa the critical radius would be $0.19 \text{ }\mu\text{m}$.

1.2.1.2 Grain boundary sliding

Grain boundary sliding can cause cavity nucleation at grain boundary triple points or particles on grain boundaries (Figure 1.8). Chokshi et al [51] proposed that grain boundary sliding is hindered by the presence of second phase particles, leading to stress concentration on them. Local diffusion creep occurring at high temperature helps in relaxing these stresses. However, for particles above a certain size the diffusion is not enough to nullify the stress concentration, leading to nucleation of cavities, see Figure 1.8 (a). Chokshi et al used, the concept of diffusion length proposed by Rice [52] which was a stress level and temperature dependent length, serving as a parameter to study the interplay of creep and diffusion during high temperature deformation. The diffusion length L is given by:

$$L = \left(\frac{\Omega \delta D_{gb} \sigma}{kT \dot{\epsilon}} \right)^{1/3} \quad (1.13)$$

Any particle with a radius greater than this length is expected to be a probable site for nucleation. For example in case of an Al based alloy deforming under a stress of 6MPa, strain rate of 10^{-4} s^{-1} and temperature of 730 K, this diffusion length L would amount to $1.7 \text{ }\mu\text{m}$ [51].

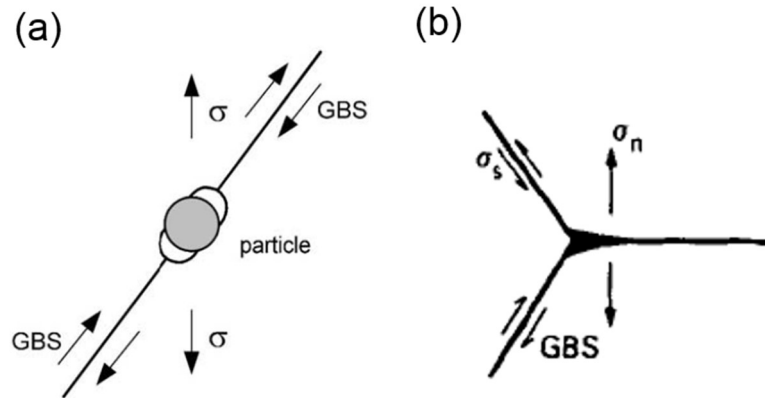


Figure 1.8 The formation of a cavity from (a) particle-obstacle during grain boundary sliding (GBS) [7] and (b) at grain boundary triple points due to stress concentration during grain boundary sliding (σ_n is the normal stress on the transverse grain boundary and σ_s is the shear stress on sliding boundary) [53].

Apart from this Chen and Machlin [54] proposed that grain boundary sliding could lead to nucleation of voids during high temperature deformation. Based on an experiment conducted by them they concluded that shear stresses along grain boundary led to grain boundary sliding. Restriction to this sliding could potentially cause void nucleation. For example, presence of jogs along grain boundary could be one such restriction to grain boundary slip. Depending on the jog orientation, tensile or compressive forces would develop on the jogs, see Figure 1.9 (a-b). Further grain boundary sliding on jogs with tensile stresses could lead to fracture along the jog surfaces resulting in void nucleation, which may then further grow via diffusion or plasticity, see Figure 1.9 (c).

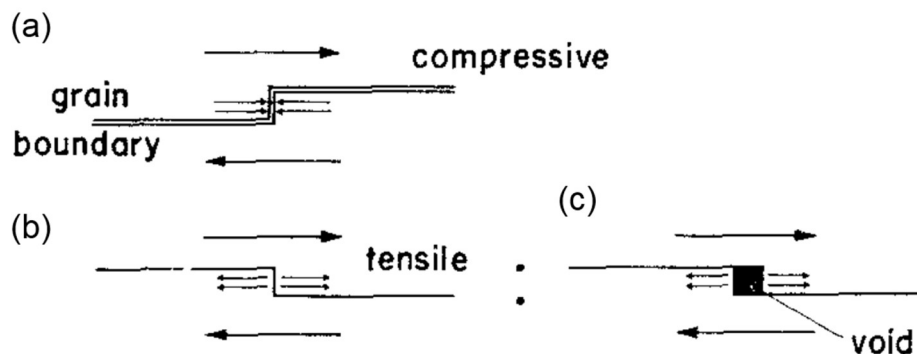


Figure 1.9 (a, b) Stress induced by boundary sliding at jogs. (c) Formation of void as a result of tensile stress on a jog [8].

1.2.1.3 Dislocation pile-ups

Some theories propose the pile up of dislocations against hard second phase particles to be a probable cause for cavity nucleation. Such pile ups may even nucleate cavities in grain interior, but their growth is believed to be rather slow.

Gifkins [55] set forward a hypothesis to explain void nucleation along transverse boundaries during high temperature deformation. Sliding along a transverse grain boundary between grain A and B, is accompanied by dynamic sliding in grain B, leading to formation of a jog. There is a possibility of significant pile up of dislocations along the jog. Further sliding of the grain boundary can lead in decohesion and void nucleation as shown in Figure 1.10.

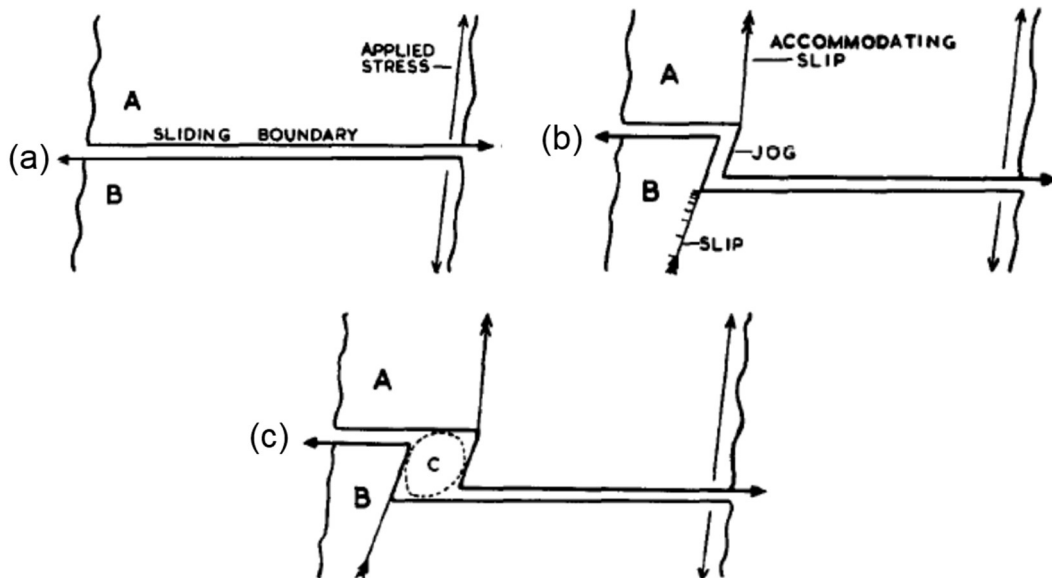


Figure 1.10 (a) Grain boundary sliding along a transverse grain boundary. (b) Formation of jog as a result of slip in grain B. (c) Decohesion along the jog as a result of further boundary sliding resulting in nucleation of cavity indicated in a circle marked c [55].

Additionally experimental evidence of nucleation of cavity via plasticity is also available in literature [56,57].

1.2.2 Growth of creep cavities

Theoretical study of growth of cavities under creep conditions help in predicting the time to failure of a material and this has hence been a subject of study for a considerable amount of research. Cavities are believed to grow by three basic mechanisms: diffusion, plasticity and grain boundary sliding. In the following section the three mechanisms would be described in brief.

1.2.2.1 Diffusion

From the pioneering work of studying diffusion based cavity growth by Hull and Rimmer [58] several other modifications to the proposed theory have been made over the years [49,56,59,60]. The basic principle is that excess vacancies are created on the grain boundary due to applied tensile stress. These excess vacancies diffuse to the cavities, which provides sinks of low chemical potential, to cause their growth.

For a periodic array of cavities with radius r , separated by a distance $2l$ lying on a grain boundary with a stress of σ acting perpendicular to the grain boundary (Figure 1.11), Raj et al [49,61] proposed volumetric growth of voids will be caused by diffusion of matter from void surface into the grain boundary. The rate of growth affected by grain boundary diffusion would then be given by:

$$\left(\frac{dV}{dt}\right)_{gb} = \frac{2\pi\Omega\delta D_{gb}}{kT} \left\{ \frac{(\sigma - \frac{2\gamma}{r})(1 - \omega^2)}{\ln\left(\frac{1}{\omega}\right) - 0.75 + \omega^2\left(1 - \frac{\omega^2}{4}\right)} \right\} \quad (1.14)$$

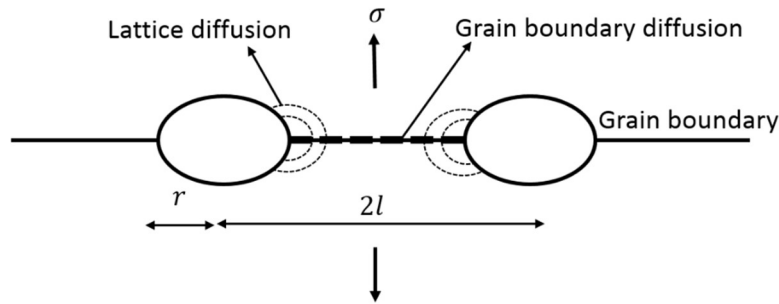


Figure 1.11 Schematic illustration of an array of cavities of radius r on a grain boundary, growing via diffusion under the effect of a stress.

Where, δ is grain boundary width ω is a parameter, normalising the cavity size with inter-cavity spacing, given by $\omega = r/l$. On the other hand if diffusion is through the lattice instead of grain boundary, the rate would be estimated using the following approximation:

$$\left(\frac{dV}{dt}\right)_l = \left(\frac{dV}{dt}\right)_{gb} \frac{(2l)D_l}{\pi\delta D_{gb}} \quad (1.15)$$

such that:

$$\left(\frac{dV}{dt}\right)_i = \frac{2\Omega D_l(2l)}{kT} \left\{ \frac{\left(\sigma - \frac{2\gamma}{r}\right)(1 - \omega^2)}{\ln\left(\frac{1}{\omega}\right) - 0.75 + \omega^2\left(1 - \frac{\omega^2}{4}\right)} \right\} \quad (1.16)$$

Diffusion based growth generally causes uniform growth in all directions of the cavity resulting in rounded cavities, provided surface diffusion is fast enough.

1.2.2.2 Plasticity

Hancock [62] proposed a model for cavity growth without the requirement of vacancy flux where the applied stress causes the surface of the cavity to strain, resulting in its growth by plasticity. The analysis of Hancock results points towards a cavity growth given by [63]:

$$\frac{dr}{d\varepsilon} = kr \quad (1.17)$$

where ε is the strain measured far from the cavity and k is a constant of the order of unity. Assuming a spherical shape of cavity and $k = 1$, the volumetric growth rate would be given by:

$$\frac{dV}{dt} = 3V\dot{\varepsilon} \quad (1.18)$$

It can be seen that diffusion based volumetric growth is predicted to be independent of existing cavity volume, while growth via plasticity is directly proportional to current volume. Plasticity based growth is generally associated with elongated cavities which align parallel to the tensile axis. And a stress triaxiality, if present would also influence growth of cavities.

1.2.2.3 Grain boundary sliding

Cavities are also known to grow by grain boundary sliding. For deformation where grain boundary sliding is considerable, the diffusive growth of cavities will be affected by grain boundary sliding. Chen [64] proposed that the combined effect of mass transport due to sliding and surface diffusion causes grain boundary cavities to grow along the plane of the boundary, as can be seen in Figure 1.12 .

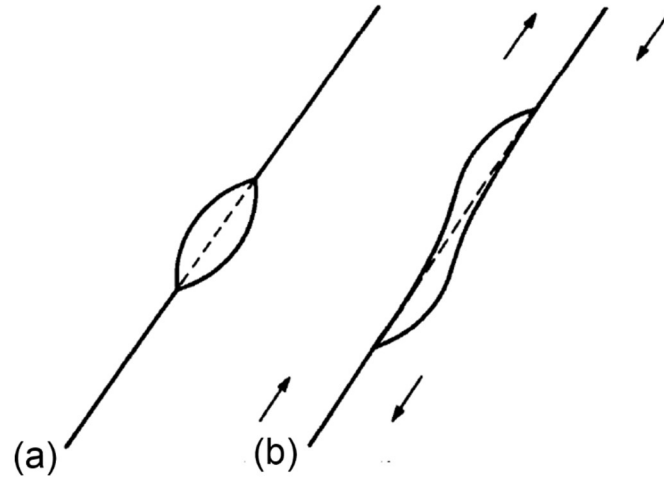


Figure 1.12 Cavity growth due to grain boundary sliding [64].

During such growth the morphology at the two tips of the cavities are expected to be asymmetric to each other. And the consequent crack sharpening makes the growth limited by surface diffusion, irrespective of the grain boundary diffusivity. Such growth was found to be independent of the sliding rate and dependent of stress to the power 3.

$$V_t \propto \Sigma^3 \quad (1.19)$$

where V_t is the normalised crack tip velocity and Σ is the normalised stress.

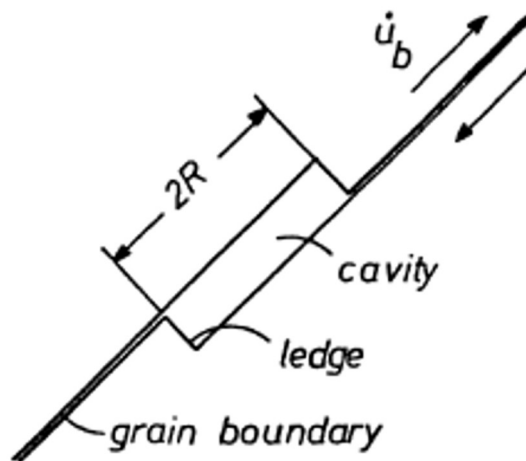


Figure 1.13 Cavity growth by grain boundary sliding at a tensile ledge [65].

Riedel [65] on the other hand proposed that cavities on tensile ledges of grain boundaries grow directly under the effect of grain boundary sliding. (Figure 1.13) The

kinetics of cavity growth in such situations is driven by the kinetics of boundary sliding. This is more probable in cavities inclined to the tensile directions. He proposed that:

$$2 \frac{dr}{dt} = \dot{u}_b = 0.55 \dot{\epsilon} f_s \quad (1.20)$$

where \dot{u}_b is the grain boundary sliding rate and f_s size of the sliding facet.

Apart from this approach, to evaluate growth of cavities during superplasticity, Chokshi and Langdon [66] proposed a modified model for diffusion based growth of cavities. In this model they considered the enhancement of growth due to diffusion of grain boundary cavities, when the cavities exceeded the grain size as seen in Figure 1.14 (b). Generally when grain size is less than say 10 μm , (and also less than cavity size) the number of diffusion paths along grain boundaries would increase leading to an enhanced growth rate which is given by:

$$\frac{dV}{dt} = \frac{180\pi\Omega\delta D_{gb}}{kT} \left(\frac{r}{d}\right)^2 \sigma \quad (1.21)$$

The model has been simplified for large values of r , so that surface tension effects are negligible. It can be seen that this growth rate is dependent on grain size, as it would affect the available diffusion paths.

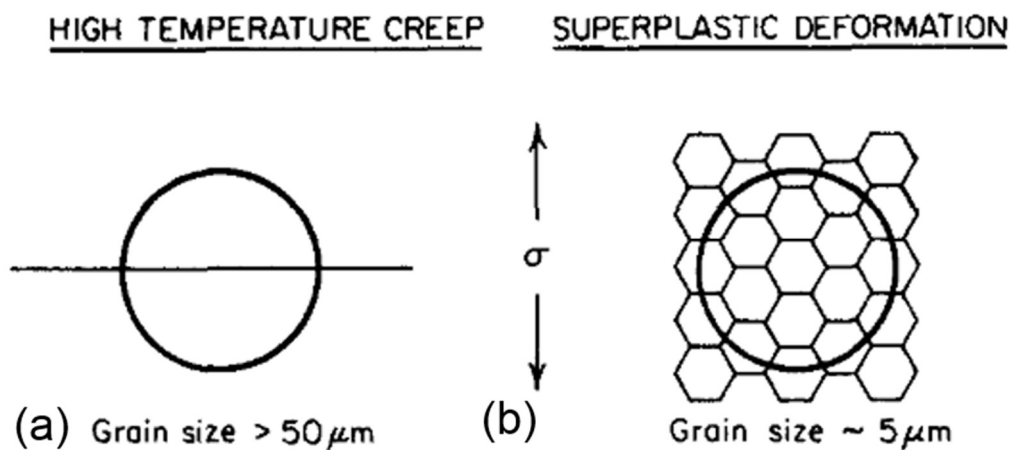


Figure 1.14 Schematic illustration of a cavity (represented by circle) in (a) high temperature creep when grain size greater than 50 μm (b) superplastic deformation when grain size nearly 5 μm [66].

1.2.2.4 Constrained diffusion

Dyson [56] pointed out that the assumptions made by the diffusion based models about the stress applied on the sample being the same as the stress the transverse boundary containing the cavity was not necessarily appropriate. Additionally the assumption that all transverse boundary facets are lined up with cavities and are free to grow under applied stress was also pointed out to be unrealistic. He instead proposed that growth of cavities in polycrystals could be constrained because cavities are in homogeneously distributed inside the polycrystal. Figure 1.15 shows a schematic of cavities lined up on an isolated facet (nearby facets not cavitated), with a stress σ_l acting on the cavities that is different from the stress σ applied on the sample. Rice [67] took forward this idea to propose a growth rate which was compatible with the deformation of the surrounding matrix.

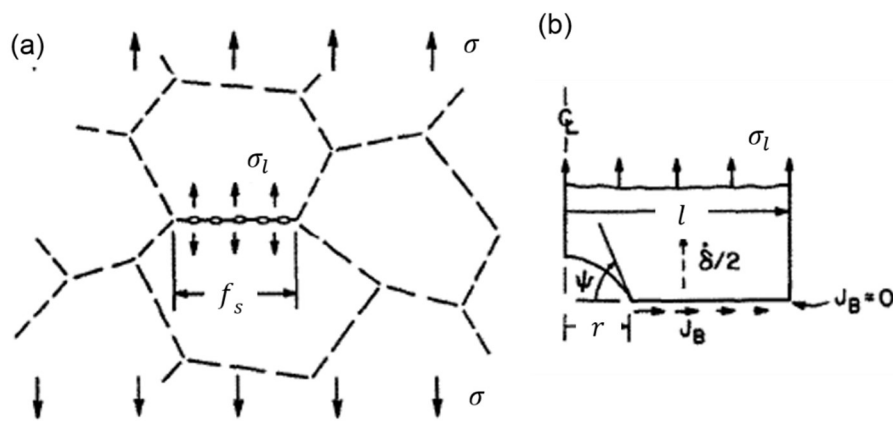


Figure 1.15 (a) Schematic illustration of an isolated cavitated grain boundary facet. (b) Zoomed view of one of the cavity [67]

He put forward a simple approximation of the opening rate of a penny shape crack in a homogenous viscous material as (see Figure 1.15 b):

$$\dot{\delta} = \frac{(\sigma - \sigma_l)(f_s)\dot{\epsilon}}{\sigma} \quad (1.22)$$

where σ_l is the local tensile stress acting in a grain boundary facet, while σ is the tensile stress acting on the sample (far from the cavitated facet) and f_s is the facet size.

This was then equated by an equivalent δ by classic diffusion models using which the local stress (σ_l) was deduced. This in turn was used to formulate the constrained grain boundary diffusion growth as:

$$\left(\frac{dV}{dt}\right)_{cgb} = \frac{4\pi\Omega\delta D_{gb}}{kT} \left\{ \frac{\sigma - (1 - \omega^2) \left(\frac{2\gamma\sin(\psi)}{r}\right)}{\frac{4L^3}{\alpha_r l^2 (f_s)} + \ln\left(\frac{1}{\omega^2}\right) - \frac{(3 - \omega^2)(1 - \omega^2)}{2}} \right\} \quad (1.23)$$

where ψ is the angle of cavity on grain boundary, $L = \left(\frac{\sigma\Omega\delta D_{gb}}{\varepsilon kT}\right)^{\frac{1}{3}}$ and α_r is a dimensionless factor. The value of α_r was given as $2/\pi$ for newtonian material and was estimated to be 0.84 for $n = 3$ and 0.9 for $n = 5$ (n is the stress exponent).

It should be noted that most of the theoretical models of creep cavity nucleation and growth are proposed assuming cavities nucleate and grow on grain boundaries, which might not always be the case. Table 1.2 summarizes the formulation for the different cavity growth mechanisms mentioned before, along with the major assumptions underlying these formulations.

Table 1.2 Summary of various cavity growth rate formulations along with the major assumption behind these.

| Growth mechanism | Cavity growth rate formulation $\frac{dV}{dt}$ or $\frac{dr}{dt}$ | Major assumptions |
|--|---|--|
| Diffusion based $\left(\frac{dV}{dt}\right)$ | $\frac{2\pi\Omega\delta D_{gb}}{kT} \left\{ \frac{\left(\sigma - \frac{2\gamma}{r}\right) (1 - \omega^2)}{\ln\left(\frac{1}{\omega}\right) - 0.75 + \omega^2 \left(1 - \frac{\omega^2}{4}\right)} \right\}$ | <ol style="list-style-type: none"> 1. Growth for equally spaced spherical cavities of radius r separated by fixed distance, lying on transverse grain boundary. 2. Stress on cavity is equal to stress applied far from the cavity 3. All transverse boundaries have cavities. 4. Diffusion via grain boundary. |

| | | |
|---|---|--|
| Diffusion based $\left(\frac{dV}{dt}\right)$ | $\frac{2\Omega D_l(2l)}{kT} \left\{ \frac{\left(\sigma - \frac{2\gamma}{r}\right)(1 - \omega^2)}{\ln\left(\frac{1}{\omega}\right) - 0.75 + \omega^2\left(1 - \frac{\omega^2}{4}\right)} \right\}$ | 1, 2 and 3 same as above 4. Diffusion via lattice. |
| Plasticity based $\left(\frac{dV}{dt}\right)$ | $3V\dot{\epsilon}$ | 1. Surface tension neglected 2. 2D model extended to 3D assuming spherical cavities |
| Growth mechanism | Cavity growth rate formulation $\frac{dV}{dt}$ or $\frac{dr}{dt}$ | Major assumptions |
| Grain boundary sliding $\left(\frac{dr}{dt}\right)$ | $\frac{dr}{dt} = \frac{\dot{u}_b}{2} = \frac{0.55 \dot{\epsilon} f_s}{2}$ | 1. 2D model extended to 3D assuming cylindrical cavity 2. Cavities located on a tensile ledge of a sliding grain boundary |
| Diffusion based superplastic growth $\left(\frac{dV}{dt}\right)$ | $\frac{180\pi\Omega\delta D_{gb}}{kT} \left(\frac{r}{d}\right)^2 \sigma$ | 1. Small hexagonal grains and 2. Spherical cavities lying on the grain boundaries 3. $\frac{1}{4\ln\left(\frac{1}{\omega}\right) - (1 - \omega^2)(3 - \omega^2)} = 1$ |
| Constrained grain boundary diffusion $\left(\frac{dV}{dt}\right)$ | $\frac{4\pi\Omega\delta D_{gb}}{kT} \left\{ \frac{\sigma - (1 - \omega^2)\left(\frac{2\gamma\sin(\psi)}{r}\right)}{\left(\frac{4L^3}{\alpha_r l^2(f_s)} + \ln\left(\frac{1}{\omega^2}\right) - \frac{(3 - \omega^2)(1 - \omega^2)}{2}\right)} \right\}$ | An average value of $\dot{\delta}$ and σ_l has been considered neglecting the non-uniformity of each facet due to: its distance with other faceted cavities, ease of grain boundary sliding and deformation mode of grain |

1.2.2.5 Transition between various cavity growth mechanism

Since there are several possible mechanisms governing growth of creep cavities, it is of interest to find out which is the more dominant mechanism. This varies,

depending upon the mechanical parameters, a material is subjected to. Plotting the theoretical rate of cavity growth (dr/dt or dV/dt , where, r is radius V is volume and t is time) against the equivalent cavity radius for different cavity growth mechanisms is a good way to analyze the various mechanisms comparatively and determine which among them is dominant, see Figure 1.16. Such plots are obtained from the equations previously mentioned, by inserting the appropriate stress, strain, grain size and temperature and other material parameters in the growth equations. From Figure 1.16 it can be seen that at lower radius, growth by diffusion is predicted to be higher while beyond a certain radius super plasticity and plasticity takes over. These plots also indicate the point of transition between the various mechanisms. Traditionally the point of transition between two mechanisms of creep cavity growth were associated with a unique radius [66], these have been indicated by dotted lines in Figure 1.16. This radius mainly depends on the mechanical parameters (stress, strain rate) and is given by the radius at which the rate of two competing mechanisms become equal.

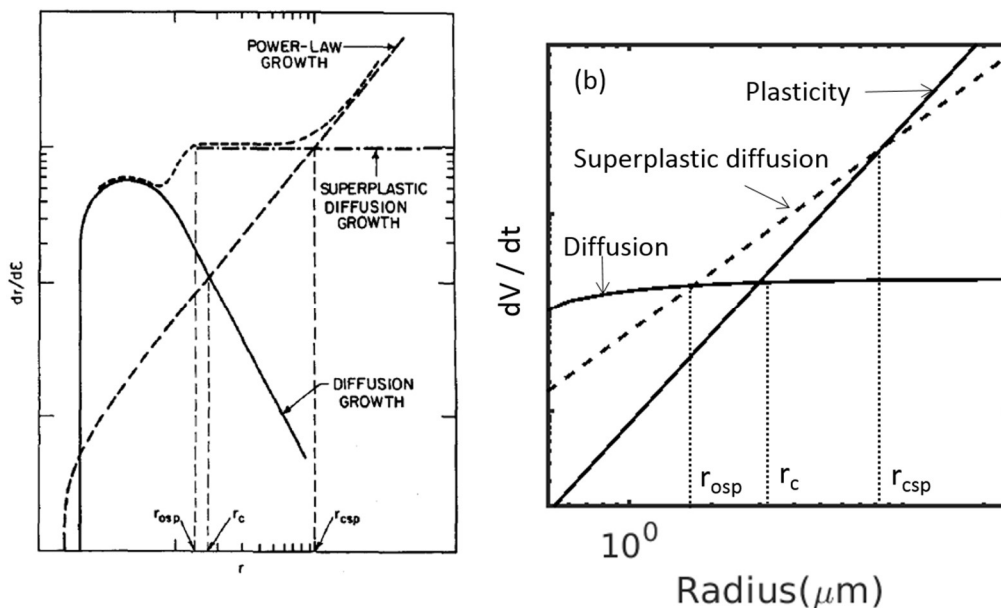


Figure 1.16 Schematic illustration showing trend of cavity growth rate obtained (a) diffusion, superplastic diffusion and power law (plasticity) models in terms of $dr/d\epsilon$ versus r [66] (b) diffusion, superplastic diffusion and plasticity model in terms in dV/dt versus r .

1.3 Characterization of creep cavities

Historically several experimental techniques have been used to characterize creep cavities. These range from indirect quantification techniques like density measurement, Small Angle X-ray Scattering (SAXS) [68,69] and Small Angle Neutron Scattering (SANS) [70–72], to 2D imaging using: Optical Microscopy (OM), Scanning Electron Microscopy (SEM), Transmission Electron Microscopy (TEM). More recently 3D imaging techniques based on serial sectioning: Focused Ion Beam Scanning Electron Microscopy (FIB-SEM) and X-ray Micro tomography (XMT) have emerged as suitable tools to study creep cavities. In the following section some of the commonly used techniques will be briefly described.

1.3.1 Density change measurements

The change in density of material due to high temperature deformation, has been used to estimate the total volume of cavities formed after creep testing. These experiments give information on the cavity volume per unit weight. Obtaining this information by deforming samples to different strains, helps in studying the evolution of cavity volume with a parameter incorporating time, strain and stress, as seen in Figure 1.17 [73]. Such data has been used in predicting time to failure of samples [74].

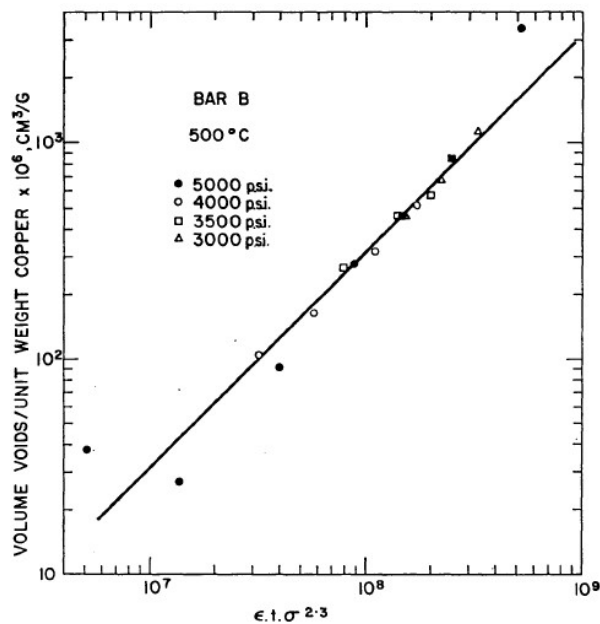


Figure 1.17 Plot showing evolution of cavity volume per unit weight with $\epsilon\sigma^{2.3}$ in copper at constant temperature and different loads (mentioned in figure) [73].

This technique works on the assumption that all the density changes occurring during the test are due to cavity formation. Isolating the effect of other phenomenon like high temperature on density change is sometimes not possible, leading to considerable errors in cavity volume estimation. Apart from this, the technique suffers from the obvious shortcoming that no information about number of cavities or their shape can be deduced from such measurements.

1.3.2 2D imaging techniques: OM, SEM, TEM

Classical imaging techniques ranging from OM to SEM and TEM have been extensively used for characterising cavities. They are effective tools to visualise cavities at different resolutions. The following sections briefly enumerate their utility and shortcomings as tools for creep cavity characterisation.

1.3.2.1 Optical microscopy and scanning electron microscopy

OM and SEM are the most effective tools for 2D visualisation of creep cavities. Over the last few decades SEM has replaced the usage of OM, owing to its better resolution (by an order of magnitude) and depth of focus, allowing visualisation of smaller cavities and better investigation of cavities on fractured surfaces respectively.

2D visualisation of cavities are done to extract useful information about them, like their: size, size distribution, shape, number and number density. It also helps in studying the vicinity in which cavities nucleate and grow, like the presence of intermetallics, second phase particles, grain boundaries (transverse or parallel to tensile direction) and triple points around them. An example of this can be seen in Figure 1.18, where cavity orientation and shape were studied for copper pulled to fracture at 823 K with two different strain rate in super plastic regime. It was observed the cavities were generally fairly small, elongated and aligned along the tensile axis when pulled at initial strain rate of $3.33 \times 10^{-2} \text{ s}^{-1}$ (Figure 1.18 a). This condition was found to indicate power-law growth. On the other hand, there were some very large cavities that were more rounded in appearance, on applying an initial strain rate of $1.67 \times 10^{-5} \text{ s}^{-1}$ (Figure 1.18 b), this suggested diffusion based growth [35]. Similarly, as seen in Figure 1.19 (a), SEM was used to study cavities in Ti-Al alloy subjected to creep deformation at 1073 K and 270 MPa. The micrographs

revealed an absence of cavities on transverse grain boundary (between grains 1 and 3), and presence of cavities along the boundaries inclined with respect to the stress axis (between grains 1 and 2 and grains 1 and 4) and also along grain boundary parallel to stress axis (between grains 1 and 5) [36]. Cavity growth can also be studied by studying the evolution of cavity number density with time or strain. An example of this is presented in Figure 1.19 (b), which shows the evolution of number of cavities per unit cross section area with strain in 12 % Cr ferritic steel, crept at 923 K and 80 MPa, showing a linear relation between cavity density and strain [37]. Such information in turn provides useful insights into creep cavity nucleation and growth mechanisms.

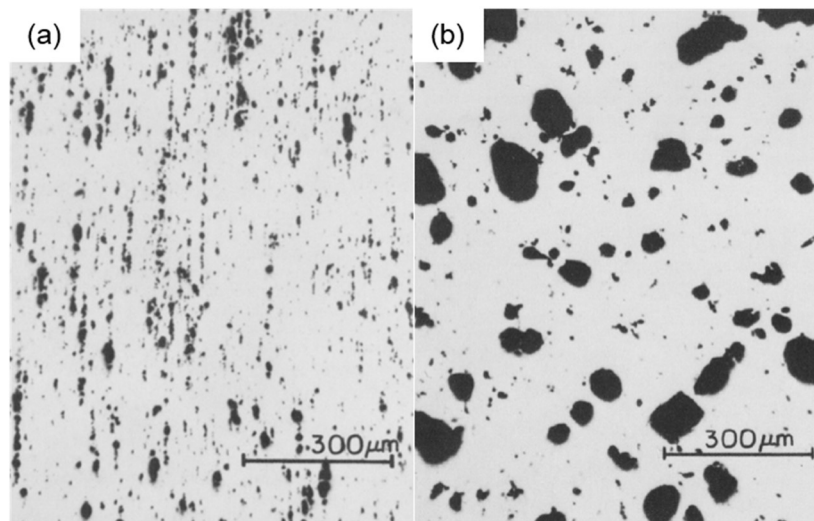


Figure 1.18 Optical micrograph of gauge section of copper pulled to fracture in superplastic regime at 823K with initial strain rate of (a) $3.33 \times 10^{-2} \text{ s}^{-1}$ and (b) $1.67 \times 10^{-5} \text{ s}^{-1}$ The tensile axis is vertical [75]

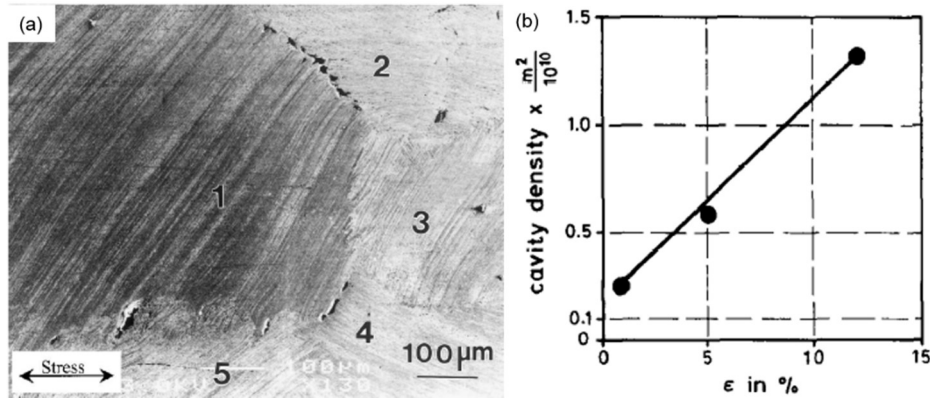


Figure 1.19 (a) SEM micrograph of Ti Al alloy subjected to creep deformation at 1073 K, 270 MPa, showing cavities with a spherical cap shape along grain boundaries of grains indicated by number 1 to 5 [76]. (b) Evolution of cavity density with strain in 12 % Cr ferritic steel, crept at 923 K and 80 MPa, [77].

However inevitably these technique suffer from several shortcoming, most of them owing the two dimensional nature of imaging, which is often not accurate [78]. The key limitations are listed below:

- Using number of cavity per unit area to estimate the number density per unit volume often fails, when cavities are interconnected.
- Deducing the shape of cavity based on 2D images is not always accurate.
- Studying connectivity of cavities is obviously not possible using 2D imaging.
- Sample preparation required for OM and SEM, may not be successful in preserving the microstructure. For example, cavities are often associated with hard second phase particles which are prone to fracture and decohesion during grinding and polishing of samples. Hence sometimes extra cavities may appear due to decohesion of intermetallics or in ductile samples, the cavities might get filled up during polishing.
- When studying deformation *in situ* for example using *in situ* SEM, the observation made on the surface may not always be representative of what happens in the bulk [79].

1.3.2.2 Transmission electron microscopy

When very high resolution of the order of a few nanometers is required for studying cavities then TEM is the preferred technique. TEM studies can help providing information regarding nature of particles and chemical compositions around cavities, helping in studying the effect of these on creep cavitation. For example when

investigating failure of AISI type 316 stainless steel from a power station steam header showing reheat cracking, TEM was used to precisely study the environment of creep cavities [40]. High Angle Annular Dark Field – Scanning Transmission Electron Microscopy (HAADF-STEM) image from grain boundary showed a faceted cavity in contact with different second phase particles and matrix, see Figure 1.20 (a). Identification of different phases by composition and selected area electron diffraction (SAED), clearly demonstrated the intimate association of the cavity with the second phases in the boundary (see Figure 1.20 b).

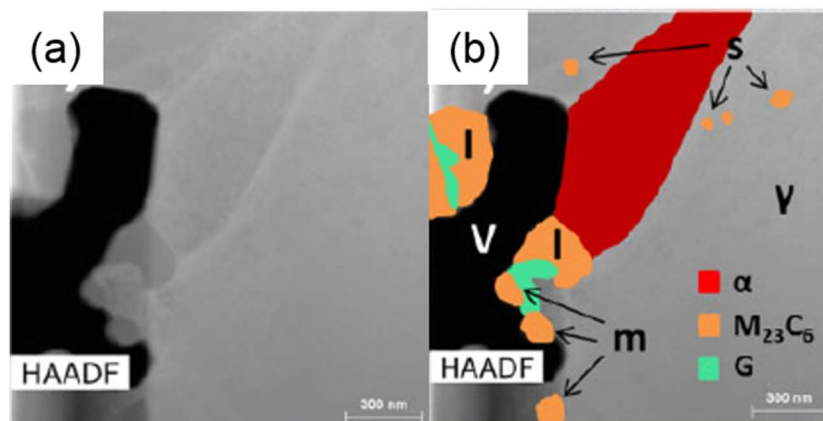


Figure 1.20 Creep cavities in AISI type 316 stainless steel from a power station steam header showing reheat cracking was studied using TEM. High Angle Annular Dark Field – Scanning Transmission Electron Microscopy Imaging (HAADF-STEM) image from grain boundary showing a faceted cavity in contact with different second phase particles and matrix. (b) Schematic diagram overlaid onto HAADF image showing different phases identified by composition and selected area electron diffraction (SAED). V is cavity, α is ferrite, γ is austenite matrix and 's', 'm' and 'l' indicated small, medium and large $M_{23}C_6$ phase particles respectively [80].

The various shortcomings of the OM and SEM are also unavoidably true in case of TEM. The effect of sample preparation being obviously much more in this case owing to the severity of preparation required and limitation due to sample dimensions. In addition, when imaging is done at a high resolution the area scanned is inevitably small (nearly $10 \times 10 \mu\text{m}^2$), and hence often not statistically significant.

1.3.3 3D imaging techniques: FIB-SEM, XMT

1.3.3.1 Focussed ion beam scanning electron microscopy

A 3D variant of SEM imaging: FIB-SEM, has the capability to extend the imaging ability of classical 2D SEM, to 3D. It employs serial milling of top layer of sample, accompanied by imaging resulting in 3D view of the sample. This technique has also

found use in creep cavity characterisation [80]. It is a very powerful tool in terms of resolution offered. In addition it does not have typical limitations related to 2D imaging and is capable of providing an accurate quantification of shape, number density, connectivity of cavity.

However because of its destructive nature, *in situ* studies cannot be made using this technique. Also the limitation of statistics due to limitation of sample size and high magnification is retained in this imaging tool.

1.3.3.2 X-ray microtomography

X-ray microtomography is a radiography based technique which is used to image a sample in 3D. This technique offers a non-destructive way of imaging creep cavities, at micrometer level resolution. The sample is rotated relative to the X-ray source about an orthogonal axis, acquiring 2D radiographs. These radiographs are then mathematically reconstructed into 3D digital images, called volumes [81]. A schematic illustration of the basic principle of XMT is shown in Figure 1.21. More information about this technique and its usage for creep cavity characterisation is detailed in the following section 1.4.

Being a 3D technique it is very suitable for studying the shape, size distribution, number density of cavities and its surrounding particles. Additionally the view is not limited to surface and the bulk can be studied. Since it is non-destructive in nature *in situ* studies can be made using this technique provided high flux of X-rays are used. Thanks to no sample preparation required, there is no tampering of microstructure. And much bigger samples as compared to SEM and TEM, can be scanned, giving statistically significant data.

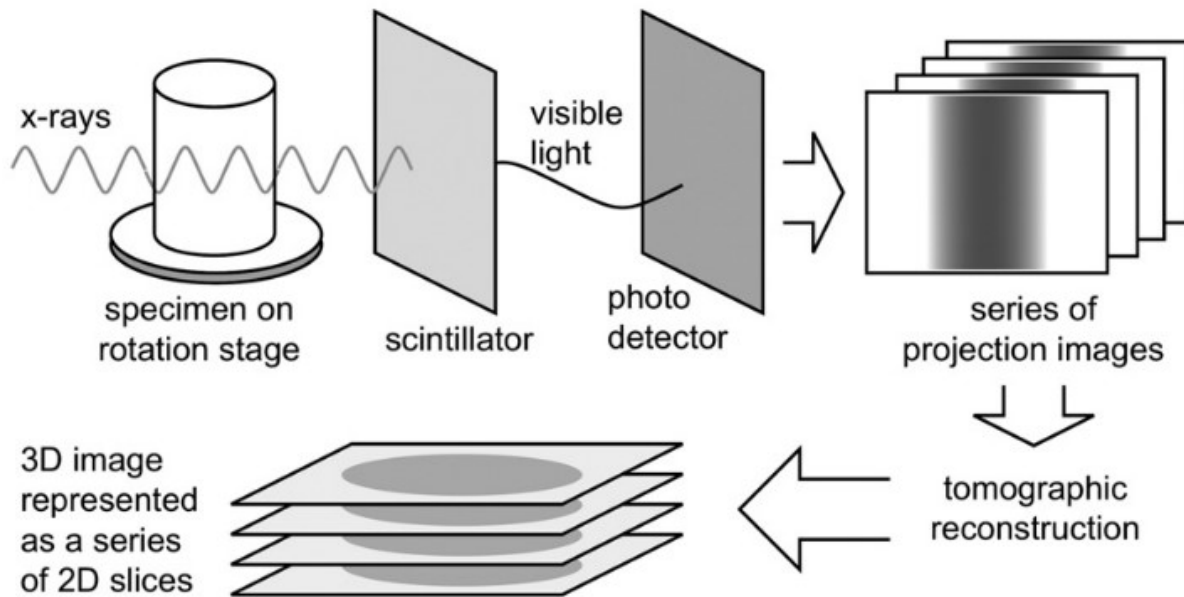


Figure 1.21 Schematic illustration of basic principle of X-ray microtomography acquisition and reconstruction into 3D volumes [81].

Owing to these advantages XMT has emerged as a convenient tool to study creep cavities in the past decade. The few shortcomings of this technique are its limited resolution (few micrometer) as compared to SEM and TEM and the inability to view grain boundaries.

1.4 X-ray Computed Tomography (X-ray CT)

X-ray CT is a 3D imaging technique using X-rays. Details regarding the physics of X-rays, its different sources and imaging modes are described in the following section. The utility of this tool in characterising creep cavities has also been detailed.

1.4.1 Physics of interaction of X-rays with matter and different contrast modes

When X-ray of wavelength λ passes through vacuum, it is associated with a wave number k given by:

$$k = \frac{2\pi}{\lambda} \quad (1.24)$$

When these rays pass through a medium of refractive index η , they undergo attenuation due to absorption, resulting in a change in amplitude and they might also

be retarded in the object resulting in a phase shift. For a medium its refractive index η is given by:

$$\eta = 1 - \delta_r + i\beta \quad (1.25)$$

The associated wave number of X-ray on passing through such a medium, changes to $k' = k\eta$ and the plane wave is of the form:

$$\exp(i\eta kz) = \exp [i(1 - \delta_r)kz] \exp(-\beta kz) \quad (1.26)$$

Consequently, we can observe that an X-ray beam that passes through a medium is both attenuated and phase shifted. The absorption index β , is related to the attenuation of the incident beam induced by the medium. The refractive index decrement δ_r , is related to the phase shift of the incident wave, due to the deflection of the wave front in the medium. These two phenomenon form the basis of two different contrasts modes used in X-ray imaging: absorption contrast and phase contrast. They are described below.

1.4.1.1 Absorption contrast

Absorption contrast tomography is the most conventional contrast mechanism used in X-ray imaging which is based on the fact that the intensity of incident beam decreases exponentially with increasing propagating distance in a homogeneous matter, see Figure 1.22 (a). This decrease is related to the absorption coefficient of a material. This absorption coefficient increases with the electron density and the atomic number of a phase. Such contrast fails when there is negligible difference between the atomic number of different constituent phases and in soft materials that offer limited absorption of X-rays.

During acquisition, sample is placed close to the detector to avoid phase effects that become prominent with increasing distance. If the transmission of X-rays is too high, the contrast is less and if it is too low the photon statistics is low. Transmission of 20% of X-rays offers a good trade-off between the two effects [82]. When the beam is monochromatic, it is possible to perform quantitative analysis since the grey level is directly linked to the absorption coefficient.

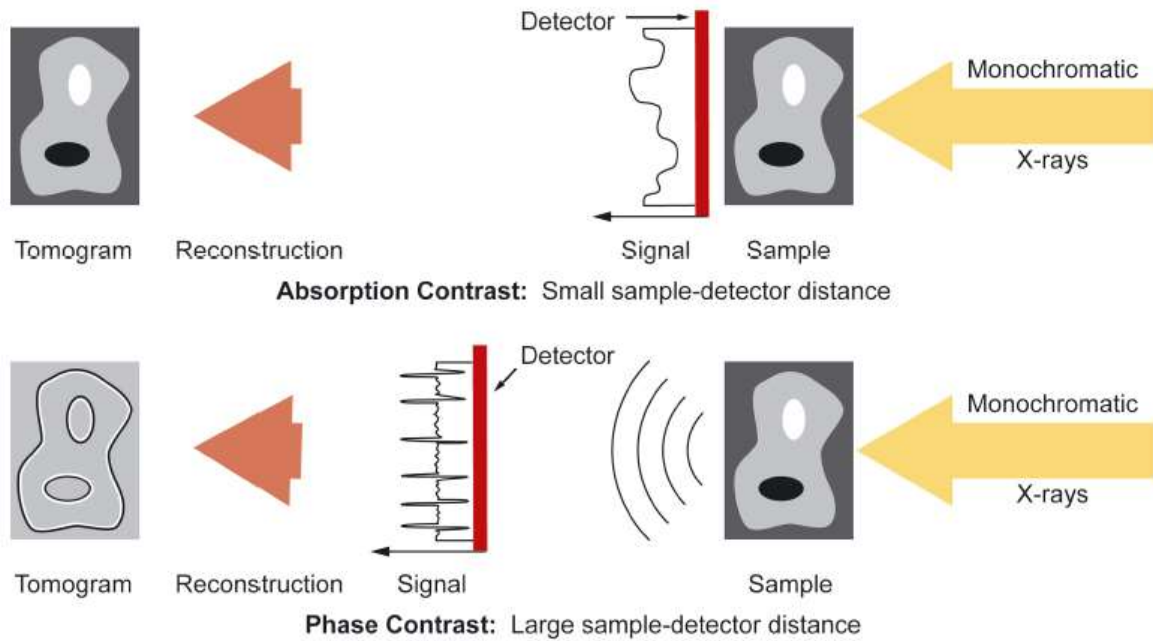


Figure 1.22 Schematic illustration of two primary contrast mechanisms employed in X-ray imaging (a) absorption contrast (b) phase contrast [83].

1.4.1.2 Phase contrast

In addition to the absorption mode, the phase shift incurred by the X-rays can also be used for imaging. Phase contrast imaging requires spatially coherent X-rays such as synchrotron X-rays. When X-rays pass through a sample, they undergo a phase shift along edges of different phases. The image is created by interference between parts of wave on either side of an interface that have suffered different phase retardation, see Figure 1.22 (b). These interferences express themselves as lateral intensity variation on the detection plane, hence lateral coherence is a pre requisite for such imaging technique. Lateral coherence increases with a decrease in source size and increase with source sample distance. Superimposition of such contrast on the conventional absorption contrast is especially useful in edge detection of small features with similar atomic density and low absorbing soft matter.

Hologtomography is another variation of this contrast mode in which radiographs are acquired at multiple distances (generally 4 to 5), see Figure 1.23 [84]. This is done to compensate for loss of information from blinding of certain frequencies in the phase distribution, owing to the Talbot effect [85].

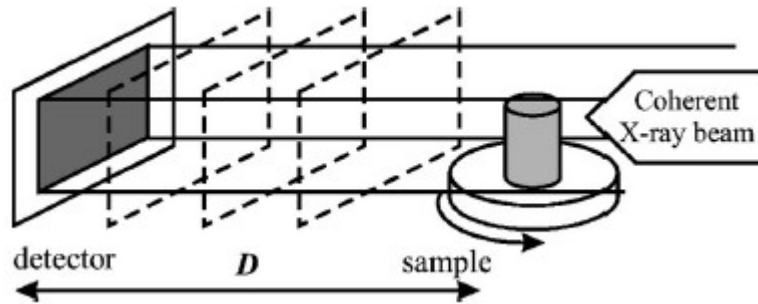


Figure 1.23 Schematic illustration of setup for holotomography [84].

1.4.2 X-ray source

In order to perform X-ray CT, two most common sources for X-ray used are: Lab based CT and synchrotrons. These sources provide X-rays in one of the three beam geometries, see Figure 1.24 [78]:

- Fan beam: this consists of a micro focus beam and a 1D detector
- Cone beam: this consists of a micro focus beam and a 2D detector.
- Parallel beam: this consists of parallel beam of X-ray and a 2D detector.

Acquisition using cone and parallel beam geometry is much faster as compared to the fan beam, thanks to the 2D detectors employed.

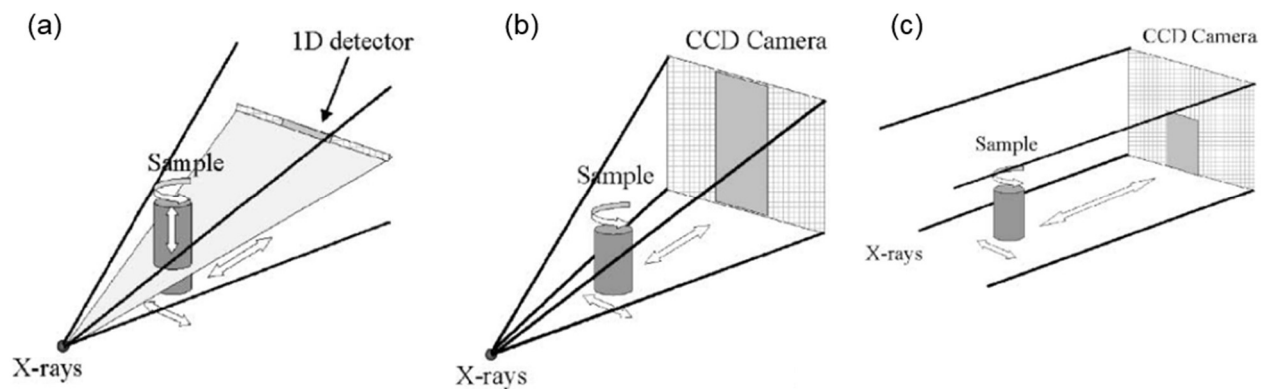


Figure 1.24 Schematic illustration of (a) fan beam geometry (b) cone beam geometry (c) parallel beam geometry. Here CCD camera is used as a 2D detector [78].

The two sources of X-rays are described below.

1.4.2.1 Lab CT

These are conventionally based on X-ray tubes which basically contain a cathode that emits electrons, which is then accelerated towards a metal target (anode), this

collision of the electrons with the metal produces X-rays in a continuous energy spectrum and isotropic emission.

Depending on the beam size, geometry and detector, the resolution of such devices can vary from 0.4 to 500 μm . However, lab CT offering nanometer scale resolution have also become common in the past few years [86] .

Due to lack of coherence of the beam, most lab based CT are restricted to use of absorption contrast for imaging, however there are a few examples where lab CT has been used for phase contrast imaging as well [87]. Also, due to the usage of white beam (with a wide range of energy), quantitative analysis of volume requires prior calibration and this can be done only in single phase materials. These sources are also limited in the flux of X-rays offered which severely restricts fast *in situ* imaging.

1.4.2.2 Synchrotron based CT

Synchrotron radiation is the wave produced when relativistic charged particles are accelerated. In the synchrotron light sources, the so-called insertion devices produces a collimated, monochromatic and coherent X-ray beam having high flux (nearly 10^{12} to 10^{13} ph/s/mm²). These characteristics lead to faster and higher resolution scans (as compared to a lab source), which is much more favourable for *in situ* studies. In addition, high coherence source allows phase contrast imaging to be performed.

1.4.3 X-ray tomography for imaging cavities

Over the past decade X-ray CT using synchrotron radiations has emerged as a convenient tool to study the evolution of cavities formed during high temperature deformation [88–90]. This is mainly because of its ability to perform non-destructive 3D imaging, giving results over a statistically significant volume, hence overcoming the major shortcoming its 2D counterparts (OM, SEM and TEM). In addition the ability to perform *in situ* imaging has been exploited by researchers to give new insights into cavity nucleation and growth [11,12,14,91,92]. One of the first studies to investigate creep cavities using *in situ* XMT was performed by Pyzalla et al. [16], on brass subjected to creep at 25 MPa and 648 K, Figure 1.25 presents the 3D volume obtained at two different time steps, showing evolution of cavities (in black) during

creep. Following this many other studies on creep cavities were made using XMT. The following sections lists out some of these.

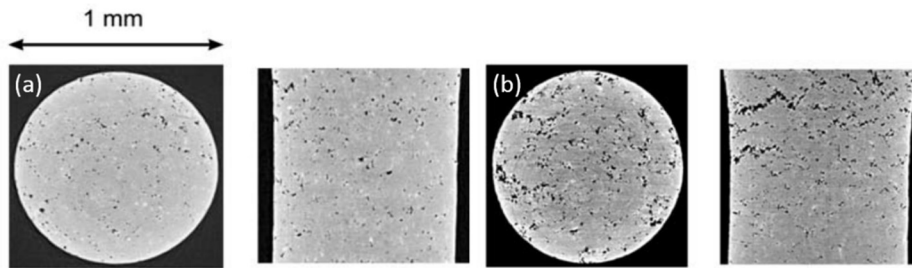


Figure 1.25 Slice of the brass sample after (a) 348 min creep and (b) 431 min creep. One voxel is about $4 \mu\text{m}^3$. Creep performed at 25 MPa and 648 K [16].

X-ray CT has extensively been used to study parameters like cavity volume fraction and number density and their evolution with respect to strain and time. Figure 1.26 (a) shows one such study, where number of cavities per unit volume (N_v), obtained using XMT is showed in comparison to how number of cavities per unit area (N_a) obtained using SEM changes with time. It can be clearly seen that beyond a strain 1.2 N_v decreases, while N_a continues to increase. This is because beyond a strain of 1.2 cavity coalesce occurs and SEM studies are unable to recognise these interconnected or coalesced cavities which can be in fact seen with XMT [38]. In addition to this X-ray CT has also been used for quantitative analysis of shape [14,93] of cavities and estimating growth rate of cavities. Figure 1.26 (b) shows an *in situ* XMT study made during high temperature deformation of copper investigating the average growth rate of voids as a function of volume. The results showed a clear proportionality between the volumetric void growth rate and void volume, hence experimentally verifying predictions made by continuum theory describing void growth in a nonlinearly viscous solid [15]. Figure 1.26 (c) shows results from an *in situ* high temperature XMT study made on AZ31 alloy, depicting 3D rendered view showing the coalescence of several small cavities (in blue) into a big cavity (in yellow) with complex shape, at voxel size $(1.2 \mu\text{m})^3$ [48].

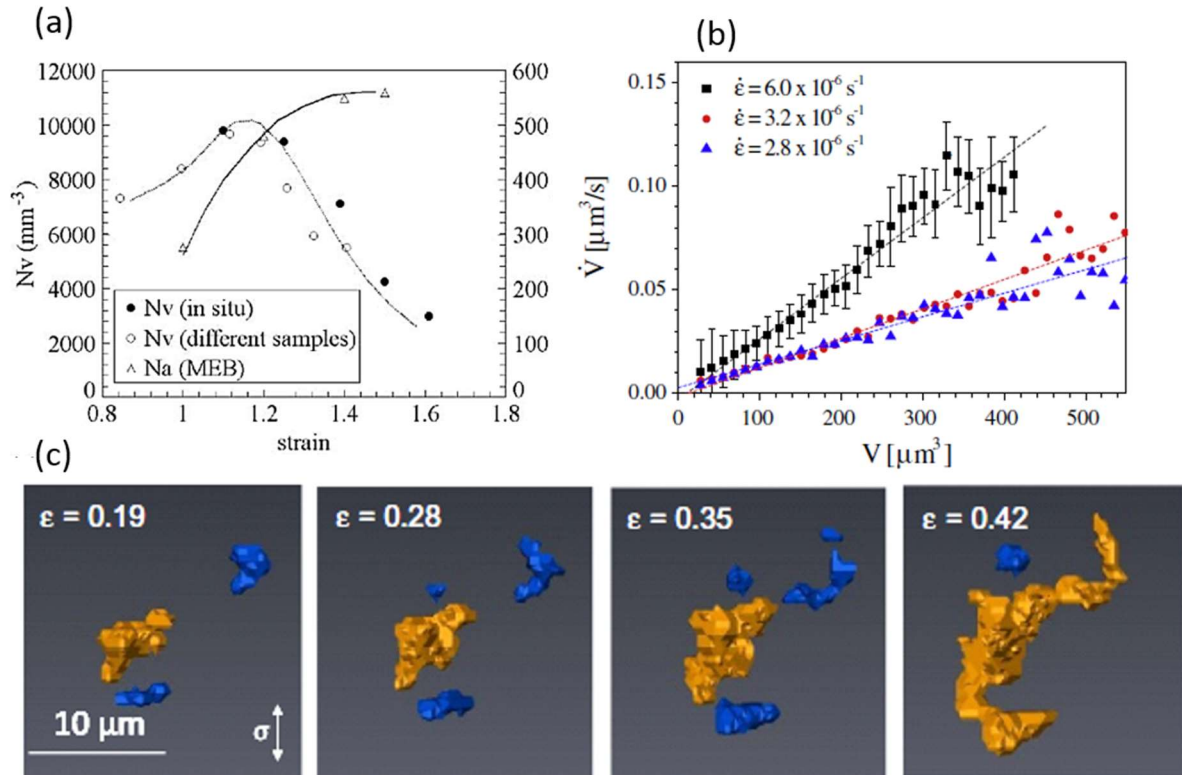


Figure 1.26 (a) Number of cavities per unit area N_a and per unit volume N_v as a function of strain. [78] (b) Average growth rate of voids as a function of volume [15] (c) 3D rendered image obtained by *in situ* X-ray microtomography of AZ31 alloy, showing an example of a coalescence event: several cavities are detected for the lowest strain and the cavities progressively connect together via a coalescence process. The largest cavity is in yellow whereas the others are in blue, voxel size ($1.2 \mu\text{m}$)³ [12].

X-ray CT has also been used for studying the environment in which cavities nucleate and grow. One such study was made on in AZ61 magnesium alloy (deformation at 623 K and strain rate $5 \times 10^{-4} \text{ s}^{-1}$ and limit to resolution of $1.8 \mu\text{m}$) where the linking of cavities with second phase particles was studied, Figure 1.27 (a) shows how a 2D view does not capture the association of cavities (shown in green) with particles (shown in red) as it can be seen in the 3D view of the same, see Figure 1.27 (b). A, B and C cavities are identified not to be connected with any particle. But, if the view is transformed into a 3D view, particles are found to be attached to the cavity regions of A and B. Cavity region C is still observed to be not connected with any particle [51].

Generally grain boundaries are not visible using X-ray CT, but gallium doping onto the grain boundaries can be used to reveal the crystallographic grains. This was demonstrated in an interrupted *in situ* XMT based study made on high temperature

deformation of Al-Mg alloy where after deformation gallium wetting was done to image grain boundaries on deformed sample [52]. Figure 1.27 (c, d) shows 3D rendered view of cavities (in red) associated with particles (in green), and in association to grain boundary shown in grey. It was observed that one of the three cavities located on the grain boundaries exhibited significant growth as compared to the cavities in the grain interior.

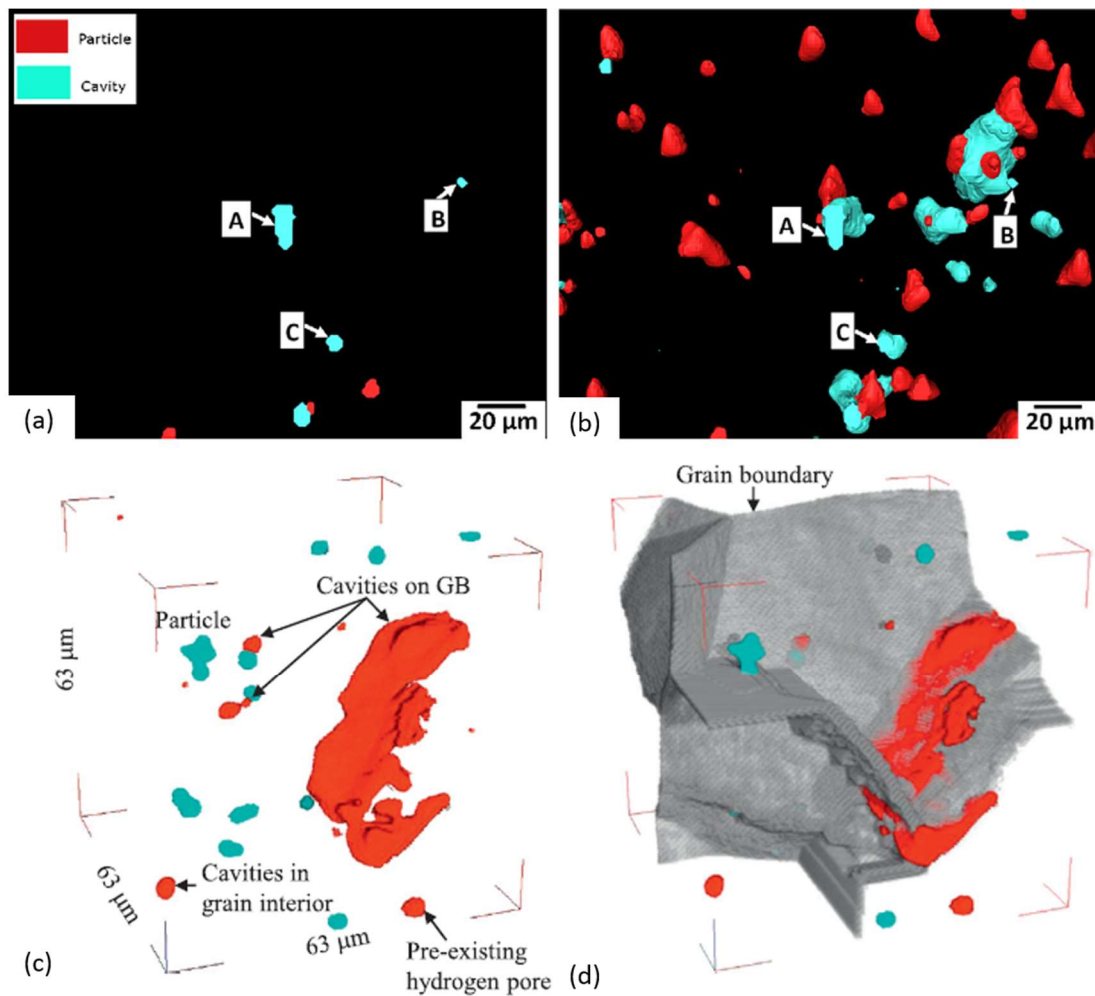


Figure 1.27 (a) A 2D surface view of a random area of the 3D volume of AZ61 at $\epsilon = 1.05$. A, B and C cavity regions are identified not to be connected with any particle. (b) Same view transformed into a 3D by extending the depth below the surface. Particles are found to be attached to the cavity regions of A and B. Cavity region C is still observed to be not connected with any particle, [90]. The limit to resolution is $1.8 \mu\text{m}$. Deformation was performed at 623 K and strain rate $5 \times 10^{-4} \text{ s}^{-1}$. (c) 3-D perspective views of pores/cavities (both are shown in red) and particles (green) captured at the final loading step in Al-Mg alloy deformed at 923 K . A grain boundary image (grey) has been superposed on (c) in (d), resolution is nearly $1 \mu\text{m}$ [11]

Recently X-ray nanotomography has emerged as a promising tool to study creep cavities. This tool helps in overcoming the limited resolution of the XMT since studies with pixel size as low as 25 nm can effectively be made using nano-holotomography. Recently one such post mortem study was done using synchrotron X-rays to analyse autonomous filling of creep cavities by gold-rich precipitates in Fe-Au alloys [93].

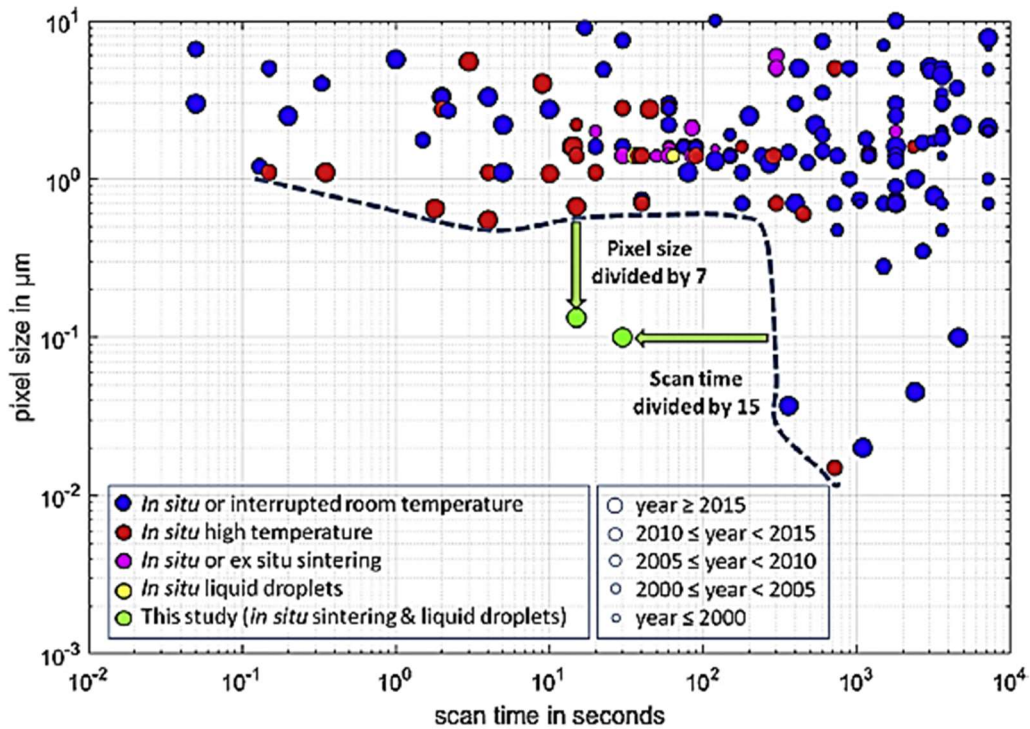


Figure 1.28 State of the art of *in situ* X-ray tomography: Pixel size versus scan time illustrating the state of the art for *in situ* X-ray laboratory and synchrotron tomography. Scan times of about 10 min are usually necessary to operate with nanometer pixel size (≤ 100 nm). Similarly, ultra-fast tomography (≤ 10 s time scan) is only attainable with micrometer resolution [94].

Performing *in situ* investigations using X-ray nanotomography is an upcoming development. Figure 1.28 shows a pixel size versus scan time map: illustrating the state of the art for *in situ* X-ray laboratory and synchrotron tomography. It can be clearly seen that imaging at high spatial resolution (nanometer) and rapid scan rates (tens of seconds) has been minimal. Such studies have been limited to imaging thermal treatments like sintering and liquid droplet nucleations and growth (indicated by green arrows in Figure 1.28) [94]. Long scan times, lack of proper detectors and difficulty of incorporating a creep device with nanotomography setup has hindered the development of *in situ* nanotomography for high temperature deformation

studies. Development of such a technique would be very useful in studying nucleation and early stages of growth of cavities.

1.5 Summary

In this chapter, there is a brief description of the various high temperature deformation mechanisms, creep cavity nucleation and growth mechanisms.

At high temperature, depending on the mechanical parameters of stress strain and temperature a material is subjected to, it undergoes deformation by one of the following mechanisms: diffusion, dislocation and superplasticity. During such deformations, damage often initiates through voids, also referred as creep cavities. The nucleation of these cavities is still debated in literature. Cavities have been mostly found to be associated with grain boundaries or second phase particles. Researchers have proposed several mechanism for nucleation of cavities. Mostly attributing it to vacancy condensation on grain boundary or stress concentrations arising during grain boundary sliding on second phase particles lying on grain boundaries. Some others also link it to dislocation accumulation against hard second phase particles or sliding grain boundaries.

Growth of cavities has also invited considerable attention and there are several theories for cavity growth in literature which can be broadly classified as:

- Diffusion based growth: involving vacancy diffusion either via lattice or grain boundary.
- Plasticity based growth: caused due to plastic deformation of material surrounding the cavity.
- Grain boundary sliding: growth resulting directly as a consequence of sliding of the boundary on which the cavity is present. Additionally grain boundary sliding is often seen in fine grained materials showing superplasticity. In such materials with very small grain size (less 10 μm), the cavity size would be greater than the grain size. This can lead to an increase in the number of diffusion paths along grain boundaries which would consequently enhance diffusion based growth rate.

Even when so many mechanism are proposed, the experimental validation of these remain handful. Most of these investigation being limited to the plasticity based growth.

Further this chapter talks about the various tools that can be used to characterise cavities. The pros and cons of each of these techniques in context of this characterisation has been mentioned.

The techniques described include, density measurement and the classical 2D imaging techniques: OM, SEM and TEM. Followed by 3D imaging techniques of FIB-SEM and X-ray CT. X-ray CT is the technique chosen for creep cavity characterisation in this thesis, thanks to its ability to perform *in situ* 3D imaging. A section is dedicated to describing the various sources of X-rays (lab and synchrotron) and presenting the different contrast mechanism (absorption and phase contrast) for this technique. Apart from this the different kind of investigations made using this technique viz a viz cavities are enumerated. It is seen that there is a need to develop a 3D characterisation tool which allows fast *in situ* imaging at sub micrometer level resolution. Such a tool would be very helpful in studying the nucleation and early stages of growth of creep cavities that form during high temperature deformation.

1.6 Objectives

The different models predicting creep cavity nucleation and growth have been fundamental in predicting failure of materials at high temperature. Plotting cavity growth rates for different models has been helpful in defining the radius range at which different mechanism drive cavity growth, in turn providing fundamental understanding of initiation and growth of damage during high temperature deformation [95]. This is shown through an example in Figure 1.29 which shows that typically diffusion is the fastest growth mechanism until a radius of r_{osp} which is followed by superplastic diffusion, while plasticity becomes active during later stages of deformation (after r_{csp}).

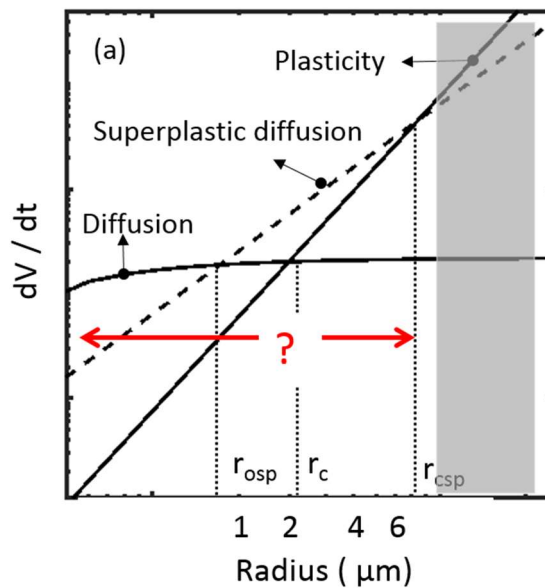


Figure 1.29 Schematic illustration of plot showing volumetric growth rates of cavities governed by different growth mechanisms

Inspite of significant progresses with theoretical models, the experimental investigation of these models have been only a handful. The main reason for this has been lack of suitable characterization tools. Mainly 2D imaging using optical micrography and scanning electron micrography have been used for such studies [10,96]. They offer good resolution and hence post mortem and ex situ experiments have provided insights into nucleation. Few studies on early stages of growth via grain boundary diffusion have also been made [10,96]. However since these techniques are not *in situ* and offer limited 2D view they do not provide complete information about the process.

In this context *in situ* microtomography emerged as a convenient tool which had the capability of real time imaging of cavities. However due to its low resolution (coarser than 1 μm) it could only be limited to studying later stages of growth (for cavity radius larger than 1 μm), hence most of such investigation were limited to the plasticity domain of growth [11,15,97], this corresponds to the grey zone in Figure 1.29.

Hence a characterization technique with resolution of (nearly 0.5 μm) and capability of *in situ* imaging would serve as an ideal tool for real time investigation of early stages of creep cavity growth

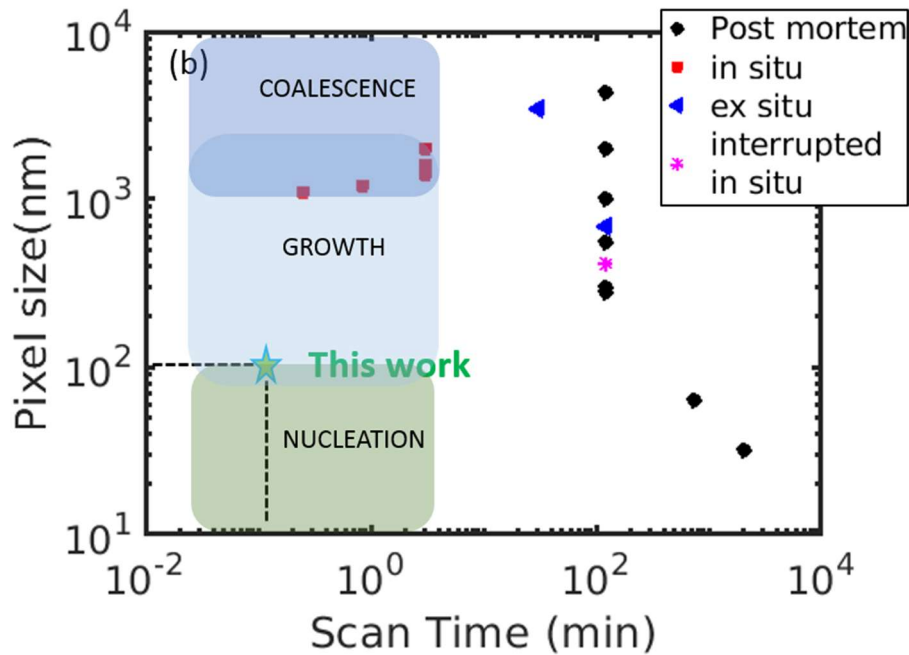


Figure 1.30 Scan time versus pixel size map showing, imaging parameters employed for tomographic investigations of creep cavities. Note that a scan time of 120 minutes was assigned to studies when no scan time was reported.[15,91,98–113]

Figure 1.30 shows a map depicting the state of the art 3D imaging capabilities for *in situ* creep cavity investigation. The map is a scan time versus pixel size map, depicting parameters used for different creep cavity investigation done using X-ray CT. From this it can be seen that most high resolution work has been done with long scan times (ex situ / postmortem investigations), while the *in situ* work has been limited to low resolutions (coarser than 1 μm). This is mainly due to the limitation of current technology. However to study nucleation and early stages of growth a resolution of less than 0.1 μm and scan times of less than 10 seconds are needed (a low scan time ensures minimum sample deformation during acquisition, thus ensuring blur free imaging) The different zones suitable for *in situ* study of nucleation, growth and coalescence of creep cavities have been marked in Figure 1.30.

In this context the objectives of this work are as follows:

1. Developing a setup to investigate damage nucleation and growth at a high resolution (nearly 100 nm) and *in situ* (scan time of less than 10 sec).

- Developing and testing a mechanical device that could be integrated with *in situ* high temperature nanotomography imaging facility at ID16B beamline of ESRF.
 - Optimising acquisition procedure for tomography (scan time, number of projections etc.) to ensure good quality volumes for productive analysis of *in situ* deformation.
 - Developing procedure for multiscale imaging at high (100 nm) and low (645 nm) resolutions periodically.
 - Developing an automatic procedure for tracking damage during deformation and segmentation of volumes for swift analysis.
2. Using this device and procedures, to investigate high temperature damage nucleation and early stages of growth in model Al-3.6 wt% Cu alloy. This involves:
- Controlled generation of second phase particles of desired size using optimised heat treatment parameters.
 - Studying cavity nucleations and growth during high temperature deformation.
 - Consequently verifying diffusion and plasticity based creep cavity growth models.
3. Extending similar studies to commercial AZ31 magnesium alloys to investigate damage during superplastic regime. This involves:
- Investigating the effect of grain boundary sliding on cavity nucleation and growth.
 - Examine the applicability of existing models in predicting growth during superplastic deformation.

Chapter 2. Materials and Method

This chapter comprises of a description of the materials that have been studied in this thesis. This is followed by a detailed description of the technique of *in situ* nanotomography and the methods used for quantitative analysis. Since this is a novel technique that was primarily developed for this work, all the developments and improvements made are distinctly highlighted by colour coded lines on the right side of the page, where the [improvements are highlighted in blue](#) and [developments in green](#).

2.1 Materials

This study focusses on high temperature deformation in light alloys, and primarily two alloys were chosen for examination. First was a model Al-Cu alloy and the second was a commercial magnesium alloy. The Al-Cu alloy being a model alloy was chosen in order to generate second phase particles of desired size and explore their effect on creep cavities. Further AZ31 alloy was also investigated to study deformation in a commercial aerospace alloy. Apart from this the two alloys offered the possibility of studying cavity growth dominated by different mechanisms where Al-Cu alloy could show diffusion and plasticity based cavity growth while AZ31 alloy could potentially exhibit superplasticity based growth in addition to diffusion and plasticity. These two alloys will be discussed individually in following sections.

2.1.1 Al-Cu alloy

Al – 3.6 wt% Cu alloy was produced from pure aluminium (99.9%) and Al - 33 wt% Cu eutectic alloy and cast using squeeze casting method with 170 MPa pressure into an ingot, as can be seen in a schematic Figure 2.1 (a). Following the casting, the ingot was solutionised at 803 K for 70 hours in a box furnace and water quenched. The solutionised sample was then cut into several rods of 5 mm diameter and 100 mm length as highlighted in grey in the schematic of the ingot in Figure 2.1 (a). The rods were further machined into notched specimen of 400 μm diameter. Figure 2.1 (b, c) shows the typical geometry of the samples for the two different mechanical devices used. The sample for compact mechanical device was machined by electro

discharge machining Figure 2.1 (b) and the one for motorised mechanical device was machined using a lathe Figure 2.1 (c). The two devices will be further explained in section 2.2.4. To ensure complete dissolution of any segregation or second phase particles, the machined sample was solutionised again at the same conditions as the ingot. Theories suggest that second phase particles act as nucleation sites for creep cavities and that the size of these particles affect their nucleation. Keeping this in mind, a heat treatment procedure was adopted which allowed us to control the size of second phase particles in the Al-Cu alloy. This is explained in detail in Chapter 3. It should be noted that all Al-Cu samples examined in this text are of the sample composition i.e. Al -3.6 wt% Cu.

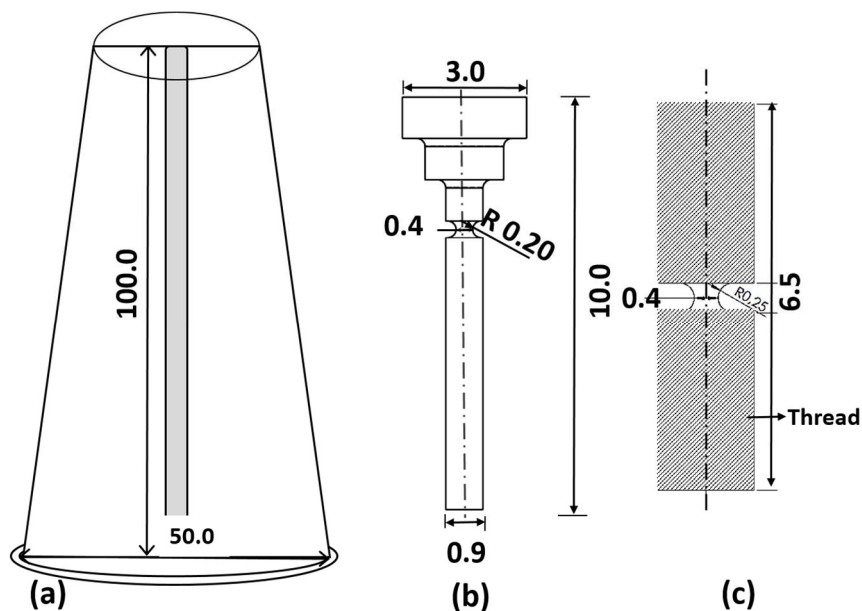


Figure 2.1 (a) Schematic illustration of ingot cast for Al – 3.6 wt% Cu sample, from which cylindrical rods (highlighted in grey) were machined. (b) Drawing of sample used for compact mechanical device (machined from the rod). (c) Drawing of sample used for motorised mechanical device (machined from, the rod). All measurements in mm.

2.1.2 AZ31

A hot rolled AZ31 alloy sheet of 2 mm thickness was procured from Satzgitter Magnesium-Technologie GmbH. Its composition was 3 wt% of Al, 1 wt% of Zn and 0.4 wt% of Mn. From this sheet cylindrical rods of 2 mm diameter and 100 mm length were machined with their axis parallel to the rolling direction (RD) (see Figure 2.2 a for a schematic illustration, rod highlighted in grey). They were then further machined into two types of notched samples for mechanical testing. Figure 2.2 (b, c) shows a

schematic illustration of the typical geometry of the two samples for the two mechanical devices. Since the max thickness of the sheet was 2 mm, samples with a top part of 3 mm diameter could not be machined from the sheet (as was done for Al-Cu alloy, Figure 2.1 b). This enlarged diameter was necessary to make it compatible for the compact mechanical device. Hence a small piece of alumina tube (length nearly 2 mm and outer diameter 4 mm) had to be glued onto the top of the sample with ceramic glue, see Figure 2.2 (b). The sample geometry used for motorised mechanical device was the same as the Al-Cu alloy, Figure 2.2 (c). Both the samples were machined using a lathe.

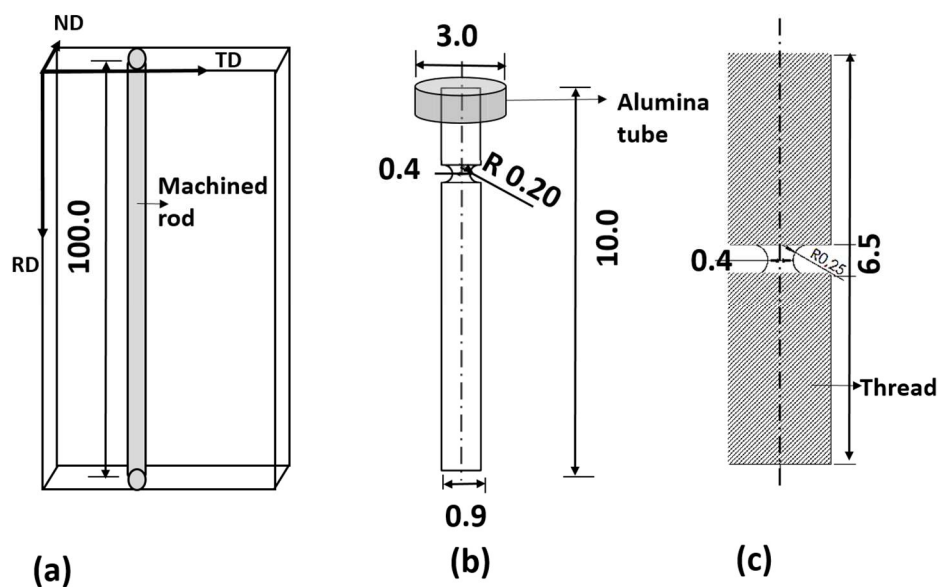


Figure 2.2 (a) Schematic illustration of AZ31 sheet of 2 mm thickness (RD: Rolling direction, TD: Transverse direction, ND: Normal direction), from which cylindrical rods were machined (highlighted in grey). (b) Drawing of sample used for compact mechanical device (machined from the rod), a small piece of alumina tube (2 mm length) was glued to the top of this, which has been marked (c) Drawing of sample used for motorised mechanical device (machined from the rod). All measurements in mm.

The optical micrograph of the material obtained after etching it (5 g of acid picric acid, 100 ml of ethanol, 10 ml of distilled water and 10 ml of acetic acid) showed a polycrystalline microstructure with heterogeneous grain size and few intermetallics, see Figure 2.3 (a). Note that the optical and EBSD micrograph presented in this text is a work of T. Dessolier [114] who made the observation on the same sheet of AZ31. The intermetallics when further analysed by SEM – EDX showed presence of aluminium and magnesium and corresponded to $Mg_{17}Al_{12}$ intermetallic precipitates.

These precipitates were also observed by Yin et al. [115] on AZ31. Figure 2.3 (b) shows a histogram of grain size distribution obtained using EBSD map (Figure 2.3 c), it can be seen that a range of grain sizes from 2-25 μm are seen in the sample. The average grain size was estimated by the fractional area method:

$$\bar{d} = \sum d_i A_i \quad (2.1)$$

where d_i is the diameter of the grain i and A_i is the area fraction of the grain i . This results in a mean grain size equal to 12 μm with a standard deviation of 4 μm .

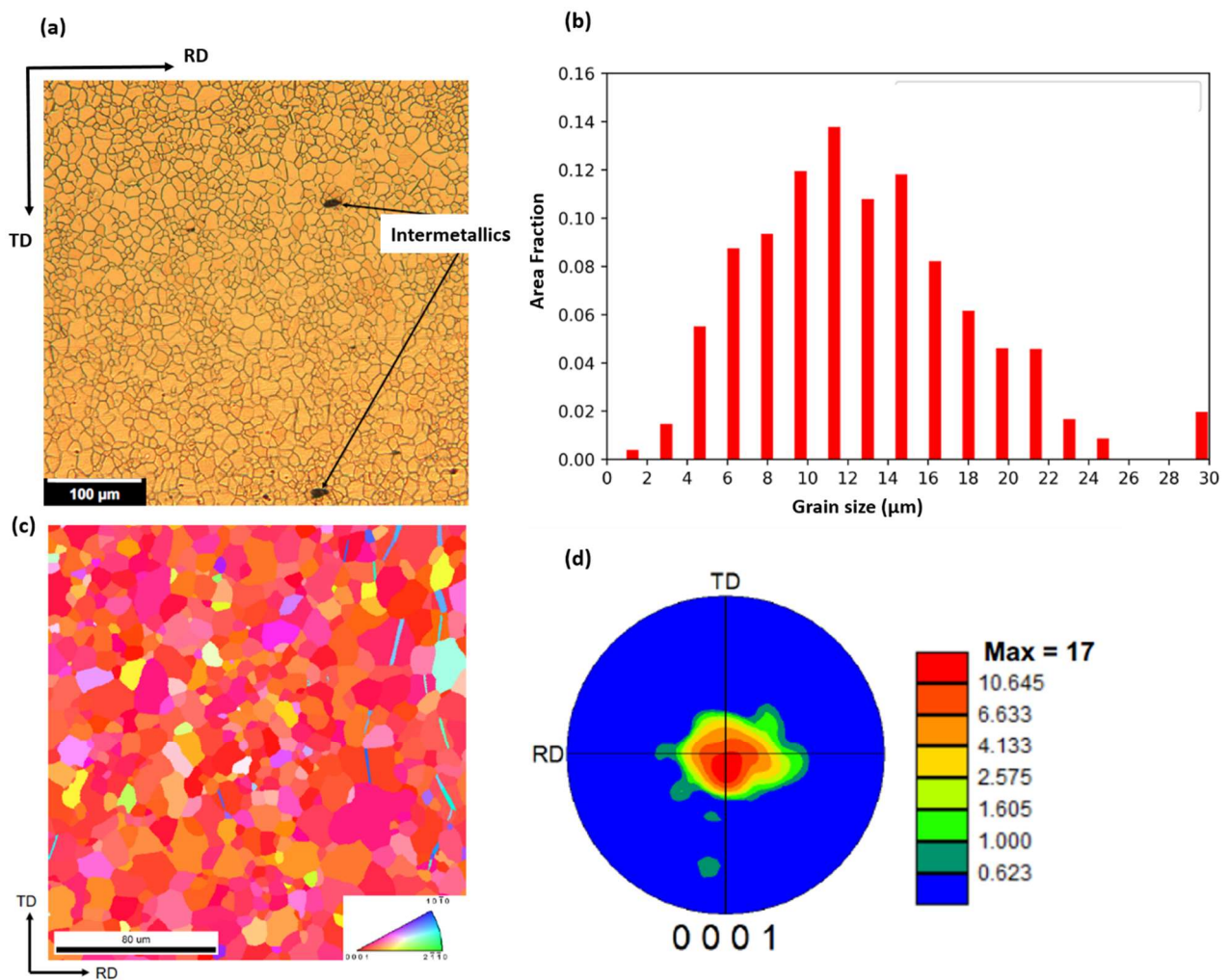


Figure 2.3 (a) Optical micrograph (b) Histogram of grain sizes observed using EBSD map (c) EBSD map (d) Inverse pole figure in the normal direction of a AZ31 sample, Work of T. Dessolier [114]. This sample was obtained from the same AZ31 sheet that was used for machining the samples for this thesis. .

The Inverse pole figure in the normal direction (IPF-ND, Figure 2.3 d) mapping of the sample shows a strong basal texture such that the c axis of the hexagonal closed packed grain is predominantly parallel to the ND.

On examining the sample using high resolution tomography the AZ31 alloy showed presence of two intermetallic phases, a grey and a black phase (Figure 2.4). The black phase was expected to be an Al-Mn intermetallic, possibly Al_6Mn . The grey intermetallic was attributed to the $Mg_{17}Al_{12}$ phase. Both these phases have been reported to be present in AZ31 rolled sheets [21]. The $Mg_{17}Al_{12}$ particles had a grey level similar to the matrix hence were difficult to segment. Since studying intermetallics was not the focus of the present study, only the black Al-Mn phase intermetallic particles were segmented for DVC tracking which will be explained in section 2.5.2. Hence all the intermetallics referred in this text correspond to the black, Al-Mn intermetallics phase.

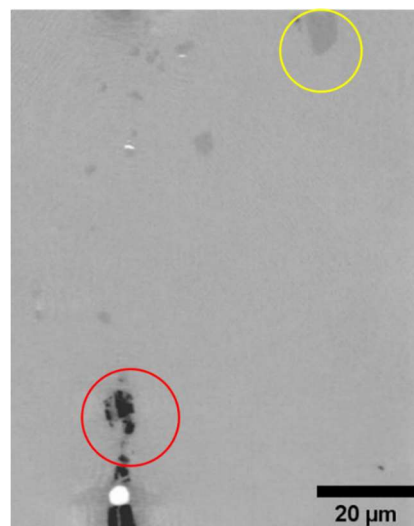


Figure 2.4 Transverse 2D slice from high resolution (pixel size 100nm) tomography of a AZ31 sample. Two types of intermetallics seen in the sample have been encircled. Yellow circle: grey intermetallic, Red circle: black Intermetallic (cavity in white)

2.2 *In situ* nanotomography setup

In situ high temperature deformation was performed using synchrotron X-ray radiation. This involved loading the sample at a constant temperature and load or strain rate, while simultaneously imaging it in 3D, using single distance X-ray phase contrast nanotomography at the ID16B beamline of the ESRF. This setup will be detailed in the upcoming sections.

2.2.1 The European Synchrotron Radiation Facility (ESRF)

The European Synchrotron Radiation Facility (ESRF) is a world leading synchrotron facility based in Grenoble, France. It was founded in 1988 and began operations in 1994. It is supported by 22 partner nations. Each year over 9000 scientists from diverse scientific areas including medicine, materials, environment and cultural heritage studies, use the ESRF facility. Currently the facility is undergoing an ambitious, EBS (Extremely Brilliant Source) upgrade to a revolutionary new storage ring by 2022, with performance increased by a factor of 100.

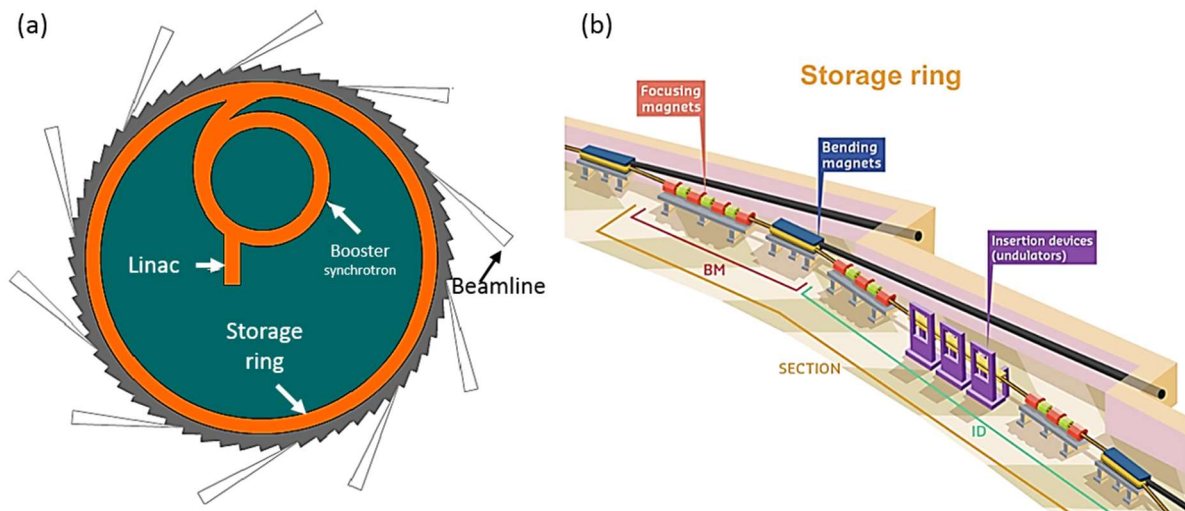


Figure 2.5 (a) Schematic illustration of the main components of the ESRF. (b) Schematic illustration of the main components of the storage ring. Source: www.esrf.eu

The Figure 2.5 (a) shows a schematic of the main components of the ESRF. In order to produce synchrotron radiations, the first step is the production of electrons, which happens in the linear accelerator or *linac*. This consists of an electron gun that produces “bunches” of electron and accelerates it to 200 million eV, to be transferred into the *booster ring*. The booster synchrotron pre accelerates the electrons to **6 GeV** before injecting them into the *storage ring*. A booster only injects electrons a few times a day when the storage ring needs to be refilled. The storage ring is a tube with a circumference of 844 m, consisting of 32 straight and curved sections in alternating order, see Figure 2.5 (b). In each curved section, two large *bending magnets* force the electrons into a racetrack-shaped path. As the electrons are deflected from their straight path when passing through these magnets, they emit a spray of X-rays tangential to the plane of the electron beam. These X-rays are used

by the BM (bending magnet) beamlines. Further, in each straight section, several focusing magnets ensure that the electrons remain close to their ideal orbital path. In addition they have *undulators* (or *Insertion Device*), which force the electrons to follow an undulating, or wavy path. The radiation emitted at each consecutive bend overlaps and interferes with that from other bends resulting in a much more focused, or brilliant, beam of radiation than that generated by bending magnets. These X-rays are used by the ID (Insertion Device) beamlines of the ESRF.

The BM beamlines produce X-rays of a wide range of energy which cannot be tuned to a specific energy, while in the ID beamline, by adjusting the spacing between magnets of insertion devices the energy can be tuned from 1-600 keV depending on the requirement of each beamline. The experiments for this thesis have been performed at the ID16B beamline of the ESRF, which is further described in the next section.

2.2.2 The ID16B beamline

ID16B is an insertion device based long, nano-analysis beamline 165 m from the source. It offers a high flux (10^9 to 10^{12} ph/s) monochromatic ($\Delta E/E$ nearly 10^{-2} to 10^{-4}) nano beam, tuneable in a large energy range (5–70 keV) [116]. The beamline allows investigations through various techniques such as X-ray fluorescence (XRF), X-ray absorption (XANES), X-ray excited optical luminescence (XEOL) and X-ray diffraction (XRD) as well as magnified phase contrast nanotomography.

The X-rays are focused into a nano beam (spot size $50 \times 50 \text{ nm}^2$) using the Kirkpatrick-Baez (KB) mirror at 165 m from the source. In order to perform tomography this spot is used as a secondary source. The detector is placed at a fixed distance from the source such that the conic beam produced covers the field of view. Thanks to this geometrical magnification the field of view on the sample can be easily adjusted between from $768 \times 768 \times 648 \text{ }\mu\text{m}^3$ to $32 \times 32 \times 27 \text{ }\mu\text{m}^3$ just by adjusting the distance of the sample from the sources (giving a pixel size in the range of $0.6 \text{ }\mu\text{m}$ to $0.025 \text{ }\mu\text{m}$). Classical phase contrast nano holotomography performed at the beamline involves multi distance acquisition, with scan time between 30 min and 2 hours in order to reach the highest resolution. For *in situ* studies, fast acquisition is crucial, hence single distance phase contrast imaging is

used instead of holotomography. Reconstruction using radiographs acquired at a single distance affects the resolution of the volumes but using a modified algorithm is effective in counteracting most of the degradation in resolution [117], bringing down the time for one full tomographic scan to 3.5 seconds. For tomography, the beamline is equipped with a PCO edge 5.5 detector (equipped with a CMOS sensor) with a pixel size of $6.5\ \mu\text{m}$, which in combination with a 10X magnification offered by Olympus optic is reduced to $0.65\ \mu\text{m}$. If used in a 2 X 2 binning mode however, the pixel size equals $1.3\ \mu\text{m}$ (which was the case for the current study). There are 3 sets of scintillators available for the detector at the beamline:

- LSO/Tb: $17\ \mu\text{m}$ thickness
- GGG/Eu: $34\ \mu\text{m}$ thickness
- LSO/Tb: $30\ \mu\text{m}$ thickness

For *in situ* tomography high thickness of scintillators are preferred since they produce higher intensity of signals (from same X-ray intensity). Further between the $34\ \mu\text{m}$ GGG/Eu and $30\ \mu\text{m}$ LSO/Tb, LSO/Tb offers an advantage of significantly reducing the afterglow as compared to GGG/Eu and is hence preferable. However both GGG $34\ \mu\text{m}$ and LSO $30\ \mu\text{m}$ were used during acquisition for this work due to constraints on the availability of LSO at the beamline initially.

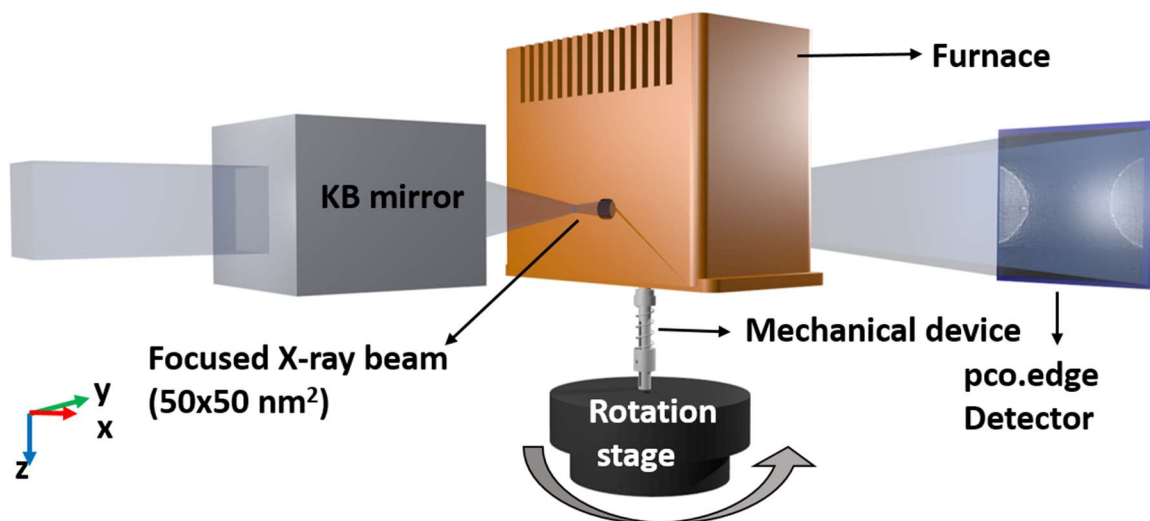


Figure 2.6 Schematic illustration of *in situ* nanotomography setup at the ID16B beamline of ESRF, showing a compact mechanical device that fits inside the beamline furnace [118].

In addition to the possibility of fast imaging at pixel sizes as low as 25 nm, the beamline is equipped with a micro furnace that allows for heating samples during tomography [94]. The furnace is mounted in such a way that it can move between the focal point and detector, along with the sample. Further, for this work mechanical devices were developed which provided the possibility for applying load / pull on the sample along with heat, simultaneously performing fast tomographic scans (less than 10 seconds) with sub micrometer resolution (100 nm). The setup for this is illustrated in Figure 2.6. The furnace and the mechanical devices are detailed in the following section.

2.2.3 Furnace (improvement of temperature calibration)

In order to heat samples for *in situ* tomography, the ID16B beamline has a rapid heat-up rate, bottom loading resistance furnace. The outer shell of the resistor is made of steel, while its core is made of a nickel-chromium alloy. This furnace allows heating up to temperatures as high as 1273 K. In order to maintain the thermal stability at the experimental hutch of the beamline, which is imperative for a nano beam [116], the furnace is equipped with an efficient water based cooling system. Further in order to insulate the sample and ensure a constant temperature, a cover of insulating wool is added at the bottom opening of the furnace. The temperature of the furnace is controlled using a Eurotherm 2408, Proportional Integral Derivative (PID) controller which is in turn connected to a Delta Electronica power supply. The PID was not calibrated as it would cause sudden jumps in temperature which would induce sample movement consequently interfering with tomographic acquisition. Hence the power on the controller is tuned manually which in turn controls the voltage of the power supply. Based on this voltage the power supply then appropriately heats up the furnace.

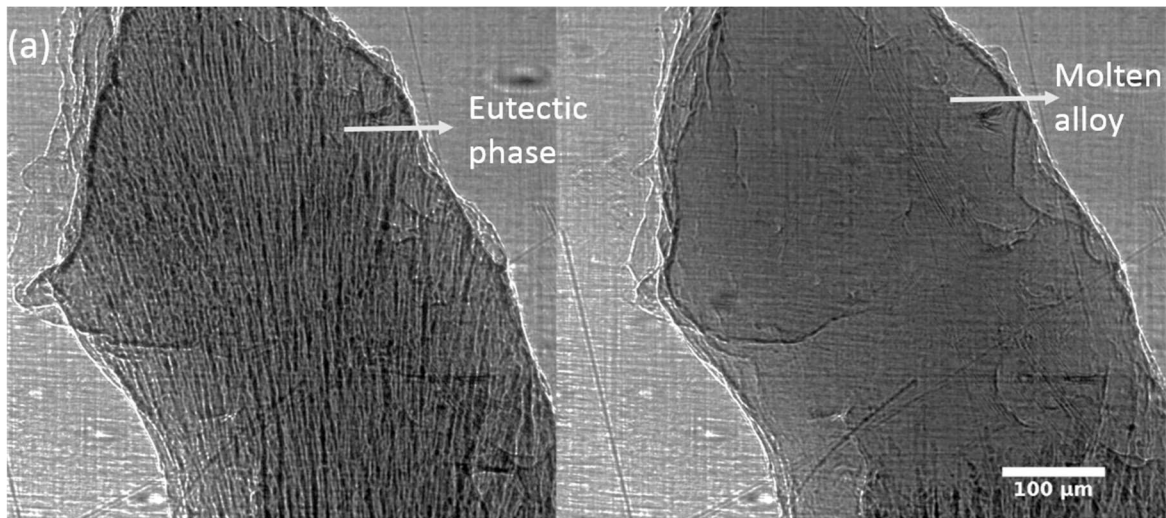


Figure 2.7 Radiograph of Al -6.1wt% Ni eutectic alloy obtained as a part of a calibration regime (a) before melting, showing solid eutectic phase, (b) after melting showing molten alloy.

The furnace is fitted with a K type thermocouple, which helps monitor the temperature of the furnace. But in order to accurately determine the temperature of sample corresponding to the measured furnace temperature, a new regime to calibrate the furnace using alloys with eutectic compositions was developed. For the calibration, these alloys were heated until they melted, and the point of melting was determined by looking at radiographs as can be seen in Figure 2.7. Since eutectic transformation occurs at an invariant temperature, the point at which the alloy undergoes transformation gives the exact sample temperature corresponding to the furnace temperature. Using this principle the furnace was calibrated over a range of temperature using different eutectics available at the beamline as listed in in Table 2.1. These eutectics were procured from Vulkam, Saint Martin d'Hères, France. For a routine calibration, different eutectics were mounted on a ceramic tube and heated inside the furnace and the furnace temperature (from the thermocouple) was plotted against the power and compared with the sample temperature as shown in Figure 2.8. This data of sample temperature corresponding to power could then be interpolated, using a polynomial fit to estimate sample temperature corresponding to any power. One such example is shown in Figure 2.8.

Table 2.1 List of alloys with eutectic composition and their corresponding eutectic transformation temperatures, available at ID16B beamline of ESRF.

| Eutectic alloy composition (wt %) | Eutectic temperature (K) |
|-----------------------------------|--------------------------|
|-----------------------------------|--------------------------|

| | |
|------------|------|
| Sn 9 Zn | 471 |
| Al 53 Ge | 697 |
| Al 33 Cu | 821 |
| Al 6.1 Ni | 913 |
| Cu 30 Si | 1075 |
| Ni 71.6 Ti | 1215 |
| Cu 9 Zr | 1253 |

For high temperature deformation study, apart from the routine calibration an additional calibration was also performed by placing the eutectic inside the mechanical device, to mimic the exact sample environment. Since all the tests were performed at 697 ± 50 K, Al- 53 wt% Ge (Eutectic temperature 697 K) was the eutectic used. This is shown in Figure 2.8 where the red star is the sample temperature while the red circle is the furnace temperature. Since it can be seen from Figure 2.8 that near 697 ± 50 K the difference in temperature between furnace and sample: ΔT (nearly 50 K), remains nearly constant, the estimate regarding the sample temperature in this range was made using this ΔT , achieved after calibration.

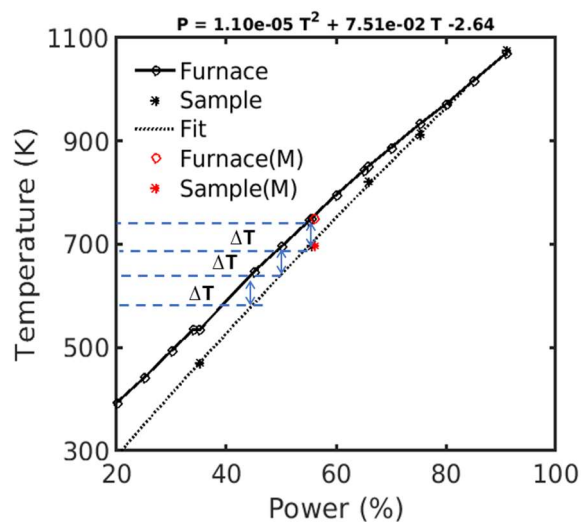


Figure 2.8 Calibration curve for furnace using different eutectics, showing the sample and furnace temperature corresponding to percentage the power supplied. Red markers indicate calibration with mechanical device (M). ΔT indicates constant difference in temperature of furnace and sample in 697 ± 50 K temperature regime. A fit to the power and corresponding sample temperature is also indicated with the defining equation mentioned on the top of the plot, where P is Power and T is Temperature.

It should be noted that sample position inside the furnace could change between experiments and this could affect the temperature on the sample. In addition the resistance of the furnace could also change over prolonged use. In order to account for these factors the calibration of the furnace was repeated at the start of each beamtime to ensure precision in temperature.

2.2.4 Mechanical devices

Two types of compact mechanical devices were developed for this work. One which only allowed constant load application and the other that permitted control of load and strain rate. The first one is referred to as **compact mechanical device** and the second one is called **motorised mechanical device** in this text. Both these devices were developed in house with the help of Xavier Bataillon and Charles Josserond, technical staff at SIMaP laboratory, University Grenoble Alpes. The design ensured that they fitted on the rotation stage of the beamline and could be easily inserted into the beamline furnace (described in section 2.2.3). The key consideration, while designing these devices were:

- The diameter of the upper part (top 20 mm) that was to be inserted in the furnace could be a maximum of 4 mm.
- The maximum height of the setup could be nearly 52 mm.
- The mass of the device had to be lower than 200 g. This was tricky especially for the motorised mechanical device.

2.2.4.1 Compact mechanical device

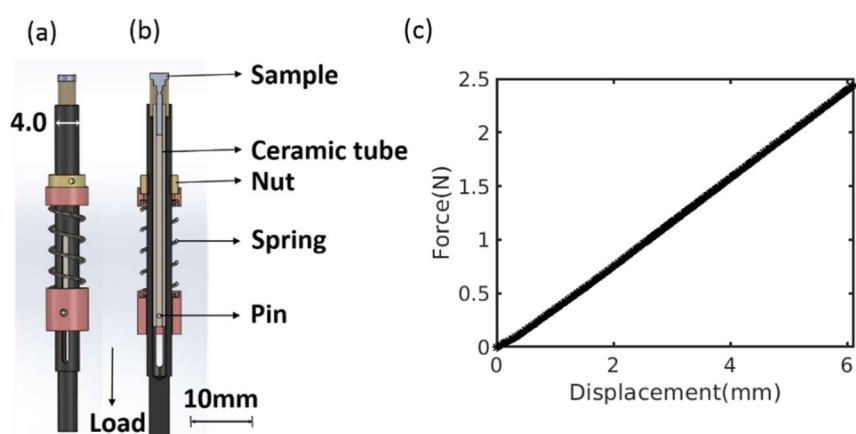


Figure 2.9 Schematic illustration of the compact mechanical device (a) front view (b) section view, used for high temperature in situ nanotomography experiment at ID16B beamline of ESRF [118]. (c) Plot showing variation of force with displacement, for the spring used in the compact mechanical device measured using a compression testing machine.

The compact mechanical device (Figure 2.9) allowed pre-stressing the sample to a constant load. The sample glued (using ceramic glue) on an alumina tube was placed in the device and a load was applied on the sample by compressing the spring to desired length using the nut (see Figure 2.9 a, b). The load was transferred from the spring to the sample via the pin. The spring was made of a nickel based superalloy to avoid creep and ensure mechanical stability at high temperature. The compression of the spring was calibrated to the effective load on the sample. This compression curve for the spring was measured on an external compression device. The calibration curve is shown in Figure 2.9 (c). Boron nitride casing around the sample ensured easy passage of X-rays through the sample for tomography acquisition. The diameter of 4 mm on the top part of the device ensured its convenient insertion into the furnace.

Theoretically with a thread pitch of 0.5 mm and an error on the nut's position of $1/12^{\text{th}}$ of a turn, the error on the load is less than 0.02 N. However the initial contact with the spring was not easy to determine and much more detrimental was the locking of the spring in the thread which changed each time. Thus the exact load on the sample was estimated using a high temperature compression test performed on the sample. More on this will be detailed in section 2.6.3.

2.2.4.2 Motorised mechanical device

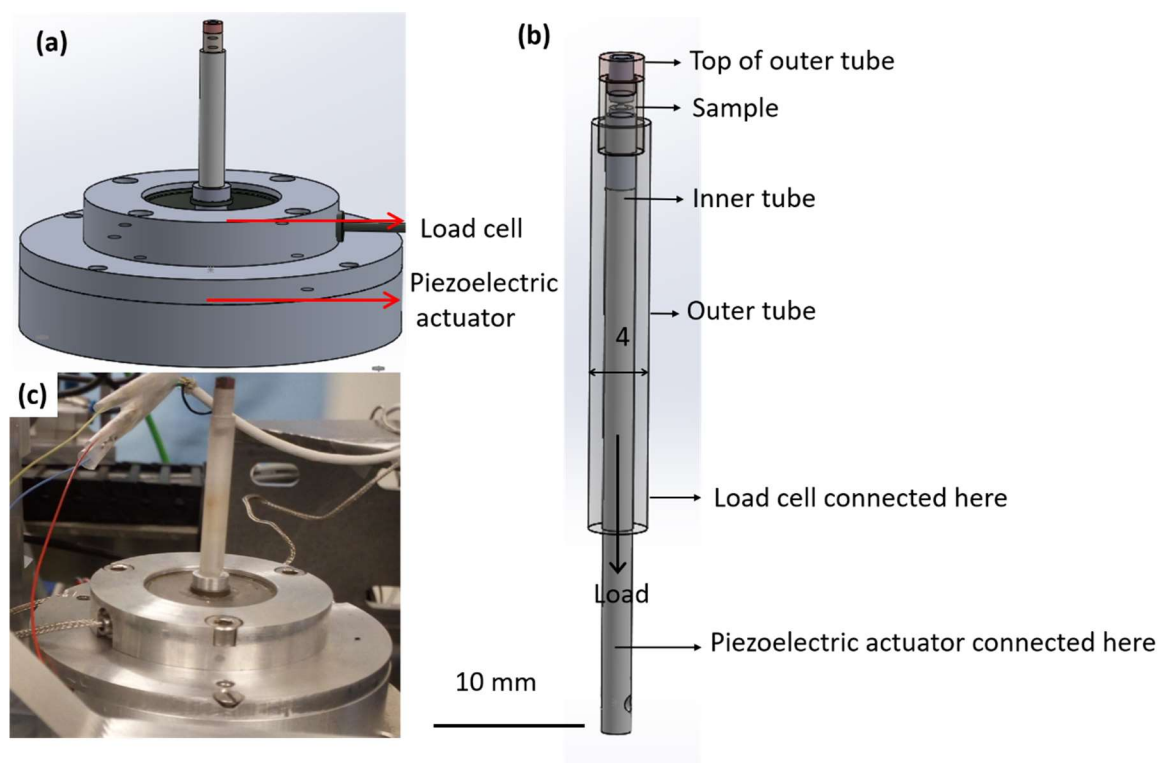


Figure 2.10 (a) Schematic depiction of the motorised mechanical device. (b) Detailed view of the top part of the device (c) Photo of device placed on the rotating stage of the beamline. Measurements are in mm.

In order to improve control, a new motorised mechanical device was developed. It consisted of a piezoelectric actuator which could strain / pull on the sample at a constant rate. It was also equipped with a load cell (20 N) which allowed measurement of the load on the sample (see Figure 2.10 a). The device consisted of two concentric quartz tubes. The bottom of the sample was screwed into the top of the inner tube and the top of the sample was screwed over the top of the outer quartz tube. Further, as can be seen in Figure 2.10 (b), the piezoelectric actuator was attached to the bottom of the inner tube, which allowed to pull the sample at a constant strain rate. This allowed application of a strain rate in the range of 10^{-5} to 10^{-2} s^{-1} with a maximum tensile displacement of $400 \mu\text{m}$. The load cell was attached on the bottom of the outer quartz tube. As a result of which, the consequent load experienced by the sample could be measured. Both the actuator and load cell were connected to a power source and could be controlled using an in house software. Like the previous device, this device could also fit on the rotating stage and inside the furnace. Since the ID16B beamline currently does not have a slip ring on the

rotating stage, the presence of wires impeded full rotation (360°). Hence acquisitions were restricted to half rotations (180°).

2.3 Data acquisition

17.5 keV, conic, pink beam ($\Delta E/E$ nearly 10^{-2}) X-rays were used to perform single distance phase contrast *in situ* nanotomography investigation. During the acquisition the sample was subjected to deformation either by applying a constant load, or by pulling it at a constant speed, at constant temperature (high temperature). The acquisition consisted of rotating the sample (placed inside the mechanical device, see Figure 2.6) 360° or 180°. Note the furnace was stationary (did not rotate), during this time.

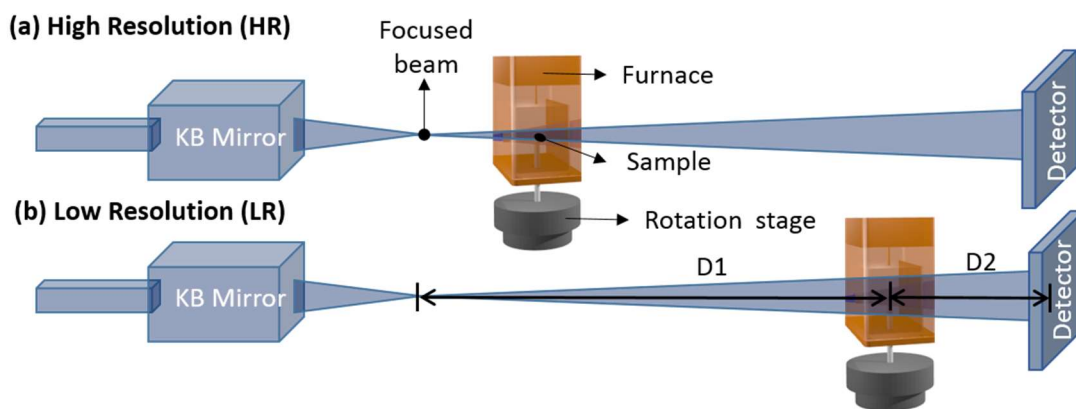


Figure 2.11 Schematic illustration of positions of furnace and sample with respect to the focussed beam at (a) High Resolution (HR pixel size is 100 nm) (b) Low Resolution acquisition (LR pixel size is 645 nm).

Table 2.2 Distance of sample from source and detector during high and low resolution scans.

| | High Resolution (pixel size 100 nm) | Low Resolution (pixel size 645 nm) |
|---|--|---------------------------------------|
| D1 (mm) | 43.05 | 278.68 |
| D2 (mm) | 518.00 | 282.38 |
| Magnification $\frac{(D1+D2)}{D1}$ | 13 | 2.01 |

While imaging high temperature deformation, it was required to image the notch for computing mechanical deformation parameters and examine deformation in real

time, which meant low resolution imaging. But at the same time imaging at high resolution was also imperative, in order to image nucleation and growth of creep cavities. Multiscale acquisition was the ideal approach for this. Thanks to the conical beam, changing the distance of the sample with respect to the detector / focused X-ray beam, changes the field of view and the consequent pixel size of acquisition, which allows multi resolution imaging. Employing this capability, a set of Low Resolution (LR) radiographs with a field of view of $826 \times 826 \times 697 \mu\text{m}^3$, pixel size of 645nm followed by a set of High Resolution (HR) radiographs with a field of view $128 \times 128 \times 108 \mu\text{m}^3$, pixel size of 100nm were acquired by moving the sample between the focused nanobeam and the detector (Figure 2.11). Remember that the motion of the furnace was synchronised with that of the sample, and consequently it also moved along with the sample. Table 2.2 lists the distance of sample with secondary source or the focussed beam (D1) and distance of sample with detector (D2) along with the resulting geometrical magnification achieved during high and low resolution scans.

Starting with this scheme, several modifications were done to the acquisition process, to tackle the different problems encountered. Specific macros were developed for each. The various acquisition schemes have been named S1 to S5 and are described below:

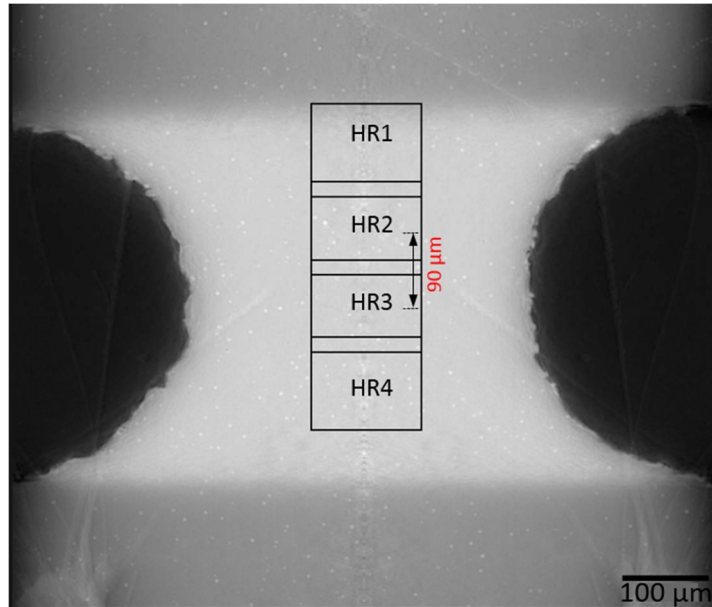


Figure 2.12 A transverse 2D slice from LR volume depicting the scheme of acquisition where 4 HR volumes are acquired as indicated by HR1 to HR4, the offset between the centres of successive HR scans is $90\ \mu\text{m}$. Remember that the HR3 volume stands in the middle of the LR field of view.

- **S1:** Acquiring, one HR volume, followed by one LR volume using continuous 360° rotation of sample. When acquiring, using this scheme it was found that the field of view imaged in HR was very small, and so only a small area could be examined in the high resolution. To tackle this hurdle the following approach was devised.
- **S2:** Acquiring four HR volumes (would be also referred as *multi z scans*) along different heights of the sample, by moving the rotation stage along z axis (see Figure 2.6 for the scheme of coordinate axis), followed by one LR volume. Note that centre of each HR volume was at a distance of $90\ \mu\text{m}$ from the other, and the acquisition started with HR1 (see Figure 2.12) followed by HR2, HR3 and HR4 following continuous 360° rotation of sample. After this the rotation stage returned to the original position (corresponding to HR3 for next set of LR scan). Figure 2.12 illustrates how the 4 HR volumes (indicated by HR1, HR2, HR3 and HR4) are positioned with respect to a transverse LR slice.

The first two approaches worked well with the compact mechanical device, since the device was standalone and had no supplementary electrical device attached to it.

However when the motorized mechanical device was introduced, continuous 360° were no longer feasible due to its electrical connections. It was seen that reconstruction using half turn projections also resulted in enough resolved volumes, this will be further explained in section 2.4.1.5 in detail. Hence further acquisitions were limited to 0 to 180° rotation and the following approaches were used:

- **S3:** Acquiring four HR volumes, such that two set of radiographs were acquired by rotating the sample 0° to 180° and then by rotating it 180° to 0°. Remember that these two sets were identical (acquired merely 18 seconds apart), therefore any one of these two was chosen for analysis, depending on the quality of 3D volume. Such sets of radiographs could also be used for z shift correction encountered by the sample during acquisition, to improve quality of reconstructed volume. This was however not done in this work. When the motorised mechanical device was introduced it was noted that the straining of sample could be monitored by monitoring movement of actuator. Hence LR volumes were not necessary. Therefore instead of acquiring LR volumes, acquisition was limited to acquiring a set of four HR volumes repeatedly as long as the deformation continued. An exception was made to this when the LR volume showed an interesting feature which could not be fully captured in HR and had to be monitored during deformation. In such cases the following approach was used.
- **S4:** Acquiring four HR volumes, such that two set of radiographs were acquired by rotating the sample 0° to 180° and then by rotating it 180° to 0° followed by a LR volume.

When strain rates was greater than $5 \times 10^{-4} \text{ s}^{-1}$, acquiring four HR volumes was not wise due to very quick deformation, hence the scanning regime was modified to acquiring 2 HR volumes instead.

S5: Acquiring two HR volumes, such that two set of radiographs were acquired by rotating the sample 0° to 180° and then by rotating it 180° to 0°, such that the two sets were identical. The position of the two HR volumes, with respect to the LR volume corresponded to the HR2 and HR3 position in Figure 2.12.

Table 2.3 summarises the different types of scan regimes adopted, along with the various parameters used for the scans and the time between consecutive scans. Several trial and errors were done to arrive at the optimum number of projections such that the scan time was not too long, in the interest of *in situ* scans at the same time ensuring good quality of acquired volumes.

It should be noted that at the beginning of *in situ* scans, ambient scans were acquired (where the sample was inside the mechanical device, but not the furnace). References needed for reconstruction that is flat field (taken by removing the sample from field of view) and dark field (taken by switching off the beam), were acquired only for ambient scans. These references were then also used for reconstructing *in situ* scans.

Table 2.3 A summary of scans routines adopted with parameters used.

| Name | Scans | Projection between angles | No. of projections | Scan time for one volume (s) | Time between (min.) | | | Scintillator used and thickness |
|------|----------------|---------------------------|--------------------|------------------------------|---------------------|-----------|----------|---------------------------------|
| | | | | | Two HR1 | HR1 & HR2 | HR1 & LR | |
| S1 | 1 HR + 1 LR | 0° to 360° | 721 | 3.5 (360p) 7 (721p) | 3. | 0.52 | | GGG/Eu: 34 µm |
| S2 | 4 HR + 1 LR | 0° to 360° | 721 | 3.5 (360p) 7 (721p) | 5.5 | 0.52 | 3.4 | GGG/Eu: 34 µm |
| S3 | 4 HR | 0° to 180° 180° to 0° | 360 | 3.5 (360p) | 2.8 | 0.7 | - | LSO/Tb: 30 µm |
| S4 | 4 HR + 1 LR | 0° to 180° 180° to 0° | 360 | 3.5 (360p) | 6.2 | 0.7 | 4.1 | LSO/Tb: 30 µm |
| S5 | 2 HR | 0° to 180° 180° to 0° | 360 | 3.5 (360p) | 1.42 | 0.7 | - | LSO/Tb: 30 µm |

Table 2.4 and Table 2.5 lists the main experiments that were conducted during the course of the thesis comprising of over 5 beam times of average 3 days each. Before these experiments an additional of 3 beam times were performed which mainly involved optimising the technique and devices. The explanation of different scan regimes listed in these tables are detailed in

Table 2.3. The load / strain rate and temperature used during the experiments were chosen so that they resulted in a strain rate:

- Which captured different regimes of cavity growth for example a slow strain rate allowed capturing of early stages of cavity growth. While in case of AZ31 this was done to fall in the superplasticity regime of cavity growth.
- The straining of the sample was not too slow: keeping in mind the limited experiment time and not too fast: to maintain good image quality.

All the acquired data was reconstructed. Among this few reconstructed volumes showed severe artefacts due to motion and or deformation of sample. Few other samples which deformed under very high load, could only be imaged for 2-3 sets of HR scans. Additionally there was a very small overlapping region of interest between the few scans because of which no meaningful *in situ* analysis could be made. This problem of limited overlapping region of interest between consecutive scans was inevitable in all S1 scans as well. Among the remaining scans an analysis of mechanical parameters (strain and strain rate) was done using DVC tracking or notch area estimation. The samples which deformed under a steady state for considerable time were selected for in depth analysis and have been presented in this work. The remaining data is however available for further analysis if needed.

Table 2.4 List of *in situ* high temperature experiments conducted with Al-Cu alloy

| File name | Heat Treatment time | Temp. (K) | Load (N) / Strain rate (s ⁻¹) | Scan Regime | Type of mechanical device |
|----------------------------------|---------------------|-----------|---|-------------|---------------------------|
| EXPERIMENT 4 May 2017 | | | | | |
| alCu_C1B | 5 min | 698 | 2.2 N | S1 | Compact |
| alCu_B2C | 3 min | 688 | 2.2 N | S1 | Compact |
| alCu_C2D | 5 min | 688 | 2.2 N | S1 | Compact |
| alCu_B3B | 3 min | 698 | 2.2 N | S1 | Compact |
| EXPERIMENT 5 July 2017 | | | | | |
| AlCu_C4 | 5 min | 698 | 2.2 N | S2 | Compact |
| AlCu_C3 | 5 min | 698 | 2.5 N | S2 | Compact |
| AlCu_E1 | 3 min | 698 | 2.5 N | S2 | Compact |
| EXPERIMENT 7 October 2018 | | | | | |
| AlCu_Z | 5 min | 698 | 5 X 10 ⁻⁵ s ⁻¹ | S4 | Motorised |

Table 2.5 List of in situ high temperature experiments conducted on AZ31 alloy

| File name | Temp. (K) | Load (N) / Strain rate (s ⁻¹) | Scan Regime | Type of mechanical device |
|-----------------------------------|-----------|---|-------------|---------------------------|
| EXPERIMENT 4 May 2017 | | | | |
| AZ31_A | 673 | 2.2 N | S1 | Compact |
| AZ31_B | 673 | 2.2 N | S1 | Compact |
| EXPERIMENT 5 July 2017 | | | | |
| AZ31_D | 673 | 2.6 N | S2 | Compact |
| AZ31_E | 673 | 2.4 N | S2 | Compact |
| AZ31_F | 673 | 3.4 N | S2 | Compact |
| AZ31_G | 673 | 5.3 N | S2 | Compact |
| AZ31_C3 | 673 | 2.8 N | S2 | Compact |
| AZ31_H | 673 | 3.6 N | S2 | Compact |
| AZ31_I | 673 | 4.2 N | S2 | Compact |
| EXPERIMENT 6 November 2017 | | | | |
| AZ31_K | 673 | 3.0 N | S2 | Compact |
| AZ31_L | 623 | 6.5 N | S2 | Compact |
| AZ31_M | 573 | 15 N | S2 | Compact |
| AZ31_N | 673 | 4.3 N | S2 | Compact |
| AZ31_O | 673 | 2.8 N | S2 | Compact |
| AZ31_P | 623 | 3.4 N | S2 | Compact |
| EXPERIMENT 7 October 2018 | | | | |
| AZ31_X | 673 | 5 X 10 ⁻⁴ s ⁻¹ | S3 | Motorised |
| AZ31_W | 673 | 1 X 10 ⁻³ s ⁻¹ | S5 | Motorised |
| AZ31_V | 573 | 5 X 10 ⁻⁵ s ⁻¹ | S3 | Motorised |

2.4 Data Processing

Once the radiographs were acquired, the next process was reconstructing 3D volumes from the radiographs, followed by segmentation of volumes to extract useful data out of them. Figure 2.13 shows a flowchart depicting the various processes

involved in obtaining a 3D volume. The following sections give the details about each of these processes.

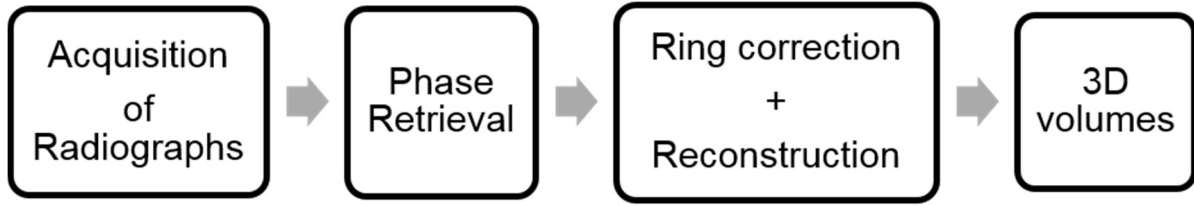


Figure 2.13 Flowchart showing steps involved in obtaining 3D volumes using X-ray tomography.

2.4.1 Phase retrieval and reconstruction

Since phase contrast tomography was carried out for this work, the first step in reconstruction of 3D volumes was retrieving the phase information. Different algorithms for phase retrieval were employed for LR and HR volumes, which are described in the following section.

2.4.1.1 Phase retrieval for LR volumes

The LR volumes were primarily used, to estimate the change in cross section of the notched sample on deformation, with time. A basic Paganin [119] based algorithm was sufficient for retrieving the phase information from these volumes.

Propagation based phase contrast imaging relies on propagation and interference of a spatially coherent beam passing through a sample. This beam when reaching the detector has both phase and attenuation information in it. Paganin proposed an approach to retrieve the phase shift information from this [120], such that phase shift incurred by is, given by:

$$\varphi(x) = \frac{\delta_r}{2\beta} \ln \left(\mathcal{F}^{-1} \left\{ \frac{\mathcal{F}(I_{\theta,D})}{1 + \pi\lambda D \frac{\delta_r}{\beta} \|f^2\|} \right\} \right) \quad (2.2)$$

where, \mathcal{F} and \mathcal{F}^{-1} denote the Fourier transform and its inverse, respectively; $I_{\theta,D}$ the intensity recorded at a distance D , the sample being rotated at an angle θ , λ the wavelength of the beam f the coordinates in the Fourier domain, δ_r the refractive

index decrement and β the absorption index of the object. This formula relies on the Transport of Intensity Equation that assumes a small propagation distance D , and that the object is homogenous with a constant $\frac{\delta_r}{\beta}$. More details about this approach have been addressed in Appendix A. The delta beta used for the different samples is listed in Table 2.6.

2.4.1.2 Phase retrieval for HR volumes

For HR volumes obtained by fast imaging, a classic Paganin formulation was not enough to provide volumes with sharp features. Further the multi distance phase contrast holotomography [84] approach that is commonly used in phase contrast imaging at the beamline could also not be used. Because in the interest of fast acquisition, multiple distance acquisition was not feasible. Hence a modified Paganin based approach was used to retrieve phase information from single distance radiographs.

In this approach using the amplitude given by the Paganin approach (equation (2.2)), further iterations were done using the non-linear conjugate gradient method [121,122] in order to improve the estimation of phase shift. It should be noted that when imaging using nanotomography, propagation distances are long with respect to the pixel sizes and so the near field approximation fails, making it imperative to estimate the non-linear terms of phase. These non-linear terms are accurately calculated using the non-linear conjugate gradient method. Figure 2.14 shows an example of a slice reconstructed by the two phase retrieval methods, (a) Paganin method (b) Iterative non-linear conjugate gradient method. Clearly the slice (b) is a sharper image in comparison to (a). While interpreting the 2D tomography slices it should be remembered that as a result of phase retrieval, the grey level distribution of the phases is such that cavities or voids are seen as white.

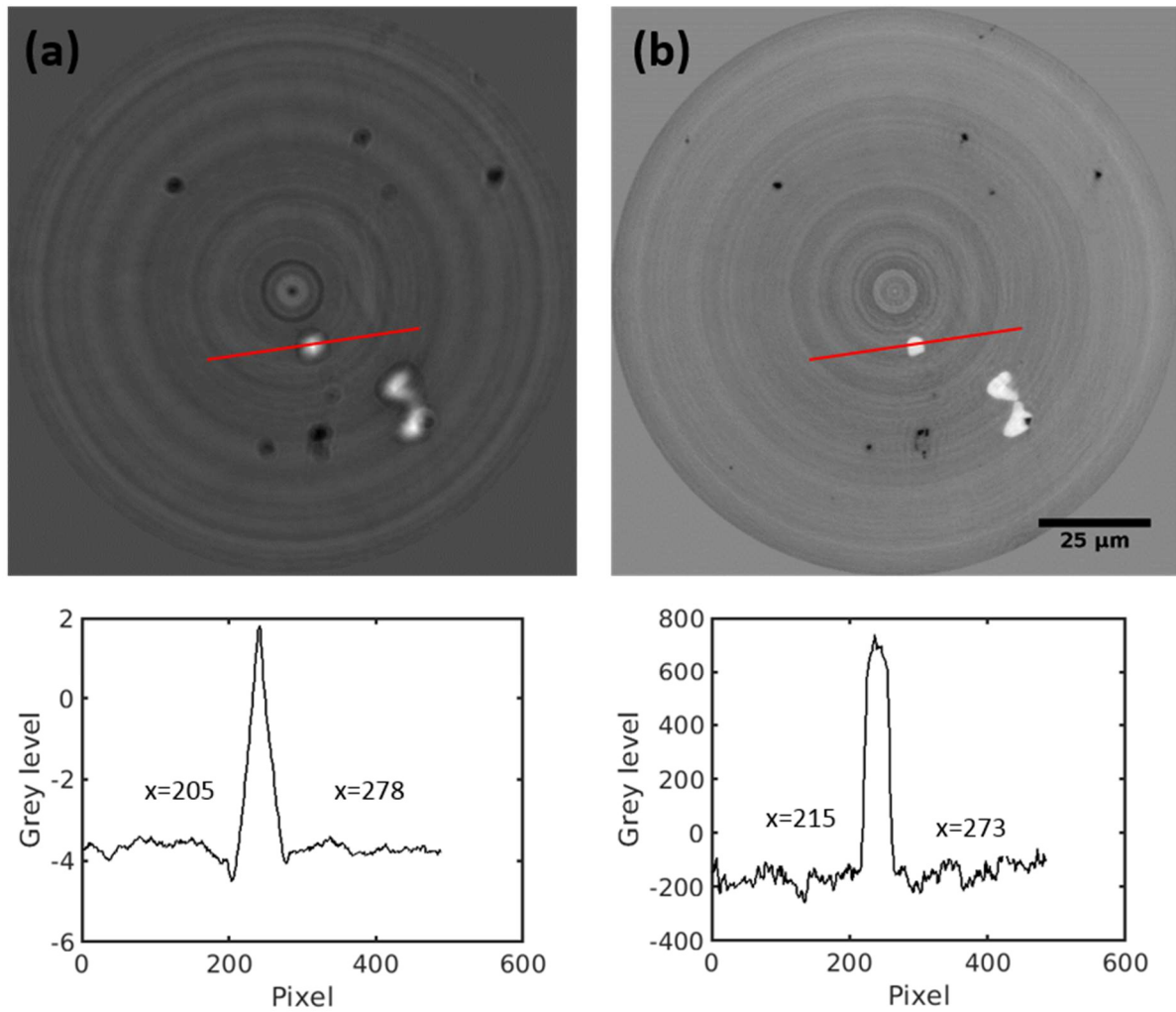


Figure 2.14 A horizontal slice from 3D HR volume of AZ31 sample for which phase retrieval was done using (a) Paganin method (b) iterative non-linear conjugate gradient method. No ring artefact correction done for both volumes the grey level profile along the red line shown below each slice (intermetallics are in black, cavities are in white and matrix is in grey)

Phase retrieval for both HR and LR volumes was done using in house GNU octave programming [123] and ImageJ. The δ_r and β values for the two alloys used were calculated using the XOP software [124] using the inputs of composition of the alloy and the energy of X-rays used.

Table 2.6 δ / β used for phase retrieval calculations.

| Alloy | δ_r / β used at 17.5 keV |
|----------------|-------------------------------------|
| Al- 3.6 wt% Cu | 183 |
| AZ31 | 280 |

2.4.1.3 Reconstruction

Reconstruction for both LR and HR volumes was done using Filtered Back Projection (FBP) technique. This involves two steps: first filtering the projections and then back projecting them into an object. This approach assumes a parallel beam geometry. The FBP algorithm is implemented in a python based software: PyHST2 [125] at the ESRF, which was used for reconstruction of all volumes. More details about this approach has been addressed in Appendix B.

It was seen that the volumes obtained after reconstruction had 'ring artefacts' and so the methodology used for correcting these artefacts is described in the following section.

2.4.1.4 Ring artefact correction

Ring artefacts are systematic intensity distortions located on concentric circles in reconstructed tomographic X-ray images [126] (example of these can be seen in Figure 2.15 a). They may arise due to different causes like: imperfect detector pixels, fault with the scintillators or improper flat field correction. A flat image is acquired by removing the object from the field of X-ray and this is then subtracted from the radiographs acquired later to remove undesired signals, the process being referred to as flat field correction. This in turn helps in removing ring artefacts. Pixel errors which cannot be removed by flat field correction enter into the sinograms as lines along the angular direction [127]. These lines become concentric circles in the reconstructed image.

In the present case, these artefacts mainly appear due to failure of the flat field correction. It should be remembered that the flat image is acquired when the sample is at ambient temperature, i.e. without the overhead furnace, while the *in situ* volumes are acquired at high temperature, in the presence of a furnace. Hence dirt particles on the furnace window or insulating wool near the sample, would inevitably lead to ring artefacts. This was also confirmed by the fact that the artefact present on ambient scans were much less than the ones on volumes obtained *in situ*.

The presence of ring artefacts on slices make post processing like segmentation of the phases difficult. Hence they have to be removed. Several methods are available to tackle this problem, which can be mainly divided into two categories. One which

targets the reconstructed volume and filters them to remove rings and the other which works on the radiographs or their sinograms. Initially post processing techniques [126] were tried for ring artefact removal but these were not very effective. Figure 2.15 shows an example of a slice with (a) no correction and (b) post processing correction. The grey level profiles along the red line on the two slices given below clearly show that ring artefacts are presents in both slices. In the absence of the artefacts the profile should look straight which is not the case in the two profiles which show severe undulations in the profile.

After the failure of post processing techniques, a combination of techniques working on phase retrieved radiographs were used to effectively remove the ring. This mainly comprised of a combination of Double flat field correction, Munch correction [128] and Dering correction. The basic principle underlying these methods are given below.

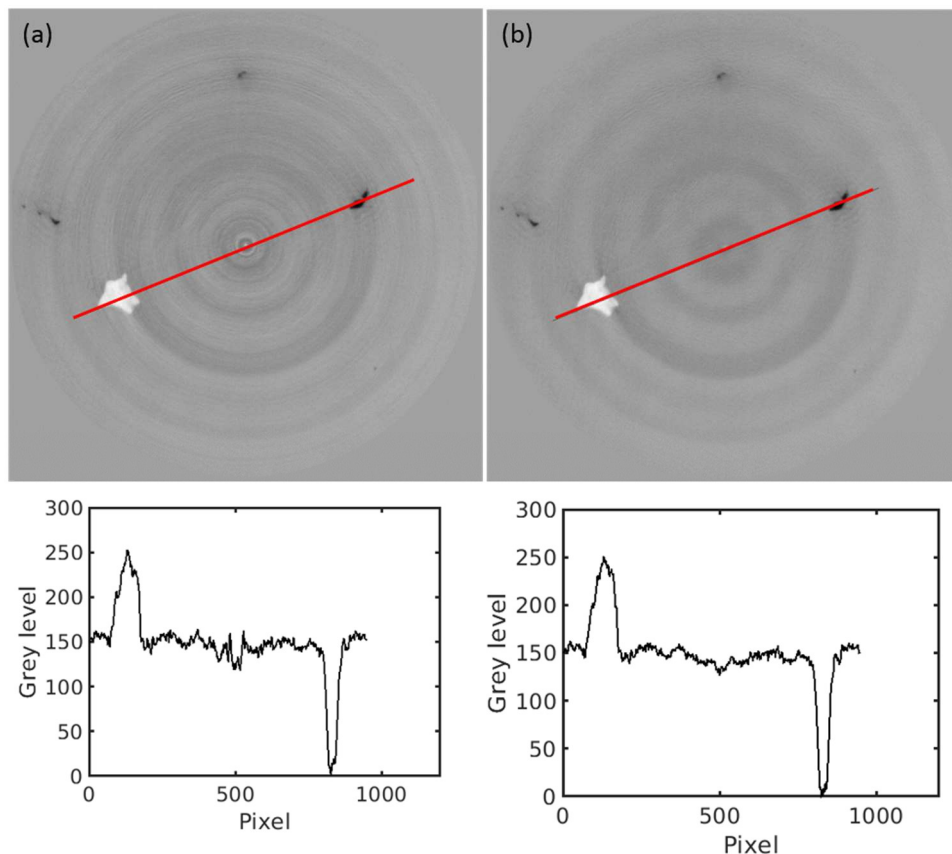


Figure 2.15 A horizontal slice from 3D HR volume of AZ31 sample reconstructed (a) without ring correction (b) with ring correction using post processing of volume [126]. The grey level profile along the red line is shown below each slice. (intermetallics are in black, cavities are in white and matrix is in grey)

Double flat field correction: this processing takes place in the radiographs space, before transposing them to sinograms. All the radiographs are averaged, into one average radiograph. During this averaging process, the fine sample features made visible by the phase contrast cancel each other out due to the rotation of the sample such that only systematic detector errors giving rise to ring artefacts remain. This "average radiograph" is then used as another flat-field correction for all the radiographs, removing most of the artefacts. This method may however fail, when a sharp surface parallel to the rotation axis is present in the imaged sample.

Munch correction: this makes use of a destriping filter based on wavelet decomposition and Fourier filtering. The method involves two steps:

First the sinograms are decomposed in a wavelet basis, giving three "detail coefficients" vectors: (H, V, D), capturing the Horizontal, Vertical and Diagonal features respectively. Here the vertical coefficients, are of importance since they correspond to the vertical stripes in the sinogram (which give the ring artefacts).

Secondly the coefficient vector "V", corresponding to vertical features, is Fourier transformed along the vertical axis. Since in the Fourier domain, a vertical stripe (transformed along vertical axis) will only contain low frequencies, a high-pass filter is applied. This consequently eliminates the stripe artefact while keeping the genuine sinogram features.

The crucial parameters when applying a Munch filter are:

- The type of wavelet chosen (FW_WNAME): different wavelets cater to rings of different size, for example the Haar wavelet filter has a length of 2, so it can only capture rings that are roughly 2 pixels wide. The symmetric-4 wavelet has a length of 8, so it can capture rings of size roughly 8.
- Choice of decomposition levels (FW_LEVELS): at each level of the wavelet transform, the sinogram size is halved. This means that 2^n pixels wide rings can be captured at FW_LEVELS of n. So higher the FW_LEVEL wider the rings that can be corrected.
- Choice of standard deviation of the Fourier Filter (FW_SIGMA): while dampening the low frequencies, this factor tunes the selectivity of the Fourier

filter. So a high value means the filter will be applied on a broader range of frequencies. Higher values of FW_SIGMA are needed to erase thick rings.

Dering correction: in this case the sinogram is averaged over all the projections. A high-band pass filter is applied to the average and the result is subtracted from all the projections.

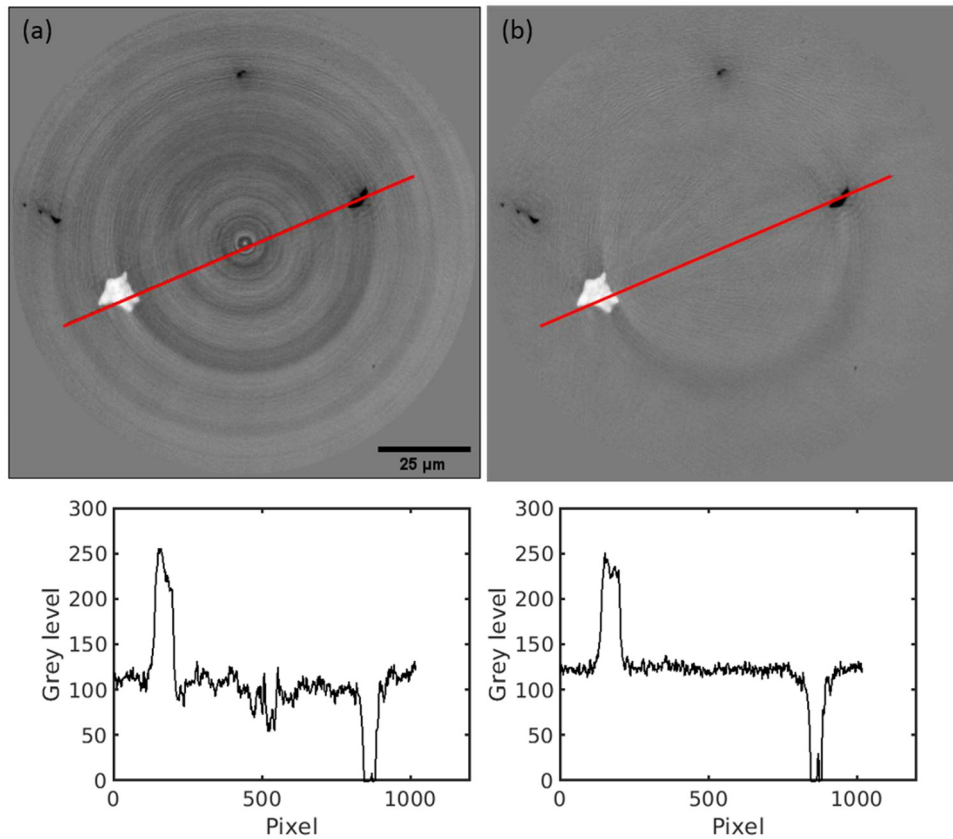


Figure 2.16 A horizontal slice from 3D HR volume of AZ31 sample reconstructed (a) without ring correction (b) with ring correction (using parameters listed in Table 2.7), the grey level profile along the red line is shown below each slice. Note that the grey levels in this slice is different from Figure 2.15 A horizontal slice from 3D HR volume of AZ31 sample because the two figures have been converted from 32 to 8 bit using different grey level range. (intermetallics are in black, cavities are in white and matrix is in grey)

Table 2.7 List of different types of ring corrections used for Figure 2.16(b) along with the relevant parameters used.

| Corrections and parameters used | |
|--|-------------|
| <ul style="list-style-type: none"> • Double flat field correction • Munch correction | |
| FW_WNAME | symmetric-4 |
| FW_LEVEL | 6 |

| | |
|----------|---|
| FW_SIGMA | 3 |
| • Dering | |

These techniques were integrated with the reconstruction process by the data processing unit of ESRF using the PyHST2 [125] software. A template of the file used for reconstruction is given in Appendix B, with example of typical ring correction parameters used. Figure 2.16 shows an example of 2D slice (from a high resolution AZ31 volume), (a) without and (b) with the ring correction algorithm, the grey level profiles below each slice (along, the red line) clearly show an extensive removal of the ring artefacts. The different corrections and parameters used for this are listed in Table 2.7

It took nearly 20 minutes for phase retrieval and reconstruction of a single volume. In an *in situ* experiment an average of 100 scans were obtained. This amounted to a total of 40 hours for reconstruction of data from one *in situ* experiment.

2.4.1.5 Reconstruction with full turn (360°) versus half turn (180°)

During reconstruction, parallel beam assumption was made, thanks to the small angle of the conic beam. Hence in principle only radiographs from 0 to 180° rotation were required for reconstructing the volumes. Nevertheless, radiographs were acquired for full 360° rotations since it was expected to result in more accurate sampling and consequently a higher resolution of the volume. But it was in fact seen that in several cases reconstructing volumes using all projections acquired from 0 to 360° resulted in blurred images (due to excess sample movement during the scan). This is demonstrated in Figure 2.17 where on the left side (a, c) are 2D slices from reconstruction using 360 projections, acquired during 0 to 180° rotations and on the right (b, d) are reconstruction using all 721 projections, acquired during 0 to 360° rotations. Between Figure 2.17 (a) and Figure 2.17 (b) the shape of the feature is clearly imaged better in Figure 2.17 (a). This can be seen both visually and by examining the grey level plots along the red lines passing through a cavity. Because of this, reconstruction was done using projections acquired during half rotations when required.

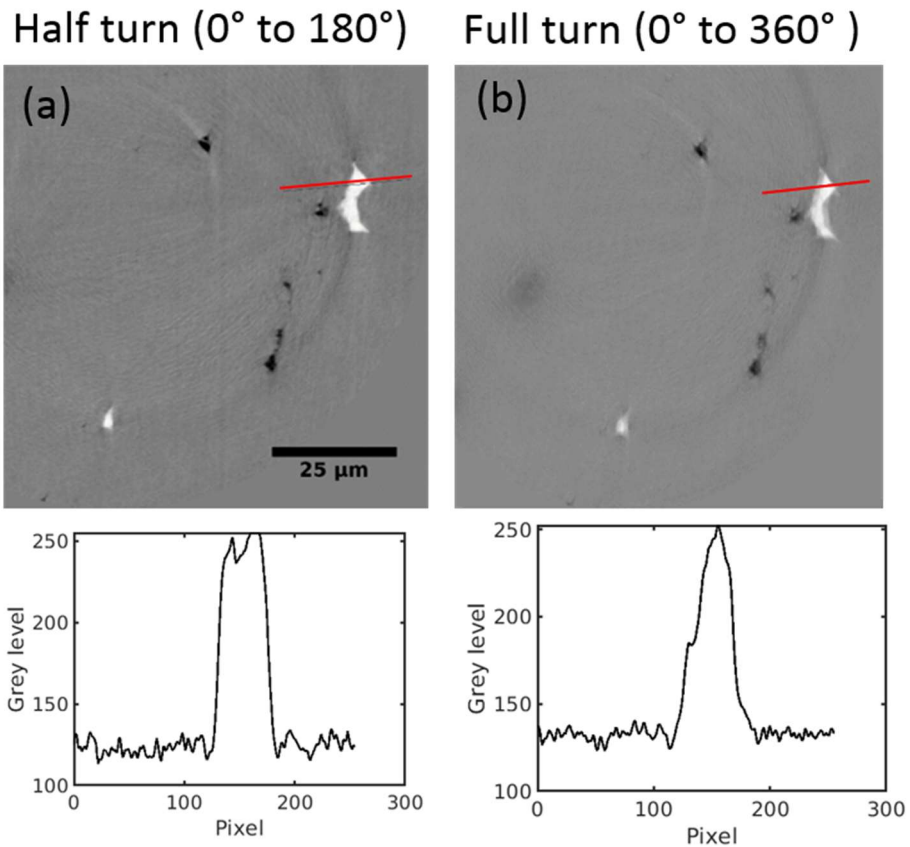


Figure 2.17 A cropped horizontal slice from HR 3D volume of AZ31 sample that has been reconstructed (a) with 721 projections acquired during full 0 to 360° rotation (b) with 360 projections acquired during half 0 to 180° rotation, the grey level profile along the red line is shown below each slice (intermetallics are in black, cavities are in white and matrix is in grey).

2.5 3D volume analysis

On obtaining the corrected 3D volumes, the next step was segmentation to separate the different phases in the volume and consequently extract quantitative information from them. To do this for 3D volumes undergoing deformation and acquired using fast nanotomography, a new data analysis framework had to be developed.

First the kind of information that is extracted from the LR and HR volumes will be enumerated. This will be followed by a description of the techniques used for this analysis

2.5.1 Analysis

Since the acquired 32 bit volumes were massive in terms of size (1 volume = 7.1 GB) the first step in data processing was reducing the 32 bit volumes into 8 bit

volumes (1 volume = 1.8 GB), which was followed by different quantitative analysis to extract different information from these volumes. The LR and HR volumes provided different information which are given below.

2.5.1.1 LR volume

The LR volumes were primarily acquired to visualise deformation, during constant load creep experiments and consequently estimate the minimum notch area with time. To do this the 3D LR volumes were segmented and the minimum notch area with deformation was estimated. This will be described in section 2.5.3.1. This was then used to estimate the mechanical parameters, which would be further discussed in section 2.6.1. The LR volumes also had sufficient second phase particles, which were easy to segment and the size and shape of which remained unchanged during deformation. Hence, these were ideal to be tracked using Digital Volume Correlation (DVC), when necessary. This was then used to estimate the positions of cavities developing in the deforming sample and also quantify the strain on the sample. Further details about this is given in section 2.5.2. The basic framework of LR data analysis is summarised in a flowchart in Figure 2.18 and in the following sections each of these steps are explained in detail.

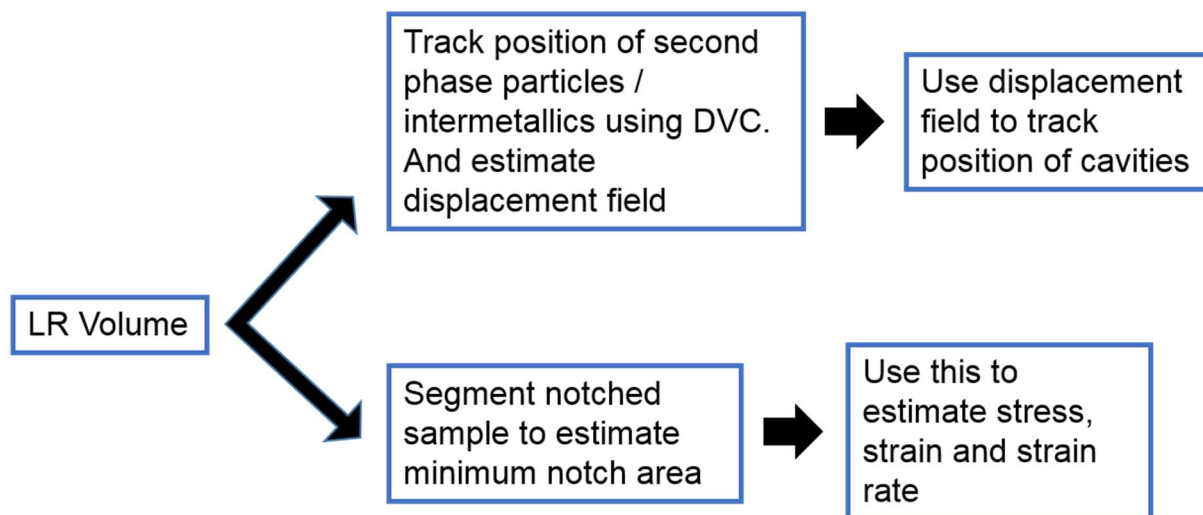


Figure 2.18 Flowchart followed for LR volume analysis.

2.5.1.2 HR volume

The HR volumes were primarily acquired to study the damage evolution during high temperature deformation, in form of nucleation and growth of cavities. This involved tracking the positions of cavities in the volumes as the sample deformed and then

further segmenting the cavities and quantifying their volume, shape and orientation. Further the second phase particles and intermetallics in the vicinity of these cavities were also segmented and similarly quantified for further examination of their contribution to damage.

The HR volumes had two primary phases in the matrix: second phase particles (in Al-Cu alloy) or intermetallics (in AZ31 alloy) and cavities. Since the second phase particles did not evolve during deformation, their positions were tracked in different volumes using Digital Volume Correlation (DVC). This gave the displacement encountered by them with time. This information was then used to deduce the position of cavities in different volumes. Using the position of cavities in volume, at different times, a small volume usually 200 X 200 X 200 voxels was cropped around the cavity and a cut off threshold was applied to these volumes to segment them. The basic framework of HR data analysis is summed in a flowchart in Figure 2.19 and in the following sections each of these steps are explained in detail.

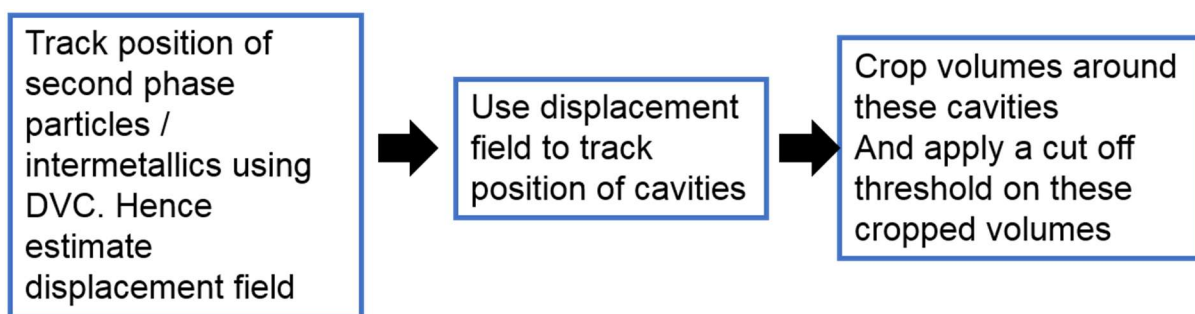


Figure 2.19 Flowchart followed for HR volume analysis.

2.5.2 Digital Volume Correlation: Tracking features

Digital Volume Correlation (DVC) based on an in-house implementation, was used to track the movement of cavities from one scan to another, the basis of which will be discussed in this section. Followed by which the usage of this technique for different types of *in situ* experiments will be elucidated.

DVC involves *identifying* certain features in the volume using the 3D Harris corner detection algorithm [129]. The identified features between two volumes are then correlated by quantifying the level of similarity of a feature between two images. This is defined by a correlation coefficient, which varies between 0 and 1, where 1 corresponds to a perfect match.

To perform DVC between two volumes such that one volume is the *original state* and second is the *deformed state*. First certain features: *guiding points* are chosen in the original state which do not evolve between the original and deformed state. They should also exhibit a large grey level gradient, so that they are easy to identify. In this study, second phase particles or intermetallics were chosen as guiding points

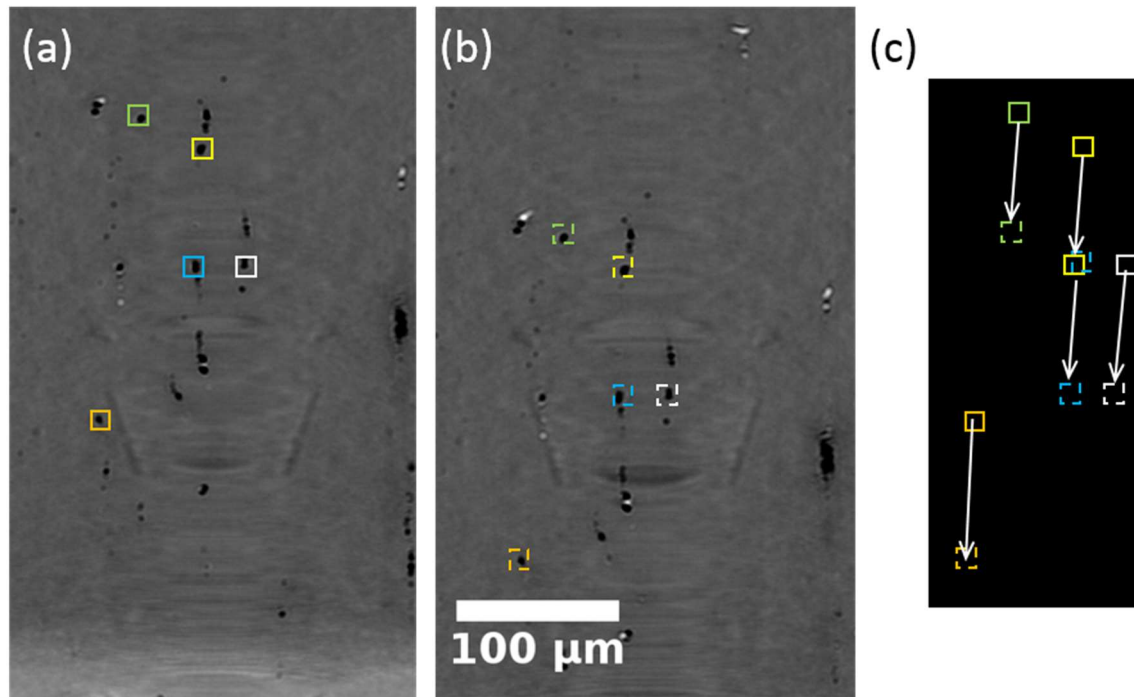


Figure 2.20 A transverse slice from 3D LR volume of AZ31 sample with intermetallics in black, which act as guiding points that are tracked between the (a) reference state and (b) and deformed state in order to estimate the displacement field. (c) Displacement of features between state (a) and (b) (intermetallics are in black, cavities are in white and matrix is in grey)

Secondly a *pattern window* is defined, depending on the size of the guiding points chosen. The identification and correlation is made within this pattern window, such that the pattern window is translated in the three directions within a *search window*. This search window is defined based on the displacement expected between two volumes.

The guiding points defined in the original state are then identified or found in the deformed state around a *guessed position*. This process is iterative. In the first iteration the guessed position for the first point is the same as its position in the original state. Once the first point is correlated, the other points (in an ascending order of distance of points from the first point) are correlated. The guessed position

for these are determined by the weighted average of displacements of the previous correlated points. The weighing is done based on Gaussian of distance from the point. This is then followed by a second iteration of identification and correlation. Based on this the final position of the guiding points in deformed state is obtained. Figure 2.20 shows an example of a transverse 2D slice from a LR AZ31 volume, with intermetallics in black, which acted as guiding points. The search windows are marked using squares where (a) shows the reference state and (b) the deformed state. The guiding point have been clearly displaced between the two states, Figure 2.20 (c) shows these displacements which are estimated by DVC, using arrows.

From the DVC tracking of second phase particles in the HR volume, the displacement of virtual points (cavities in the present case) can be estimated based on a quadratic fit of the displacement of nearby guiding points (particles). Utilising this principle, different approach to tracking cavities and particles were undertaken for different experiments. These are specifically enumerated as follows:

For multi z scans for Al-Cu samples,

These samples were studied at strain rates lower than nearly $5 \times 10^{-5} \text{ s}^{-1}$. Hence the strain on sample between consecutive HR scans was not considerable (less than 2 pixels or $0.2 \mu\text{m}$) making it possible to concatenate the four HR volumes into a single stack, based on the initial offset applied during acquisition (see Figure 2.12). Since this concatenated stack had enough second phase particles (more than 100) present in all deformed states and since they do not evolve during deformation, these second phase particles were tracked using DVC.

The position of second phase particles in the last scan was estimated by segmentation (further detailed in section 2.5.3). These acted as guiding points, and using DVC their position in different deformed states was found. This gave the displacement field in the volume. Position of cavities in the final deformed state then acted as virtual points, over which the displacement was estimated.

The tracking was initiated from last scan in order to account for any cavity which would have nucleated during the deformation. It should be remembered that tracking from last scan would not have been feasible if there was active coalescence of cavities. However in the Al-Cu sample scanned it was manually checked that no

coalescence of cavities was visible in the volumes hence using the last scan for tracking was justified.

For multi z scans on AZ31 alloys with LR volumes

For AZ31 samples most investigations were conducted at higher strain rate (greater than $5 \times 10^{-5} \text{ s}^{-1}$), hence it was not feasible to apply the initial offset to concatenate the volumes accurately. In a single HR volume that is deforming at high strain rate the number of intermetallics that can be tracked from the start till the end of deformation were few (less than 100). Hence in such cases it was much more convenient to track intermetallics on LR volumes which had high number of trackable intermetallics (more than 300). Once displacements of particles on LR volume was known, the displacement on the HR volume was estimated, since the position of the HR volume, with respect to the LR volumes was known, see Figure 2.12. An example of such a tracking has been illustrated in Figure 2.20. Table 2.8 lists typical parameters used for DVC tracking for another AZ31 sample that uses intermetallics in LR volumes to track the cavities.

Table 2.8 Typical parameters used for DVC tracking of a LR volume.

| | |
|---|--------------------|
| Number of 3D volumes | 20 |
| Size of 3D volumes | 1280 X 1280 X 1080 |
| Strain increment between volumes | nearly 0.02 |
| Number of guiding points | 406 |
| Pattern window size [voxels] | 25 X 25 X 25 |
| Search window size [voxels] | 10 X 10 X 20 |
| Initial point research window size [voxels] | 30 X 30 X 60 |
| Number of tracked cavities | 60 |

For multi z scans on AZ31 alloys with no LR volumes

Here strain estimation was a little tricky because of absence of LR volume. In addition when HR volumes deformed at a high strain rate ($5 \times 10^{-5} \text{ s}^{-1}$), concatenation of volumes was impossible. To tackle this case the intermetallics in each HR were tracked separately such the tracking between consecutive scans was

affected using new guiding points for each consecutive tracking. Using this, the displacement in different HR volumes was interpolated at all times, which in turn was used to estimate position of cavities. It can be seen as an interlaced approach.

2.5.3 Segmentation

Segmentation is separating different phases in a volume and assigning a specific range of grey level value to all features that belong to the same phase. In the present case the 3D volumes consisted of matrix, second phase particle or intermetallic and cavities as the three phases. 2D slices from HR volumes of Al-Cu and AZ31 samples respectively are presented in Figure 2.21. Further segmentation was also used to calculate the notch area for the sample. Different approach was used to segment the phases, depending upon the requirements as explained below.

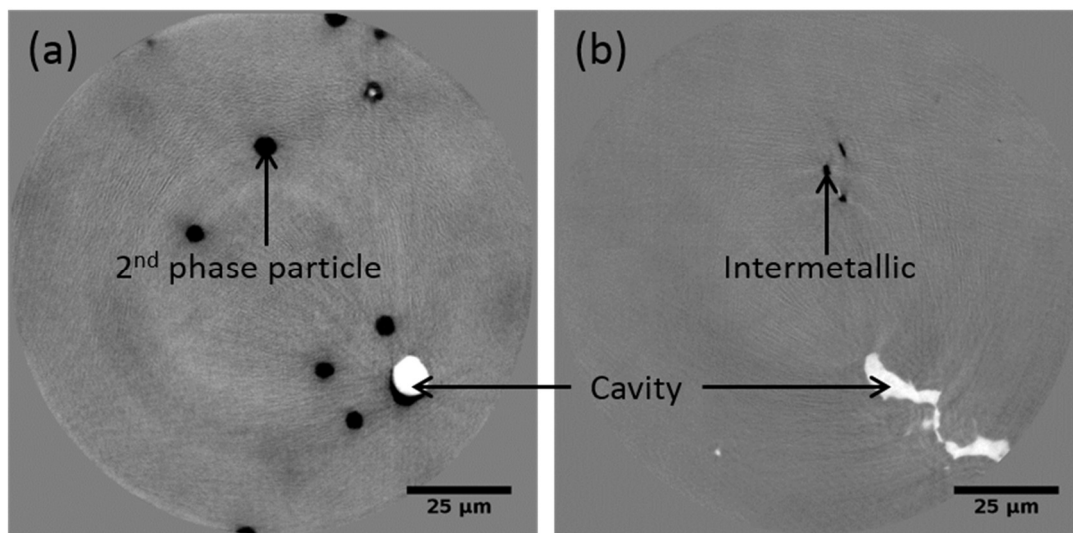


Figure 2.21 A horizontal slice from 3D HR of (a) Al-Cu sample where the second phase particles are seen in black, cavity in white and matrix in grey (b) AZ31 sample where the intermetallic particles are seen in black, cavity in white and matrix in grey.

2.5.3.1 Sample / notch area

The minimum area of the notch was estimated by segmentation of LR volumes. This involved using the iterative intermeans [130] threshold technique of the open source image analysis tool: ImageJ. This method segments a phase by first making an initial guess. Using this the mean values of pixel segmented in the two categories are calculated. The threshold is then changed to lie exactly halfway between the two means. This process is iteratively repeated until the threshold stops changing its

value, this is then the desired threshold. This technique was very effective in separating the notch from the surrounding air in the volume.

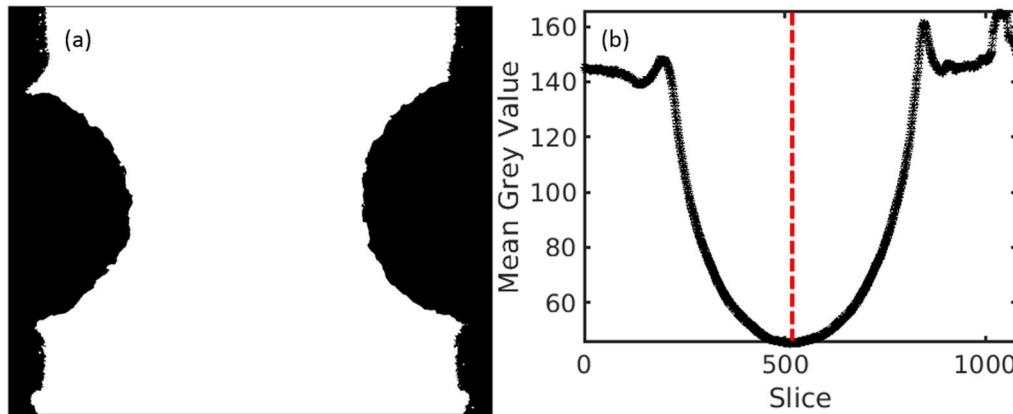


Figure 2.22 (a) Transverse cross section view of a LR 3D volume, where a threshold has been applied to separate the notch and air (b) Plot of mean grey value for different slices, where a slice 0 corresponds to top of the notch and slice 1080 to the bottom. The dotted line indicates the minimum in the grey value, which corresponds to minimum notch area (sample is in white and air is in black)

A slice where the notch area is small, such that substantial amount of air is present in the field of view, was used to arrive at a cut off threshold, which was then used for all the slices. Figure 2.22 (a) corresponds to the 2D transverse cross section view of the volume, after applying the threshold. Using this volume the minimum notch area was estimated using the mean grey value. A plot of the mean grey value versus slice (using Z-axis profile tool of ImageJ [131]), gave the variation of the grey value along length of the sample as can be seen in Figure 2.22 (b), the minimum of which corresponded to minimum notch area. Since a grey level of 255 (white) corresponded to the notch and a grey level of 0 (black) corresponded to air, the mean grey value is given by:

$$\text{Mean Grey Value} = \frac{0 \times A_{air} + 255 \times A_{notch}}{A_{slice}} \quad (2.3)$$

where A_{air} is area occupied by air in the slice, A_{notch} is the area occupied by notch in the slice and A_{slice} is the total area of the slice.

Such estimations were made for all LR volumes obtained as the sample deformed giving the evolution of notch area, as the sample deformed.

2.5.3.2 Particles

The particles were segmented for two purposes: for quantitative analysis like shape and volume fraction and in order to identify the guiding points for DVC tracking in both HR and LR volumes. The procedure adopted was the same for both purposes:

The particles were identified using the iterative intermeans threshold [130] of ImageJ, on any cropped slice, which had a high fraction of second phase particle, this threshold was then applied on the whole volume. Examples of the threshold values used are listed in Appendix C. Before segmentation, an edge preserving filter: mean shift filter [132] was applied on the volume to counter any remaining ring artefacts or other noise. This filter for each pixel, identified neighbouring pixels based on specified spatial radius and colour distance, and calculated a mean spatial centre and mean colour value from these. These calculated mean values then served as the new centre for the next iteration. The described procedure was repeated until the spatial and the colour (or grayscale) mean stopped changing. At the end of the iteration, the final mean colour was assigned to the starting position of that iteration.

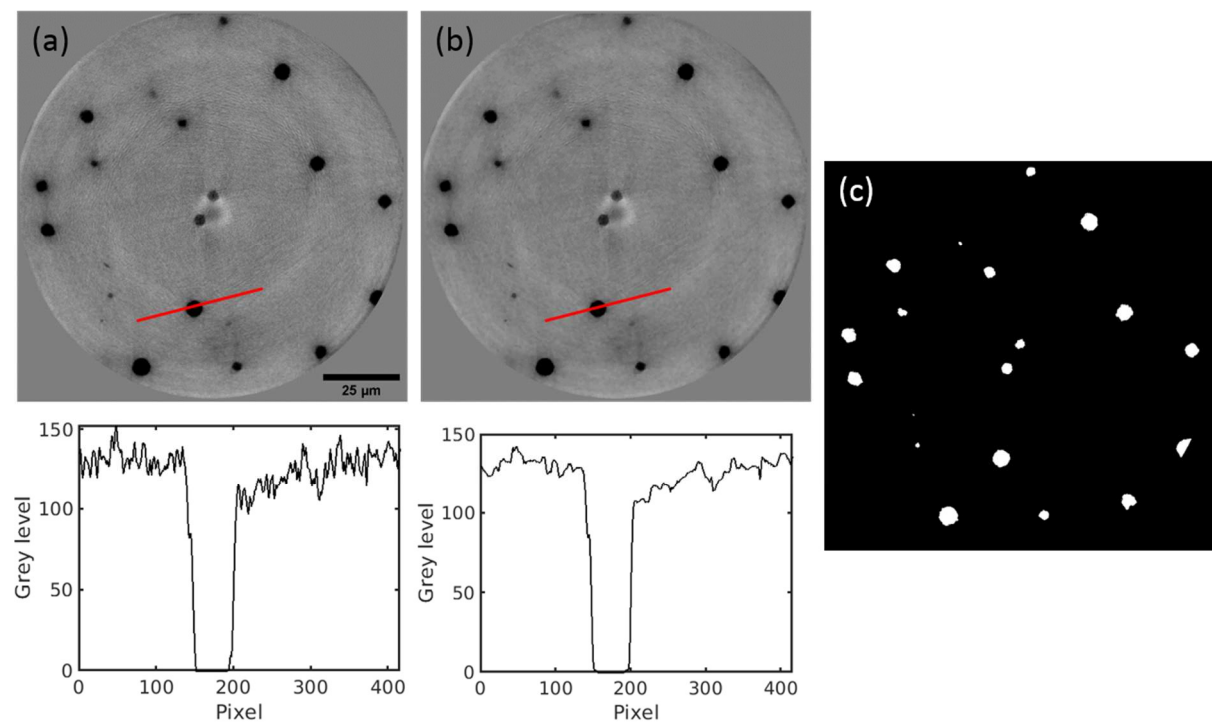


Figure 2.23 A horizontal slice from 3D HR Al-Cu volume (a) before applying filter (b) after applying a mean shift filter, along with a grey level plot along the red line for the two slices. (c) A segmented image of the filtered slice.

Figure 2.23 (a) shows an example of a 2D slice of an Al-Cu volume, with second phase particles in black. This slice was subject to a mean shift filter (colour distance = 10, spatial radius = 5), the filtered slice is shown in Figure 2.23 (b). The filtering helped in reducing the noise in grey level of the matrix, this is demonstrated by the grey levels plot along the red lines indicated in Figure 2.23 (a, b) where the filtered slice shows lower variations of grey level in the matrix. This slice when segmented using the intermeans threshold is shown in Figure 2.23 (c), where the particles are shown in white.

2.5.3.3 Cavities

Since the volume fraction of cavity in a volume was very less as compared to the matrix, applying automatic threshold on a slice did not work. So in turn cavities of different sizes were cropped such that iterative intermeans threshold was able to segment it from the matrix, an example of this can be seen in Figure 2.24 (a1). The black box indicates the region that was cropped and Figure 2.24 (b) is the segmented image from this cropped slice. Several such threshold values were determined on various cavities, of different volumes, from an experiment. An average of this value then gave a suitable threshold value which was used for segmentation of cavities. Another technique used for cavity segmentation was based on edge detection which was developed later to allow better detection of interface between different phases. This involved cropping a cavity from a HR slice, and using “Find edges” tool of imageJ to determine the edges of the cavity and then use an average of the grey level along the edge, to segment the cavity. The find edge tool is based on Sobel edge detector [133] to highlight sharp changes in intensity in the image. The segmentation procedure has been illustrated in Figure 2.24, where first the edges of the cropped slice (Figure 2.24 a1) was detected by subjecting the slice to edge detection (Figure 2.24 c1). The plot profile along the red line was used to detect the coordinates at the edges ($x = 46$ and $x = 101$ from Figure 2.24 c2) and the grey levels corresponding to these were then determined (198 and 191 from Figure 2.24 a2) and then an average of the two i.e. nearly 195 was chosen as a threshold for the cavity such that all pixels with grey level 195-255 was considered to be a cavity. The segmented slice corresponding to this threshold is shown in Figure 2.24

(d). Examples of the threshold values estimated for other samples are listed in Appendix C.

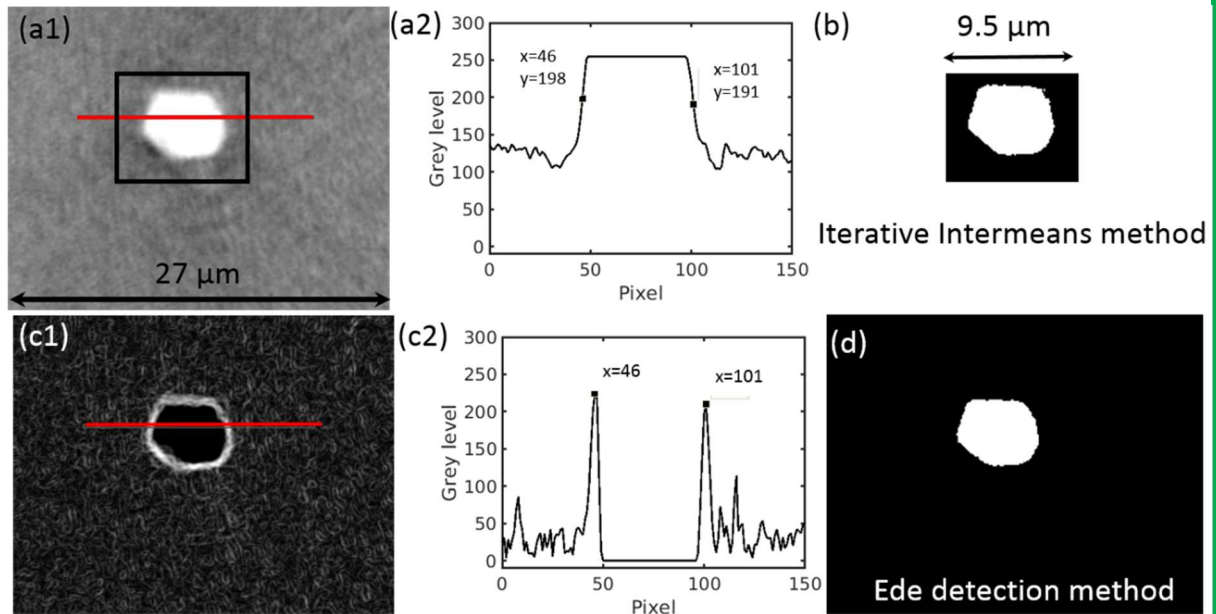


Figure 2.24 Example of segmentation of cavity in Al-Cu sample by 2 different methods. The region indicated by black box in (a1) was cropped and threshold using iterative intermeans threshold which is shown in (b). The slice in (a1) was subjected to edge detection and is shown in (c1) the corresponding plot profile grey level along the red lines are shown in (a2) and (c2). (d) is a cropped segmented slice based on the average threshold of 195.

It should be noted that when segmentation was done to identify virtual states for DVC tracking, a prior mean shift filter was used as in case of particles. However, when cavities were segmented for quantitative analysis like volume and shape a small volume of nearly $20 \times 20 \times 20 \mu\text{m}^3$ was cropped around each cavity from the HR, 3D volumes at all times. And these cropped volumes were subjected to a cut off threshold. Remember this time no prior filtering of volume was done.

After segmentation, Avizo software was used for visualization and 3D rendering of the volumes. It should be noted that the threshold values are very critical in the quantitative analysis of the volumes and so to estimate the error in volume estimation, two threshold values were chosen: one which clearly overstated and the other which clearly understated the cavity volume. Using this conservative range of threshold, the error in quantitative analysis of the volumes was calculated which is reported in the results of the following chapters.

2.5.4 Sphericity and volume estimation

Sphericity was used to quantify the morphology of the second phase particles and cavities. This is given by:

$$sphericity = 6 * Volume * \sqrt{\frac{\pi}{SurfaceArea^3}} \quad (2.4)$$

Its value ranges between 0 and 1, where sphericity of a perfect sphere is 1.

The volume of the cavities was measured using the Analysis 3D plugin of imageJ which is based on the marching cube algorithm [134]. It is an algorithm for creating iso surface for a 3D function. The 3D region is divided into cubes, such that vertices of each cube is a voxel. Therefore each cube has 8 voxels associated with it.

The algorithm scans through each voxel of the 3D region and decides whether a surface passes through the voxel or not. For example in the present case if all the vertices are equal to 1 (or have a grey level of 255 in segmented volume) then the cube does not lie on the surface. If however few vertices of the cube are equal to zero (or have a grey level of 0 in segmented volume) while others one, then the cube lies on the surface. The function of the algorithm is then to determine the shape of this surface.

A cube with 8 voxels, which can have value 0 or 1, can have $2^8 = 256$ cube configurations. This equals 15 unique configurations (taking into account all the symmetries). Depending upon which of these configurations corresponds to the cube, its triangular shape is determined. This in turn defines the iso surface of the whole 3D volume. This surface is then used to compute the net volume from the 3D segmented data.

2.6 Determination of mechanical parameters

Since unconventional devices were used to perform high temperature deformation, different techniques were used to estimate or cross check the deformation parameters of strain, strain rate and stress.

2.6.1 Stress, strain and strain rate: notch area

For experiments, where LR volumes were acquired, the minimum notch area was determined as the sample deformed, this is detailed in section 2.5.3.1. Using this area an estimate of true strain (ε) was obtained using:

$$\varepsilon = \ln \frac{A_0}{A_t} \quad (2.5)$$

where, A_0 was notch area at the beginning of deformation and A_t was notch area at any time t . Since this strain was known at different time of deformation, strain rate ($\dot{\varepsilon}$) was obtained by using the strain ($\varepsilon_{t2}, \varepsilon_{t1}$) at two different times ($t2, t1$):

$$\dot{\varepsilon} = \frac{\varepsilon_{t2} - \varepsilon_{t1}}{t2 - t1} \quad (2.6)$$

In case of constant load experiments, initial load on the sample was known and using the notch area (A_t), the stress (σ) on the sample could be estimated:

$$\sigma = \frac{\text{load}}{A_t} \quad (2.7)$$

It should be noted that the strain was also further estimated using DVC which is detailed below.

2.6.2 Strain and strain rate: DVC

Using the DVC of particles or intermetallics, their displacement was known over time. Further a mesh with several 8 noded brick were defined over the region of interest and the displacement of each node was estimated based on a quadratic fit of the displacement of nearby guiding points. Initial and deformed meshes were then processed by a finite element code Cast3M [135], to compute local strain fields. Strain at different time was then used to compute strain rate using equation (2.6)

2.6.3 Stress: ex situ high temperature deformation tests

In addition to performing *in situ* high temperature deformation tests, constant strain rate high temperature compression tests were also performed ex situ using a MTS DY34 compression device which was equipped with an in house developed die punch and a furnace with very accurate temperature control of ± 1 °C.

These tests were mainly performed to calibrate the compact mechanical device as it was acknowledged that the accuracy in load estimation by counting the number of turns of the nut was not sufficiently precise. Hence the strain rate obtained from DVC was calibrated with the strain rate from these compression tests, so that the initial load on the sample could be precisely known. These were restricted to Al-Cu samples.

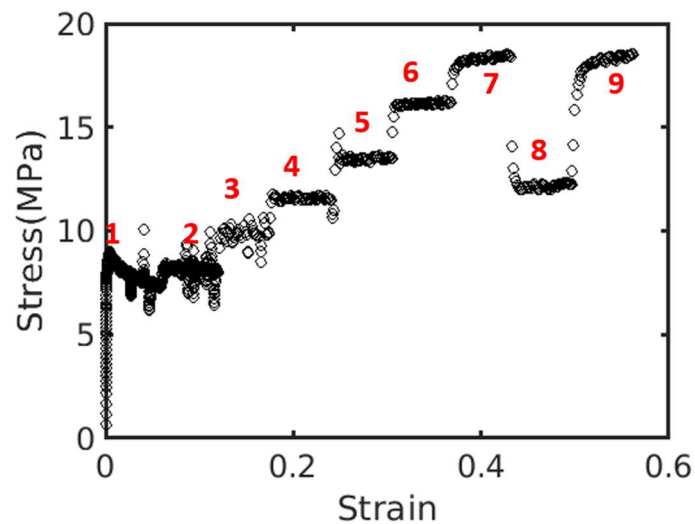


Figure 2.25 Plot of stress versus strain from a strain rate jump test on AC5 sample (698 K). Each number marked in red corresponds to a different strain rate. The strain rate and stress corresponding to each number is listed in Table 2.9

Table 2.9 The strain rate and mean stress corresponding to the strain rate jump test in Figure 2.25

| No | Strain rate (s ⁻¹) | Mean stress (MPa) |
|----|--------------------------------|-------------------|
| 1 | 1 X 10 ⁻⁵ | 7.5 |
| 2 | 2 X 10 ⁻⁵ | 7.9 |
| 3 | 7 X 10 ⁻⁵ | 9.7 |
| 4 | 1 X 10 ⁻⁴ | 11.6 |
| 5 | 2 X 10 ⁻⁴ | 13.4 |
| 6 | 6 X 10 ⁻⁴ | 16.1 |
| 7 | 1 X 10 ⁻³ | 18.3 |
| 8 | 1 X 10 ⁻⁴ | 12.2 |
| 9 | 1 X 10 ⁻³ | 18.3 |

Cylindrical Al-Cu alloy rods of length 5 mm and radius 2.5 mm were heat treated along with notched Al-Cu specimens and then subjected a high temperature compression test at a temperature of 698 K. This test was done for several strain rates, bearing in mind the expected strain rates from the *in situ* high temperature

tests. Figure 2.25 shows the results from the strain rate jump test performed at different strain rate such that each number shown in red corresponds to a strain rate that the sample was subjected to and Table 2.9 lists the strain rate corresponding to each number and also the corresponding mean stress corresponding to these strain rates.

2.6.4 Triaxiality

It should be noted that the samples used during for the mechanical tests were notched samples which had variable cross sections along the length. Because of this a tri-axial stress state would inevitably be present during the deformation. Based on the Bridgman analysis [136] the maximum triaxiality would be given by:

$$Triaxiality = \frac{1}{3} + \ln \left(1 + \frac{r_{section}}{2r_{notch}} \right) \quad (2.8)$$

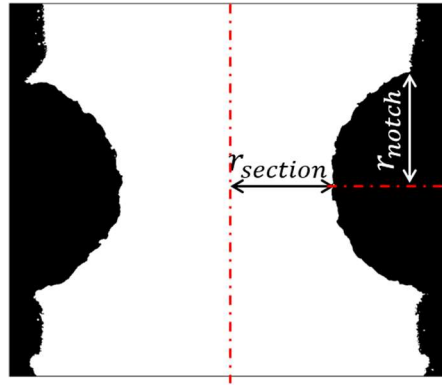


Figure 2.26 Schematic of the notched sample showing definitions for $r_{section}$ and r_{notch} .

where definitions for $r_{section}$ and r_{not} and shown in Figure 2.26. Using this the maximum triaxiality at the start of deformation in the centre of the notch, would be 0.7. Further this is expected to change as the dimensions of the sample changes during to sample deformation. This change is shown in Figure 2.27 for an AZ31 sample undergoing deformation up to a strain of 0.9.

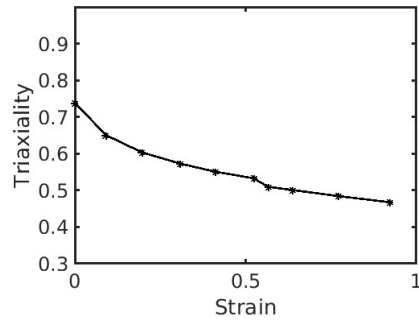


Figure 2.27 Plot showing change in triaxiality during sample deformation.

It is seen that during deformation at higher strain values (between 0.5 and 0.9) the triaxiality remains nearly constant. Nevertheless a variation in triaxiality from 0.4 to 0.7 is seen, and this is expected to effect the high temperature behaviour of the samples. In fact effect of triaxiality has been widely studied during deformation [137–139]. However for this work these effects have not been accounted for. It is acknowledged that accounting for such effects, in the future, would help in improving the analysis made in this thesis.

Chapter 3. High temperature deformation of Al-Cu alloy

The present study focussing on damage initiation during high temperature deformation of light alloy, was initiated on a model alloy: Al-3.6wt% Cu. This alloy was chosen primarily because by controlling the heat treatment parameters, second phase particles of desired size could be grown in the alloy. It is known that damage in form of cavities during high temperature deformation, often nucleates on intermetallics, grain boundaries, triple junctions etc. Theories also suggest that the size of second phase particles affects the nucleation of damage. Keeping this in mind second phase particles were grown in the Al-Cu alloy to act as nucleation sites for cavities. A controlled heat treatment was carried out to prepare samples with model microstructures containing spherical second phase particles of desired size, homogenously distributed within the grains. The size of these particles was controlled to study their effect on cavity nucleation.

In this chapter the growth of second phase particles, their characteristics and further nucleation and growth of cavities in Al-Cu alloys have been discussed at length. **It should be noted that all Al-Cu samples referred in this thesis have a composition of Al-3.6wt% Cu.** The details regarding sample preparations, machining are provided in section 2.1.1

3.1 Second phase particles

Second phase particles that were generated in the Al-Cu samples to act as probable sites for cavity nucleation are copper rich phases, which formed as a result of solidification of semi-solid Al-Cu alloy [94].

When solutionised Al-Cu samples were heated in a semi solid regime, copper rich liquid phase nucleated and grew with time. On quenching the sample these liquid droplets turned into spherical copper rich second phase particles. This semi solid regime is indicated by the grey portion in the schematic of Al-Cu phase diagram in Figure 3.1. Since the size of these particles could be controlled by controlling the heat treatment parameters, this model alloy appeared as a convenient choice to

study the effect of particle size on cavity nucleation. In the following section more details about the generation of these particles and their size, shape will be presented.

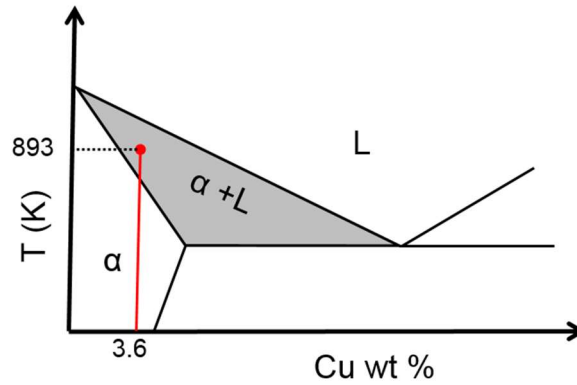


Figure 3.1 Schematic illustration of a portion of the Al-Cu equilibrium phase diagram (x axis: Cu in weight %, y axis: Temperature in Kelvin). The different phases are single phase solid solution of Al and Cu (α), the liquid (L) and semi-solid region ($\alpha + L$) (indicated in grey).

3.1.1 Generation of second phase particles

Second phase particles can be developed by heating a solutionised Al-Cu sample in a semi solid regime for a certain amount of time. In order to link the temperature and time of this heat treatment to the size of particles formed, heat treatment of samples were carried out while performing *in situ* 3D imaging. This involved heating solutionised Al-Cu sample at a fixed temperature and recording radiographs to image nucleation and growth of these phases, followed by air quenching. The temperatures tried were 883, 888, and 893 K making sure that it fell in the semi-solid regime for Al-Cu alloy.

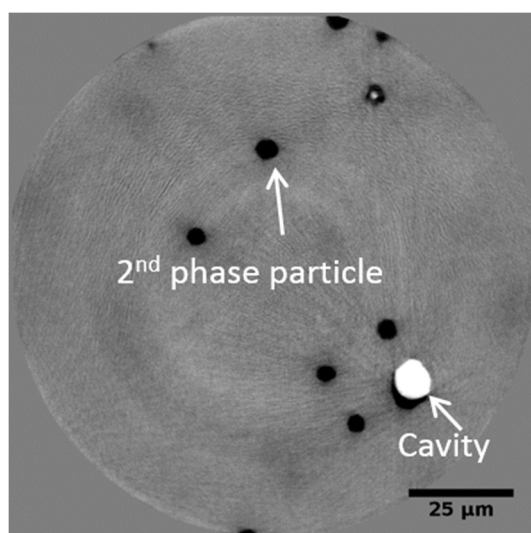


Figure 3.2 Horizontal 2D slice showing second phase particle and pre-existing cavities in an Al-Cu solutionised sample heat treated at 893 K for 5 minutes.

It was seen that heating at a constant temperature while increasing the time of heat treatment, progressively increased the size of the particles generated. While the effect of temperature on particle size was not visible. These *in situ* tests for particles generation were used to infer the effect of time and temperature on particle growth and with this information the heat treatment parameters were optimised. Further the notched samples used for *in situ* high temperature deformation, were heat treated ex situ in a box furnace using the optimised parameters.

Ex situ particle generation was done by heating solutionised sample at 893 K for two different heat treatment time of 3 minutes and 5 minutes. This resulted in particles with radius falling below and above the critical radius (nearly 1 μm) for cavity nucleation as proposed by theories, this will be discussed at length in section 3.2.7.1. The size and shape of particles resulting from this heat treatment will be detailed in the following section. Figure 3.2 shows an example of typical 2D slice obtained from high resolution tomography of one such solutionised Al-Cu sample, heat treated at 893 K for 5 minutes.

3.1.2 Characteristics of second phase particles

The two different heat treatment parameters resulted in second phase particles of different characteristics in terms of their size volume fraction and shape. The results from two Al-Cu solutionised samples heat treated at 893 K for 3 minutes and 5

minutes will be discussed in this section and they will be referred as AC3 and AC5 in the text, the same is summarised in Table 3.1.

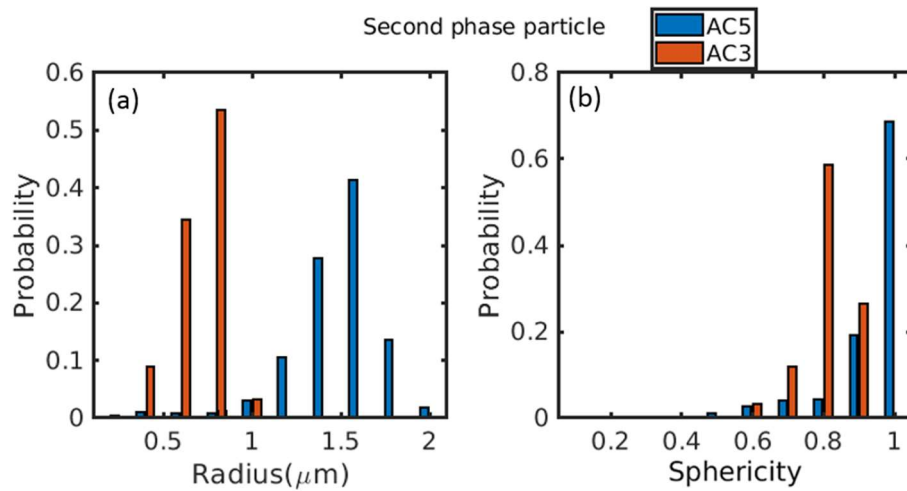


Figure 3.3 Probability of (a) equivalent radius and (b) sphericity of second phase particles produced by heat treatment for 3 (AC3) and 5 minutes (AC5).

Figure 3.3(a) shows a probability histogram of the equivalent radius of particles produced by the two different heat treatment times. Here the probability was calculated by dividing the number of elements in a bin by total number of elements considered. It should be noted that the equivalent radius is the radius calculated from the volume assuming a spherical shape of the particle and cavity, and all the radii mentioned in the text are in fact equivalent radii. It can be clearly seen that the radius of particle after a 3 minutes heat treatments is smaller than that of 5 minutes heat treatment.

Table 3.1 Summary of characteristics of second phase particles formed as a result of by different heat treatments

| Heat treatment | Solutionised at 803 K for 100 hours + Heat at 893 K for 3 minutes (AC3) | Solutionised at 803 K for 100 hours + Heat at 893 K for 5 minutes (AC5) |
|------------------------------------|---|---|
| Average radius (μm) | 0.6 | 1.4 |
| Volume fraction | 3.7×10^{-4} | 4.3×10^{-3} |
| Number density (/mm ³) | 353343 | 344158 |
| Average sphericity | 0.7 | 0.9 |

Further details about the average particle size, volume fraction and number density are summarised in Table 3.1. For nearly the same number of particles per unit volume, a heat treatment of 5 minutes results in particles with a larger average size and consequently occupying a higher volume fraction as compared to that formed by 3 minutes heat treatment.

Figure 3.3(b) shows the sphericity of the second phase particles generated from the two heat treatment. It can be seen that most of the particles have a sphericity of 0.7-1, which indicates that the particles were rounded in shape. Further it can also be seen that sphericity of particles formed from 5 minutes heat treatment are higher (see Table 3.1) than the other. In case of 5 minutes heat treatment, most of the particles with a lower sphericity values were particles associated with pre-existing cavities. This is further discussed in the following section.

3.1.3 Pre-existing cavities

On quenching the droplets formed by heating the solutionised Al-Cu sample in the semi-solid regime (see section 3.1.1 for details of heat treatment), it was seen that a few particles developed micro porosities, these will be referred as pre-existing cavities. The presence of micro porosities in cast aluminium alloys is well reported and the probable cause is attributed to the lower solubility of hydrogen in solid state as compared to the liquid state [11,124,125].

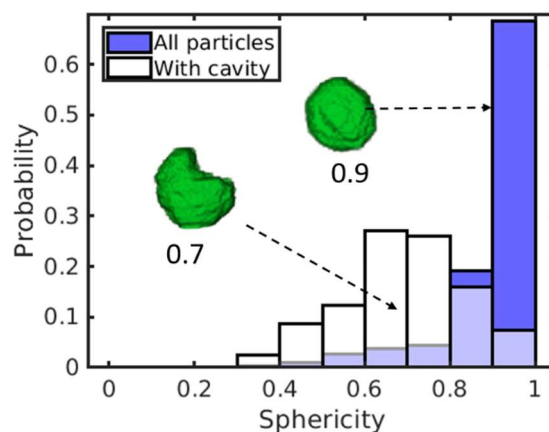


Figure 3.4 Histogram showing probability of second phase particles produced by 5 minutes heat treatment (blue histogram), among these the particles associated with pre-existing cavities are separately plotted (white histogram).

It was seen that all pre-existing cavities were associated with a second phase particles further the shape of the otherwise spherical particles were affected when then were associated with a pre-existing cavity. A lot more particles associated with cavity had a lower sphericity as compared to the ones without, see Figure 3.4. Recalling formation of the second phase particles, the sample undergoes a transformation in semi-solid region, and liquid phase nucleates in the sample. This liquid phase is expected to have higher dissolved hydrogen (owing to higher solubility of hydrogen in liquid). On quenching however, during liquid to solid transformation the excess hydrogen from the liquid phase probably gets trapped as bubbles near the formed particles. This could be a probable explanation for irregularity in shape of particles associated with pre-existing porosities.

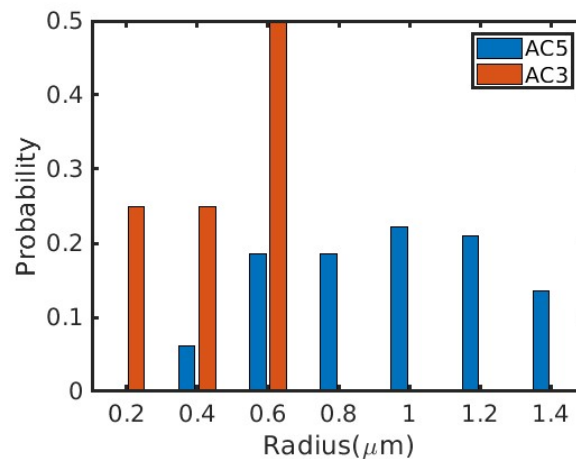


Figure 3.5 Probability of equivalent radius of pre-existing cavities produced by heat treatment for 3 (AC3) and 5 (AC5) minutes

Table 3.2 Table summarising statistics for pre-existing cavities formed by two heat treatments conditions.

| Pre-existing cavity characteristics | Heat at 893 K for 3 minutes (AC3) | Heat at 893 K for 5 minutes (AC5) |
|-------------------------------------|-----------------------------------|-----------------------------------|
| Average radius (μm) | 0.4 | 0.8 |
| Volume fraction | 1×10^{-6} | 5.9×10^{-5} |
| Number density (/mm ³) | 3769 | 17208 |
| Average sphericity | 0.7 | 0.8 |

Figure 3.5 shows the histograms depicting the size of the pre-existing cavities that formed, and further characteristics of the cavities are summarised in Table 3.2. It was seen that the cavities formed after 5 minutes heat treatment were higher in number and occupied a higher volume fraction than cavities after 3 minutes. This is expected as a higher heat treatment time results in greater volume of droplets to form. This in turn results in higher hydrogen to diffuse out of them, consequently forming more pre-existing cavities, of bigger sizes. This is further illustrated in Figure 3.6 which shows a scatter plot of radius of pre-existing cavities along with the radius of particles they are associated with. It can be seen that there is a trend of smaller cavities to be associated with smaller particles, and bigger cavities with bigger particles.

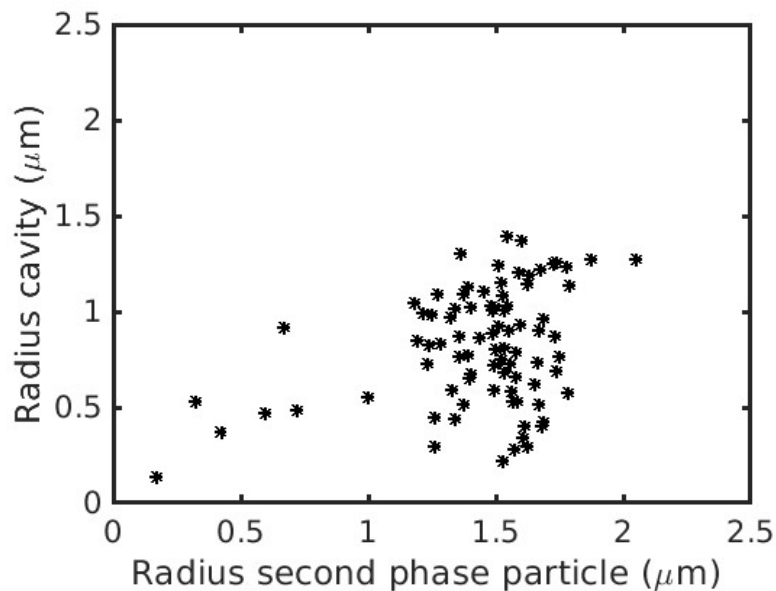


Figure 3.6 Plot showing radius of pre-existing cavities versus radius of the particles they were associated with.

3.1.4 Summary

Second phase particles, of two different size ranges (average radius 0.6 and 1.4 μm) were grown in Al-Cu sample by performing controlled heat treatment. These particles were expected to be sites of cavity nucleation during high temperature deformation. This heat treatment also resulted in formation of pre-existing cavities. Further on performing high temperature deformation of AC3 and AC5 under same conditions it was seen that AC5 sample did not show significant nucleation of cavities as damage mainly proceeded in growth of pre-existing cavities (see section 3.2.5 for further

details). Since no link between cavity nucleation and particle size could be conclusively established, further analysis of AC3 was abandoned and the focus was on studying the initial stages of growth of cavities in AC5. In the following sections the evolution of damage in the AC5 sample due to formation of creep cavities, will be discussed at length.

3.2 Cavity nucleation and growth during high temperature deformation

In this section the damage in Al-Cu alloy occurring during high temperature deformation in form of nucleation and growth of cavities will be examined. We start with revisiting the setup and acquisition parameters in brief since they have already been detailed in Chapter 2. The data analysis techniques used for the investigations has been listed briefly and appropriate references to the relevant sections have been provided. This is then followed by defining the high temperature deformation parameters that the sample was subjected to, followed by results related to initial 3D tomography, and nucleation and growth of cavities. First the results will be presented which will be followed by a discussion on the results.

3.2.1 *In situ* high temperature deformation nanotomography setup

With the aim to study the nucleation and early stages of growth, *in situ* high temperature deformation was performed using synchrotron X-ray radiation, on the AC5 sample. This involved loading the sample at a constant temperature and load while simultaneously performing 3D phase contrast tomography. The experiment was performed at the ID16B beamline of the European Synchrotron Radiation Facility (ESRF), which is described at length in section 2.2.2. The high temperature tensile deformation was performed using the resistance furnace (described in section 2.2.3) and a compact mechanical device (detailed in section 2.2.4.1). A schematic of the setup can be seen in Figure 2.6.

The notched specimen (Figure 2.1 b) was mounted in the mechanical device, subjecting the sample to a constant load which amounted to an initial stress of 7.9MPa ($\pm 10\%$). This pre-stressed sample mounted in the device was placed on the rotating stage in the experimental hutch of the beamline, while the furnace (set to 698 K and placed from the top) enclosed the mechanical device. This setup allowed

the sample to be subjected to a constant load and temperature. The initial stress and temperature were chosen to have a strain rate which was slow enough to capture the early stages of cavity growth, and further examine a change in growth mechanism, if any. This rate of straining was also contributive in acquiring good quality images.

Thanks to the multiscale acquisition capability, a set of four **High Resolution (HR)** scans at multiple heights (see Figure 2.12), with **pixel size 100 nm** (total field of view $128 \times 128 \times 377 \mu\text{m}^3$) were performed followed by a **Low Resolution (LR)** scan of **pixel size 645 nm** (field of view $826 \times 826 \times 697 \mu\text{m}^3$), see Figure 2.11 and Table 2.2. The acquisition parameters are discussed in section 2.3 and corresponds to scan type S2 described in this section and summarized in Table 2.3

A set of twenty-five, HR and LR scans were performed cyclically, with time between the scans being approximately 5 minutes. For imaging, 721 projections were acquired by rotating the sample by 360° , using a fast pco.edge 5.5 detector (with CMOS sensors) equipped with $34 \mu\text{m}$ GGG ($\text{Gd}_3\text{Ga}_5\text{O}_{12}:\text{Eu}$) scintillator, resulting in an acquisition time of 7 seconds for a full tomography. This very fast acquisition, at a high resolution, allowed good quality (blur free) images even during sample straining.

3.2.2 Data analysis

3.2.2.1 3D reconstruction

In order to obtain 3D volumes, phase retrieval calculation of radiographs was done using iterative Paganin based approach (see section 2.4.1.2) with a fixed delta over beta of 183, followed by reconstruction using filtered back projection with the ESRF software PyHST2 (see section 2.4.1.3). Reconstruction was accompanied by ring artefact corrections to enhance image quality by removal of ring artefacts, (see section 2.4.1.4).

3.2.2.2 HR volume analysis

Segmentation of the two primary phases in the HR volume: second phase particles and cavities was done using a cut off threshold determined using the iterative intermeans method, see section 2.5.3.2 and section 2.5.3.3).

Digital Volume Correlation (DVC) based on an in-house implementation, was used to track the movement of cavities from one scan to another. From the DVC tracking of second phase particles in the four HR volumes, local strain field was estimated, which in turn allowed the estimation of strain rate, this has been detailed in section 2.5.2 (For multi z scans for Al-Cu samples).

3.2.2.3 LR volume analysis

The evolution of stress was measured by estimating the minimum area of the notch, as the sample deformed. This was done using the LR scans that incorporated the full view of the notch. Segmentation for notch area is detailed in section 2.5.3.1.

3.2.2.4 Shape and volume estimation

In order to determine the shape of the cavity, the lengths of the cavity in the tensile direction as well as the directions perpendicular to the tensile axis were determined. This was done using ImageJ by evaluating the dimensions of a bounding box surrounding the cavity in the frame of reference of the loading direction. Sphericity and volume were also quantified details for which are provided in section 2.5.4

3.2.3 High temperature deformation parameters

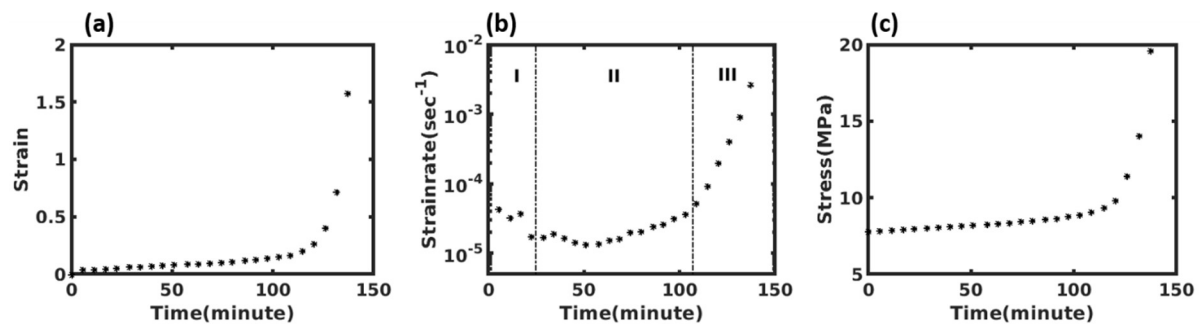


Figure 3.7 Evolution of mechanical parameters of the AC5 sample with time (a) strain versus time (b) strain rate versus time (c) stress versus time. The 3 stages of creep: primary (I), secondary (II) and tertiary (III) are marked in (b)

The sample: AC5 on being subjected to constant load and temperature, using the compact mechanical device, underwent a creep deformation. The strain versus time curve and the corresponding evolution of strain rate with time is shown in Figure 3.7 (a, b). In the strain rate versus time curve (Figure 3.7 b), the three regimes of creep: primary, secondary and tertiary can be identified. The primary stage showed a decrease in creep rate which was followed by a region of approximately constant

strain rate corresponding to the secondary regime. The steady state strain rate for the sample under the given conditions of deformation was between $1 \times 10^{-5} \text{ s}^{-1}$ and $2 \times 10^{-5} \text{ s}^{-1}$, with an average of $1.6 \times 10^{-5} \text{ s}^{-1}$. Towards the end, an increase in strain rate indicated the onset of tertiary creep. As the sample deformed, the stress on the sample changed due to a reduction in area. Figure 3.7 (c) shows the evolution of stress with time. These parameters were later used to evaluate growth rate of cavities based on existing models of cavity growth.

3.2.4 3D tomography results

Figure 3.8 (a, b) shows 2D slices from a LR volume of the AC5 sample (top view: XY, side view: YZ). The second phase particles are shown in black. The top of the sample shows a preferential nucleation of particles along the grain boundary while in the rest of the sample no such pattern is visible. Hence it can be concluded that the Region of Interest (ROI) on the LR sample (see Figure 3.8 b), that is examined in HR during the *in situ* test lies completely inside a single grain. The ROI was found to be at least $80 \mu\text{m}$ away from the grain boundary.

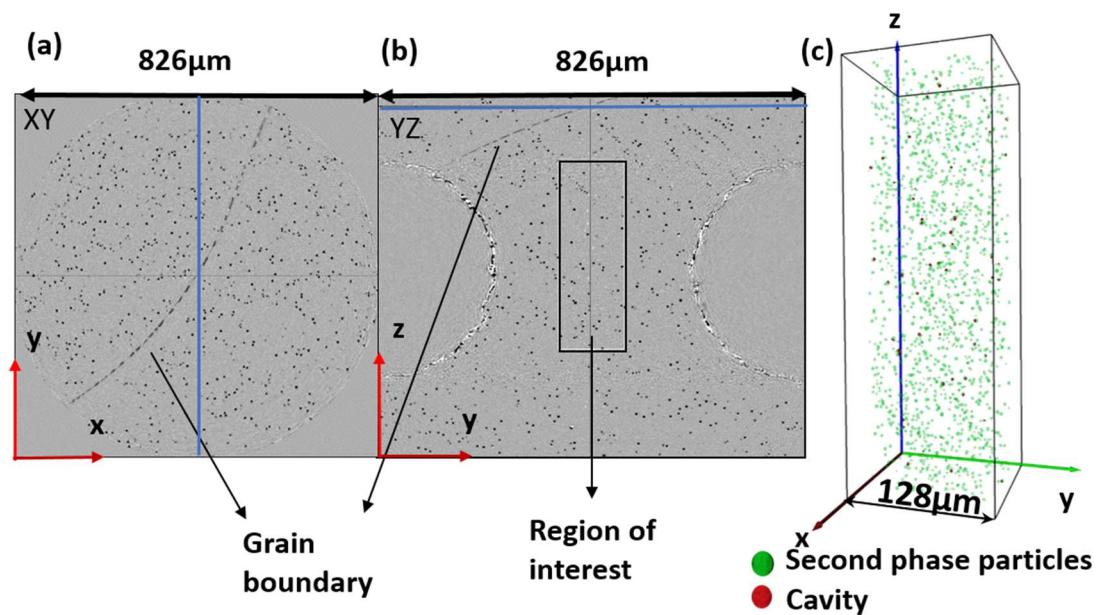


Figure 3.8 2D slices (a) of top view (XY) and (b) side view (YZ) from low resolution volume of AC5 sample at the start of deformation, the second phase particles are indicated in black and they are seen to line up along the grain boundary. Also, the region of interest is indicated, which is probed in the high resolution scans. The position of the two slices with respect to each other are indicated by the blue line. (c) High resolution 3D rendering of AC5 sample at start of deformation, with second phase particles (green) and pre-existing cavities (red)

Figure 3.8 (c) shows a 3D rendered HR volume at the start of the *in situ* high temperature deformation. From the volume it can be seen that there is a homogenous distribution of second phase particles (shown in green). Along with the particles, the pre-existing cavities (shown in red) can also be seen even at the beginning of deformation. All pre-existing cavities were associated with a second phase particle. Further information about the size and shape of the particles and pre-existing cavities were provided in section 3.1.2

The error induced by image processing in volume estimation, was estimated for two cavities with extreme sizes (a large one with initial radius 1.40 μm and a small one with initial radius 0.55 μm) using the method previously described in section: 2.5.3.3. The error on the radius ranged from 0.033 to 0.10 μm with a mean value of 0.05 μm .

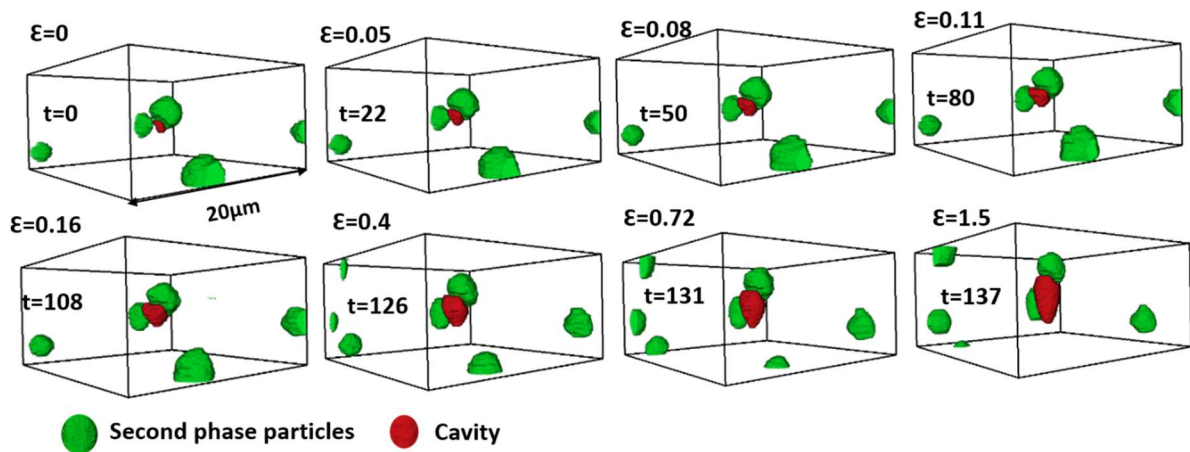


Figure 3.9 3D rendered view of growth of cavity (red) alongside a second phase particle (green) as the AC5 sample strains (ϵ) with time (t , in minutes)

Thanks to the *in situ* scans conducted on the deforming sample and the tracking of the cavities and particles with time, it was possible to study the evolution of cavities as the sample strained. Figure 3.9 shows 3D rendered image of a pre-existing cavity present on a particle, and its evolution with strain. As the sample strained, the volume of the cavity was seen to increase, accompanied by a change in shape.

3.2.5 Nucleation of cavities

Grain boundaries, second phase particles and triple junctions are expected to be probable sites of cavity nucleation. In the AC5 sample, an abundance of second phase particles make them probable sites for cavity nucleation. However during the

course of deformation only two nucleations were seen within the ROI probed. Both the cavities nucleated in association to a second phase particle and had an equivalent radius of 0.17 μm and 0.19 μm respectively, when nucleation was detected. A 3D rendered view of nucleation of a cavity along a second phase particle and its eventual growth on straining, is shown in Figure 3.10.

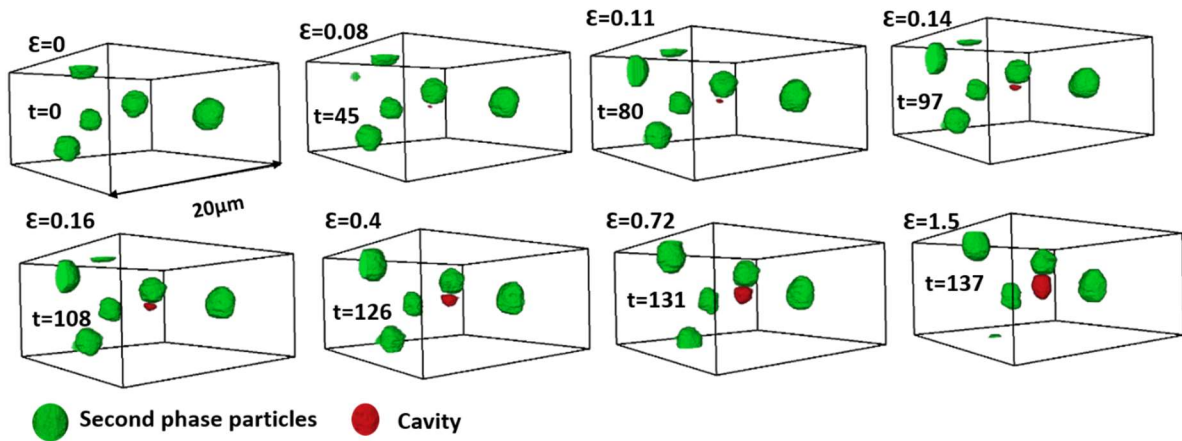


Figure 3.10 3D rendered view of nucleation and growth of cavity (red) alongside a second phase particle (green) as the AC5 sample strains (ϵ) with time (t , in minutes)

Here it should be pointed out that there were few cavities at the start of deformation that were visible, but could not be segmented using automatic segmentation, because they were too small initially. One such cavity can be seen in Figure 3.11, volume versus time plot of various cavities (Figure 3.11 is further explained in section 3.2.6). However, only those cavities that were not visible at the start of deformation have been considered as newly nucleated, these are marked in Figure 3.11.

3.2.6 Growth of cavities

Since the deformation overwhelmingly involved growth of pre-existing cavities, this section will focus on the growth of these cavities. Many cavities which were present in the ROI at the start of the deformation, escaped the ROI as sample strained. In addition, many cavities did not experience enough strain, owing to sample geometry (region far from the notch) and so they did not grow. In the following section, growth data from 16 pre-existing cavities and 2 new cavities which could be tracked from the start of the deformation till the end, and that experienced enough strain to grow, will be presented. In order to understand the underlying mechanism of cavity growth, the

evolution of shape of cavities was studied. To quantify the shape, the length of cavities was studied in, two directions perpendicular: X and Y, and a direction parallel: Z, to the tensile axis. Their evolution with time is shown in Figure 3.12 (a, b, c) respectively. It was seen that the length in all the three directions grew at a steady rate till a certain time, this indicated an isotropic growth, later however, an accelerated growth in the direction along the tensile axis (Z) was noted, this pointed towards a change of shape of cavity into an ellipse (see Figure 3.9). This change in trend points towards a probable change in growth mechanism. The time marking a change in shape, referred as transition time: T_t , was identified for each cavity. This transition time ranged between 97 and 120 minutes for the various cavities, as highlighted by the grey region in Figure 3.12 (c), while the average of this (110 minutes) has been marked by a dotted line.

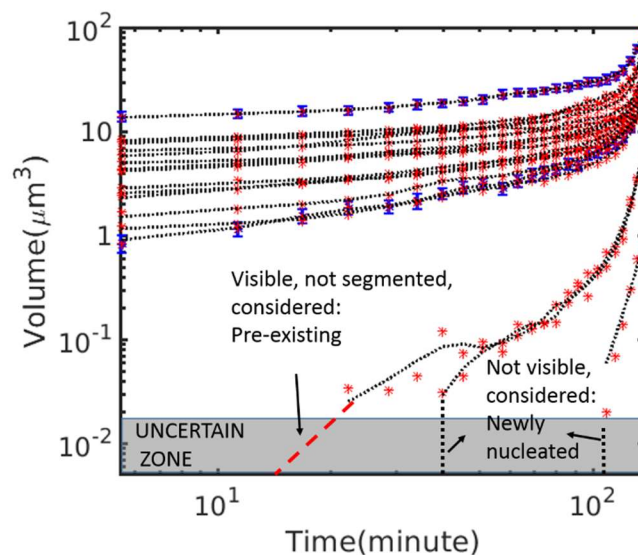


Figure 3.11 Volume of pre-existing and newly nucleated cavities with time, as seen in AC5 sample on subjecting it to high temperature deformation. The uncertain zone indicates the limit to resolution. The pre-existing cavity which was visible in the uncertain zone, but could not be segmented is marked separately. The two cavities that were not visible in the uncertain zone are marked as newly nucleated. The error bar (in blue) has been calculated as per technique mentioned in section: 2.5.3.3 and is shown for only two cavities to maintain clarity in the plot.

Further, the rate of growth of the cavities was determined, by measuring volume and calculating growth in terms of dV/dt . Figure 3.11 shows how the volume of various cavities change with time. It can be seen that at time zero the initial volume of the

various cavities varies between 0.03 and $12.25 \mu\text{m}^3$. Error bars on the volume are shown for a large and a small cavity as described in section 3.2.4.

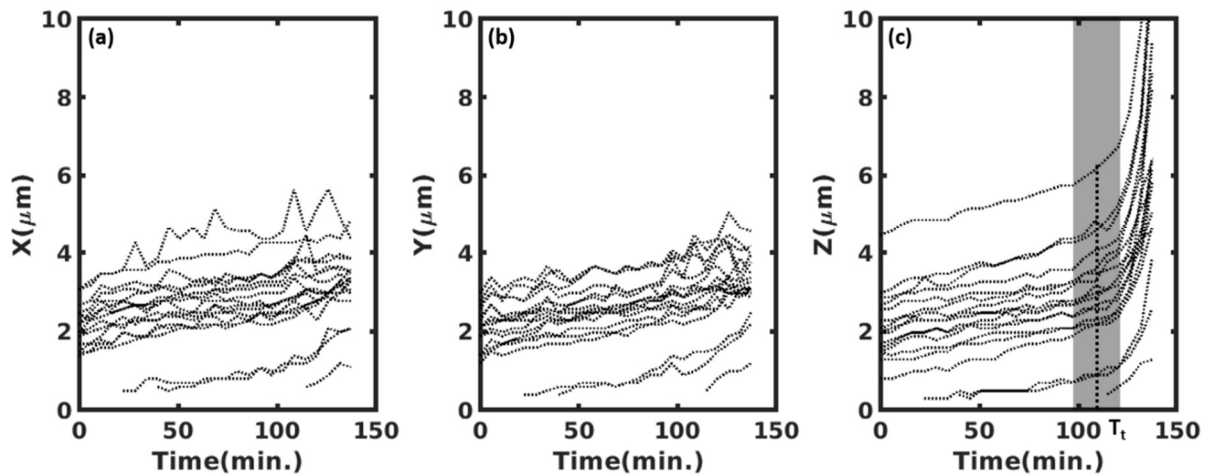


Figure 3.12 Shape change of pre-existing and newly nucleated cavities as a function of time in direction (a), (b) Perpendicular to tensile axis X and Y respectively and (c) Parallel to the tensile axis: Z (refer to Figure 3.8 for coordinate axis). The experimental transition time (T_t) for the various cavities is indicated by the grey region, average transition time is indicated by dotted line.

In addition to this, a clear change in rate of volume growth was observed between 100-120 minutes. To explore this further, rate of cavity growth (dV/dt) is plotted against radius in Figure 3.13. Such plots were traditionally used to identify the cavity growth mechanisms [63,95]. From the experimental data it can be seen that there is a change in trend of volumetric growth rate. This plot only includes growth that falls in the secondary and tertiary regime of creep (see Figure 3.7). It can be seen that the rate is initially weakly dependent on the radius and later it begins to increase substantially with the increase in the radius. It should be noted that this change occurs at different equivalent radius for different cavities.

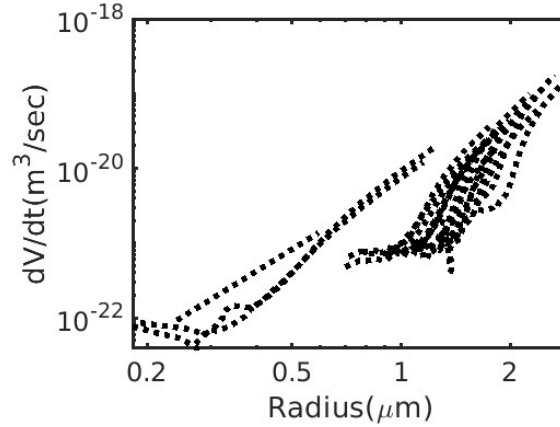


Figure 3.13 Plot of cavity growth rate (dV/dt) versus equivalent radius showing experimental cavity growth rate data for pre-existing and newly nucleated cavities, seen in AC5 sample on subjecting it to high temperature deformation.

3.2.7 Discussion

3.2.7.1 Nucleation of cavities

Second phase particles lying on grain boundaries are expected to be a probable site for cavity nucleation during high temperature deformation [9]. As per theories the stress accumulated on these particles during deformation should be a trigger for cavity nucleation. It is believed that the size of the particle has a role to play in this. Rice proposed a diffusion length which was a stress and temperature dependent length, serving as a parameter to study the interplay of creep and diffusion during high temperature deformation [52]. Chokshi et al used this length to give an estimate of a length above which diffusion is no longer able to nullify the stress concentrations on the second phase particle due to grain boundary sliding [51]. Hence any particle with a radius greater than this length was expected to be a probable site for nucleation. The diffusion length (L) was given by:

$$L = \left(\frac{\Omega D \sigma}{\pi k T \dot{\epsilon}} \right)^{1/2} \quad (3.1)$$

Where, Ω is the atomic volume, D is the lattice diffusion coefficient, σ is the stress, k is the Boltzmann constant, T is the absolute temperature and $\dot{\epsilon}$ is the strain rate.

The value of Ω ($1.66 \times 10^{-29} \text{ m}^3$), and Dl ($1.7 \times 10^{-4} \exp\left(-\frac{8.5 \times 10^{28}}{kT}\right) \text{ m}^2/\text{s}$) [142] for pure aluminium was used.

It should be pointed out that the particles in the sample do not lie on a grain boundary, as is hypothesized by the original model hence lattice diffusion is considered instead of grain boundary diffusion. Calculating diffusion length at the various stresses and strain rates (see Figure 3.7) experienced by the sample during deformation, the diffusion length ranges between 0.13 and 1.16 μm . Hence, any second phase particle with a radius greater than 1.16 μm should be a probable site for cavity nucleation. From Figure 3.4 (a) we know that the sample has several second phase particles with a radius greater than 1.16 μm , cavity nucleation was however very scarcely encountered. The limit in spatial resolution of the technique could be a probable explanation, that the nucleated cavities might be too small to be visible.

Taking the classical theory of nucleation into account, Raj and Ashby proposed a critical radius (r_c) for cavity nucleation, this being the radius above which the nucleated cavities would be stable to grow [49]. A simplified expression of this is:

$$r_c = \left(\frac{2\gamma}{\sigma} \right) \quad (3.2)$$

Where, γ is the surface energy. The value of γ (0.98 J/m²) [50] for pure aluminium was used. This critical radius, for the range of stress experienced by the sample, ranges between 0.19-0.25 μm . This is the size range in which the nucleated cavities were in fact observed (see section 3.2.5).

Keeping this in mind, the absence of major stress concentration features like grain boundary and triple junction, might be the reason why the prediction of cavity nucleation on second phase particles by Chokshi et al fails in the present case. In addition to this the presence of pre-existing cavities would also deter nucleation, because most of the stress concentration and vacancies generated would be used up in the growth of cavities instead of nucleation.

3.2.7.2 Mechanism of cavity growth

The shape of cavities are considered to be an indicator of the mechanism underlying its growth [143]. A more rounded shape of cavity resulting from a uniform growth in all directions indicates diffusion based growth. Plasticity based growth on the other

hand is generally associated to elongated cavities which align parallel to the tensile axis.

In the AC5 sample, similar rate of growth of cavity along directions perpendicular as well as parallel to tensile axis: X, Y, Z (Figure 3.12) resulted in well-rounded cavities (Figure 3.9, Figure 3.10 $t < 100$ minutes), for initial part of deformation (before T_t in Figure 3.12 c). This indicates that cavities grew predominantly via diffusion. An accelerated growth rate along the direction parallel to the tensile axis: Z (Figure 3.12 c) and an alignment of elongated cavities (Figure 3.9, Figure 3.10 $t > 100$ minutes), along the tensile axis points towards a predominantly plasticity based growth at the later stages of deformation.

To further explore the change in trend of cavity growth rate with radius as seen in Figure 3.13 and to determine any inherent change in growth mechanism, we compare the experimental cavity growth rate of a few cavities to diffusion and plasticity models in Figure 3.14. For convenience growth data from four cavities have been presented, the remaining cavities also show similar trends, see Appendix D.

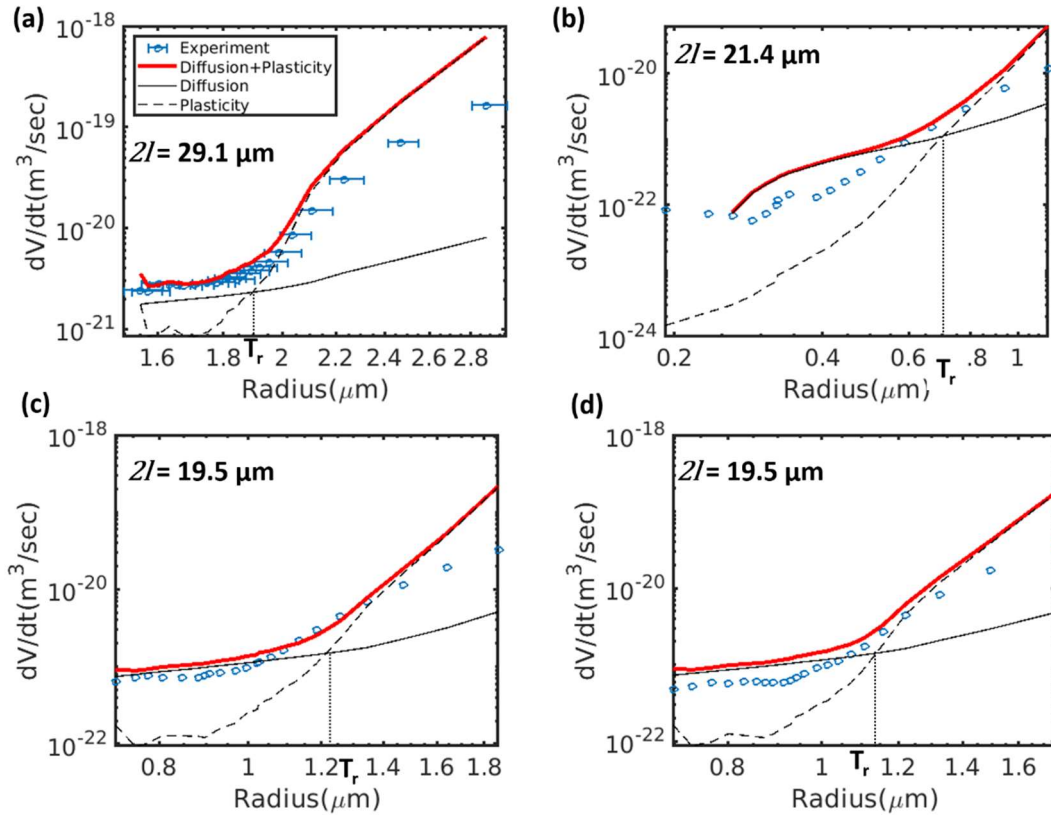


Figure 3.14 Plot of cavity growth rate (dV/dt) versus equivalent radius, showing comparison of experimental cavity growth data with diffusion and plasticity based cavity growth models in AC5 sample for 4 different cavities. The inter cavity spacing ($2l$) used in calculation has also been indicated for each cavity. The error bar (in blue, in (a)) has been calculated as per technique mentioned in section: 2.5.3.3. The transition radius (T_r) for the various cavities is indicated by dotted line.

Many diffusion models for cavity growing on a transverse grain boundary have been proposed [7,58]. These models were proposed for several cavities of radius r , separated by a distance $2l$ lying on transverse grain boundary. Dyson [56] and later several others [7,67] also proposed constrained grain boundary models, pointing out that previous models, ignore the fact that cavities might not be uniformly distributed on all grain boundary facet in a polycrystalline materials. In the present case since all cavities lie inside one grain and not on the grain boundary, we use the modified formulation proposed by Raj et al [49,61] for diffusion via lattice instead of the grain boundary. When a stress of σ is applied on the sample, the rate of cavity growth (dV/dt) for cavities of radius r , separated by a distance $2l$ is given by:

$$\frac{dV}{dt} = \frac{2\Omega D_l(2l)}{kT} \left\{ \frac{\left(\sigma - \frac{2\gamma}{r}\right)(1-\omega^2)}{\ln\left(\frac{1}{\omega}\right) - 0.75 + \omega^2 \left(1 - \frac{\omega^2}{4}\right)} \right\} \quad (3.3)$$

Where, ω is a parameter, normalising the cavity size with inter-cavity spacing, given by $\omega = r/l$. The cavity growth rate via diffusion in Figure 3.14 was calculated from equation (3.3) by accurately determining each parameter. Thanks to the *in situ* test, the change in radius of cavity with time was known (Figure 3.11) and so was the stress (Figure 3.7 c), this gave the correct stress corresponding to each radius. For each cavity, its distance to the nearest cavity was measured in the 3D volume of the initial state and this was used as the inter-cavity spacing.

For comparison with the plasticity based growth, a modified form of the model by Hancock [62] was considered. This model predicted a direct proportionality between the rate of cavity growth and cavity volume, strain rate of deformation. The growth rate was given by:

$$\frac{dV}{dt} = 3V\dot{\epsilon} \quad (3.4)$$

As described before, the strain rate (Figure 3.7 c) and volume (Figure 3.11) corresponding to each time was also known experimentally. And so the strain rate corresponding to each volume was used to estimate the plasticity growth rate using Equation (3.4), in Figure 3.14

On comparing the growth rate based on diffusion and plasticity model in Figure 3.14, it can be seen that before transition radius (T_r), diffusion rate is much higher than plasticity and so it should be the dominant growth mechanism while beyond it plasticity should dominate growth. It is also seen that the experimental volumetric growth rate shows a good match with the cumulative rate of the two models (red line in Figure 3.14). It should be noted that even when two growth mechanisms are competing, in principal both should be simultaneously propelling the growth of cavities, hence the sum of rates have been considered for comparison. Further, at the very end the model over predicts the growth rate. Due to very fast deformation at the end, limited data is available in this region, making further probe difficult. It is speculated that very fast plastic deformation near failure might not have manifested as cavity growth.

Hence it can be concluded that during deformation, cavity initially grows via diffusion followed by plasticity. It should be noted that the strain rate varied during the deformation and that the observed change in mechanism is in tandem with an increase in strain rate towards the later stage of deformation, corresponding to tertiary creep.

3.2.7.3 Point of transition between growth mechanisms

Traditionally the point of transition between mechanisms of creep cavity growth is associated with a unique radius [66]. This radius mainly depends on the mechanical parameters (stress, strain rate) and is given by the radius at which the rate of growth by diffusion equals the rate of growth by plasticity. Hence, when transformation occurs while sample is deforming in steady state (constant strain rate), the point of transition is given by a unique radius. A simplified form of this radius, which is referred as the transition radius: T_r , is obtained by solving equation (3.3) and

equation (3.4) and by assuming $\left\{ \frac{(1-\omega^2)}{\ln\left(\frac{1}{\omega}\right) - 0.75 + \omega^2 \left(1 - \frac{\omega^2}{4}\right)} \right\} \cong 1$ [66], is given by:

$$T_r = \left(\frac{\Omega LD_0 \sigma}{\pi k T \dot{\epsilon}} \right)^{1/3} \quad (3.5)$$

Since in the case examined, the test is not carried out in steady state creep, it is expected that the radius of transition will not be a unique value. Figure 3.15 (a) shows how this value varies over time of the test. It is computed by incorporating the mechanical parameter changes with sample deformation. Hence each point in Figure 3.15 (a), corresponds to a set of stress and strain rate experienced by the sample during the test (see Figure 3.7). This gives the range of radius values in which the transition can occur in the sample.

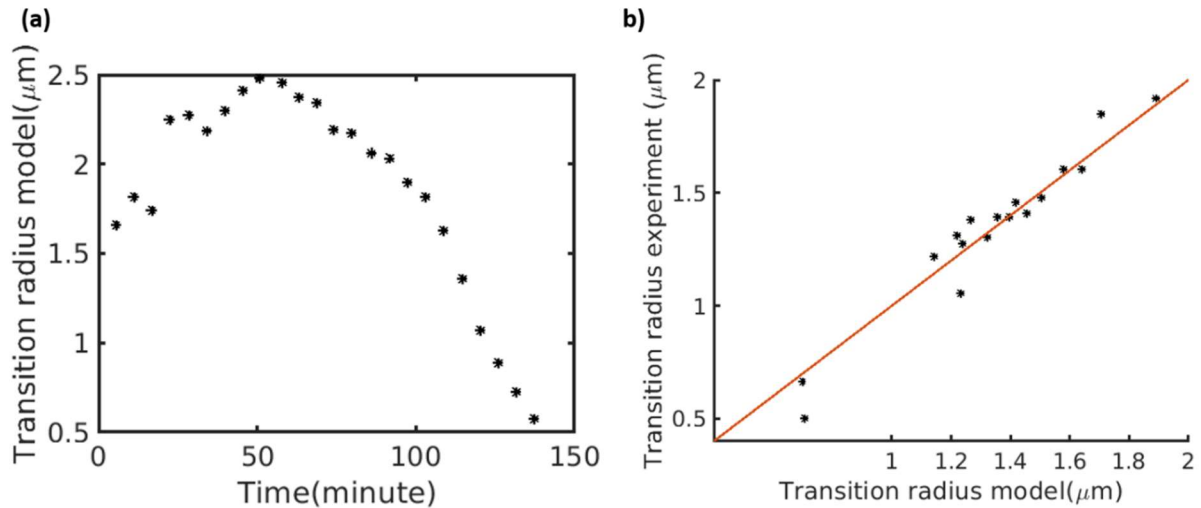


Figure 3.15 (a) Plot showing change in transition radius obtained from model with time of sample deformation (b) Transition radius obtained experimentally versus transition radius from model, for AC5 sample. The red line is a straight line with a slope of 1.

However for the case at hand, the radius of transition changes for each cavity present in the sample, owing to the distinct conditions of its growth. To investigate this, we refer to Figure 3.14. It can be seen that the transition radius obtained from models (indicated by T_r in Figure 3.14), is different for the four different cavities. This is because the model has been estimated keeping in mind the change in mechanical parameters and local inter-cavity distance. Hence, at the same radius of $1.5 \mu\text{m}$ the cavity in Figure 3.14 (a) has a smaller volumetric growth rate for both plasticity and diffusion as compared to the cavity in Figure 3.14 (c). This is because at the same radius, the two cavities grew under different stress and strain rate and had different inter-cavity separation.

Now, in order to validate this with the experimental values, the experimental radius of transition was determined from the shape data. From Figure 3.12 (c) the time at which the length in tensile direction deviates from a growth at constant rate, transition time has been determined for each cavity. This time then in turn leads to the corresponding experimental transition radius. Figure 3.15 (b) is a comparison of transition radius determined experimentally and via the models at hand. The two agree quite well, since most of the data points fall close to the straight line of slope 1. Hence we can say that the transition radius is a good way of predicting the transition in cavity growth mechanisms, but in case of non-steady state deformations, the

change in mechanical parameters must be accounted for, while making such estimations.

3.3 Constant strain rate high temperature deformation

In order to study cavity growth mechanism during deformation at a constant strain rate, Al-Cu sample was also subjected to deformation using a motorized mechanical device. The results from this sample will be presented in this section.

We begin with describing the sample preparations and acquisition parameters with appropriate reference to Chapter 2.

3.3.1 Sample preparation and acquisition parameters

The sample preparation and machining for this sample was described in section 2.1.1, the sample used has been schematically depicted in Figure 2.1 (c). The deformation was using a furnace (section 2.2.3) and motorized mechanical device (see Figure 2.10) detailed in section 2.2.4.2 which together were expected to provide deformation at a constant strain rate and constant high temperature.

Accompanied by the deformation was *in situ* tomography acquisition, with 4 HR and one LR scan, corresponding to scan S4 detailed in section 2.3 and briefed in Table 2.3. This was essentially similar to that used for sample AC5, the key difference being: acquisitions for this sample was limited to 180° rotations.

The phases retrieval reconstruction and segmentation was entirely similar to that used for AC5 sample and would not be repeated, please see section 3.2.2 for details.

3.3.2 Mechanical parameters

The sample was subjected to a strain rate of $5 \times 10^{-5} \text{ s}^{-1}$ at a temperature of 698 K. The area of LR notch (see section 2.5.3.1 for methodology) acquired during sample deformation was used to estimate the strain on the sample by using equation (2.5). This was then used to estimate the strain rate on the sample using equation (2.6). Figure 3.16 shows the strain versus time and strain rate versus time measured on the sample, with a red line indicating the expected strain rate applied on the sample.

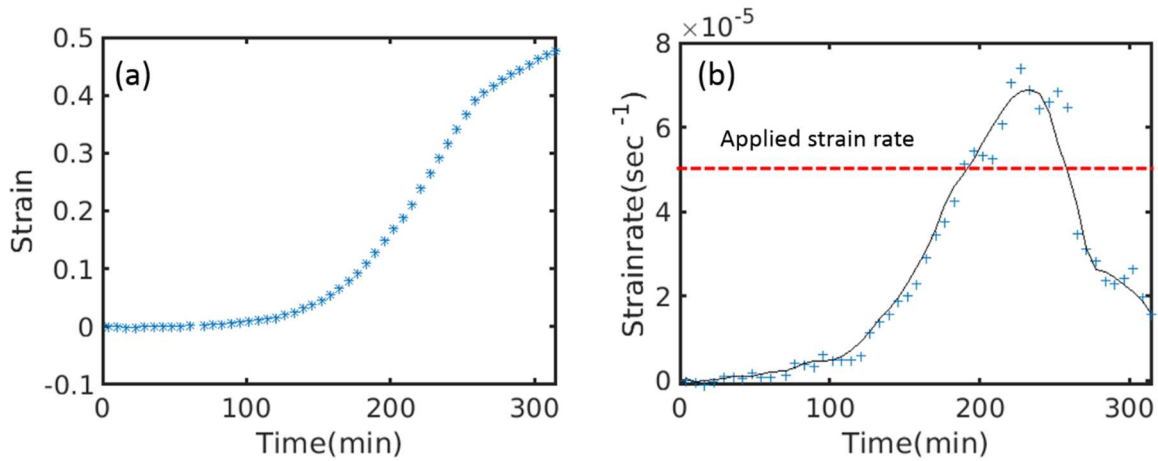


Figure 3.16 Plot showing (a) strain versus time and (b) strain rate versus time with applied strain rate indicated by red line.

It can be seen that until a time of 100 min sample did not strain. After this the sample strained at a strain rate ranging from $1.5 \times 10^{-5} \text{ s}^{-1}$ to $7 \times 10^{-5} \text{ s}^{-1}$. Beyond 250 min the test had to be abandoned due to some technical fault with the mechanical device. Since the inner tube of the device broke during the beamtime it was replaced by an alumina tube which was glued using ceramic glue to the bottom part. It was concluded this ceramic glue near the bottom pin, restricted load transfer hence failing to strain the sample for nearly an hour. Hence it was concluded that the design of the motorised mechanical device needed to be more robust. This is addressed at length in the perspectives of the thesis.

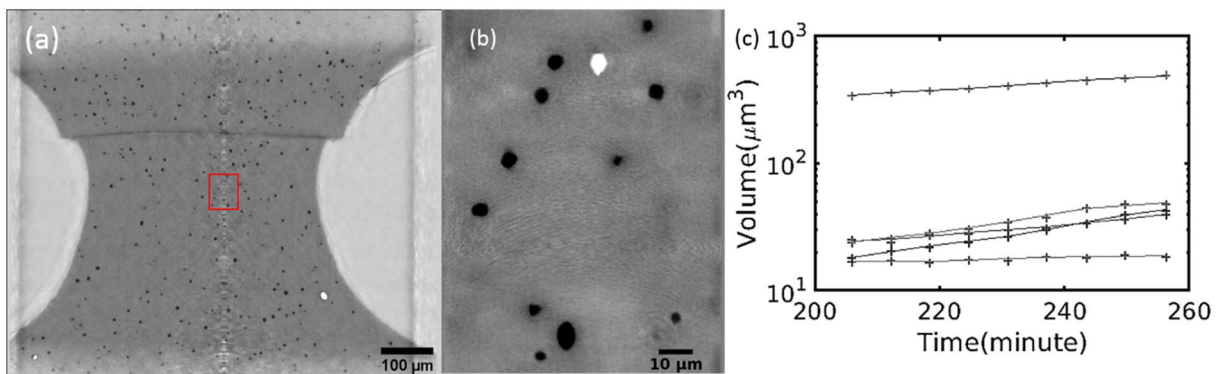


Figure 3.17 (a) LR Transverse 2D slice for Al-Cu sample after deformation at 250 min with region of 1 HR scan indicated by red box (b) HR Transverse 2D slice for Al-Cu sample after deformation at 250 min. (c) Volume versus time plot showing growth of cavities between 200 and 260 minutes. (cavities are in white and second phase particles in black)

However the volumes obtained while the sample deformed were of good quality and satisfactory reconstruction could be performed while the sample deformed at 7×10^{-5}

s⁻¹. Figure 3.17 (a, b) shows a transverse 2D LR and HR slice of the sample at 250 min of deformation. Volume versus time of 5 cavities tracked in the HR volume in the nearly constant strain rate regime is also provided (Figure 3.17 c) and reconstructed data is available for analysis.

3.4 Conclusions

- *In situ* nanotomography investigation of cavity nucleation and growth during high temperature deformation was carried out in Al -3.6 wt% Cu alloy.
- Second phase particles, of two different size ranges (average radius 0.6 and 1.4 μm) were grown. Initial investigation of the sample revealed the presence of pre-existing cavities. Because of this deformation mainly involved growth of cavities, while nucleation was barely seen. Therefore no link between cavity nucleation and particle size could be conclusively established.
- Fast 3D imaging was done while deforming sample (at 7.9 MPa, 698 K using compact mechanical device) containing second phase particles (average radius of 1.4 μm) to track nucleation and volumetric growth of individual cavities during deformation.
- Change in shape of cavities with straining was studied. Also, the change of volumetric cavity growth rate versus equivalent radius of individual cavities was compared to existing models of cavity growth by diffusion and plasticity.
- The experimental data of growth rate matched well with the studied models and it was concluded that cavities initially grew by diffusion, while the growth mechanism changed to plasticity near failure (corresponding to a rapid increase in strain rate).
- It was noted that models for grain boundary cavity growth were also valid for intra-granular cavity growth due to diffusion.
- Another Al-Cu sample was subjected to deformation using the automated mechanical device at a constant strain rate and high temperature ($5 \times 10^{-5} \text{ s}^{-1}$, 698 K). It was found that the sample did not deform at the applied strain rate due to technical faults with the device. Hence further trials to improve the robustness of this device were needed.

Chapter 4. High temperature deformation of Mg alloy (AZ31)

This chapter extends the study of damage initiation and growth at high temperature to commercial AZ31 alloy. This alloy is known to show superplastic deformation under specific range of temperatures and strain rates [6,114]. The primary motive of this chapter is to study the nucleation and growth of cavities while the material deforms under superplastic conditions, using the novel *in situ* nanotomography technique. During this PhD, AZ31 samples were deformed under several mechanical conditions. After preliminary analysis of all the samples, one sample was chosen for in depth analysis. This sample showed steady deformation for long time under superplastic deformation regime and hence was appropriate choice for the analysis. Results from this will be presented in the following sections. The details regarding sample preparations, machining for which are provided in section 2.1.2 The chapter begins with a description of the initial microstructure of the sample. This is followed by a discussion of the setup, acquisition parameters and data analysis in brief since they have already been detailed in chapter 2. Subsequently, high temperature deformation parameters that the sample was subjected to, are described. Thereafter, the results and discussions on cavity nucleations are presented. The chapter ends with the details on cavity growth during high temperature deformation and concluding remarks.

The details regarding sample preparations, machining for which are provided in section 2.1.2

4.1 Initial microstructure

Initial nano tomographic examination of the high resolution volume of the sample showed the presence of two types of intermetallic phases. Presence of pre-existing cavities were also seen. The intermetallic phases were expected to an Al-Mn phase and $Mg_{17}Al_{12}$ (see section 2.1.2 for details). The $Mg_{17}Al_{12}$ particles had a grey level similar to the matrix hence were difficult to segment. Since studying intermetallics was not the focus of the present study, only Al-Mn phase intermetallic particles were

segmented for DVC tracking. In the following section, details about these intermetallics and pre-existing cavities are presented.

A 3D rendered volume of combination of the 4 high resolution (HR) volumes recorded at the start of the high temperature deformation is shown in Figure 4.1 (a). The intermetallics are shown in green and cavities in red. It can be seen that the sample contains an inhomogeneous distribution of intermetallics, which are present in a variable size ranges, and are sometimes seen to be elongated along the rolling direction. In addition to the intermetallics, a few cavities are also present at the beginning of deformation. These cavities are sometimes found to be associated with intermetallics and sometimes not. In this chapter they will be referred as pre-existing cavities. A total of about 1415 intermetallics and 73 pre-existing cavities was found in the 4 HR volumes (the dimension of which was a cylinder with radius 64 μm and height of 348 μm).

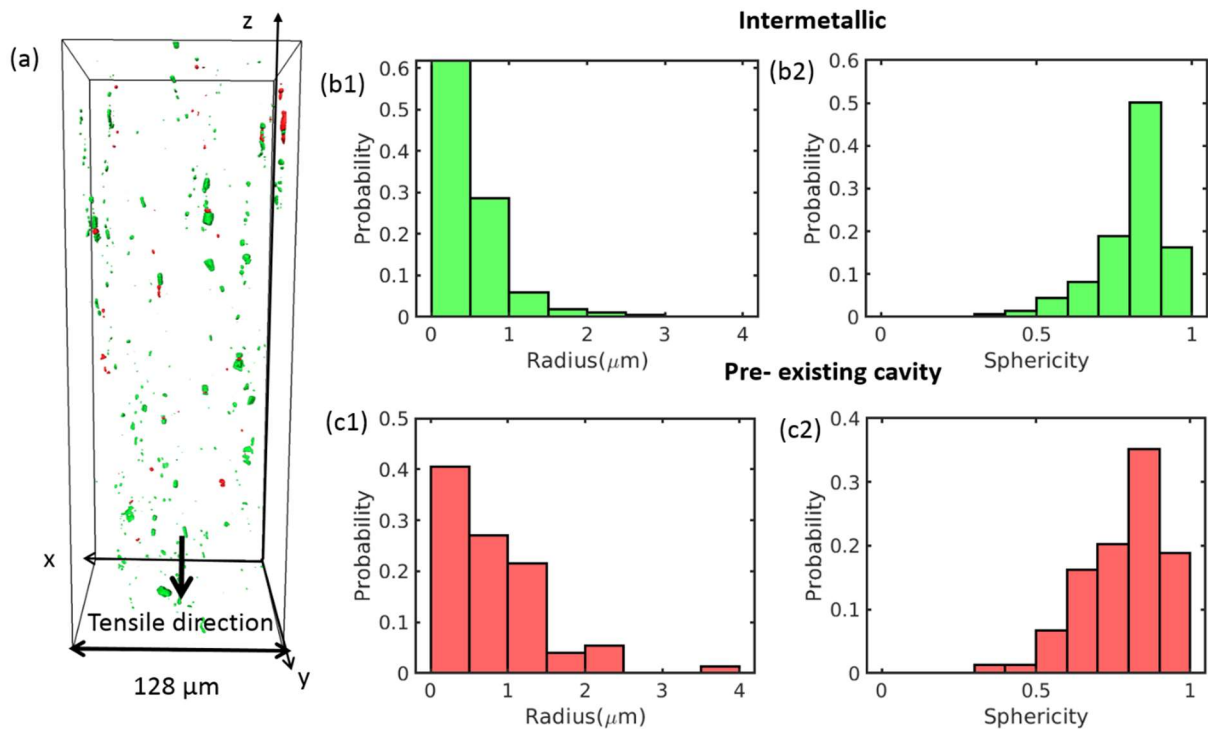


Figure 4.1 (a) 3D rendered volume (combination of 4 HR volumes pixel size 100 nm) of sample at the start of deformation (cavities in red and Intermetallics in green). (b) Histogram showing probability of (b1) radius and (b2) sphericity of intermetallic. (c) Histogram showing probability of (c1) equivalent radius and (b2) sphericity of pre-existing cavity. Rolling direction is parallel to tensile direction.

Figure 4.1 (b1, b2) shows the probability distribution of radius and sphericity of the intermetallics seen in the sample. Here it should be pointed out that the radius was calculated from the volume, assuming a spherical shape of the intermetallics and cavities and is hence the equivalent radius. All the radii mentioned in this chapter are in fact equivalent radii. The histogram suggests that majority of the intermetallics have a radius of less than 0.5 μm and that the sphericity of most of them are greater than 0.9, indicating equiaxed shapes. However, their size is not uniform as the sample shows intermetallics with radius ranging from 0.17 to 3.7 μm . The sample had 8.5×10^{-4} volume fraction of intermetallics, with a mean radius of 0.54 μm .

Further looking at the statistics of the pre-existing cavities in Figure 4.1 (c1, c2), it can be seen that majority of these have an equivalent radius of less than 1 μm and that the sphericity of most of them are greater than 0.9. Most of the pre-existing cavities are small and fairly equiaxed. The sample had a 1.5×10^{-4} volume fraction of cavities, with a mean radius of 0.8 μm with a range of 0.17 – 3.8 μm .

Pre-existing cavities have been reported in hot rolled sheets of AZ31 alloys, and they are considered to be originating as a by-product of the thermo mechanical treatment undergone by the sample [104]. However when high temperature *in situ* examinations are done with an effective resolution of nearly 2 μm , most the small intermetallics and especially pre-existing cavities are not visible [11,12]. Then during deformation, as these cavities grow and become visible, they are classified as nucleated cavities, which is in fact a faulty assumption. Additionally, due to low volume fraction and small sizes as compared to the intermetallics, these pre-existing also go undetected when rigorous optical micrographic examination is not carried out. **In the present work thanks to imaging at pixel size of 0.1 μm , it is possible to have a more comprehensive information about the initial microstructure of the sample.**

4.2 Technical details

In this section the technical details about the *in situ* setup, data acquisition and analysis relevant to this study will be revisited in brief (these have already been detailed in chapter 2). Key informations have been highlighted in bold letters for

convenience. Following this the mechanical parameter of deformation for the sample will be detailed.

4.2.1 *In situ* high temperature deformation nanotomography setup and acquisition

With the aim to study the nucleation and early stages of growth, *in situ* high temperature deformation was performed using synchrotron X-ray radiation, on the AZ31 sample. This involved loading the sample at a constant temperature and load while simultaneously performing 3D phase contrast tomography. The experiment was performed at the ID16B beamline of the European Synchrotron Radiation Facility (ESRF), which is described at length in section 2.2.2. The high temperature tensile deformation was performed using the resistance furnace (described in section 2.2.3) and a **compact mechanical device** (detailed in section 2.2.4.1). A schematic of the setup can be seen in Figure 2.6.

The notched specimen (Figure 2.1 b) was mounted in the mechanical device, subjecting the sample to a constant load which amounted to an initial stress of 3.2 MPa (± 0.5). This pre-stressed sample mounted in the device was placed on the rotating stage in the experimental hutch of the beamline, while the furnace (set to 673 K and placed from the top) enclosed the mechanical device. This setup allowed the sample to be subjected to a constant load and temperature.

Thanks to the multiscale acquisition capability, a set of four **High Resolution (HR)** scans at multiple heights (see Figure 2.12), with **pixel size 100 nm** (total field of view $128 \times 128 \times 377 \mu\text{m}^3$) were performed followed by a **Low Resolution (LR)** scan of **pixel size 645 nm** (field of view $826 \times 826 \times 697 \mu\text{m}^3$), see Figure 2.11 and Table 2.2. The acquisition parameters are discussed in section 2.3 and corresponds to **scan type S2** described in this section and briefed in Table 2.3.

A set of **forty, HR and LR scans** were performed cyclically, with period of the cycle time between the scans being approximately 5 minutes. For imaging, 721 projections were acquired by rotating the sample by 360° , using a fast pco.edge 5.5 detector (with CMOS sensors) equipped with $34 \mu\text{m}$ GGG ($\text{Gd}_3\text{Ga}_5\text{O}_{12}:\text{Eu}$) scintillator, resulting in an acquisition time of 7 seconds for a full tomography.

4.2.2 Data analysis

4.2.2.1 3D reconstruction

In order to obtain 3D volumes, phase retrieval calculation of radiographs was done using iterative Paganin based approach (see section 2.4.1.2) with a fixed delta over beta of 280, followed by reconstruction using filtered back projection with the ESRF software PyHST2 (see section 2.4.1.3). Reconstruction was accompanied by ring artefact corrections to enhance image quality by removal of ring artefacts, (see section 2.4.1.4).

4.2.2.2 HR volume analysis

Segmentation of the two primary phases in the HR volume: intermetallics and cavities was done using a cut off threshold determined using iterative intermeans method for the intermetallics and edge detection method for the cavities see section 2.5.3.2 and section 2.5.3.3).

Digital Volume Correlation (DVC) based on an in-house implementation, was used to track the movement of cavities from one scan to another. From the **DVC tracking of intermetallics in the LR volume**, macro strain on the sample was estimated, which in turn allowed the estimation of strain rate, this has been detailed in section 2.5.2. (For multi z scans on AZ31 alloys with LR volumes)

4.2.2.3 LR volume analysis

The evolution of true stress was measured by estimating the minimum area of the notch, as the sample deformed. This was done using the LR scans that incorporated the full view of the notch. Segmentation for notch area is detailed in section 2.5.3.1.

4.2.2.4 Shape and volume estimation

Quantification of sphericity and volume are detailed in section 2.5.4

4.2.3 Mechanical parameters

The sample was subjected to a constant load of 0.72 (± 0.2) N, amounting to an estimate of initial stress of 3.2 (± 0.5) MPa. On heating at a temperature of 673 K, the sample underwent creep deformation. The strain versus time curve and the corresponding evolution of strain rate with time are shown in Figure 4.2. The deformation was stopped after about 230 minutes (corresponding to a strain of 0.9),

before the sample failed. On the strain versus time curve the primary regime of creep is barely visible. The sample strains fairly uniformly throughout deformation, maintaining a constant strain rate of nearly $6.6 \times 10^{-5} \text{ s}^{-1}$. Thanks to this steady strain rate deformation it was possible to study the growth of cavities under a steady state up to a considerably large strain (0.9).

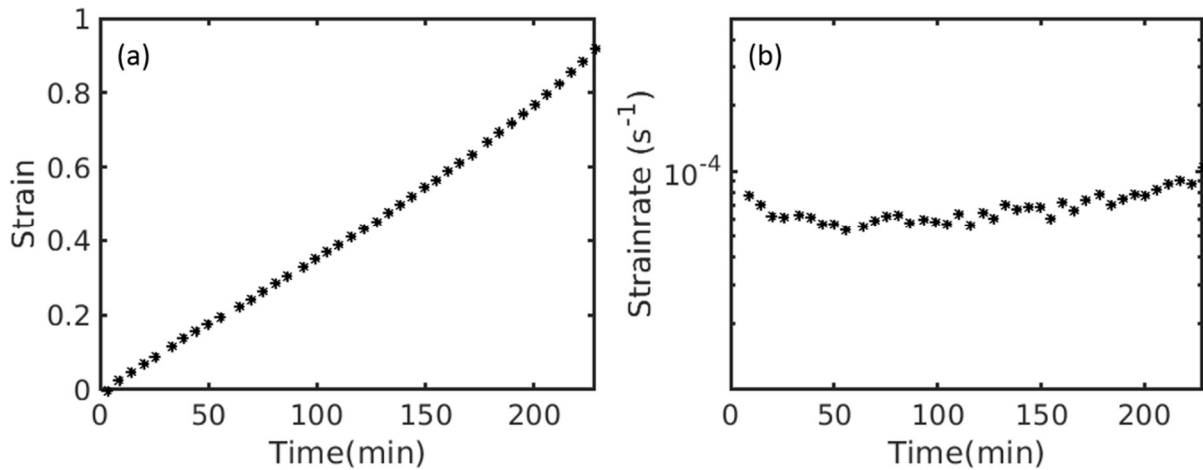


Figure 4.2 Plot showing evolution of (a) strain with time and (b) strain rate with time in sample.

Figure 4.3 shows the strain rate jump test performed on an AZ31 sample (obtained from the same rolled sheet that was used to machine the sample for the current work). This test was performed as a part of PhD thesis of R. Boissière. This was used to estimate the initial load on the sample being studied based on the macro strain rate estimated on the sample using DVC (The relevant strain rate jump test has been indicated with a red arrow in Figure 4.3).

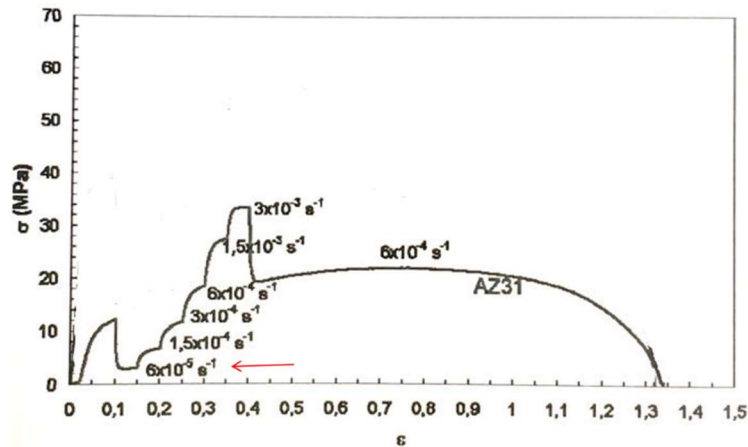


Figure 4.3 (a) Strain rate jump test for AZ31 sample at 673 K. The data relevant for the current work has been marked in red. Work of R. Boissière [144]. NOTE comma represent decimal point

4.3 Nucleation of cavities

On subjecting the sample to high temperature deformation the sample showed damage in form of nucleation and growth of cavities. In this section the result and discussion related to cavity nucleation will be presented.

4.3.1 Results

Grain boundaries, second phase particles and triple junctions are expected to be major sites of cavity nucleation. In the samples an abundance of intermetallics and grain boundaries make them probable sites for cavity nucleation. However during the course of deformation only three nucleations were seen within the Region of Interest (ROI) probed. None of the three nucleated cavities were associated with an intermetallic. They nucleated at a strain 0.31, 0.69 and 0.74 with initial radius when segmentation was possible being 0.17 μm , 0.19 μm and 0.17 μm respectively. Figure 4.4 shows a cropped 3D volume showing nucleation of a cavity (cavity in red intermetallic in green) at a strain of 0.72 and further growth of the cavity. The last scan is presented with two different orientations, for better comprehension of the 3 dimensional shape of the cavity.

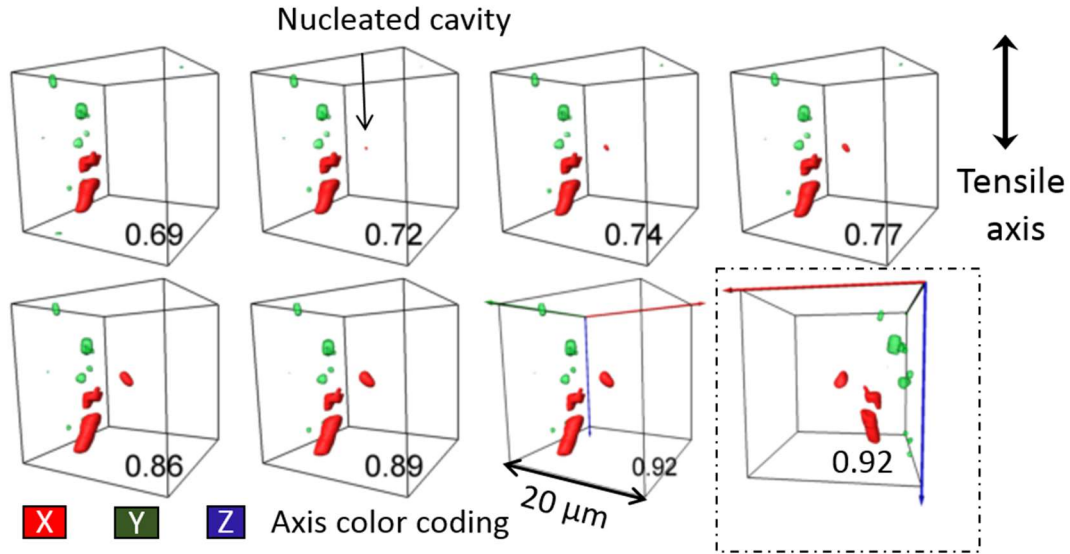


Figure 4.4 3D rendered volumes showing nucleation and growth of a cavity with strain, (marked at the bottom of each box) in sample. A different view of the cavity at the last scan is also shown, highlighted by a box for better comprehension of the 3 dimensional shape of the cavity (cavities are in red and intermetallics in green).

4.3.2 Discussion

Second phase particles lying on grain boundaries are expected to be a probable site for cavity nucleation during high temperature deformation [9]. As per theories the stress accumulated on these particles during grain boundary sliding should be a trigger for cavity nucleation. However the nucleations that were seen in this sample were not on an intermetallic. Further grain boundary jogs and grain boundary triple points have also been suggested as possible sites for cavity nucleation especially for sliding grain boundaries [54] see section 1.2.1 and Figure 1.8(b) , Figure 1.9.

Figure 4.5 (a1, b1 and c1) shows transverse 2D slices of the three nucleated cavities (encircled) and (a2, b2 and c2) shows them after straining. At nucleation the cavities are too small and not much information about the shape can be obtained. After straining however, observation of shape of cavities suggests that the nucleation happened at grain boundary jogs in Figure 4.5 (a) and at grain boundary triple points Figure 4.5 (b and c). 3D rendered view of cavities have been presented Figure 4.5 (a3, b3, c3) for clarity.

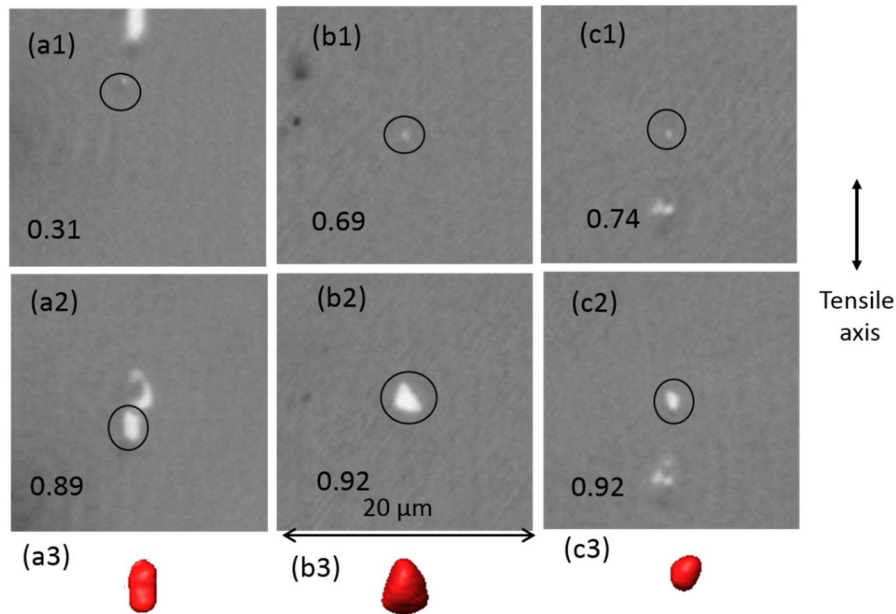


Figure 4.5 Transverse 2D slice of three cavity (a1) (b1) and (c1) at the time of nucleation and after growth (a2), (b2) and (c2). The relevant cavities have been encircled and the strains have been marked at the bottom left corner. (a3), (b3) and (c3) is 3D rendered image of cavities at strains corresponding 0.89, 0.92 and 0.92 respectively.

It is acknowledged that the region tracked from beginning till end was small, and it is highly plausible that other nucleation events happened during deformation which could not be tracked. In the region that could be tracked, it is evident that most of the deformation manifested in growth of pre-existing cavities and nucleation was rarely seen.

4.4 Growth of cavities: average measurements

Moving on to damage due to growth of cavities, in this section first average growth statistics of creep cavities will be presented. This includes cumulative results on cavity growth obtained from the four high resolution volumes (total dimension of which is a cylinder of radius 64 μm and height 348 μm) that were acquired during deformation. Most previous *in situ* tomography of damage have focussed on analysis of this nature. This will be followed by a post mortem tomography analysis of sample for general overview of damage.

In order to study the evolution of damage, first the average trends of number of cavities, volume fraction and total volume of cavities with strain is studied (see Figure 4.6). Since a small portion of the sample was viewed in HR, several cavities

moved in and out of the ROI at high resolution because of sample deformation (red box in Figure 4.7 (a) represents the region of sample visible in one HR volume). In addition during acquisition the sample was also moved along z axis, time to time, in order to compensate for the change in ROI due to deformation. Hence the number of cavities is seen to vary with strain in Figure 4.6 (a). However barring these variations the number of cavities remains nearly constant during deformation. This indicates that during deformation nucleation and coalescence of cavities is insignificant and that deformation mainly proceeded in growth of cavities. The total volume and volume fraction of the cavities increase with strain, showing an exponential growth at strains higher than 0.3 (see exponential fit in Figure 4.6 c)

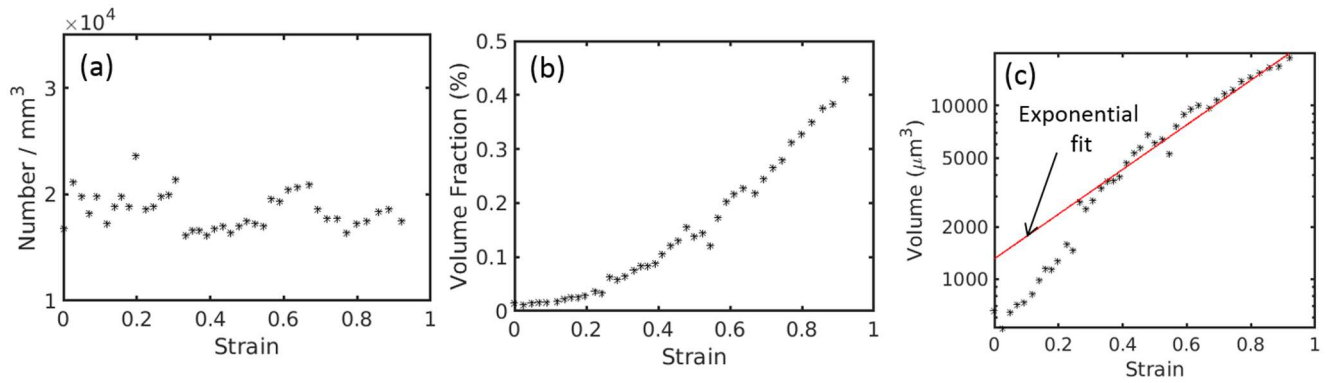


Figure 4.6 Average evolution of cavity statistics with strain (a) number density (b) volume fraction (c) total cavity volume.

Traditionally inferences for the cavity growth mechanisms were drawn from the volume or volume fraction versus strain data. Since it is known that under plasticity volume varies exponentially with strain:

$$\frac{dV}{d\varepsilon} = \eta_d V \quad (4.1)$$

The pre exponential factor of an exponential fit of volume versus strain plot was used as the factor for comparison between experiments and models. [104,145]. Theoretically η_d is a factor of the strain rate sensitivity (m). An additional factor for grain boundary sliding: k_{gbs} is added to account for the superplasticity (varies from 0 to 1, 1 indicating freely sliding grain). It is given by:

$$\eta_d = \frac{3}{2} \frac{m+1}{m} \sinh \left(\frac{2(2-m)}{3(2+m)} (1 + k_{gbs}) \right) \quad (4.2)$$

For the present case since m is 0.8 (estimated from the strain rate jump test) hence the η_d would vary between 1 and 2 for k_{gbs} varying between 0 and 1. Experimentally the pre-exponential from the exponential fit in Figure 4.6 (c) corresponds to a value of 2.96, which is higher than 2. Therefore this estimation shows the limit of such macro analysis of damage for understanding damage mechanisms.

Figure 4.7 (a) shows a 2D transverse slice from LR volume of sample strained at 0.9 strain where very limited view of cavity is possible while the red box in this figure marks the approximate dimension of the region that is viewed in a single HR volume (Figure 4.7 b). Four such HR volumes were acquired for each step of acquisition. Further analysing the 3D HR volume in Figure 4.7 (b) (cavities shown in red and intermetallics in green) it can be seen that unlike the Al-Cu alloy analysed in the previous chapter, sample show no preferential elongation of cavities in the tensile direction.

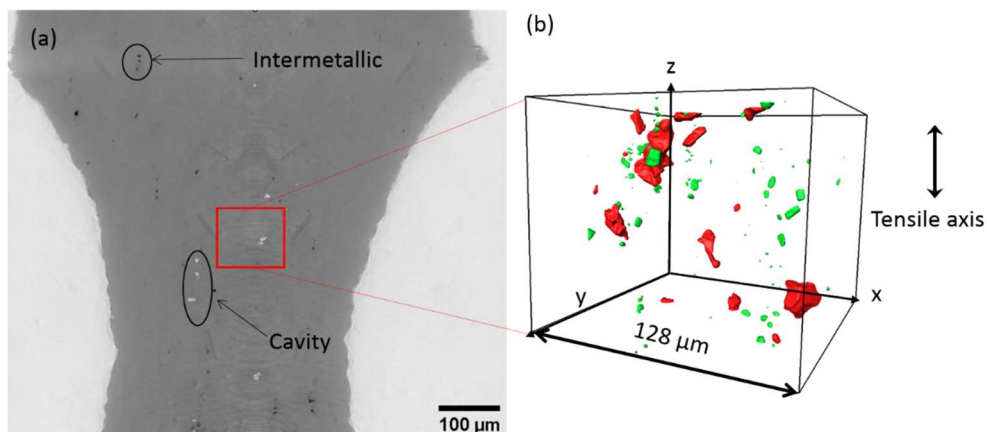


Figure 4.7 (a) Transverse 2D slice from LR volume (pixel size 645 nm) at strain of 0.9. The red box presents the approximate dimension which is probed in a single HR volume (pixel size 100 nm, cavities are in white and intermetallics in black). (b) 3D rendered volume showing cavities and intermetallics in one high resolution (HR) volume imaged at strain of 0.9 (cavities are in red and intermetallics in green).

Further it was noted that the cavities took complex shapes during deformation. Since *in situ* analysis is the key novelty of this thesis the following sections will focus on dissecting the pathway of evolution of cavities into these complex shapes.

4.5 Growth of cavities: individually tracked cavity measurements

In order to probe the evolution of damage during high temperature deformation in superplastic regime **a total of 30 cavities were tracked** from the last scan acquired towards the beginning, using reverse tracking. As already mentioned, since the ROI probed was not constant many of these 30 cavities (27 pre-existing + 3 nucleated) could not be tracked over the entire test, results from strains at which cavities are present in ROI have been presented. Apart from the 30 cavities, many other cavities that moved in and out of the ROI, could not be tracked for a considerable deformation were therefore excluded. Growth measurements of these 30 cavities are further presented in the following section.

This section has been broadly divided into two parts. The first part deals with classifying the evolution of shapes seen in the cavities, and later conclusion about the possible mechanisms responsible for these evolutions will be determined. The second part will be dedicated to comparison of experimental volumetric growth data of cavities with relevant growth models.

4.5.1 Growth classifications and mechanism

On analysing the evolution of shapes of cavities during deformation it was seen that cavities showed different patterns of growth. After carefully analysing these growth patterns seen in several cavities and in the interest of understanding damage mechanism based on cavity shapes, the evolution of damage has been classified into 4 types.

Before proceeding, a few things must be clarified:

- ✓ This classification is purely based on evolution of shapes of cavity. This has been done in order to decipher the evolution of highly complex shapes, from small equiaxed pre-existing cavities. These classification will be referred as **evolution types**.
- ✓ Based on the shapes of each evolution type, preliminary conclusion about responsible **growth mechanism** (diffusion, grain boundary sliding etc.) will be made.

- ✓ It should be noted that during the deformation a cavity evolves by a succession of different evolution types and different growth mechanisms.

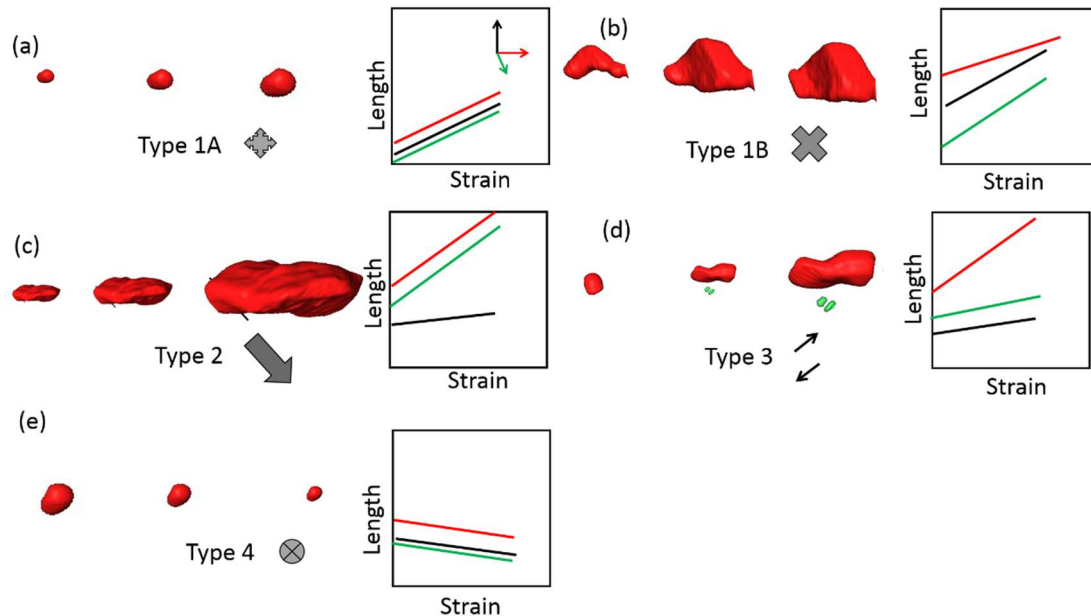


Figure 4.8 Schematic showing typical examples of evolution of cavity shape for (a) type 1A (b) type 1B (c) type 2 (d) type 3 (e) type 4 along with assigned symbols. Accompanied by a corresponding plot showing evolution of lengths with strain, along the principle growth directions. Orientation of the 3 directions is on the basis of coordinate system shown on top right corner of (a).

The classification of evolution type is the following:

- Type 1A evolution is where the growth is equal in all directions such that the volumetric increase is not accompanied by any change in shape of the cavity (see Figure 4.8 a).
- Type 1B evolution is similar to type 1A in the sense that the cavity grows multi-directionally. However the difference lies the fact that growth is not uniform in all directions (see Figure 4.8 b). Following variations were observed in this evolution:
 - Growth concentrated in a small portion of the cavity
 - Growth preferential in certain directions (not the direction of tensile loading)
 - Growth restricted in a certain direction

Nevertheless, this type of growth ensures that cavities are fairly equiaxed but faceted.

- Type 2 corresponds to growth which is considerably accelerated in two dimensions as compared to the third, resulting in a flat or planar cavity (see Figure 4.8 c).
- Type 3 evolution corresponds to a very specific pattern of growth where growth is highly accelerated in one dimension accompanied by the formation of two equally opposite parts (see Figure 4.8 d).
- Type 4 pertains to the cases where instead of growth there is a decrease in volume of the cavity, this decrease may or may not involve a change in shape of the cavity (see Figure 4.8 e).

Table 4.1 Summary of definition of different evolution types.

| Type | Explanation | Symbol |
|---------|--|---|
| Type 1A | Equal growth in all direction with no change in shape |  |
| Type 1B | Multidirectional growth, but not equal in all directions resulting in equiaxed, faceted cavities |  |
| Type 2 | Accelerated growth in two dimensions leading to flat planar features |  |
| Type 3 | Accelerated growth in one dimension developing as asymmetric crack tip, in two diametrically opposite directions |  |
| Type 4 | Decrease in volume, may or may not be accompanied by change in shape |  |

Table 4.1 lists a summary of explanation of these different evolution types along with corresponding symbol that has been assigned to each type. Keeping these classifications (and symbols) in mind the growth of cavities seen during the high temperature deformation under superplastic regime is examined through some representative examples.

We begin by examining evolution patterns of cavities using 3D rendered view of evolution of cavities with strain (Figure 4.9, Figure 4.12, Figure 4.14 and Figure

4.16). A constant orientation is chosen for 3D view at each strain except for the last scan which is presented with two different orientations for better comprehension of the 3 dimensional shape of the cavity. The two orientations are specified using the x, y and z axis bars in last 2 rendered volumes. It should be noted that the 2D view presented are chosen ensuring the view shows the maximum growth directions, and most important features of cavity, this become important when analysing such shapes and hence has been taken in mind for all 2D views presented in this chapter. To further quantify growth the dimensions of the cavity along a bounding box was also studied (dimension L, W and D, Figure 4.10, Figure 4.13, Figure 4.15 and Figure 4.17) such that its orientation corresponds to the principal directions of growth. A unique orientation of bounding box was chosen for measurement of each cavity a schematic of this has been presented with the L, W, D parameters. However it should be remembered that identifying principle growth directions for all cavities is not straightforward as this often changes during the deformation.

4.5.1.1 Type 1A and 1B

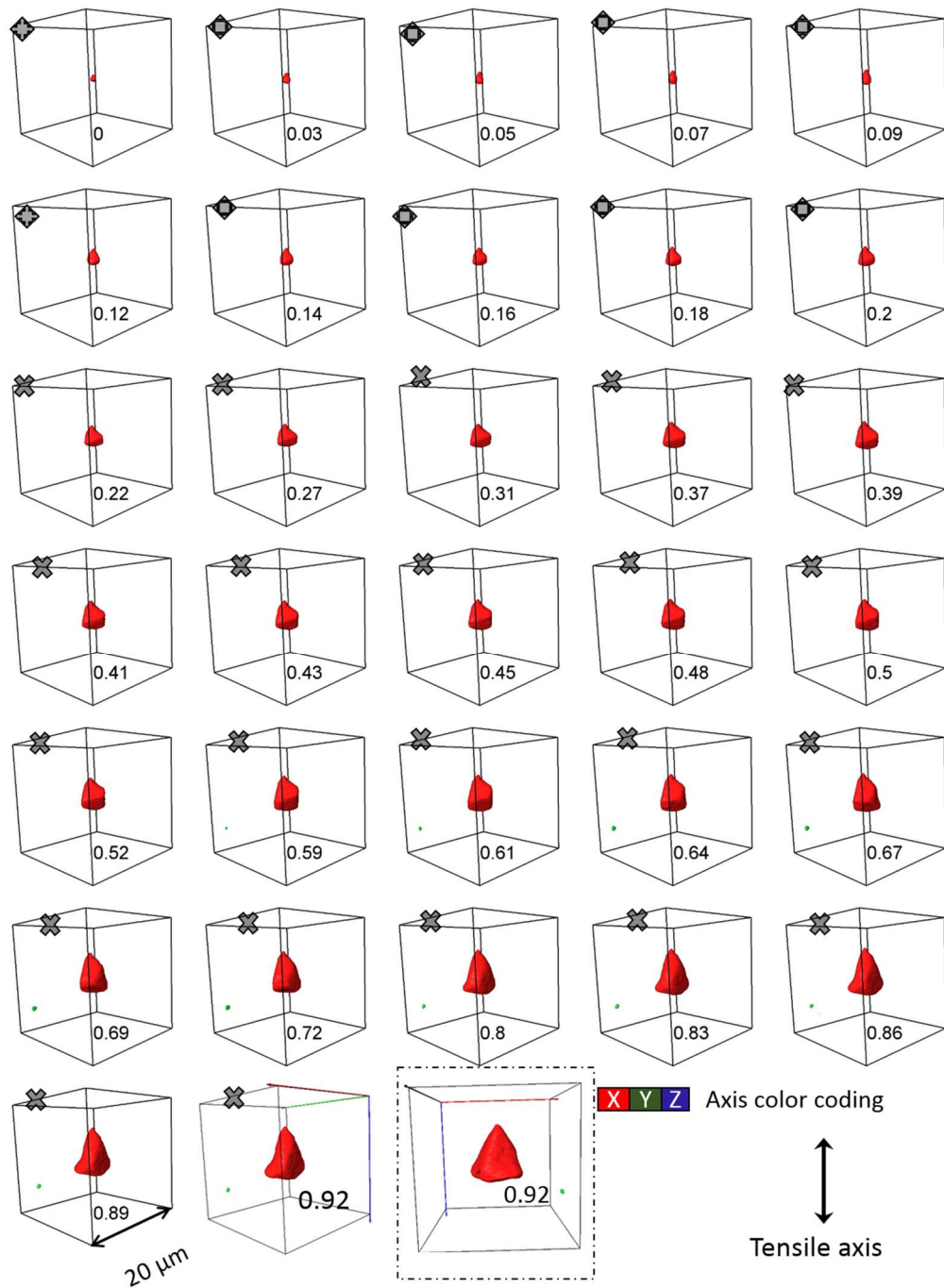


Figure 4.9 3D rendered volumes showing evolution of a cavity with strain (marked at the bottom of each box) in sample. Type of evolution has been marked using symbols at top left corner (see Table 4.1 for reference). A different view of the cavity at the last scan is also shown, highlighted by a box for better comprehension of the 3 dimensional shape of the cavity (cavities are in red and intermetallics in green).

Cavity in Figure 4.9, had an equiaxed shape at the beginning. As the sample strains the cavity grows multi-directionally with equal growth in all directions hence type 1A evolution is seen until a strain of 0.2. Figure 4.10 shows change in L, W and D

dimension of the cavity with strain. The plot shows that dimensions increase at equal rate in all three directions upto a strain of 0.2 while growth predominates in the Land W dimension for a larger strains. This brings on a change in shape of the cavity hence the evolution is classified as type 1B from strain of 0.2 to 0.9.

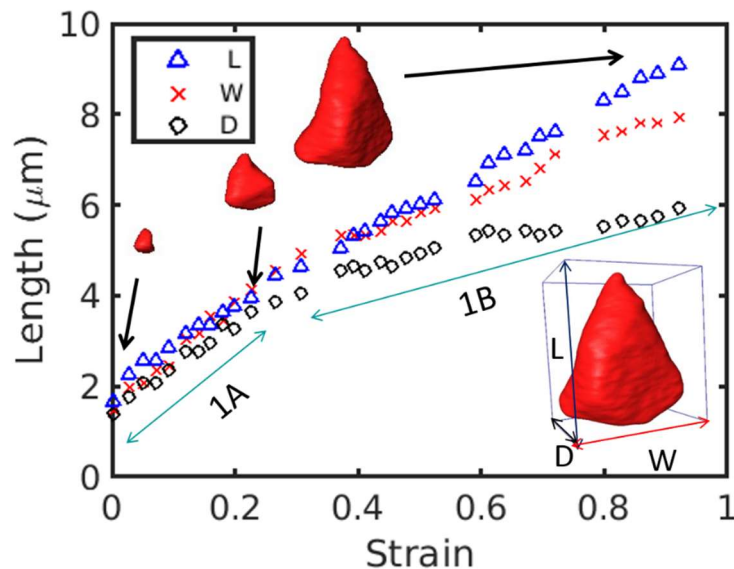


Figure 4.10 Evolution of length of cavity (shown in Figure 4.9) along L, W, D dimension (represented by bounding box in right bottom) with strain. The type of evolutions have also been marked along with 3D rendered view of cavities in different evolution regimes.

Growth mechanism type 1A: This mechanism of growth involved nearly equal growth in all dimensions and was accompanied by no visible shape changes in the cavity. It is known that if a cavity grows by diffusion then the growth is expected to be equal in all directions, and hence such growth is expected to lead to no change in shape of a cavity, provided surface diffusion is comparable to grain boundary diffusion rate [146].

Since this mechanism was generally seen in cavities with small volumes (less than $30 \mu\text{m}^3$ volume or $2 \mu\text{m}$ equivalent radius) any changes in shape arising as a result of possible difference between grain boundary and surface diffusion rate was not comprehensible at this resolution. Hence type 1A evolution was concluded to be diffusion driven. This could be lattice or grain boundary depending on the position of the cavity. Cavities present on grain boundaries are expected to grow predominantly by grain boundary diffusivity, since grain boundary diffusivity is significantly higher

than lattice diffusivity for most metal (also true for pure Mg). While cavities lying inside a grain can only grow via lattice diffusion. In the present case however due to limitations of the tomography technique it cannot be known if cavities were present inside grain or on grain boundary and consequently it cannot be determined precisely which diffusion: lattice or grain boundary, was driving cavity growth during type 1A evolution.

Growth mechanism type 1B: This was the most common evolution type visible during the deformation. It involved multidimensional growth that was unequal along different directions. However no preference of growth along the tensile axis or any particular direction was noted.

It is known that plasticity based growth of cavities leads to preferential growth of cavities along the direction of applied stress. This results in elongated cavities lined up along the tensile axis. Since no such preference to growth along the tensile axis was seen (Figure 4.7 b), plasticity due to uniaxial tensile stress was ruled out as a dominant growth mechanism.

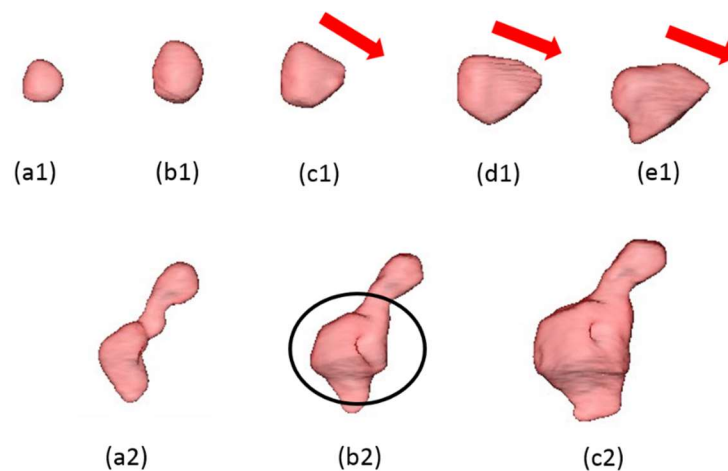


Figure 4.11 Schematic illustration showing evolution of cavities during high temperature deformation, affected by grain boundary sliding.

The multidimensionality of the growth showed sign of growth driven by diffusion. However, there were certainly other factors influencing the growth which led to the complex shapes of cavities. It was seen that sometimes cavity growth was oriented in a certain direction, while at other times there was preferential growth in small part of the cavity.

This is illustrated through few examples showing evolution of cavities schematically. In Figure 4.11 (a1 to e1), between a1 and b1 cavity grows multi-directionally, but later from b1 onwards it appears to grow in a direction indicated by red arrow, possibly under a local stress (remember that this is not the direction of tensile stress). In Figure 4.11 (a2 to c2) growth was concentrated in a small part of the cavity (region encircled in Figure 4.11 b2) while being minimal in the rest of the cavity.

Moreover, each cavity followed a different direction and no specific pattern could be established. Such patterns of growth indicated that local factors or stress were driving the growth. Since the material is expected to show grain boundary sliding, it was concluded that the local factor affecting growth was in fact sliding of grain boundaries.

Hence by examining the shape of cavities growing by type 1B it was concluded that diffusion along with grain boundary sliding were responsible for such evolution.

4.5.1.2 Type 2

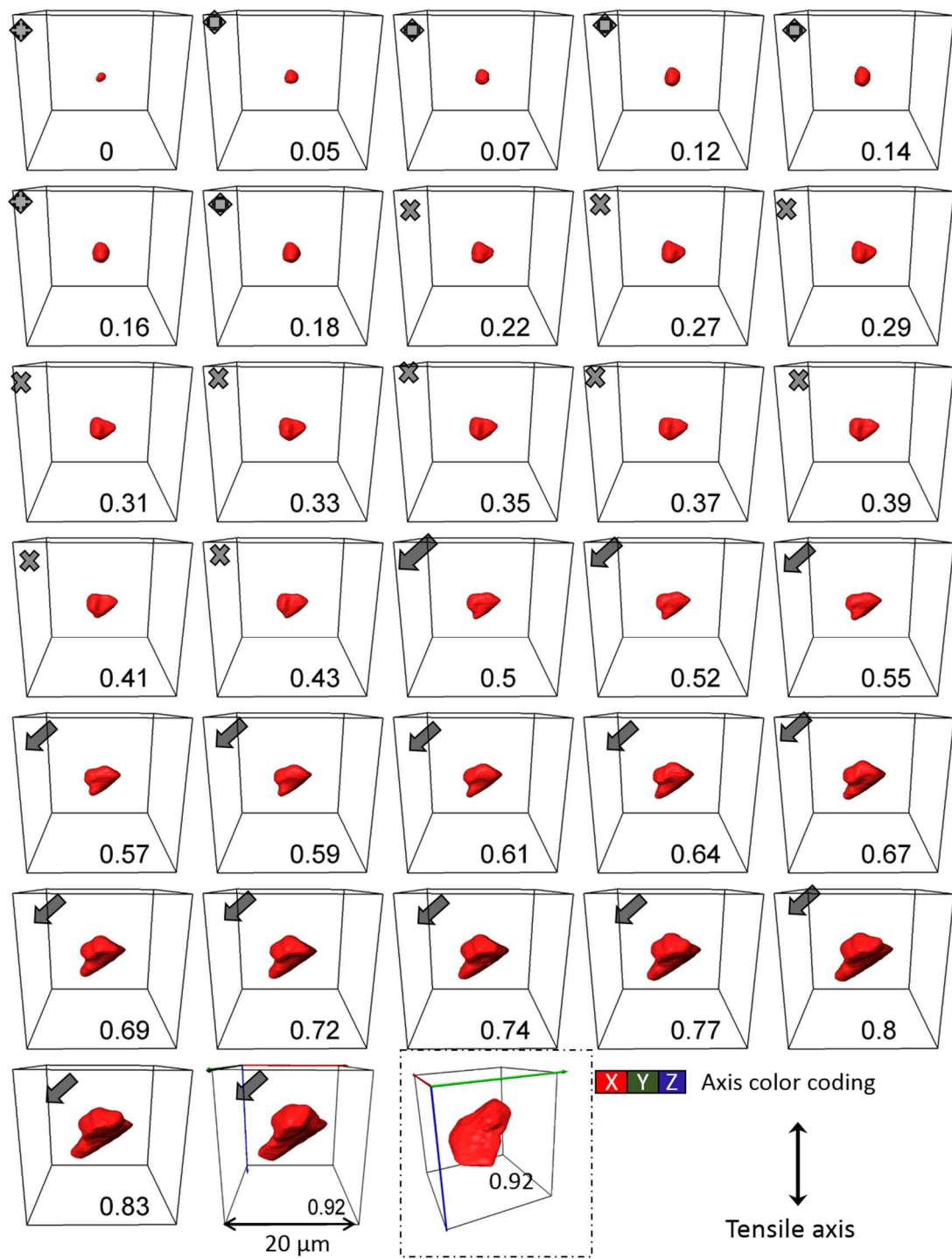


Figure 4.12 3D rendered volumes showing evolution of a cavity with strain, (marked at the bottom of each box) in sample. Type of evolution has been marked using symbols at top left corner (see Table 4.1 for reference). A different view of the cavity at the last scan has been also shown, highlighted by a box for better comprehension of the 3 dimensional shape of the cavity (cavities are in red).

Figure 4.12 presents a more complex case of growth. At the beginning a small cavity grows by type 1A up to a strain of 0.18 showing no shape changes. This is then followed by a multidimensional growth which is preferentially occurring in a particular direction hence type 1B evolution is seen upto strain of 0.43. This is swiftly followed by the cavity developing a distinctly flat or planar shape taking on type 2 growth. Examining these transitions quantitatively in Figure 4.13, type 1A can be seen through equal growth rate of all 3 dimensions followed by growth in all three dimensions but at different rates, which is typical of type 1B. After a strain of 0.5 however this changes into a growth highly accelerated along L and W, as compared to D showing a signature for type 2 evolution.

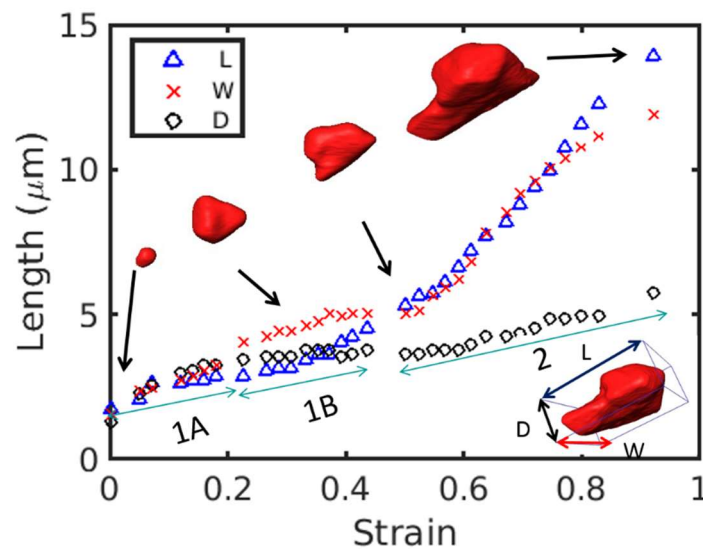


Figure 4.13 Evolution of length of cavity (shown in Figure 4.12) along L, W, D dimension (represented by bounding box in right bottom) with strain. The type of evolutions have also been marked along with 3D rendered view of cavities in different evolution regimes.

Growth mechanism type 2: It has been reported that normal stress gradient developed due to grain boundary sliding can lead to crack propagation along grain boundary [145] acting as a accommodating mechanism during relative sliding and rotation of grains. And since type 2 evolution showed a two dimensional planar growth, this was the most likely driving force for such evolution.

4.5.1.3 Type 3

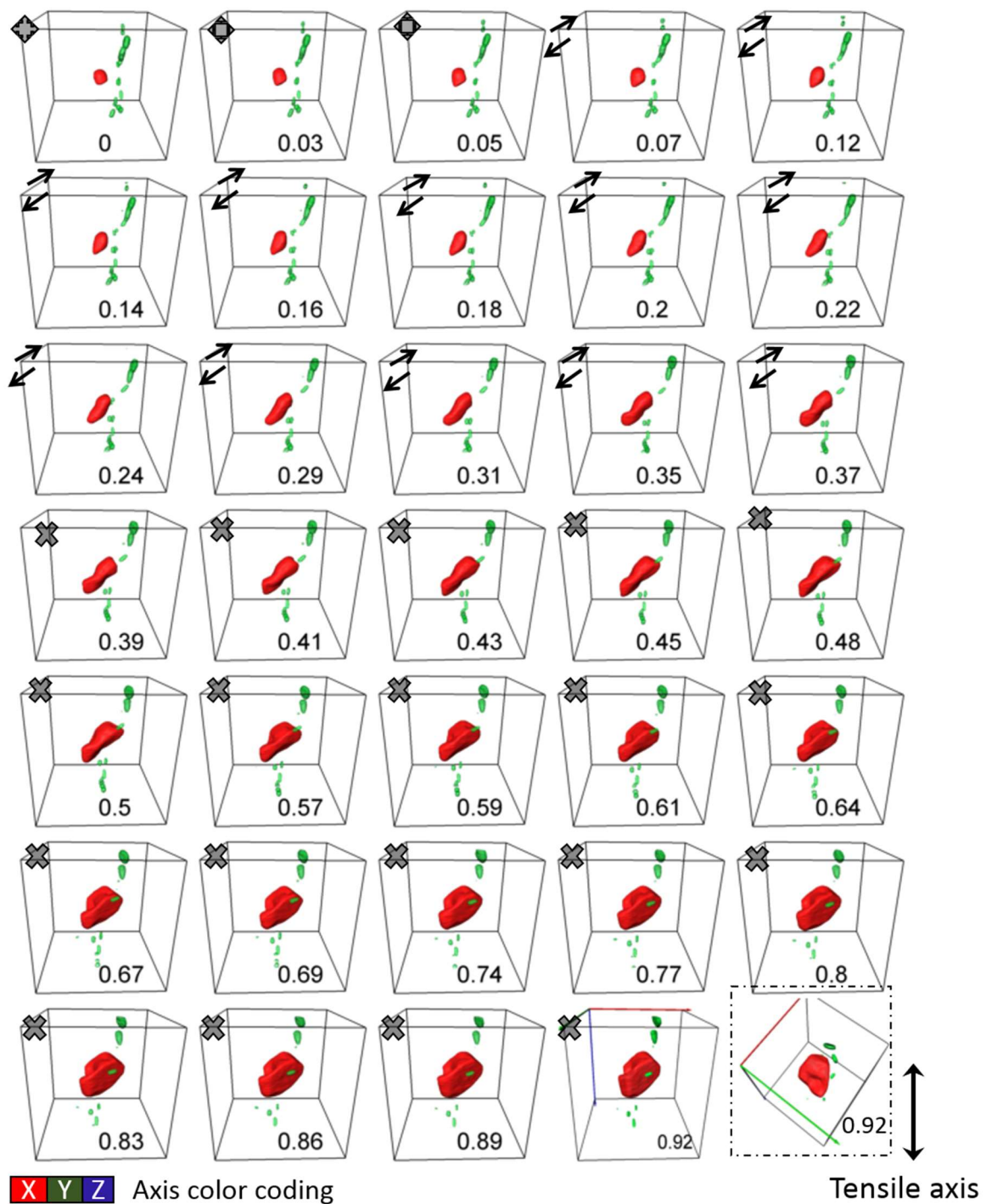


Figure 4.14 3D rendered volumes showing evolution of a cavity with strain, (marked at the bottom of each box) in sample. Type of evolution has been marked using symbols at top left corner see Table 4.1 for reference. A different view of the cavity at the last scan has been also shown, highlighted by a box better comprehension of the 3 dimensional shape of the cavity. (cavities are in red and intermetallics in green).

Another example of a highly unique growth pattern is shown in Figure 4.14. In the 3D rendered volumes it can be seen that after a brief period of homogenous growth the cavity starts preferentially growing in one direction accompanied by an equally opposite growth, showing typical signature for type 3 growth. Quantitatively this can be seen as an accelerated growth along the L dimension in Figure 4.15. After a strain of 0.37 growth picks up along W eventually stopping along L. Since the growth proceeds multi dimensionally (along W and D) at different rates it has been classified as type 1B growth.

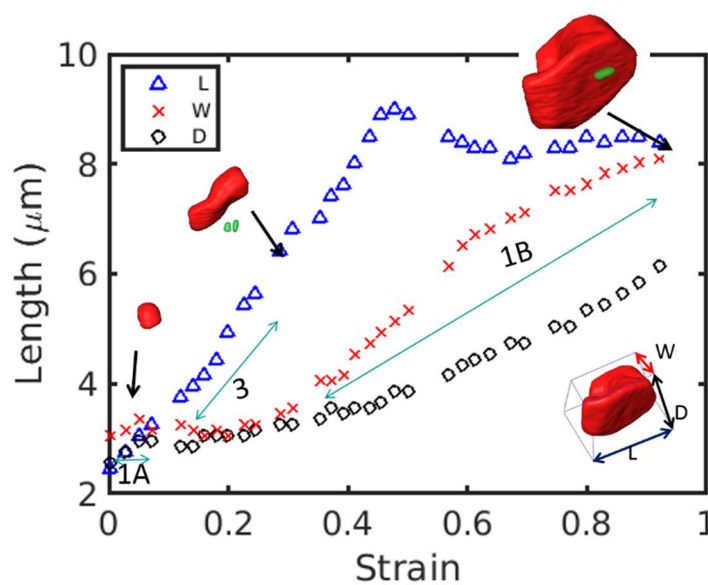


Figure 4.15 Evolution of length of cavity (shown in Figure 4.14) along L, W, D dimension (represented by bounding box in right bottom) with strain. The type of evolutions have also been marked along with 3D rendered view of cavities in different evolution regimes.

Growth mechanism type 3: Such elongation of cavities has been attributed to growth of cavities on sliding grain boundaries [64]. Under condition where surface diffusion is slow such growth is expected to be directly proportional to grain boundary sliding rate.

4.5.1.4 Type 4

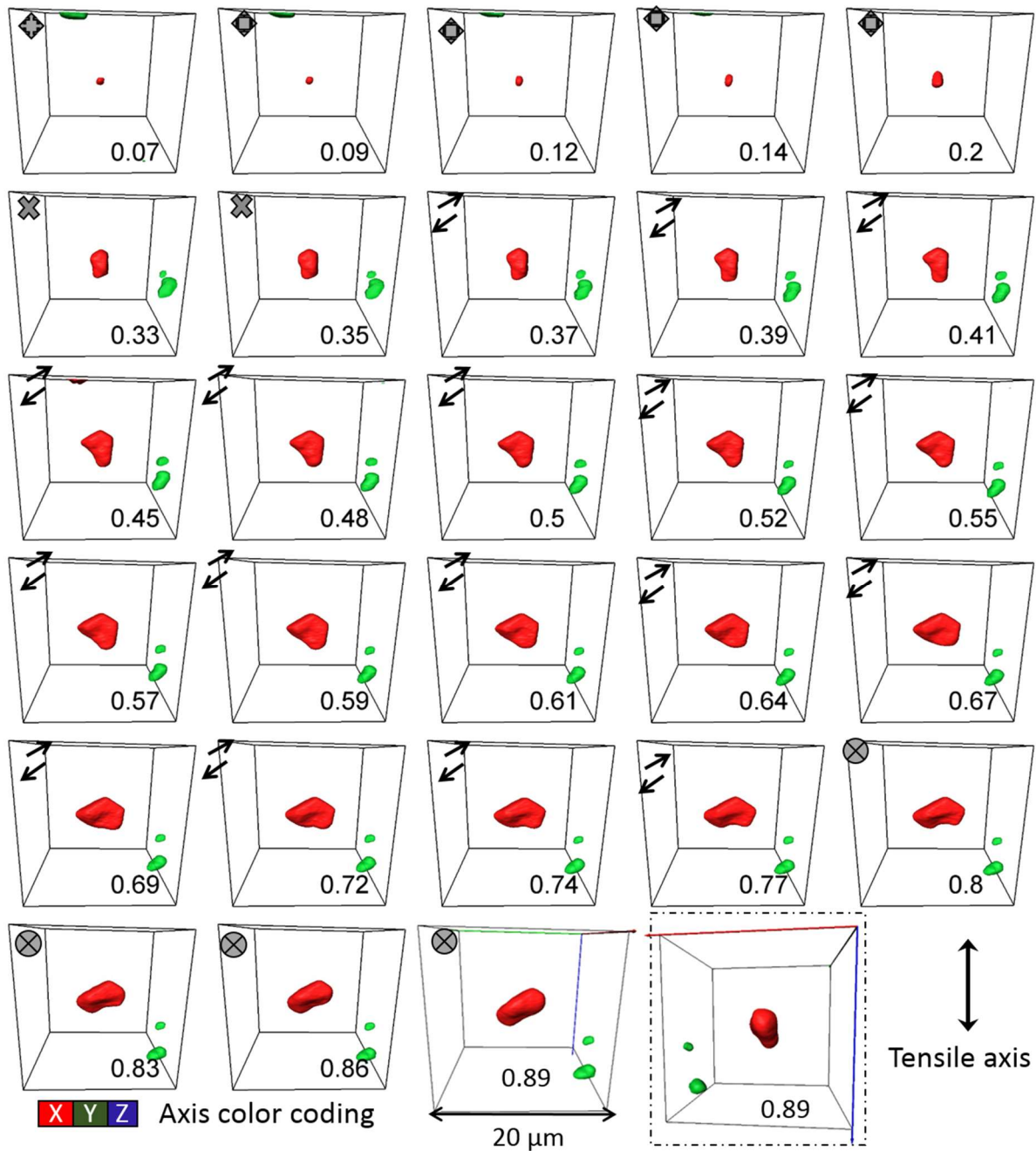


Figure 4.16 3D rendered volumes showing evolution of a cavity with strain, (marked at the bottom of each box) in sample. Type of evolution has been marked using symbols at top left corner see Table 4.1 for reference. A different view of the cavity at the last scan has been also shown, highlighted by a box for better comprehension of the 3 dimensional shape of the cavity (cavities are in red and intermetallics in green).

Lastly we examine a case through Figure 4.16 which begins with a regular type 1A and 1B growth proceeding into a type 3 growth. This type 3 growth initially manifests as an increase in growth rate along L (Figure 4.17) however after a strain of nearly

0.6, L grows at the expense of shrinkage along W such that after a strain of 0.8 a decrease in volume or type 4 evolution is seen.

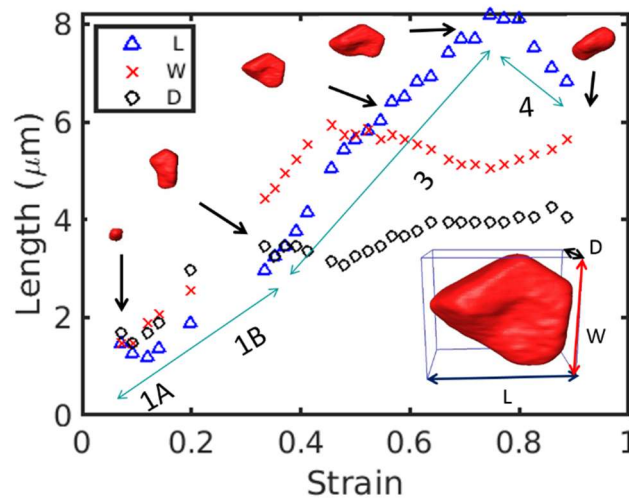


Figure 4.17 Evolution of length of cavity (shown in Figure 4.16) along L, W, D dimension (represented by bounding box in right bottom) with strain. The type of evolutions have also been marked along with 3D rendered view of cavities in different evolution regimes.

Shrinkage mechanism type 4:

Since no external compressive forces were applied on the sample, shrinkage of cavities was not expected during deformation. On examination of shapes during shrinkage, it was seen the big and complex shapes cavities, showed a tendency to transform into simpler shapes with lower surface area, this was accompanied by reduction in volume. While the small and equiaxed cavities, showed no change in shape during shrinkage. It is known that only when applied tensile stress is greater than sintering stress, cavities grow. In absence of enough tensile stress, sintering of cavity would occur. In the present case shrinkage of cavities is attributed to such diffusion based sintering due to absence of enough external stress (due to uncertain local factors). Such self-healing tendencies have been reported in high temperature deformation when alternate annealing / straining of superplastic Al alloys was carried out at high temperatures [5].

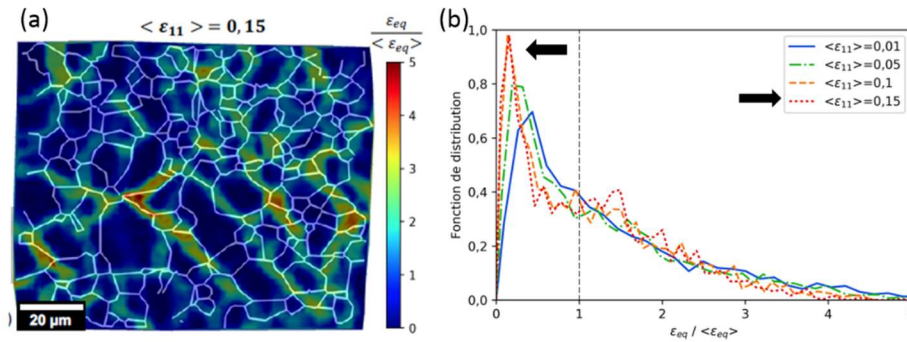


Figure 4.18 Normalized deformation fields or $\mathcal{E}_{eq} / \langle \mathcal{E}_{eq} \rangle$ strain component at 573 K at $\langle \mathcal{E}_{eq} \rangle = 0.15$. (b) Equivalent normalised deformation distribution function at 573 K and for different states of deformation. Work of T. Dessolier [114]

Inhomogeneity in strain in the sample, during deformation under superplasticity has in fact been reported by T. Dessolier [114] in his PhD thesis under similar conditions. Figure 4.18 (a) shows the deformation field of equivalent strain in an AZ31 sample (from the same rolled sheet as the current sample) at a strain of 0.15 and temperature of 573 K. The complementary histogram of the probability distribution of the same is shown in Figure 4.18 (b), at different strains (the strain corresponding to (a) has been indicated by black arrow). Strain inhomogeneity is distinctly visible, in the cross section. A considerable section of the sample is seen to experience strains much lower than the equivalent strain and additionally a big portion of the sample shows strain concentration upto five times the equivalent strain. These surface observations were made at a lower temperature and strain, as compared to the current sample under study however they are expected to be relevant even in the current case.

These observations provide further clarification for the fact that some cavities experience near to zero stress resulting in their shrinkage.

4.5.2 Predominant evolution type

In order to study the predominant evolution type the probability of evolution by each type was plotted with strain in Figure 4.19. While until 0.3 strain type 1A was the predominant evolution type, during further deformation type 1B was the most prevalent type of evolution. Among the rest type 2 showed prominence at no specific strain levels while type 3 mostly occurred during low strains (0.15 - 0.25) and type 4 mostly during high strain (0.8-0.9).

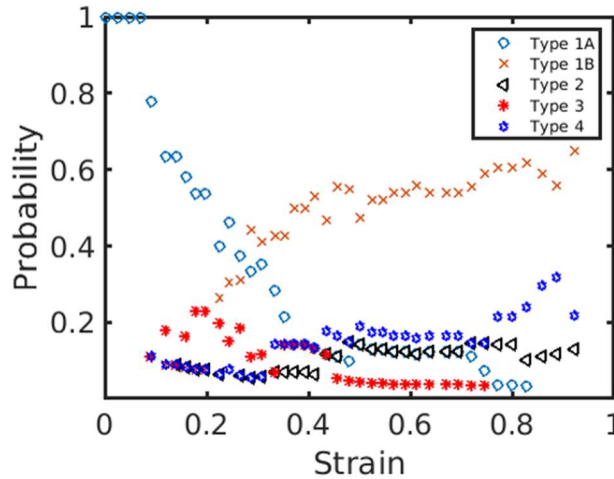


Figure 4.19 Plot showing probability of different type of evolution mechanisms with strain.

Figure 4.20 shows the pathway of different types of evolution, shown for the 30 tracked cavities with strain. Absence of data for certain strain values is because the cavity was no longer in ROI and so could not be studied. Cavities generally grow by more than one type of evolution mechanism. Type 1B is the most frequent evolution type and is seen during evolution of nearly all cavities. Type 2 and 3 are less commonly observed. Type 4 evolution on the other hand is frequent. It has been seen that sometimes cavities show an increase in volume, which is then proceeded by shrinkage. While sometimes cavities shrink throughout deformation (for all recorded scans).

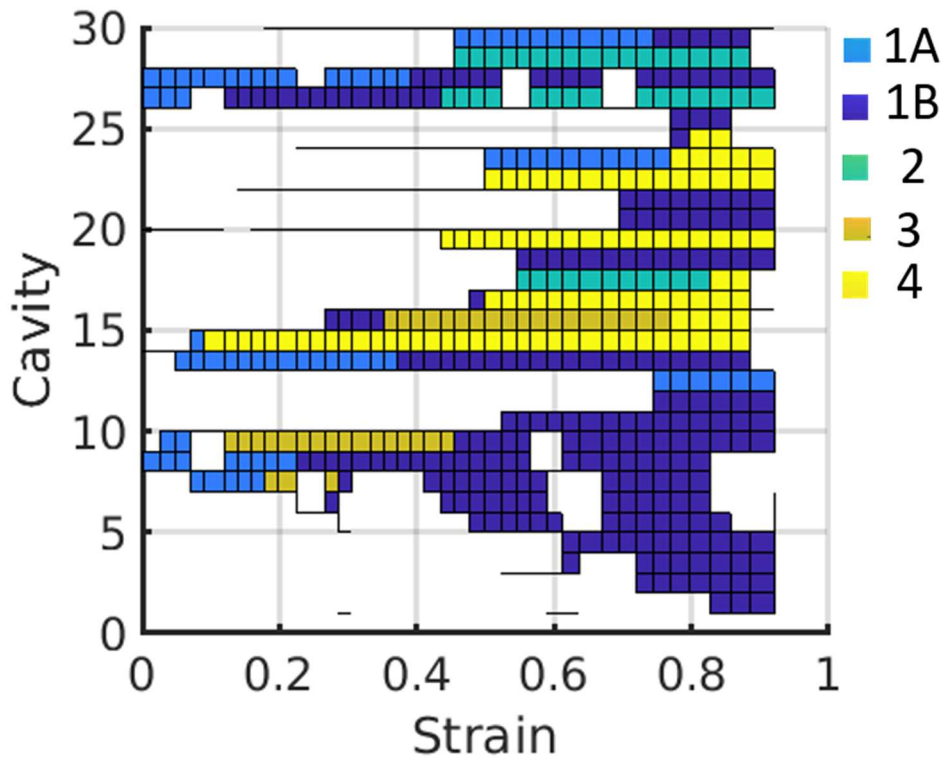


Figure 4.20 Plot showing pathway of different types of evolution, shown for the 30 tracked cavities with strain.

Here it should be reminded that this sample is expected to show a strain rate sensitivity of nearly 0.8. It is known that sample showing a strain rate sensitivity of 1 (or stress exponent of 1) deform primarily through diffusion while those with 0.5 sensitivity (or stress exponent of 2) deform primarily via grain boundary sliding (see Table 1.1, remember $m = 1/n$). Any values in between are regions where an amalgam of the two deformation mechanisms operate. In the present case type 1B is seen as the predominant evolution mechanism for cavity growth and this evolution type is expected to be driven by a combination of diffusion and grain boundary sliding. Hence it can be seen that cavity deformation is in accordance with the expected mechanism for sample deformation.

4.5.3 Volumetric growth rate: comparison with models

In this section the experimental volumetric growth data will be compared to relevant growth models. First generic comparison of experimental data from all cavities will be made, to establish suitability of different models. This will then be followed by comparing growth rate observed for different evolution types with appropriate models.

4.5.3.1 General comparison with all tracked cavities

From the shape analysis of different evolution types seen during high temperature deformation, two key mechanisms responsible for cavity growth were: diffusion and grain boundary sliding. In this section models defining these mechanisms will be compared with experimental data. Growth rate from all 30 tracked cavities will be compared together.

4.5.3.1.1 Classical diffusional growth models

Shape analysis indicated diffusion to be affecting type 1A and 1B growth and from Figure 4.19 it can be seen that type 1B is a highly dominant evolution type in the present case. There are three major diffusional growth mechanisms that could be applicable in the present case:

1. Grain boundary diffusion: see section 1.2.2.1 and equation (1.14)
2. Lattice diffusion: see section 1.2.2.1 and equation (1.16)
3. Superplastic diffusion: see section 1.2.2.3 and equation(1.21)

All these models are applicable in the present case. Between grain boundary and lattice diffusion however the applicability depends on the position of cavity. And it is unknown whether a cavity lies on a grain boundary due to limitation of the tomography technique. To investigate this the cavity size is compared with the grain size using a SEM micrograph (superimposed by a micro grid) with the grain boundaries highlighted in Figure 4.21 (a). The micrograph is of an AZ31 sample, derived from the same rolled sheet from which the current sample under examination was machined, and is hence a representative microstructure. The red box in this indicates a 20 X 20 μm^2 box. A cropped 2D slice of the same dimension obtained from HR tomography of the sample (strain 0.9) under examination is presented in Figure 4.21 (b). Comparing the two images it is safe to assume that cavities greater than 3 μm radius (length nearly 6 μm) are very likely to lie on a grain boundary. Roughly cavities with length equivalent to a facet size of the grain, which is nearly half the grain diameter ($12/2 = 6 \mu\text{m}$) is expected to lie on a grain boundary.

Additionally, the shape evolution patterns associated with type 1B also show influence due to grain boundary sliding combined with diffusion. This further provides indication of proximity of cavities with grain boundaries.

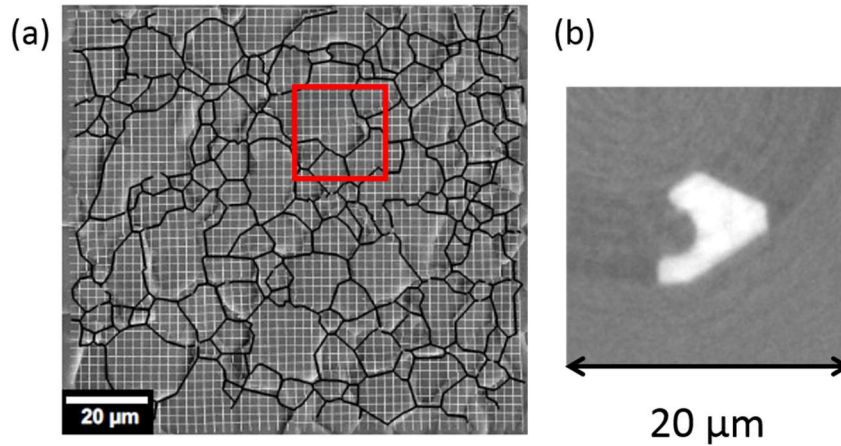


Figure 4.21 (a) SEM micrograph of a AZ31 sample with an imposed micro grid (b) a cropped 2D slice showing cavity in a matrix , work of T. Dessolier [114]. The red box in (a) indicates the size of the cropped slice shown in (b).

With this information the applicability of the different models is tested. Since the geometry for which the classical models are proposed are different from the current case, appropriate adjustments are made beforehand.

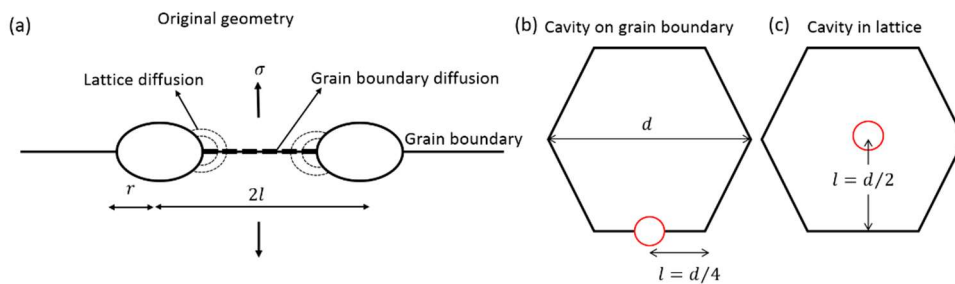


Figure 4.22 Schematic illustration of geometry of cavity (a) geometry for classical model. Geometry modifications used while applying (a) grain boundary diffusion model (b) lattice diffusion model.

The lattice and grain boundary models were defined for several cavities of radius r lying on a transverse grain boundary, with an inter cavity distance of $2l$ and effective diffusion flux (of vacancies generated due to tensile stress on transverse boundary) becoming zero at distance l , shown schematically in Figure 4.22 (a) (see section 1.2.2.1 for details). In the current sample however the inter cavity distance (average $14 \mu\text{m}$) was found to be greater than the facet size of the grain (nearly $6 \mu\text{m}$). Note that the facet size is taken as half the average grain size, assuming the grain geometry to be that of a regular hexagon. Hence if the cavities were present on grain

boundary, not more than one cavity were expected to be present on a grain boundary facet. Therefore, the distance l at which the diffusion flux became zero was taken to be equal to half the facet size (see Figure 4.22 (b) for schematic illustration). Additionally, it was also possible that the cavities were present inside the lattice, (and not on the grain boundary). For such cases the geometry is represented in Figure 4.22 c. If the cavity is located in the centre of the grain, the diffusion distance l is taken as nearly half of grain size.

Taking into account these modifications, the volumetric growth rate from the three models are plotted (in Figure 4.23) for a range of radius considering parameters listed in Table 4.2.

Table 4.2 Parametrs used for plotting volumetric growth rate of cavities for different diffsuion based models

| Variable | Value | Reference |
|---|-------------------------------------|------------------|
| Ω (m ³) | 2.33×10^{-28} | |
| δD_{gb} (m ³ s ⁻¹) | $5 \times 10^{-12} \exp(-92000/RT)$ | [147] |
| D_l (m ² s ⁻¹) | $1 \times 10^{-4} \exp(-135000/RT)$ | [147] |
| T (K) | 673 | |
| σ (MPa) | 3.2 | |
| γ (Jm ⁻²) | 0.78 | [148] |
| α_r | 0.8 | |
| ψ | 70 ° | |
| $\dot{\epsilon}$ (s ⁻¹) | 6.6×10^{-5} | |
| f_s (m) | 6×10^{-6} | |
| d (m) | 12×10^{-6} | |

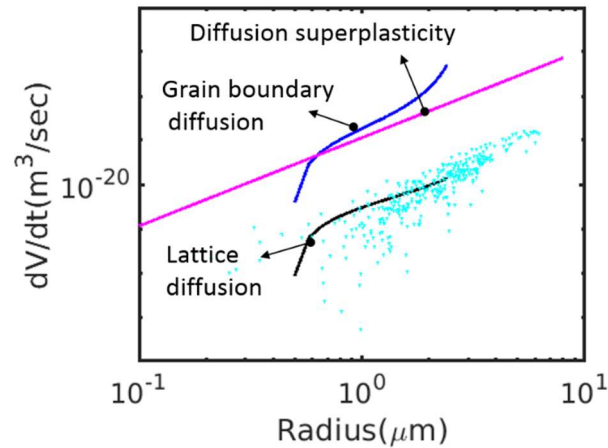


Figure 4.23 Plot showing volumetric growth rate as per grain boundary diffusion, lattice diffusion and diffusion superplasticity, along with experimental data (cyan markers)

From Figure 4.23 it can be seen that grain boundary diffusion is fastest in comparison to the other two. In the absence of experimental data, it would be concluded that grain boundary diffusion is the dominant growth mechanisms. However on comparing the models with the experimental volumetric growth rates (indicated by cyan markers in Figure 4.23), it can be clearly seen that both the grain boundary diffusion and diffusion based superplasticity models overestimate the growth rates by nearly two orders of magnitude. Similar over estimation has been reported in other experimental investigations [10]. The growth rate by lattice diffusivity does not over predict the growth rates, however it is very unlikely that all the cavities tracked were present inside the grain and were driven by solely by lattice diffusion. The two-fold reason for this based on comparable cavity radius and grain size and grain boundary sliding effecting growth patterns of cavities have already been indicated above.

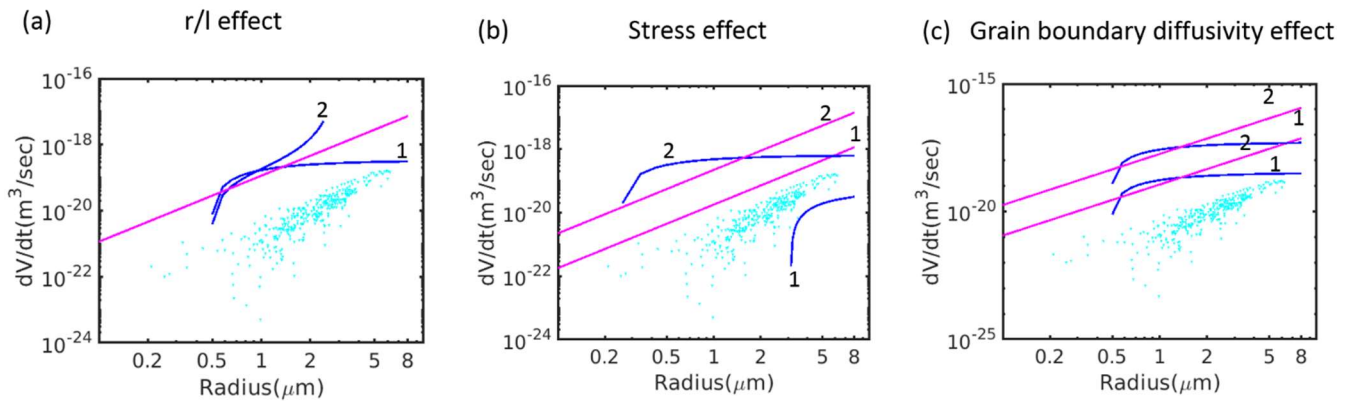


Figure 4.24 Effect of (a) r/l (b) stress (c) grain boundary diffusivity on volumetric growth rate based on grain boundary diffusion, lattice diffusion and diffusion superplasticity models. The parameters variations relevant to the plots are listed in Table 4.3.

Table 4.3 Table showing the minimum and maximum value of different variables used in plots Figure 4.24 (a) (b) and (c)

| Variable | Value used for 1 | Value used for 2 |
|---------------------------------|--|--|
| $\omega^2 = (r/l)^2$ | 0.1 | Real |
| σ (MPa) | 0.5 MPa | 6.2 MPa |
| δD_{gb} (m^3s^{-1}) | $5 \times 10^{-12} \exp(-92000/RT)$ [148] | $8 \times 10^{-10} \exp(-105000/RT)$ [149] |

Following this observation the possible reasons for the over predictions by the two models were examined. For this the effect of different parameters used in the two models (listed in Table 4.2) on the growth rate was tested. It was found that varying stress, grain boundary diffusivity and $\omega = r/l$ parameters affected the growth rates considerably. Figure 4.24 shows the effect of each of these parameters. Table 4.3 lists the range of values used for each variable. The logic for choosing these ranges is explained further. Assuming ω^2 as a constant, often equal to 0.1 is usual practice [95]. This is because diffusion is generally relevant during early stages of growth, the increase in radius as compared to the inter cavity spacing is considered to be negligible. This would not necessary be a correct assumption in the present case, as large cavities show indications of diffusion based growth. Hence the change in ω arising due to an increase in radius is also plotted. The stress value has been chosen based of indications of variation in stress seen in sample (this will be detailed in section.4.5.3.2.4.1). While the

diffusivity value has been taken based on two different reported values found in literature for Mg. It should be noted that nearly a difference of an order of magnitude is seen in the two values.

Now examining the effect of each of these variations, in Figure 4.24 (a) it can be seen that using a constant ω value made the lattice and grain boundary growth rates independent of the radius. For Figure 4.24 (b) and (c) ω and other parameters have been kept constant to highlight the contribution of stress and diffusivity values. From the two figures it can be clearly seen that modifying stress and diffusivity values influence the growth rates significantly. It is known that local stress within a polycrystalline sample undergoing grain boundary sliding can vary immensely. Further the grain boundary diffusivity values used for the calculation are those obtained from the activation energy of pure magnesium in Coble creep. This is because no direct measurement of grain boundary diffusivity for AZ31 alloy was found in the literature. Hence variation of these values could be a possible explanation for the fact that the models fail to predict experimental results. But lack of appropriate knowledge makes further comments difficult.

4.5.3.1.2 Constrained diffusion model

Another possible explanation for the failure of the classical models was pointed out by Dyson [56]. He proposed that the classical models are bound to over predict the growth rates, due to their short coming which were explained in section 1.2.2.4. He instead defined a constrained diffusion model. In the present case the sample is a polycrystalline material with fine grain size and so the constraints proposed by him are likely to be present in the sample. Therefore the volumetric growth rate of by the constrained growth model (see equation (1.23)) is plotted in Figure 4.25. The geometry is same as proposed in Figure 4.22 (c) and the relevant parameters used are listed in Table 4.2. It can be seen that this model clearly predicts the growth rates to be at par with experimental values (indicated by cyan markers) in terms of orders of magnitude. Hence we conclude that constraints are in fact present during grain boundary diffusion based growth of cavities.

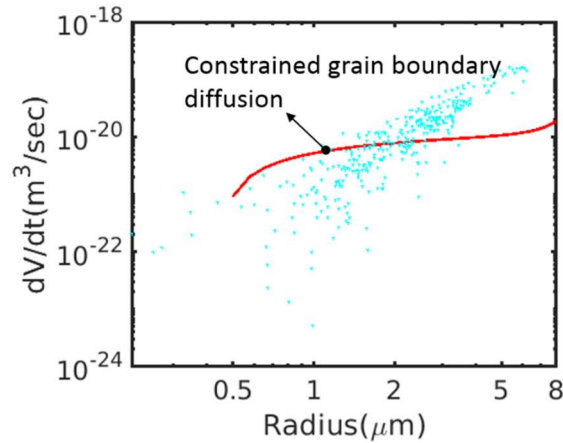


Figure 4.25 Plot showing volumetric growth rate as per constrained grain boundary diffusion model (red), along with experimental data (cyan markers)

4.5.3.1.3 Grain boundary sliding model

Further the applicability of grain boundary sliding model in defining volumetric growth rate is examined. Riedel proposed a 2D model for this, defined by the idea that rate of increase in length of the cavity ($2r$) is directly proportional to the grain boundary sliding rate and is given by:

$$2 \frac{dr}{dt} = \dot{u}_b = 0.55 \dot{\epsilon} f_s$$

where \dot{u}_b is the rate of grain boundary sliding rate and f_s is the size of the sliding grain facet. See Figure 4.26 (a) for reference.

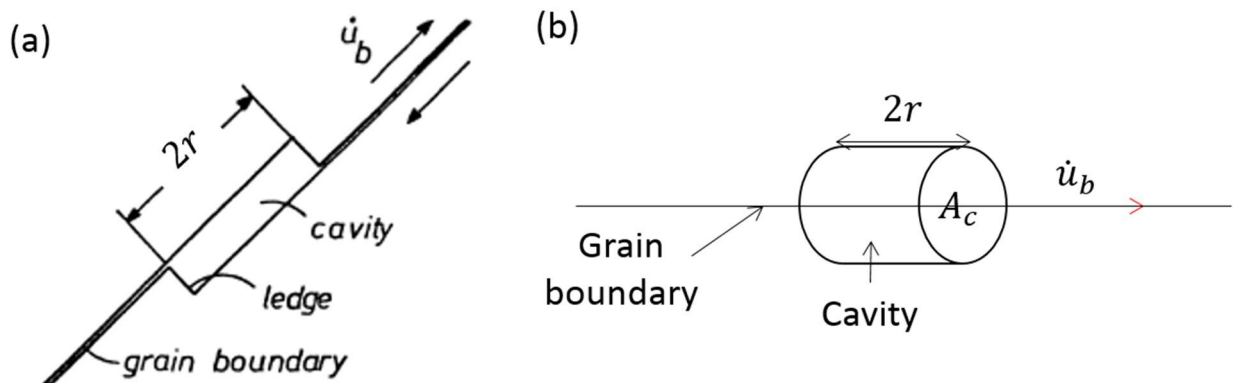


Figure 4.26 Schematic showing a cylindrical cavity of cross section area A_c and length $2r$ lying on a grain boundary, sliding at a rate of \dot{u}_b (a) in 2D [65] (b) in 3D

Since the experimental data available is in 3D, the proposed 2D model is adapted to 3D. For a cylindrical cavity of length $2r$ and cross section A_c lying on a grain boundary sliding at rate \dot{u}_b (Figure 4.26 b) if the cross section transverse to the sliding direction remains constant, only the length of the cavity would increase due to sliding. This would lead to a volumetric growth rate of:

$$\frac{dV}{dt} = 2A_c \frac{dr}{dt} = A_c \dot{u}_b = A_c 0.55 \dot{\epsilon} f_s \quad (4.3)$$

Figure 4.27 shows volumetric growth rate based on this model, given by red lines. Each line corresponds to a different cross section A_c and consequently a different cavity. The corresponding cross sections for three cavities have been marked, (for clarity all cross sections have not been marked). Depending on the cross section transverse to the sliding direction, a cavity should follow growth by one of the red lines. For example a cavity with an equivalent radius of $3 \mu\text{m}$ and a transverse cross section of $3.14 \mu\text{m}^2$ is expected to grow at a rate corresponding to the line A_{c1} , while one with equivalent radius of $5 \mu\text{m}$ and transverse cross section of $78.5 \mu\text{m}^2$ is expected to grow at a rate corresponding to the line A_{c3} and so forth.

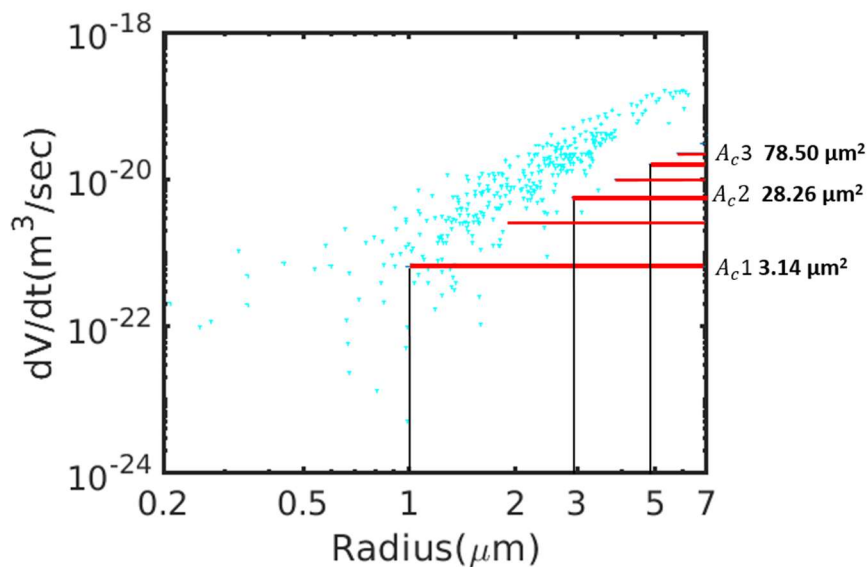


Figure 4.27 Plot showing volumetric growth rate as per grain boundary sliding model corresponding to different cross section, transvers to sliding direction, along with experimental data (cyan markers)

The experimental values for all tracked cavities are shown by cyan markers. On comparing the growth rates given by the model to the experimental values, it can be

seen that the model predicts the growth rate in the correct order of magnitude. The value predicted by the model is however highly dependent on the transverse cross section area and local grain boundary sliding rate. The sliding rate in turn is a function of the strain rate. Hence information about these two is necessary for accurate comparison of experimental results with the model.

4.5.3.2 Comparison with individual evolution types

In this section growth under individual evolution types will be compared with relevant models. This comparison will be done on experimental data from individual cavity. It should be noted that a cavity grows by more than one evolution type during deformation, however only growth corresponding to one evolution type will be compared at once. Table 4.4 summarises the proposed mechanisms responsible for different evolution types based on shape analysis.

Table 4.4 Table summarising possible mechanism leading to the different evolution mechanisms based on shape evolution

| Evolution type | Possible mechanism |
|-----------------------|---|
| Type 1A | Lattice / grain boundary diffusion |
| Type 1B | Grain boundary diffusion and grain boundary sliding |
| Type 2 | Grain boundary sliding |
| Type 3 | Grain boundary sliding |
| Type 4 | Diffusion based sintering |

4.5.3.2.1 Type 1A

Shape analysis of type 1A indicates that cavities following this evolution grow via diffusion. Since this type of growth was seen when cavity radius was small, both lattice and grain boundary diffusion could be a possible growth mechanism. In Figure 4.28 (a, b1, c1) experimental cavity growth rate (shown by red markers) for three cavities is compared with lattice (black line) and constrained grain boundary diffusion model (red line). Volumetric growth rate for all tracked cavities is presented using cyan markers in background, while data for individual cavity growing under type 1A are shown by red markers. This is done to show general and specific trends in the same plot.

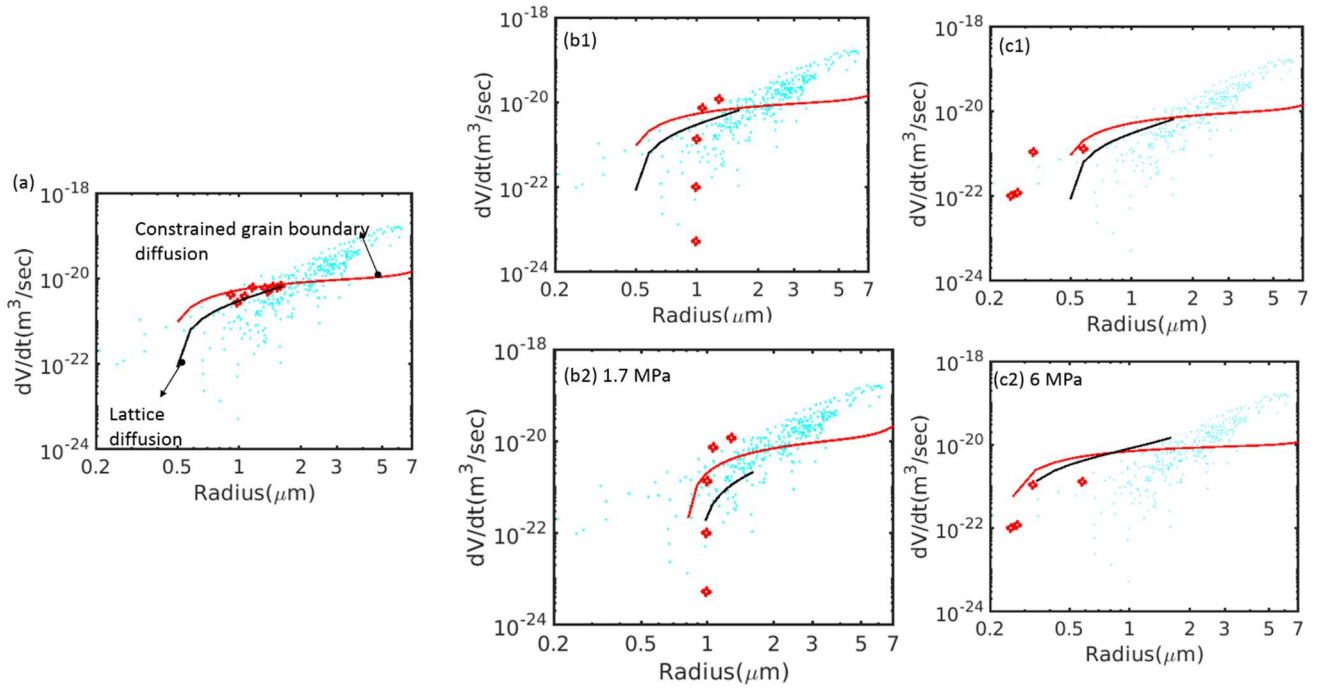


Figure 4.28 Plots showing volumetric growth rate for three cavities in (a) (b1) and (c1) growing by type 1A mechanism. Experimental data shown by red markers. Cyan markers in the background are experimental data from all cavities. (b2) and (c2) are plots with constrained growth model with adjusted stress values corresponding to (b1) and (c1) respectively.

Both models predict growth rates in similar order of magnitude as seen experimentally. And the trend of growth rate being nearly constant with radius is also seen in the experimental results. However the radius at which the cavity begins to grow at a constant rate is not consistent with the models for cavities in Figure 4.28 (b1) and (c1). This radius is dependent on the stress responsible for the growth of a cavity. When this stress exceeds the surface tension ($\frac{2\gamma}{r}$) the cavity begins to grow under diffusion at a constant rate. Hence changing the stress value in equations equation (1.16) and equation (1.23) changes the models. In Figure 4.28 (b2) and (c2) the stress has been changed to 1.7 MPa and 6 MPa respectively, and it is seen that under these stresses the model is consistent with the experimental result for these two cavities. Such variation in local stress fields in a polycrystalline materials undergoing grain boundary sliding is in fact expected. Similar variations have been experimentally observed in this material while deforming under grain boundary sliding regime [114], which were shown previously in Figure 4.18.

Hence a cavity growing under type 1A mechanism grows via diffusion. The experimental results are consistent with constrained grain boundary and lattice diffusion model. Additionally it is seen that this type of evolution is dominant until a strain of 0.3 (see Figure 4.19), therefore it can further be inferred that diffusion dominates cavity growth until this strain.

4.5.3.2.2 Type 1B

From the shape analysis of type 1B growth it was found to be dominated by diffusion and grain boundary sliding. Hence the experimental growth results are compared with constrained diffusion and grain boundary sliding models.

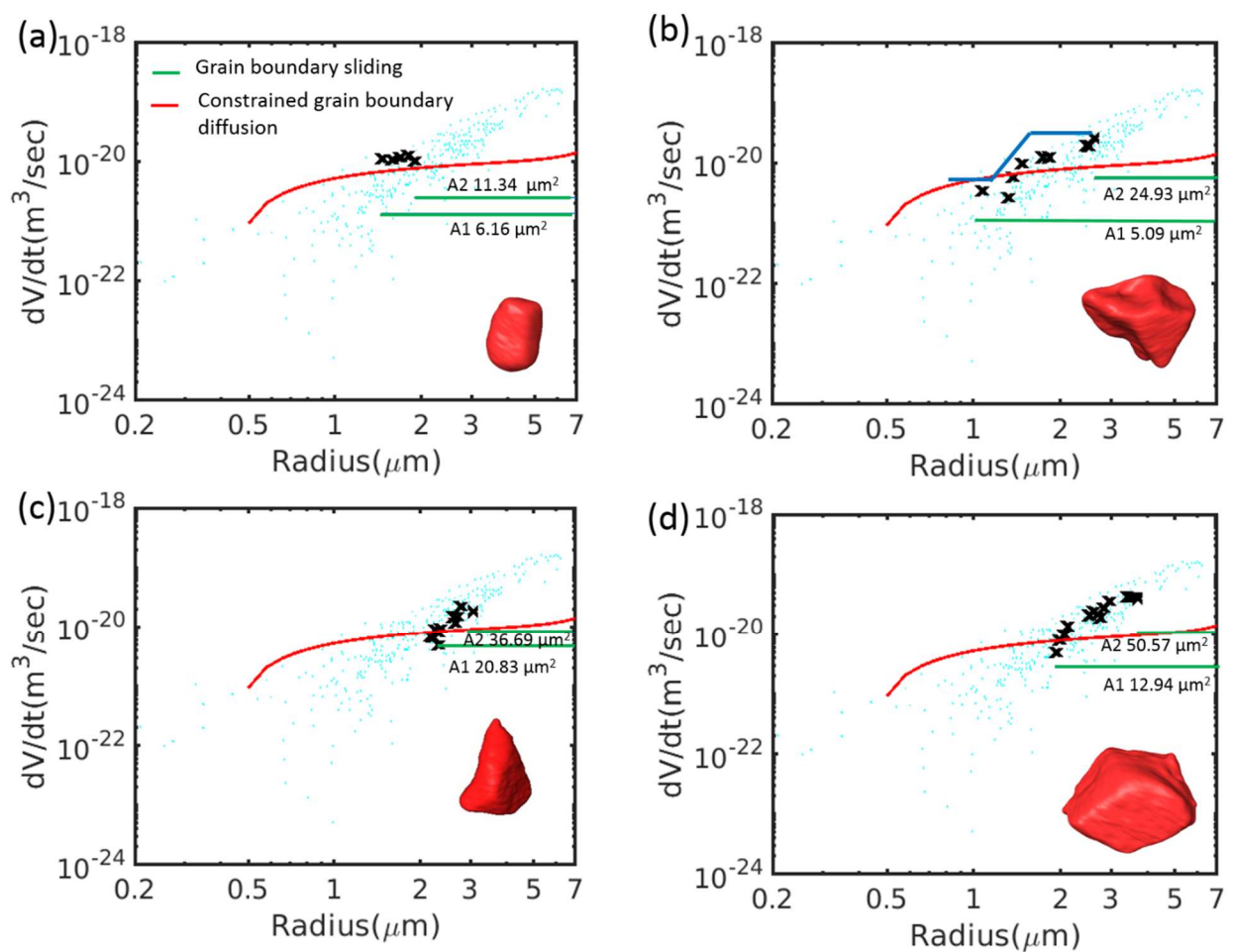


Figure 4.29 Plots showing volumetric growth rate for four cavities in (a) (b) (c) and (d) growing by type 1B mechanism. Experimental data shown by black markers. Cyan markers in the background are experimental data from all cavities. A 3D rendered view of the cavity corresponding to each plot is provided on the bottom right corner for reference.

Figure 4.29 shows for volumetric growth rates for four cavities. The volumetric growth rate predicted by constrained grain boundary diffusion is shown in red and

the grain boundary sliding models are indicated by green lines. Different lines correspond to different cross section area of plane transverse to the sliding direction. These areas are indicative of minimum and maximum possible cross section for each cavity and have been indicated in each figure. The experimental data of growth of cavities by type 1B evolution are indicated by black markers. In the background cyan markers show the growth rates of all cavities. A 3D rendered view of relevant cavity at 0.9 strain has been added for reference.

The cavity in Figure 4.29 (a) grows at a constant rate and the experimental values are predicted correctly by the constrained diffusion model. Further the shape of the cavity is fairly rounded, with minimum facets. Based on this it can be concluded that this cavity grows by diffusion and grain boundary sliding does not affect its growth considerably.

Moving on to the other cases in Figure 4.29 (b), (c) and (d). It can be seen that both models predict that the growth rate should remain constant with increase in equivalent radius or volume of the cavity. Experimentally however the growth rate is seen to increase with an increase in equivalent radius in most cases (Figure 4.29 b, c, d).

This increase however is not continuous. It proceeds in step, involving regions of constant growth followed by regions of increased rate, highlighted by blue steps in Figure 4.29 (b). It should be remembered that the sliding model does not account for the diffusional growth and vice versa, while the shape analysis indicates a confluence of both these mechanism affecting growth. Further it is also possible that the cross section area transverse to sliding direction could change due to a change in the sliding direction. A combination of these two factors could be the reason for the discrepancy in growth trends observed experimentally and that given by the models.

Additionally looking at the values predicted by the sliding model, it can be seen that even at the maximum cross section (corresponding to A2) the model under predicts the growth rate. A possible reasons for this is attributed to high strain localisation, causing an increased sliding rate, as compared to that predicted by the model. Such

local variation and stress and strain rate is consistent with observation of type 1A growth.

Further models accounting for combined effect of diffusion and grain boundary sliding combined with a knowledge of the local stress state would be needed to accurately predict the volumetric growth rate under this evolution regime.

4.5.3.2.3 Type 2

This is a specialised type of planar growth which is similar to crack like growth. Excess transverse stress generated due to grain boundary sliding could be a reason for these. Hence we compare the grain boundary sliding model with cavities showing type 2 evolution in Figure 4.30. Different lines correspond to different cross section area of plane transverse to the sliding direction (values indicated by A1 and A2 in figure). These areas are indicative of minimum and maximum possible cross section for each cavity and has been indicated in both figures. The experimental data of growth of cavities by type 2 evolution are indicated by green markers. In the background cyan markers show the growth rates of all cavities. A 3D rendered view of both cavities at 0.9 strain has been added for reference.

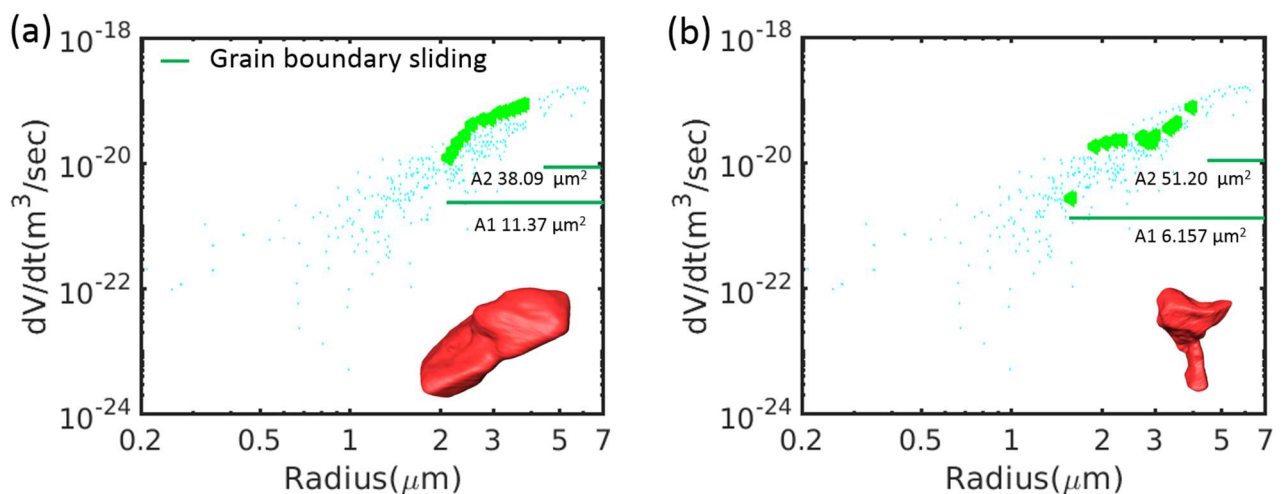


Figure 4.30 Plots showing volumetric growth rate of two cavities in (a) and (b) growing by type 2 mechanism. Experimental data shown by green markers. Cyan markers in the background are experimental data from all cavities. A 3D rendered view of the cavity corresponding to each plot is provided on the bottom right corner for reference.

Similar to type1B here too an uneven growth pattern composing of regions with constant and increasing growth rates are seen experimentally. Further the **values**

predicted by the model even for highest cross section area (A_2), are quite less as compared to experimental measurements. This could be because the model is inept to predict such planar crack like growth, or simply a much higher local grain boundary sliding rate could be the reason for this discrepancy. However the reason cannot be conclusively established.

4.5.3.2.4 Type 3

Type 3 growth is a unidirectional growth that was expected to be initiated as a direct consequence of grain boundary sliding. An indirect signal for grain boundary sliding was in fact visible in one cavity showing this type of growth. This cavity (see Figure 4.14) was surrounded by a line-up of intermetallic particles that were present above and below the cavity. On closely examining these intermetallics, it was seen that as the sample strained the intermetallics showed displacement in opposite directions. This has been illustrated by a schematic in Figure 4.31 (a).

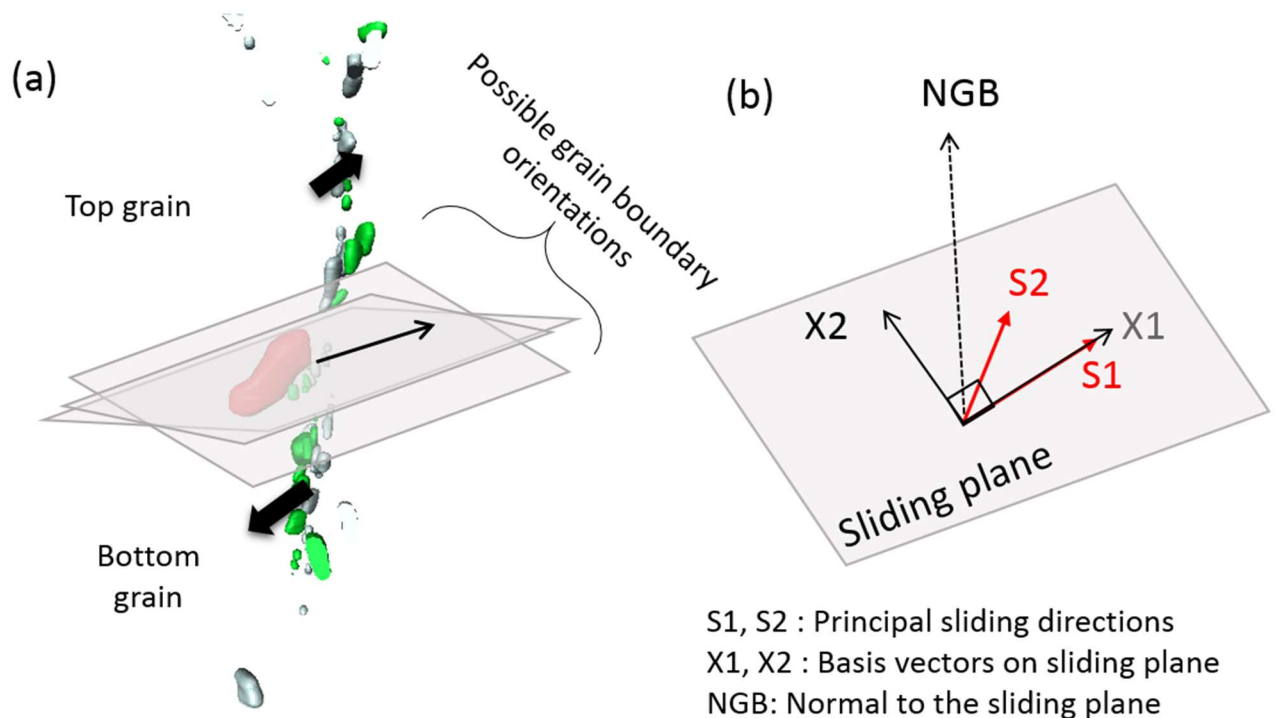


Figure 4.31 Schematic illustration (a) showing indication of grain boundary sliding seen through superimposed 3D rendering of position of intermetallic in a low (grey) and a high strain state (green) (cavity in red) (b) of definition of different vectors and directions used in quantifying grain boundary sliding.

In the figure intermetallics at two different strains have been superimposed to see the relative deformation experienced. Intermetallics presented in grey are at a low strain state and those in green are at a high strain state, the cavity (in red) in the high strain state has also been shown for reference. Now examining the position of green intermetallics with respect to grey, it can be seen that the relative direction of movement of the intermetallics are opposite in the two parts: top and bottom, this has been indicated by black arrow in Figure 4.31 (a). This is a clear indication that the top part, now referred as top grain is sliding with respect to the bottom grain and that the cavity is present on a grain boundary in between. The orientation of this boundary is unknown, but it should be a plane containing the sliding direction (indicated by black arrow) and has been schematically depicted through planes in the figure.

In order to quantify the grain boundary sliding several intermetallics on each side of the grain boundary were chosen and their average displacement vector with strain was computed. The displacement between the two sides gave the net grain boundary displacement vector. It was seen that all displacement vectors were nearly coplanar and that sliding was primarily seen in two directions (named S1 and S2). Direction normal to S1 and S2 was determined by taking a cross product of the two vectors, and was named NGB. This was the vector normal to the sliding plane. Figure 4.31 (b) shows a schematic representation of the definition of the different vectors. Based on these, two basis vectors (perpendicular to each other) were determined on the plane of sliding. The first vector was defined as equivalent to S1 and will be called X1 the second basis vector was determined by taking a cross product of S1 and NGB and was called X2.

Figure 4.32 (a) shows the displacement of the intermetallics in the X1 and X2 directions (from 0 to 0.9 strain). The displacement in NGB direction (from 0 to 0.9 strain) is also shown in Figure 4.32 (b). Firstly it is seen that the displacement is negligible in the NGB direction i.e. the direction perpendicular to the sliding plane, as compared to the directions X1 and X2 in the sliding plane. Further initially the displacement is dominant in X1 or S1 while as the sample strains, the sliding direction gradually changes. The displacement of the intermetallic is in fact an

indirect quantification of the grain boundary displacement, therefore henceforth the intermetallic displacement will be referred as grain boundary displacement.

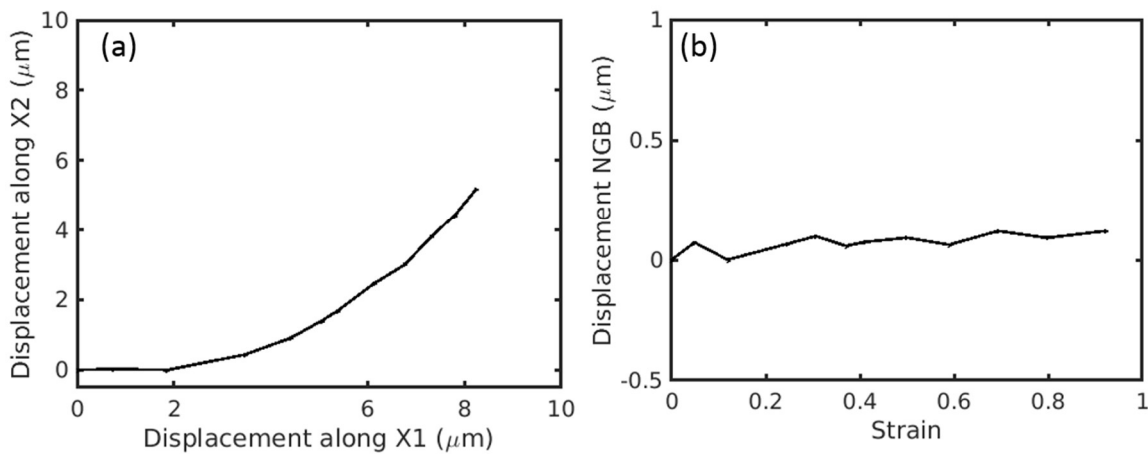


Figure 4.32 Plots showing displacement of intermetallics in (a) X1 and X2 direction (from 0 to 0.9 strain) (b) NGB direction with strain.

Further the displacement of grain boundary was compared with the cavity growth. For this, the length of cavity was determined along the S1 and S2 direction. This was done by obtaining an oblique slice along the sliding plane from the 3D volume of the cavity and determining the length of cavity along the two principal sliding directions S1 and S2. Figure 4.33 shows a plot of cavity length along S1 and S2 directions along with the displacement of grain boundary along these directions in (a) and (b) respectively. The length of the cavity has been subtracted from the initial length of the cavity for easy interpretation of the increase in length.

The net increase in length of the cavity is seen to be equal to the grain boundary displacement in S1 direction until a displacement of nearly 6 μm, this corresponded to a strain of 0.5. After this the cavity did not grow in S1, Further net growth of cavity along S2 was initially negligible however after a displacement of nearly 6 μm it was seen to increase proportionally to the displacement along S2, this corresponded to a strain of 0.59. Hence the length of cavity increased proportional to the displacement of intermetallic in S1 direction until a strain of 0.5. After this however the increase of cavity along S1 stopped and instead the cavity grew along the S2 proportional to displacement of grain boundary. Based on this it was concluded that the increase in length of cavity was in fact proportional to the grain boundary displacement and this increase was seen as a direct consequence of grain boundary sliding.

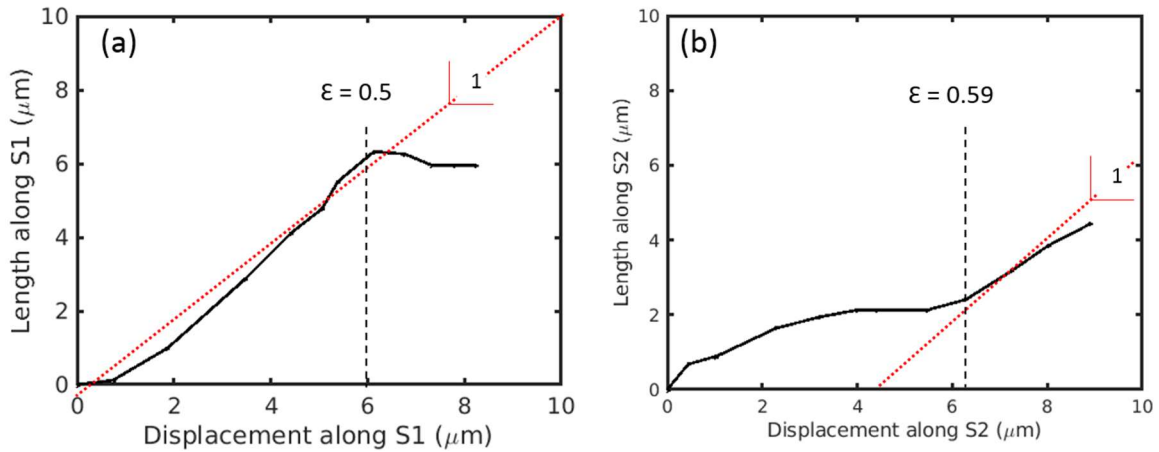


Figure 4.33 Plot showing net length of cavity along (a) S1 direction versus displacement of grain boundary in this direction (b) S2 direction versus displacement of grain boundary. Red lines are straight lines with slope one, shown to indicate a direct proportionality.

The average grain boundary sliding rate was measured in the two directions and was found to be nearly the same: $6.5 \times 10^{-10} \text{ ms}^{-1}$. Using this sliding rate and the cross section of cavity transverse to the sliding directions, the volumetric cavity growth rate was determined using the grain boundary sliding model.

Figure 4.34 shows the volumetric growth rate of this cavity in comparison with the grain boundary sliding model. It was seen in Figure 4.33 that the cavity showed growth in proportion to grain boundary displacement throughout the deformation. Since the cavity grew via type3 and type1B evolution during deformation, experimental data from both these regimes are plotted in Figure 4.34 for comparison (magenta: type3 black: type1B). Further there were two primary sliding directions measured, hence growth rate corresponding to the respective cross sections are plotted by green and red lines. Such that A1 and A2 correspond to cross section of the cavity transverse to S1 and S2 at the strain where these directions become the dominant sliding direction. Additionally the volumetric growth rate for all tracked cavities is presented using cyan markers in background. A 3D view of the cavity growing under S1 and S2 sliding are also shown for reference.

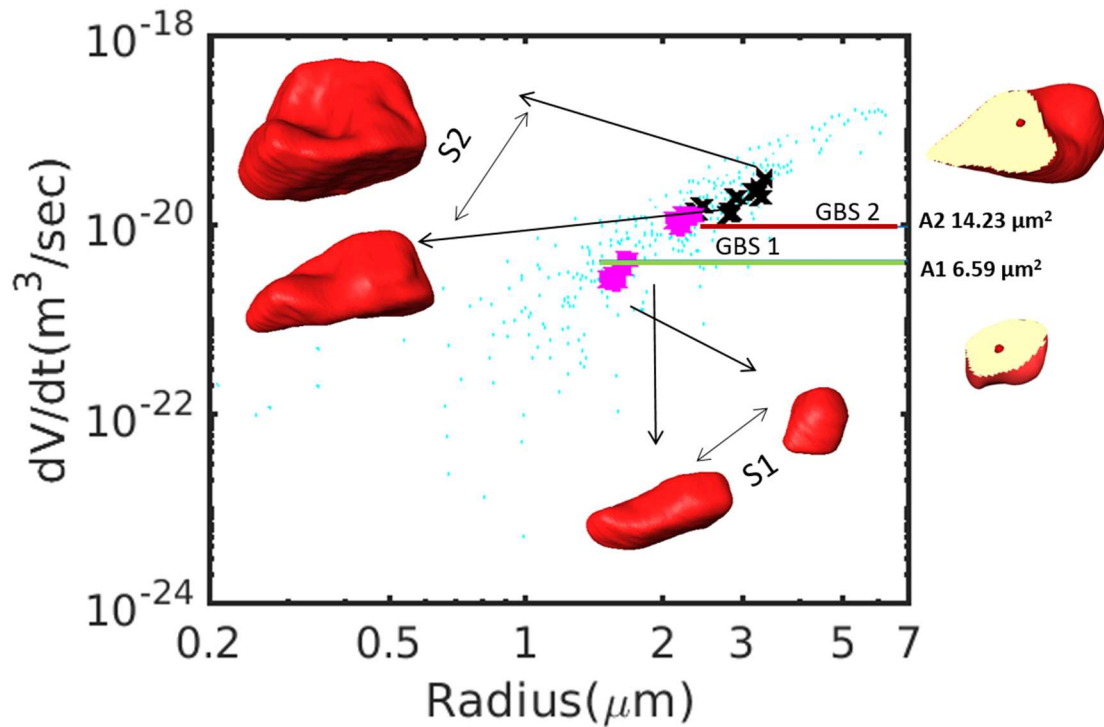


Figure 4.34 Plot showing volumetric growth rate of a cavity shown by magenta (type 3) and black (type 1B) markers. The growth rate by grain boundary sliding (GBS) model corresponding to sliding along S1 shown by green line, (A1 is cross section transverse to S1) and corresponding to sliding along S2 shown by red line, (A2 is cross section transverse to S2). 3D rendered view of cavity growing under S1 and S2 sliding have also been shown for reference. (See Figure 4.14 for growth montage of this cavity)

Now as per the model if the cavity grew with S1 as the primary sliding direction the growth rate must have remained constant even with increase in volume or equivalent radius, at a rate indicated by green line. However it is seen that the growth rate in fact increase as the equivalent radius (or volume) of the cavity increases. However from Figure 4.32 (a) it can be seen that the sliding direction is in fact changing throughout the deformation, this would inevitably be accompanied by a change in the transverse cross section area. If the cross section area increases, correspondingly the growth rate would increase too. In the figure the red line corresponding to the transverse section A2 shows the effect of such an increase.

In addition the contribution of diffusion must not be forgotten. Diffusion would both increase the volume, and this increase would consequently also increase the cross section, even if no change in sliding direction is seen. Hence a confluence of these two factors: variation in sliding direction and diffusion, were concluded to be the

cause of the increase in volumetric growth rate, with an increase in radius of the cavity.

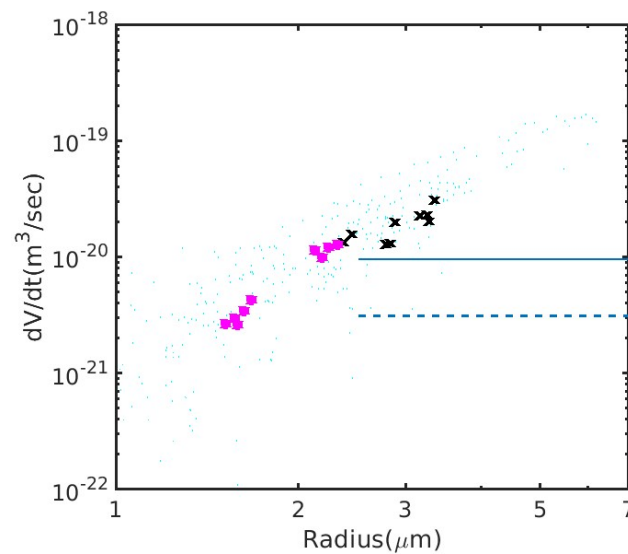


Figure 4.35 Plot showing a comparison of volumetric rate predicted from grain boundary sliding model using $\dot{\epsilon}_b$ estimated from macro strain rate (dashed blue line) and that measured locally (dashed blue line).

However barring this increase **the experimental data of volumetric growth rate shows a good match to the grain boundary sliding model. This was contrary to what was seen in the previous cases Figure 4.29 and Figure 4.30. This was because in the current case the local grain boundary sliding rate was measured**, while in the previous cases, in absence of this data the macro strain rate was used to estimate this value ($0.55 \dot{\epsilon}_s$), see equation (4.3) for details

To elucidate this further Figure 4.35 shows a comparison of the two values for the current sample, where the dashed line corresponds to the growth rate using the sliding rate estimated from macro strain and full blue line indicate the growth rate using the measured sliding rate. It can be seen that the local sliding rate is almost thrice the sliding rate calculated using the macro strain and so are the corresponding growth rates. And this increased growth rates matches the experimental data (corresponding to a particular equivalent radius). Hence it was seen that local measurement enabled the accurate prediction of volumetric growth rates (Recalling the results in Figure 4.18, this is expected, since a strain concentration of thrice the uniaxial value was in fact commonly seen).

4.5.3.2.4.1 Type 4

This evolution catered to a very interesting mechanism which was seen during the high temperature deformation, where the volume of few cavities reduced during deformation. A cavity is expected to grow if the stress on the cavity is greater than surface tension ($2\gamma/r$). The fact that few cavities showed shrinkage indicates that the net stress on these cavities was less than the surface tension. Figure 4.36 shows a plot of the surface tension versus strain for all cavities that showed type 4 evolution.

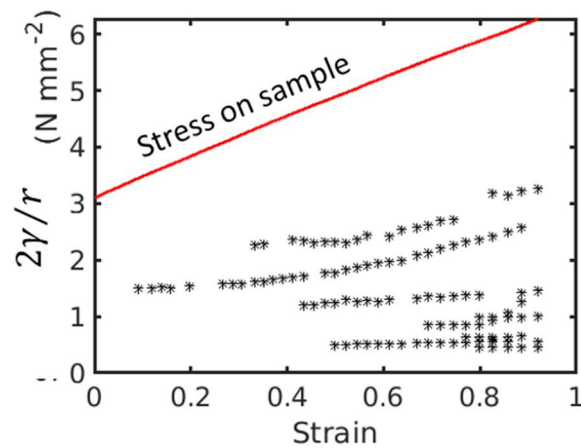


Figure 4.36 Plot showing $2\gamma/r$ versus strain for different cavities that evolved by type 4 mechanism during deformation of the sample,

The values of surface tensions vary between 0.5 and 3.3 MPa. The initial stress applied on the sample was 3.2 MPa which varied with strain up to 6.2 MPa (due to reduction in notch area during deformation), this has been indicated using a red line on the same plot. Normally this stress should be enough to overcome surface tension of all these cavities that showed type 4 evolution. Since experimental observation are contrary to this, it is safe to conclude that the net stress acting on these cavities much less than the applied stress. This further reaffirms the fact that stress state in a polycrystalline sample showing prominent grain boundary sliding is highly variable. Such that few cavities may experience stress much less than applied stress.

The volumetric shrinkage rates of these cavities is compared to a model for diffusive sintering [150]:

$$\left(\frac{dV}{dt}\right)_s = -\frac{8\Omega D_l(2l)r^2}{kT}\alpha_s\Delta P \quad (4.4)$$

where $\Delta P = \text{External Pressure} + \frac{2\gamma}{r}$, external hydrostatic pressure being zero and α_s is a constant dependent of cavity radius and inter cavity spacing, which can be assumed as 1 if cavity radius is small as compared to inter cavity spacing.

Figure 4.37 shows comparison of the volumetric growth rate for three cavities (a, b, c1) in red markers with the model in (black). Data for remaining cavities showing type 4 evolution is indicated by cyan markers in the background.

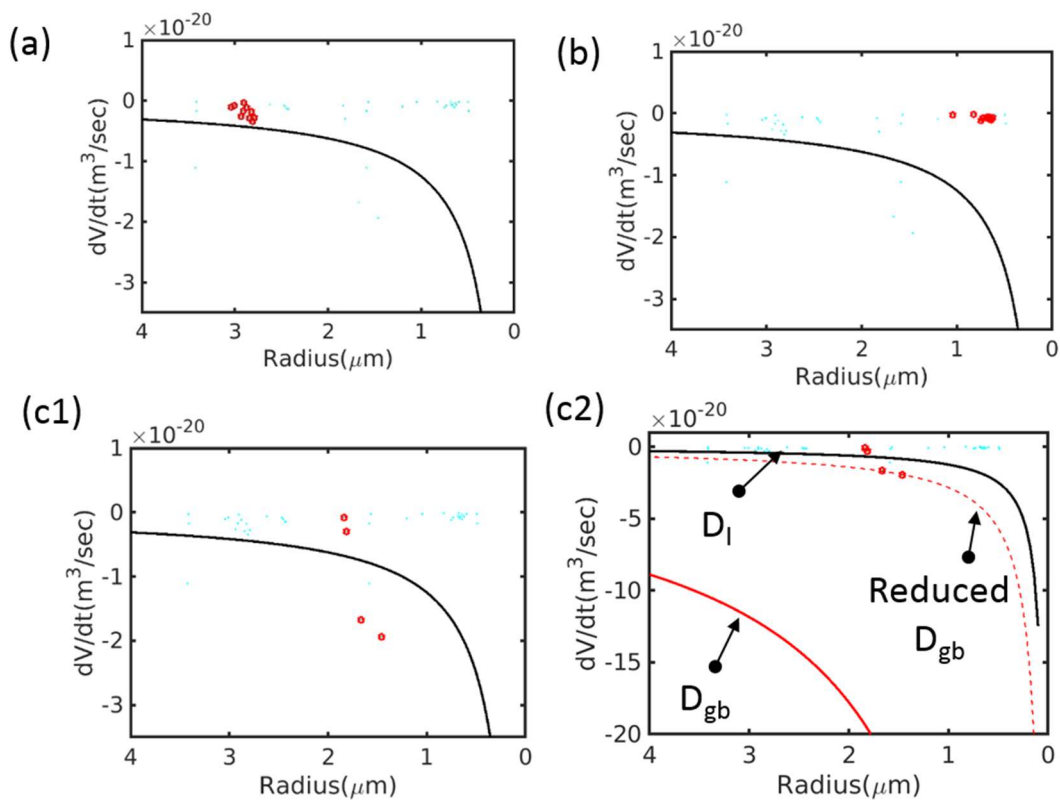


Figure 4.37 (a,b,c1) Plots showing comparison of experimental data from 3 cavities (red markers) of shrinkage of cavity compared with diffusion based sintering (in black). (c2) Plot showing data from cavity in (c1) compared with shrinkage rate due grain boundary diffusivity. Data for remaining cavities showing type 4 evolution is indicated by cyan markers in the background.

It can be seen that the shrinkage rate remains nearly constant with radius, both experimentally and as per the model. Only a rapid increase in this rate is expected as the radius approached zero, this was not seen experimentally. A lack of ability to resolve the volume at very small radius at the current resolution could be a reason for the inability to compute precisely the shrinkage rate at such volumes. Further,

while a constant shrinkage rate corresponding to the model was seen in most case, an exception was seen in the cavity represented in Figure 4.37 (c1), here the shrinkage rates were much greater than the rest. To explore this further, the variation of volume with time was examined.

Figure 4.38 (a) shows a plot showing normalised volume of cavities showing type 4 evolution with time. Here it can be seen that the volume for all cavities decreases at a nearly constant rate except for one that has been highlighted in red. This cavity corresponds to the one in Figure 4.37 (c1). Examining the 3D volume (Figure 4.38 b) of the cavity it was seen that this was in fact a very specific cavity. During deformation, a cavity nucleates near the shrinking cavity and eventually the two cavities coalesce. Despite of this coalescence however a rapid decrease in the volume was observed.

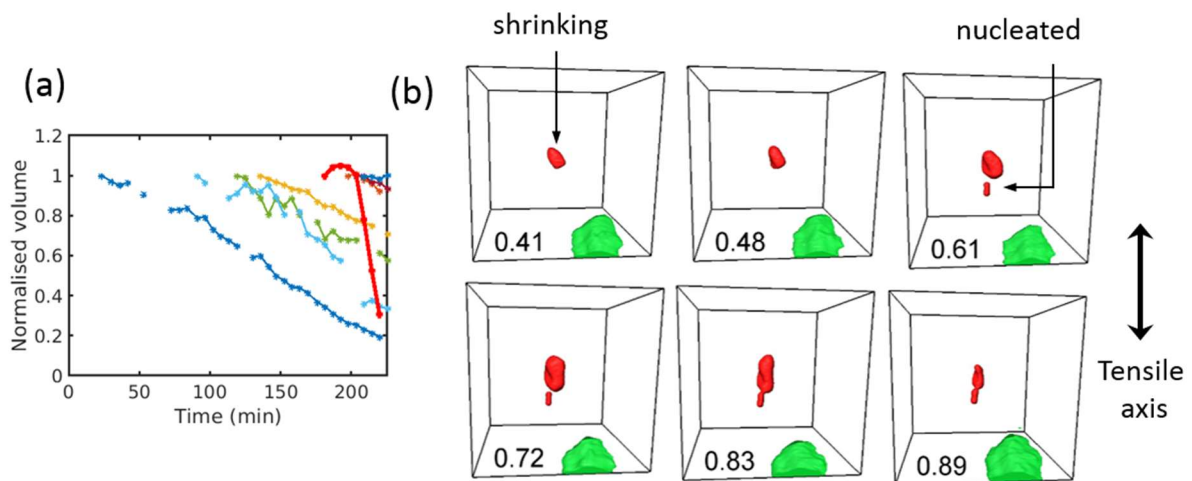


Figure 4.38 (a) Plot showing normalised cavity growth versus time for cavities evolving by type 4 mechanism. (b) 3D rendered view showing the evolution of a cavity with strain.

One possible explanation for this fast shrinkage is the presence of a grain boundary nearby. This is in fact expected, because the nucleated cavity is expected to be present on a grain boundary jog. When modifying the equation and using grain boundary diffusivity (full red line) instead of lattice diffusivity in Figure 4.37 (c2) the growth rate predicted is quite higher as compared to the experimental value. It has already been pointed out that the grain boundary diffusivity values in literature are not very consistent. And it was noted that if the grain boundary diffusivity value, was

reduced by an order of magnitude less (red dashed line in Figure 4.37 c2) than the reported value it would appropriately to fit the experimental data.

Overall shrinkage of cavities seen during deformation was attributed to drastic reduction in local stress, leading to diffusive sintering of these cavities.

4.6 Conclusions

In this chapter results from *in situ* high temperature deformation of an AZ31 sample (3.2 MPa, 673 K) has been presented. One sample was deformed until a macro strain of 0.9 with an average strain rate of $6.6 \times 10^{-5} \text{ s}^{-1}$. The main focus of the investigation was investigation cavity nucleation and growth during superplastic deformation of the alloy. During this investigation the following conclusions were drawn:

- Three cavity nucleations were seen during the deformation in the region investigated at high resolution. Visual observations of these nucleations indicated that they were caused due to grain boundary sliding on grain boundary jogs or triple points.
- Most deformation proceeded in growth of pre-existing cavities. These cavities which were small (average initial radius $0.8 \mu\text{m}$) and spherical (most had a sphericity greater than 0.9) at the start, grew into big cavities with complex shapes during deformation.
- To dissect this, the evolution patterns were classified into different types. And it was seen that each cavity grew by a combination of these evolutions. Based on the shape analysis of these evolution types, diffusion and grain boundary sliding were inferred to be the primary growth mechanisms responsible for the evolution of cavities. Table 4.5 shows explanation for each of the evolution types and summarizes the comparison of experimental data for these with relevant models.

Table 4.5 Summary of definitions of different evolution patterns and the key conclusions based on comparison of experimental data with different cavity growth models.

| Type | Pattern of evolutions | Lattice diffusion | Constrained grain boundary diffusion | Grain boundary Sliding (GBS) |
|------|-----------------------|-------------------|--------------------------------------|------------------------------|
|------|-----------------------|-------------------|--------------------------------------|------------------------------|

| | | | | |
|-----------|--|----------------|---|--|
| 1A | <ul style="list-style-type: none"> ▪ Equal growth in all direction ▪ No change in shape | Yes | Yes | Not applicable |
| 1B | <ul style="list-style-type: none"> ▪ Multidirectional growth, not equal in all directions ▪ Equiaxed, faceted cavities | Not applicable | <ul style="list-style-type: none"> ▪ Growth rate in correct order of magnitude predicted by both models ▪ Need for combined model | |
| 2 | <ul style="list-style-type: none"> ▪ Accelerated growth in two dimensions ▪ Flat planar features | Not applicable | Not applicable | No (Probably need for local GBS rate estimation.) |
| 3 | <ul style="list-style-type: none"> ▪ Accelerated growth in one dimension ▪ Asymmetric crack tip in two diametrically opposite directions | Not applicable | Not applicable | Yes If local GBS rate is used |
| 4 | <ul style="list-style-type: none"> ▪ Decrease in volume ▪ Shape may or may not change | Yes | Need for more accurate diffusivity value | Not applicable |

- Classical grain boundary diffusion model over predicted the volumetric growth rates by two orders or magnitude as compared to the experimental measurements.
- Constrained grain boundary model and grain boundary model were successful in predicting the volumetric growth rates in correct order of magnitude as that observed experimentally.
- It was seen that initially cavities predominantly grew by diffusion (until 0.3 strain).
- In a specific case, thanks to presence of intermetallic markers, grain boundary displacement was computed. And a direct link between cavity growth and the displacement was observed. An average grain boundary sliding rate of $6.5 \times 10^{-10} \text{ ms}^{-1}$ was measured.
- While the models predicted growth in correct order of magnitude the trends of growth observed experimentally i.e. change in growth rate with increase in volume/radius was not precisely captured by the models. A model which

combined diffusion and grain boundary sliding effects would be better equipped for such predictions.

- Further a very interesting observation was that several cavities showed a decrease in volume during deformation. While some cavities shrunk throughout deformation (for the scans in which they could be imaged) other initial showed growth which was followed by a decrease in volume.
- It was concluded that several cavities did not experience enough stress to cause growth even when an external stress greater than the surface tension was present. This strongly indicated that stress state inside the polycrystalline sample was highly variable.
- Further diffusion based sintering was concluded to be the driving force for the shrinkage seen in the cavities.

Conclusions

Synchrotron X-rays were used to carry out *in situ* nanotomography investigation of high temperature deformation in model Al-3.6 wt%-Cu alloys and commercial magnesium alloy: AZ31. Nucleation and growth of cavities were measured and compared to existing models of nucleation and growth. The following conclusions were drawn from the study:

Conclusions on the *in situ* nanotomography high temperature deformation setup

- Two mechanical devices were integrated with the existing furnace at the ID16B beamline of the ESRF. This was done to enable *in situ* imaging during high temperature deformation imaging.
- The first setup allowed constant load deformation, however no control on the strain rate was possible. The second device was designed to allow precise control of load and strain rate, however further trials need to be conducted to make the device more robust.
- Multi resolution data acquisition procedures were developed which allowed cyclic low (pixel size 645 nm) and high (pixel size 100 nm) resolution imaging.
- Thanks to very fast imaging (7 seconds) and development of data processing techniques to analyze the *in situ* data, blur free reconstruction and segmentation of volumes deforming with strain rates as high as $5 \times 10^{-4} \text{ s}^{-1}$ was possible.
- A culmination of these developments allowed *in situ* tomography with a pixel size 100 nm and scan time of 7 seconds during high temperature deformation of lights alloys. And this novel technique was used to examine nucleation and growth of creep cavities driven by diffusion, plasticity and superplasticity.

Conclusions from study on Al-Cu alloy

- A model Al-Cu alloy (Al-3.6 wt%-Cu) was heat treated to generate copper rich second phase particles of controlled size (1.4 μm).

- Nucleation of cavities with equivalent radius, as small as 0.17 μm , was imaged in Al-Cu alloy. However the nucleation events were scarce, as most of the deformation manifested in growth of pre-existing cavities.
- Growth of cavities was studied *in situ* by studying the change in shape of cavities with strain. It was seen that the shape of the cavities was initially sphere like, followed by elongation of cavities into ellipsoidal shape towards the end of deformation. This indicated growth of cavities by diffusion, followed by plasticity based growth.
- The trend of volumetric cavity growth rate was studied with increase in radius during straining. This experimental data was compared with the models of cavity growth rate of diffusion by Raj and Ashby and plasticity model by Hancock. The growth rate measured experimentally was in close agreement with predictions based on models, indicating that these models could be used for intra-granular cavity growth also. Comparatively studying the growth rate based on the two mechanisms reaffirmed the previous conclusion of cavities initially growing by diffusion and later by plasticity. The observed change in mechanism was in tandem with an increase in strain rate towards the later stage of deformation, corresponding to tertiary creep.
- There was no unique radius of transition for change in cavity growth mechanism from diffusion to plasticity, because the deformation studied was not in steady state creep regime. However on considering the real experimental deformation parameters for stress, strain rate and inter-cavity spacing for each cavity, the transition radius predicted by models matched well with the experimental values.

Conclusions from study on AZ31 alloy

- Imaging of nucleation of cavity with radius as small as 0.17 μm was possible thanks to the *in situ* nanotomography setup. Nucleation of three cavities were observed during deformation, none of which nucleated on an intermetallic particle. These were instead concluded to be present on triple points and jogs of sliding boundaries.
- Tracking of evolution of individual cavities revealed that most of the damage proceeded in growth of pre-existing cavities, during which nearly spherical

equiaxed pre-existing cavities grew into complex shapes. It was further seen that during deformation each cavity's shape evolved in a different manner.

- Based on the analysis of the evolution of shapes of cavities, diffusion and grain boundary sliding were concluded to be the dominant growth mechanism.
- Classical grain boundary diffusion over predicted the cavity growth rates by few orders of magnitude as compared to the experimental results. Hence it was concluded that these models are useful in predicting the maximum growth rates due to diffusion. In contrast the constrained grain boundary diffusion model predicted growth rates in correct order of magnitude as observed experimentally.
- The initial stages of growth (until 0.3 strain), of cavities involved uniform growth in all directions with no visible shape changes, which indicated diffusion based growth. The lattice and constrained grain boundary diffusion models were successful in predicting cavity growth during such evolutions.
- Further growth (after nearly 0.3 strain) involved an interplay of diffusion and grain boundary sliding. In the absence of a suitable model, incorporating both the processes it was difficult to precisely compare the experimental growth data with models.
- In a very specific case, intermetallics acted as markers around a grain boundary. The displacement of these markers was used to estimate the grain boundary sliding.
 - It was seen that during deformation the direction of grain boundary sliding changed.
 - A direct proportionality was found between grain boundary displacement and cavity growth. This confirmed the influence of grain boundary sliding on cavity growth.
 - Using the measured grain boundary sliding rate, the grain boundary sliding model was successful in predicting the cavity growth rate in the cavity.
- In addition to growth, cavities actively showed a decrease in volume during deformation. This was attributed to sintering of cavities via diffusion due to reduced local stress.

- While some cavities grew at very high rates (in comparison to that predicted by models) other cavities showed a decrease in volume during deformation. This indicated large inhomogeneity in the stress and strain fields inside the polycrystalline sample which was probably due to sliding grain boundaries.

Conclusions on applicability of different cavity growth models

- The lattice diffusion model was found to be applicable even to cases where cavities were present inside the grain and not on grain boundaries, when applied to model Al-Cu alloy, taking into account changes in local stress, strain rates and measurement of the real inter cavity spacing.
- Plasticity growth was appropriate for predicting cavity growth at high strain rates, in the Al-Cu alloy.
- The classical grain boundary diffusion models over predicted growth rate when applied to commercial Mg alloy. It was seen that the constrained grain boundary models were more appropriate for this case.
- Grain boundary sliding model showed good match with experimental data, when compared using the experimentally measured grain boundary sliding rate.
- Further developments of a model accounting for both grain boundary sliding and diffusion together would be more suitable to predict growth trends in superplastic materials.

Perspectives

1. Technical improvements: Motorised mechanical device

On using the motorised mechanical device for *in situ* deformation studies several road blocks were encountered. In this section the possible improvements to the device or the beamline setup will be presented.

- **Electrical wires**

It was seen that the presence of electrical wires made the acquisition difficult. Continuous rotation of the device and its motion between the source and detector (for multi resolution scans) effected the electrical connections (see Figure P. 1). Such motions led to loosening or breaking of electrical connection during deformation. This was highly undesirable. In order to avoid this problem an introduction of a slip ring on the rotating stage of the beamline would be highly beneficial.

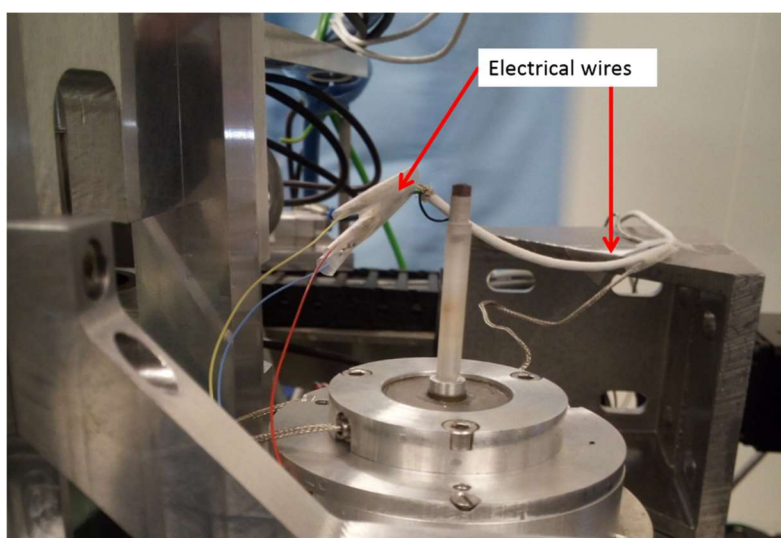


Figure P. 1 Picture showing the setup of motorised mechanical device on the rotating stage of ID16B beamline. The electrical wires associated to the device are indicated by an arrow

Addition of slip ring would help facilitate continuous rotation of sample, which would in turn increase acquisition speed. Additionally it would reduce the risk of hindrance to sample rotation due to presence of external wires. Lastly it would make the

mounting of the mechanical device on the rotating stage un-complicated (no special organisation of wires would be needed).

In fact on such a ring is integrated to the rotating stage of ID19 beamline of ESRF. Mechanical devices with electrical connections have been seamlessly integrated with *in situ* microtomography imaging at this beamline. However it is acknowledged that addition of a slip ring might compromise the accuracy of movement of the rotating stage. This might have a deleterious effect on the high precisions in stage movement, needed for other nano probe characterisations carried out at the beamline.

- **Improvement for automated mechanical device**

Quartz was chosen to fabricate the automated mechanical device thanks to its low thermal dilatation at high temperature. However based on its performance during the experiment it was noted that, it was quite brittle. This made the device susceptible to damage if not handled carefully. In this context probably alumina rods would be a better choice, to make the device more robust. Although they do not have as good thermal dilatation resistance as quartz, they are less brittle and fragile. Therefore in order to make the device more reliable, further trials by machining alumina rods could be done.

2. Technical improvements: Furnace

One major short coming related to the usage of the furnace was linked to the lengthy calibration process. Initially attempts were made to attach a thermocouple to the sample. However it was difficult to keep the thermocouple straight, during sample rotation. The external wire of the thermocouple being a major hindrance during the rotation. Hence to overcome this calibration was done using eutectic samples. While this process was highly reliable, it used up a lot of time from each beam time of a synchrotron experiment. Saving this time is possible by using a PID (Proportional Integral Derivative) based system for calibration. Due to lack of time such calibration was not pursued in the current thesis. However developing this would be immensely beneficial as it would save time for repetitive calibration. Additionally it would also allow direct determination of temperature of the furnace instead of an indirect route

based on power supplied to the furnace that is currently employed. And this would also allow easy programming of heat treatment cycles.

3. Data acquisition improvements

Due to the local nature of high resolution tomography at ID16B beamline, it was not possible to image the whole sample during deformation. And in such configuration, as a consequence of sample deformation, the region of interest being viewed on the sample changed. This drastically limited the region in which the deformation could be followed in real time. Since this is a key advantage offered by *in situ* imaging, it is imperative to image a constant region, even as the sample deforms. One possible solution to this is integrating the sample deformation with sample movement in z direction. This is possible when performing constant strain rate deformation using motorised mechanical device. Based on the strain rate applied, the net strain on the sample can be estimated between consecutive scans. This can then be integrated with corresponding sample movement along the z axis after each scan.

Another solution for this could be based on using features on low resolution radiographs acquired *in situ* to calculate the displacement of the sample in real time. This information could then be used to compensate for motion of sample on the rotation stage. Additionally data on the net displacement of sample would also be immensely useful in calculating the strain on the sample in real time. This information would come in handy to cross check whether straining of the sample is consistent with that applied using the mechanical device.

4. Data processing improvements

The amount of data acquired during an *in situ* tomography is generally quite huge (acquiring 4 high resolution and 1 low resolution volumes for a deformation lasting 80 minutes corresponds to 15 scan cycles amounting to nearly 75 volumes). Hence, automating the reconstruction of the volumes becomes extremely important. While most of the work in this thesis was automated, finding the position of centre of rotation for reconstruction, was still performed manually. This was done by reconstructing a transverse slice for several positions of centre of rotation and choosing the most suitable position based on visual examination. Being a hit and trial

method, the process was time consuming and repetitive. One alternative to this was anticipating the centre of rotation for a scan based on that of the previous scan. While this reduced the number of trials required, the choice still had to be made manually.

A major improvement to the process of data processing would be integrating an algorithm to determine the position of centre of rotation automatically, into the reconstruction procedure at the ID16B beamline. Such an automation would facilitate complete integration of phase retrieval and reconstruction of the 3D volumes thus drastically reducing effort in processing *in situ* data.

5. Further scientific investigation on the available data

- **Al-Cu data**

The digital volume correlation tracking of second phase particles during deformation can in turn be used to estimate the local strain associated with each cavities. This could in turn be used to estimate the stress triaxiality map of the notched sample.

- **AZ31 data**

AZ31 samples that were investigated had several grain boundaries owing to their small grain sizes. The presence of these grain boundaries greatly influenced the cavity growth due to grain boundary sliding. However, nanotomography was unable to provide information on where these grain boundaries were present with respect to the cavities. In this regard, post-mortem investigation of the sample can be done by wetting it with gallium. On doing so, the gallium is expected to preferentially wet the grain boundaries. Imaging such samples using nanotomography in the same region of interest as previously imaged, can then provide complete information on position of cavities in a grain or grain boundary. Such investigations have in fact been carried out by Toda et al [11] on Al-Mg alloy. Initially the sample was subjected to interrupted *in situ* deformation which was imaged using synchrotron X-rays. The deformed sample was then wetted with gallium to reveal the grain boundaries in the sample. Figure P. 2 (a) shows cavities (in red) seen in the sample and Figure P. 2 (b) shows these cavities superimposed on the grain boundary imaged post gallium wetting.

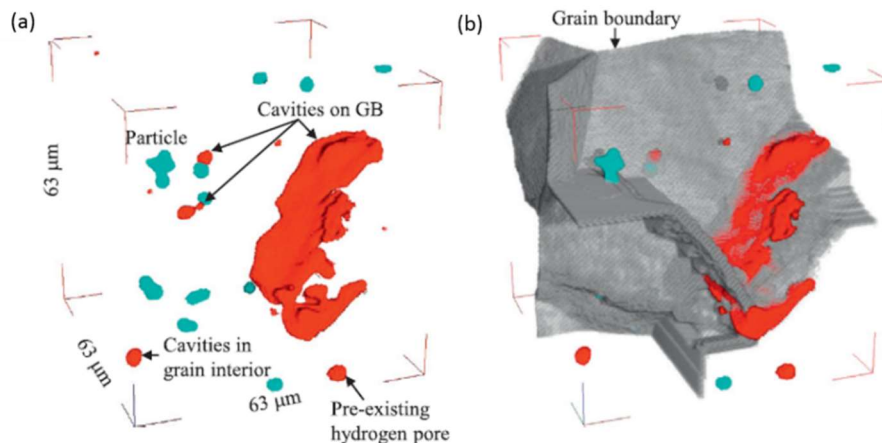


Figure P. 2 3D perspective views of pores/cavities (both are shown in red) and particles (green) captured at the final loading step in Al-Mg alloy. A grain boundary image (grey) has been superposed on (a) in (b) [11].

Additionally, an investigation of the deformed sample using diffraction contrast tomography would add useful insights into the grain orientation mapping. Such analyses would provide further information about any possible changes in cavity growth due to crystal orientation.

6. Further scientific investigation using similar setup

- **Indirect measurements of material properties**

The setup of *in situ* tomography can be extended to studying specifically designed bi-crystals. Samples with large grains (can be achieved by annealing) can be machined using focussed ion beam (FIB) cutting. The sample could be machined inside a grain they have 1 or 2 grain boundaries along the length. These grain boundaries could be lined with second phase particles allowing visibility of the boundary via tomography (such lining of second phase particles allowed imaging of grain boundaries in Al-Cu sample examined in this work, see Figure P. 3 a). FIB can be used to machine a sample with a geometry nearly as seen in Figure P. 3 (b).

Pre-examining the sample using tomography would then reveal the grain boundaries and pre-existing cavities. Based on this examination, an appropriate region of interest can be used for different fundamental examinations.

For a ROI with nearly transverse boundary with a no pre-existing cavities on the boundary (ROI 1 Figure P. 3 b) could be used to study nucleation of cavity on transverse boundaries. Ideally no pre-existing cavities in the grain near the grain boundary would cause high temperature deformation to proceed via nucleation of new cavities. Transverse grain boundary would offer a suitable position for such nucleations. In such conditions favouring nucleation of cavities, kinetics of nucleation and shape characteristics of nucleated cavities could be studied.

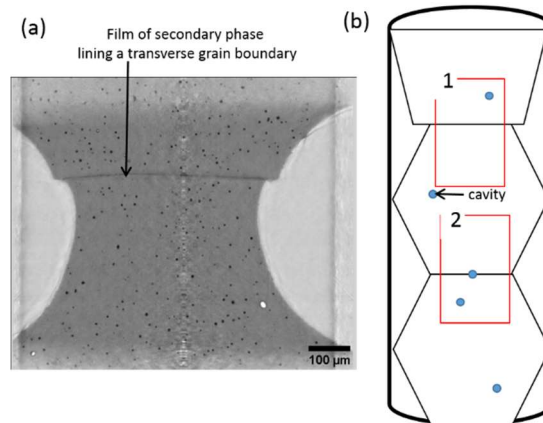


Figure P. 3 (a) Example of a transverse section of Al-cu alloys observed via low resolution tomography with thin film of second phase lining a transverse grain boundary (b) schematic showing an ideal design of sample using FIB cutting cavities are shown in blue. The red boxed highlight two ROI in which in situ studies can be made

A ROI with small pre-existing cavities on the grain boundary (ROI 2 in Figure P. 3 b) can be used to indirectly measure the grain boundary diffusivity. On deforming such a sample under low strain rates and high temperature diffusion would be expected to drive cavity growth. Under such conditions the cavity growth rate can be used to indirectly measure the grain boundary diffusivity in the alloy.

- **Damage in nano composites and solid state transformation in model alloys**

One of the interests of this model alloy is that it is possible to control the microstructure. In this PhD we focused on Al-Cu with particles with 1.4 μm in radius but it is possible with a very short heat treatment to produce very fine particles (submicron in size) and thus investigate the damage in such nano-composites with controlled particle size.

Additionally the development of high temperature *in situ* nanotomography could also be used to investigate solid state transformation such as the growth and coalescence of theta precipitates during ageing.

- **Nuclear applications**

The developments made during the course of this PhD could be of interest for nuclear science as well. Since creep of components is a subject of vital importance, the development of generation IV nuclear power plant could benefit a lot from the fundamental knowledge of damage mechanism in 316L(N) enriched in B and N. For example, the understanding of the creep life time relies on fundamental micromechanical models which requires several parameters that can be obtained by post mortem nanotomography. Conducting *in situ* or interrupted *in situ* experiments in conditions where the life time is short can provide experimental information on nucleation, growth and coalescence of cavities during creep and validate such models. Furthermore, research on damage during creep of Oxide Dispersed Strengthened (ODS) materials could also benefit from *in situ* nanotomography through comparison of experimental data obtained with existing models.

Appendix A

Paganin based phase retrieval

Propagation based phase contrast imaging relies on propagation and interference of a spatially coherent beam passing through a sample. This beam when reaching the detector has both phase and attenuation information in it. Paganin proposed an approach to retrieve the phase shift information from this [120]. To understand this first we will look at the basics of image formation using X-rays:

When X-rays interact with an object, at each angle θ , the interaction can be described by a transmittance function T_θ :

$$T_\theta(x) = \exp[-B_\theta(x) + i\varphi_\theta(x)] \quad (\text{A.4.5})$$

Where, B_θ and φ_θ are the terms denoting attenuation (due to absorption) and phase shift suffered by X-rays, at an angle θ respectively. Now if u_{inc} represents the incident wave front, then after interaction with the object it would be given by u_0 :

$$u_0(x) = T_\theta(x) u_{inc}(x) \quad (\text{A.4.6})$$

After this interaction, the wave is propagated over a certain distance D until it reaches the detector. Incorporating this free space propagation based on Fresnel transform [151] using propagator P_D gives us:

$$u_{\theta,D}(x) = P_D(x) * u_0(x) \quad (\text{A.4.7})$$

Further on substituting equation (A.4.6) in this:

$$u_{\theta,D}(x) = T_{\theta,D}(x) = (T_\theta * P_D)(x) \quad (\text{A.4.8})$$

Considering a unitary wave front, that is $u_{inc}(x) = 1$. Hence the intensity of wave reaching the detector can be given by:

$$I_{\theta,D}(x) = |T_{\theta,D}(x)|^2 \quad (\text{A.4.9})$$

Paganin gave a formulation using this intensity to compute the phase shift incurred by it, given by:

$$\varphi(x) = \frac{\delta_r}{2\beta} \ln \left(\mathcal{F}^{-1} \left\{ \frac{\mathcal{F}(I_{\theta,D})}{1 + \pi\lambda D \frac{\delta_r}{\beta} \|f^2\|} \right\} \right) \quad (\text{A.4.10})$$

Where, where \mathcal{F} and \mathcal{F}^{-1} denotes the Fourier transform and its inverse, respectively; $I_{\theta,D}$ the intensity recorded at a distance D , the sample being rotated at an angle θ , λ the wavelength of the beam, f the coordinates in the Fourier domain, δ_r the refractive index decrement and β the absorption index of the object. This formula relies on the Transport of Intensity Equation that assumes a small propagation distance D , and that the object is homogenous.

Template: phase retrieval (iterative Paganin method)

A template of the typical code for phase retrieval used during phase retrieval using iterative Paganin method is given below:

```
function [] = ht_tricome_25nm(varargin)
```

```
global FT_CENTRALPART
```

```
FT_CENTRALPART = 0
```

```
switch nargin
```

```
    case 0
```

```
        projections = [];
```

```
    case 1
```

```
        switch length(varargin{1})
```

```
            case 0
```

```
                projections = [];
```

```

        case 2
            projections = varargin{1}(1):varargin{1}(2);
        otherwise
            projections = varargin{1};
        endswitch
endswitch

#####
#### info on scan ####
#####

#####

##REMEMBER TO CHANGE!!!
## 1.    sx0h    ,sx0v,    z1_2    2.    Energy    3.
correct_distortion_par{k}.filename 4. delta beta

# filenames
nvue= 360; #!
refon= 361; #!
dir=  "/data/id16b/inhouse3//richi_oct18/AlCu_Z_ordered/"; #
with / at the end
namestr= "AlCu_Z_tensileHR3_001_01";
numbers= [1 ];
vers=''; # will be added to name of phase maps to distinguish
different versions

```

```

#####

sx0h = 1.000911030565047; #1.077165773192669 for 75nm.
sx0v = 0.9880788736304761; #1.110243284221266 for 75nm.
z1_2 = 0.5609882118862128; # total distance focus- detector

sx = ht_get_motorpos(dir,namestr,numbers,"sx"); # read
distances on the fly# 44.2438
z1h = (sx-sx0h)/1000; # distance source-sample
z1v = (sx-sx0v)/1000; # distance source-sample
check_z1v = 0; # determine z1v # 1 : checks vertical direction
(case ID19) ; # 2 checks both directions
magnification = 1; # consider finite distance of source
(spherical wave)
z2h = z1_2 - z1h; #!
z2v = z1_2 - z1v; #!
magnification_large = 1; # 0 parallel 1 projection -1 for
finding pos_feature
correct_shrink = 0;

#####

# wavelength
energy = 17.5; # energy in kev
lambda = 12.4e-10/energy; #!
printf("Energy is %g kev ; wavelength is %g Ang\n", energy,
lambda*1e10)

#####

```

```

# pixelsize
pixelsize = 2*6.5e-07; #!

#####

# optics
optic_used = "OP10x04LS020"; # see mncf #!
oversamp = 1; #!
correct_detector = 0; # correction for detector or not
correct_ccd = 'correct_ccd_4Mdsp';
correct_ccd_par =
header2correctccdpar(header(sprintf('%s/%s_1_/%s_1_%4.4i.edf',
dir,namestr,namestr,0)));
correct_distortion = []; #'ht_undistort2';
detector_distortion_prefix =
'/data/id16b/inhouse1/archive/optique_peter_distortion/detecto
r_distortion2d_';
for k = 1:length(numbers)
    correct_distortion_par{k}.filenameh = sprintf('%sh.edf',
detector_distortion_prefix);
    correct_distortion_par{k}.filenameev = sprintf('%sv.edf',
detector_distortion_prefix);
    correct_distortion_par{k}.filename =
sprintf('/data/id16b/inhouse3/richi_oct18/talbotgrid2/talbotgr
id_50nm_bin2edf_/grid_distortion_%d_.mat', numbers(k));
endfor
remove_spikes = 0.04;
correct_flat = 'distorted_flat'

#####

```

```

##### info on reconstruction #####
#####

# number of pixels (in reconstructed image)
n = 1080; # vertical, row, y
m = 1280; # horizontal, column, x
vb = 1; # first pixel in vertical direction
hb = 1; # first pixel in horizontal direction
pad_images = [2160 2560]; # pad images to nearest power of two
or give sizes

#####

#### shifts #####
#####

shift = 0; # set to 1 to determine the shifts, set to 0 if
they are determined and stored in rhapp.mat
reference_quali = 0; # set to 1: does quali90 for all scans to
see which moves less
reference_plane = 1; # plane with respect to which other
planes will be aligned
reference_moved = 0; # take into account motion of reference
plane or not
centralpart = 0;
shift_iterative = 0;

#####

#### approach ####

```

```

#####

# only correction of shifts
# 0 no phase reconstruction
# only phase
# 1 pamsin
# phase + absorption
# 2 pamsin with absorption (absorption is slow envelope)
(division by absorption)
# 3 pamcossin (absorption is weak)
# 4 mixture tie / pamsin
# 5 TIE with absorption
# 8 Paganin

approach = 8
paganin_multiple_distance = 1
delta_beta = 183
var_cut = 1;
recursive = 1;
recursive_purephase = 5;
recursive_constrain_grad = 0.5;
nloopm = 10

#####

# limits for 'wiener' filtering

```

```
lim1 = 10^-20 # low frequencies
lim2 = 0.01
axisposition = 'accurate'
holotomo_slave
```

Appendix B

Reconstruction: Filtered Back Projection (FBP)

A simple back projection is spreading the projection in the object domain and then integrating them over all angle. This process can be represented by the following equation where the sum of all projections p_θ over angle θ is given by:

$$f_{bp} = \int p_\theta(x \cos\theta + y \sin\theta) d\theta \quad (\text{B.1})$$

Pictorially this can be seen in Figure B 1 where summing of various projections leads to reconstruction of a blurry circle, where the circle was the initial object. However it can be seen that the image is blurred, this is mainly due to over sampling of low frequencies.

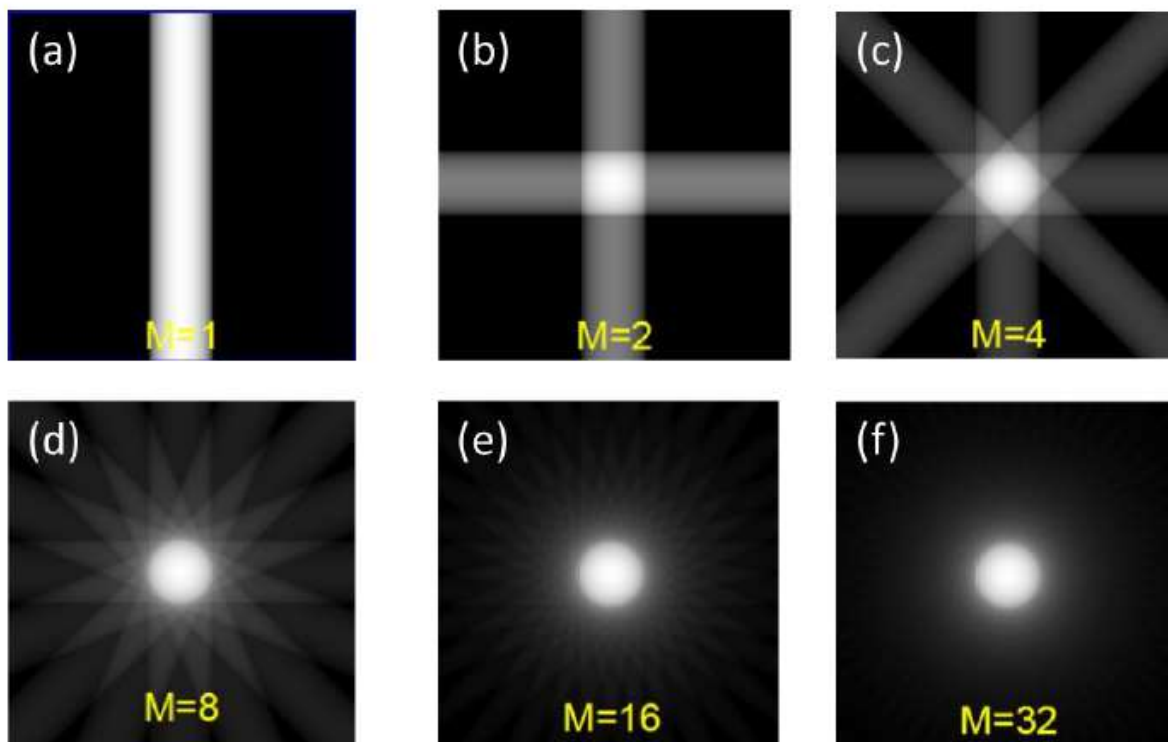


Figure B 1 Illustration of the reconstruction of a circle by simple back projection where M gives the number of projection (a) 1 projection, (b) 2 projections, (c) 4 projections, (d) 8 projections, (e) 16 projections and (f) 32 projections. A halo is visible around the circle on (f). [152]

To tackle this problem the projections are filtered using a high pass filter in the Fourier domain of the detector function which involves Fourier transforming the projections and multiplying by a high frequency filter $|\omega|$. The inverse transform of this is then back projected to given the object. This is schematically represented in Figure B 2, where the projections: p_θ are Fast Fourier transformed (FFT) into P_θ and then a filter: $|\omega|$ is applied on it giving a new function: Q_θ . This is then inverse transformed (IFFT) into a filtered detector function q_θ , which is given by:

$$q_\theta = \int P_\theta \omega |\omega| e^{i2\pi\omega t} d\omega \quad (B.2)$$

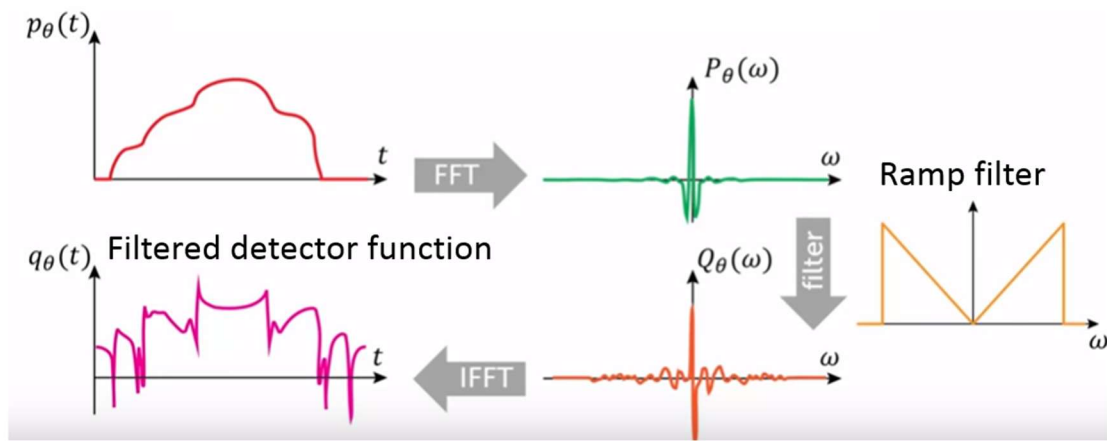


Figure B 2 Flowchart depicting steps used in the filtered back projection of radiographs. Source: "Computed Tomography and the ASTRA Toolbox" training course, developed at the Vision Lab at the University of Antwerp, Belgium (<http://visielab.uantwerpen.be>)

The filtered back projection f_{fbp} is simply the back projection of this filtered radiographs over the object domain and is given by:

$$f_{fbp} = \int q_\theta(x \cos\theta + y \sin\theta) d\theta \quad (B.3)$$

A typical parameter file that has been used for reconstruction, using PyHST2 [125] software is given below. This includes a typical ring parameter correction regime that was adopted for the 3D volumes in this text.

Template: reconstruction using FBP and ring artefact correction

```

## PYHST PARAMETER FILE

## Parameters defining the projection file series
FILE_PREFIX
/data/id16b/inhouse3//richi_oct18/AlCu_Z_ordered/AlCu_Z_tensileHR3_001_01_/AlCu_Z_tensileHR3_001_01_
NUM_FIRST_IMAGE = 0 # No. of first projection file
NUM_LAST_IMAGE = 359 # No. of last projection file
TRYEDFCONSTANTHEADER = 0 # assume constant edf header size
NUMBER_LENGTH_VARIES = NO
LENGTH_OF_NUMERICAL_PART = 4 # No. of characters
FILE_POSTFIX = .edf
FILE_INTERVAL = 1 # Interval between input files

## Parameters defining the projection file format
NUM_IMAGE_1 = 1280 # Number of pixels horizontally
NUM_IMAGE_2 = 1080 # Number of pixels vertically
IMAGE_PIXEL_SIZE_1 = 0.0997649 # Pixel size horizontally (microns)
IMAGE_PIXEL_SIZE_2 = 0.0997649 # Pixel size vertically

## Parameters defining background treatment
SUBTRACT_BACKGROUND = NO # No background subtraction
BACKGROUND_FILE = N.A.

## Parameters defining flat-field treatment
CORRECT_FLATFIELD = NO # No flat-field correction
FLATFIELD_CHANGING = N.A.
FLATFIELD_FILE = N.A.
FF_PREFIX = N.A.
FF_NUM_FIRST_IMAGE = N.A.
FF_NUM_LAST_IMAGE = N.A.

```

```

FF_NUMBER_LENGTH_VARIES = N.A.
FF_LENGTH_OF_NUMERICAL_PART = N.A.
FF_POSTFIX = N.A.
FF_FILE_INTERVAL = N.A.

TAKE_LOGARITHM = NO # Take log of projection values

## Parameters defining experiment
ANGLE_BETWEEN_PROJECTIONS = 0.500000 # Increment angle in
degrees
ROTATION_VERTICAL = YES
ROTATION_AXIS_POSITION = 629.32 # Position in pixels

## Parameters defining reconstruction
OUTPUT_SINOGRAMS = NO # Output sinograms to files or not
OUTPUT_RECONSTRUCTION = YES # Reconstruct and save or not
START_VOXEL_1 = 1 # X-start of reconstruction volume
START_VOXEL_2 = 1 # Y-start of reconstruction volume
START_VOXEL_3 = 1 # Z-start of reconstruction volume
END_VOXEL_1 = 1280 # X-end of reconstruction volume
END_VOXEL_2 = 1280 # Y-end of reconstruction volume
END_VOXEL_3 = 1080 # Z-end of reconstruction volume
OVERSAMPLING_FACTOR = 4 # 0 = Linear, 1 = Nearest pixel
ANGLE_OFFSET = 0.000000 # Reconstruction rotation offset angle
in degrees

## Parameters extra features PyHST
DO_CCD_FILTER = NO # CCD filter (spikes)
CCD_FILTER = "CCD_Filter"
CCD_FILTER_PARA = {"threshold": 0.040000 }
DO_SINO_FILTER = NO # Sinogram filter (rings)
SINO_FILTER = "SINO_Filter"

```

```

ar = Numeric.ones(1280,'f')
ar[0]=0.0
ar[2:18]=0.0
SINO_FILTER_PARA = {"FILTER": ar }
DO_AXIS_CORRECTION = NO # Axis correction
AXIS_CORRECTION_FILE = correct.txt
OPTIONS= { 'padding':'E' , 'axis_to_the_center':'Y' ,
'avoidhalftomo':'N'} # Padding and position axis
ZEROOFFMASK = 1 # Mask to zero region that is not covered by
field of view
#IGNORE_FILE = ignore_angles.txt
FBFILTER = 0 #

## Parameters defining output file / format
OUTPUT_FILE
/data/id16b/inhouse3//richi_oct18/AlCu_z_ordered/volfloat/AlCu
_z_tensileHR3_001_01_.vol

## Reconstruction program options
DISPLAY_GRAPHICS = NO # No images
#####
#####RING CORRECTIONS
#####
#####----Double flat field correction
DOUBLEFFCORRECTION = "projectionsmean.edf"
#####---- Munch correction
FW_LEVELS = 6
FW_SIGMA = 3.0
FW_WNAME = "sym4" # larger wavelet for large rings
W_SWT = 1 # use stationary wavelet transform
STRAIGHTEN_SINOS = 1 # "subtract background" to avoid large
grey levels near the edges
#####-----Dering correction

```

```
DO_RING_FILTER = 1
DO_SINO_FILTER = 1 # Compatibility
RFILTER_TYPE = "RING_Filter"
RING_FILTER = RFILTER_TYPE
SINO_FILTER = RFILTER_TYPE # Compatibility
```

The parameters used for post proceeding ring filter correction in Figure 2.15 (b) is given below:

| | |
|------------------|----------|
| preset | = MR |
| reconstruction | = normal |
| general_filter | = 0 |
| rec_overwrite | = 0 |
| scan_suffix | = none |
| dir | = auto |
| clean_radix | = auto |
| dirlist | = auto |
| input_file_type | = auto |
| output_format | = raw |
| output_data_type | = 8 |
| compression | = none |
| jp2factor | = 0 |
| minmax | = [0,0] |
| cropxy | = [1,1] |
| binning | = 0 |
| autocrop | = 0 |
| rotate_im | = 0 |
| overwrite | = 0 |
| series | = 0 |
| multiseries | = 0 |
| basic_overlap | = 0 |
| research_range | = 10 |
| skip | = 5 |

```
ring = 1
median_size = 70
number_of_pass = 4
structure_removal_level = 0.4
blur_angle = 15
fusion_angle = 15
strong_rings = 10
double_polar_corr = 1
visualization = 0
test = 0
remove_EDF = 0
access_permission = 777
%endofinfo-----
-----
```

Appendix C

Examples of threshold used for segmentation of different phases

| Sample | Phase | Threshold Value | Method |
|---------------|-----------------------|------------------------|---|
| Al-Cu | Cavity | 200-255 | Average of iterative intermeans threshold |
| Al-Cu | Second phase particle | 0-124 | Average of iterative intermeans threshold |
| AZ31 | Cavity | 158-255 | Edge detection method |
| AZ31 | Intermetallic | 0-85 | Average of iterative intermeans threshold |

Appendix D

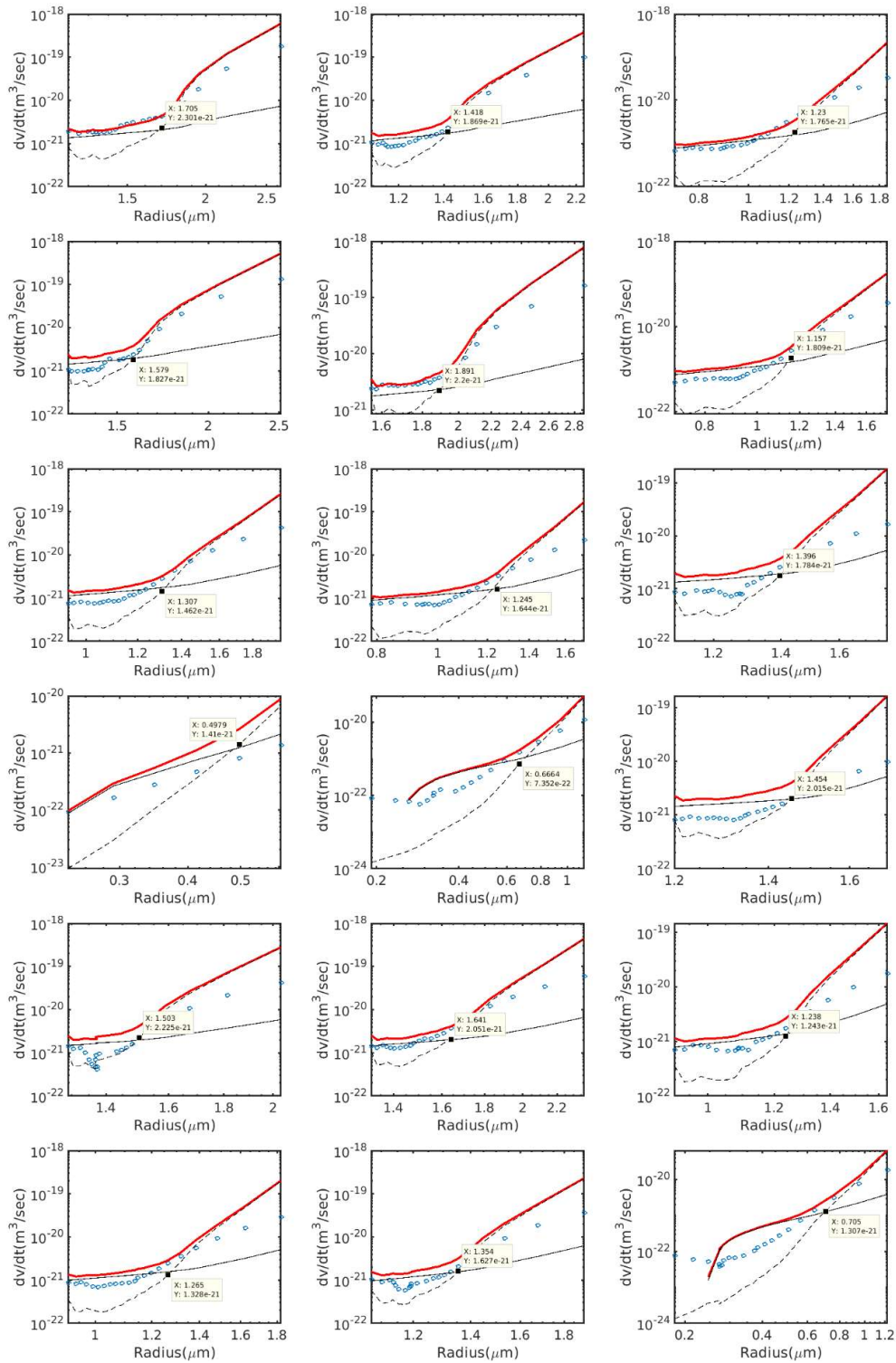


Figure D 1 Plot of cavity growth rate (dV/dt) versus equivalent radius, showing comparison of experimental cavity growth data with diffusion and plasticity based cavity growth models in AC5 sample for 18 tracked cavities. The inter cavity spacing ($2l$) used in calculation has also

been indicated for each cavity. Transition radius obtained from the models are indicated for each plot.

Bibliography

- [1] B.L. Mordike, T. Ebert, Magnesium Properties - applications - potential, *Mater. Sci. Eng. A.* 302 (2001) 37–45. [https://doi.org/10.1016/S0921-5093\(00\)01351-4](https://doi.org/10.1016/S0921-5093(00)01351-4).
- [2] Z. Yang, J.P. Li, J.X. Zhang, G.W. Lorimer, J. Robson, Review on Research and Development of Magnesium Alloys, *Acta Metall. Sin. (English Lett.* 21 (2008) 313–328. [https://doi.org/10.1016/S1006-7191\(08\)60054-X](https://doi.org/10.1016/S1006-7191(08)60054-X).
- [3] S. Toros, F. Ozturk, I. Kacar, Review of warm forming of aluminum-magnesium alloys, *J. Mater. Process. Technol.* 207 (2008) 1–12. <https://doi.org/10.1016/j.jmatprotec.2008.03.057>.
- [4] G.S. Cole, A.M. Sherman, Light weight materials for automotive applications, *Mater. Charact.* 35 (1995) 3–9. [https://doi.org/10.1016/1044-5803\(95\)00063-1](https://doi.org/10.1016/1044-5803(95)00063-1).
- [5] A. Varloteaux, J.J. Blandin, M. Suéry, Control of cavitation during superplastic forming of high strength aluminium alloys, *Mater. Sci. Technol.* 5 (1989) 1109–1117. <https://doi.org/10.1179/mst.1989.5.11.1109>.
- [6] J.J. Blandin, Superplastic Forming of Magnesium Alloys: Production of Microstructures, Superplastic Properties, Cavitation Behaviour, *Mater. Sci. Forum.* 551–552 (2007) 211–217. <https://doi.org/10.4028/www.scientific.net/msf.551-552.211>.
- [7] M.E. Kassner, T.A. Hayes, Creep cavitation in metals, *Int. J. Plast.* 19 (2003) 1715–1748. [https://doi.org/10.1016/S0749-6419\(02\)00111-0](https://doi.org/10.1016/S0749-6419(02)00111-0).
- [8] A.J. Perry, Cavitation in creep, *J. Mater. Sci.* 9 (1974) 1016–1039. <https://doi.org/10.1007/BF00570398>.
- [9] R. Raj, Nucleation of cavities at second phase particles in grain boundaries, *Acta Metall.* 26 (1978) 995–1006. [https://doi.org/10.1016/0001-6160\(78\)90050-0](https://doi.org/10.1016/0001-6160(78)90050-0).

- [10] J. He, R. Sandström, Creep cavity growth models for austenitic stainless steels, *Mater. Sci. Eng. A.* 674 (2016) 328–334. <https://doi.org/10.1016/j.msea.2016.08.005>.
- [11] H. Toda, Z. Azri, B. Shamsudin, K. Shimizu, K. Uesugi, Cavitation during high-temperature deformation in Al – Mg alloys, *Acta Mater.* 61 (2013) 2403–2413. <https://doi.org/10.1016/j.actamat.2013.01.012>.
- [12] P. Lhuissier, M. Scheel, L. Salvo, M. Di Michiel, J.J. Blandin, Continuous characterization by X-ray microtomography of damage during high-temperature deformation of magnesium alloy, *Scr. Mater.* 69 (2013) 85–88. <https://doi.org/10.1016/j.scriptamat.2013.03.001>.
- [13] H.M.M.A. Rashed, J.D. Robson, P.S. Bate, B. Davis, Application of X-ray microtomography to analysis of cavitation in AZ61 magnesium alloy during hot deformation, *Mater. Sci. Eng. A.* 528 (2011) 2610–2619. <https://doi.org/10.1016/j.msea.2010.11.083>.
- [14] A. Isaac, F. Sket, W. Reimers, B. Camin, G. Sauthoff, A.R. Pyzalla, In situ 3D quantification of the evolution of creep cavity size, shape, and spatial orientation using synchrotron X-ray tomography, *Mater. Sci. Eng. A.* 478 (2008) 108–118. <https://doi.org/10.1016/j.msea.2007.05.108>.
- [15] K. Dzieciol, A. Borbély, F. Sket, A. Isaac, M. Di Michiel, P. Cloetens, T. Buslaps, A.R. Pyzalla, Void growth in copper during high-temperature power-law creep, *Acta Mater.* 59 (2011) 671–677. <https://doi.org/10.1016/j.actamat.2010.10.003>.
- [16] A. Pyzalla, B. Camin, T. Buslaps, M. Di Michiel, H. Kaminski, A. Kottar, A. Pernack, W. Reimers, Simultaneous Tomography and Diffraction Analysis of Creep Damage, *Science* (80-.). 308 (2005) 92 LP – 95. <http://science.sciencemag.org/content/308/5718/92.abstract>.
- [17] P. Shahbeigi, A. Sarkar, K. Linga, H. Brody, R. Scattergood, Materials Science & Engineering A Grain boundary sliding mechanism during high temperature deformation of AZ31 Magnesium alloy, *Mater. Sci. Eng. A.* 669 (2016) 171–177. <https://doi.org/10.1016/j.msea.2016.05.076>.

- [18] P.S. Roodposhti, A. Sarkar, K.L. Murty, Fracture Behavior of AZ31 Magnesium Alloy During Low-Stress High-Temperature Deformation, *Metallogr. Microstruct. Anal.* 4 (2015) 91–101. <https://doi.org/10.1007/s13632-015-0189-1>.
- [19] C.J. Lee, J.C. Huang, Cavitation characteristics in AZ31 Mg alloys during LTSP or HSRSP, *Acta Mater.* 52 (2004) 3111–3122. <https://doi.org/10.1016/j.actamat.2004.03.012>.
- [20] R.B. Figueiredo, T.G. Langdon, Characteristics of cavitation in a superplastic magnesium AZ31 alloy processed by equal-channel angular pressing, *Rev. Adv. Mater. Sci.* 25 (2010) 249–255.
- [21] H.R. Abedi, A. Zarei-Hanzaki, S. Khoddam, Effect of γ precipitates on the cavitation behavior of wrought AZ31 magnesium alloy, *Mater. Des.* 32 (2011) 2181–2190. <https://doi.org/10.1016/j.matdes.2010.11.029>.
- [22] M.E. Kassner, M.-T. Pérez-Prado, Five-power-law creep in single phase metals and alloys, *Prog. Mater. Sci.* 45. 45 (2000) 1–102.
- [23] J. Bird, A.K. Mukherjee, J.E. Dorn, Correlations between high-temperature creep behavior and structure, in: *Int. Conf. Quant. Relat. Between Prop. Microstruct.*, 1969. <https://doi.org/10.1007/978-3-319-46448-0>.
- [24] F. MONKMAN, C., N.J. Grant, A Simple Relationship Between Minimum Creep Rate and Time to Fracture, *Proceeding ASTM.* 56 (1956) 593--596. <http://ci.nii.ac.jp/naid/10006401917/en/> (accessed February 4, 2019).
- [25] D.C. Dunand, B.Q. Han, a. M. Jansen, Monkman-grant analysis of creep fracture in dispersion-strengthened and particulate-reinforced aluminum, *Metall. Mater. Trans. A.* 30 (1999) 829–838. <https://doi.org/10.1007/s11661-999-1016-6>.
- [26] J.-P. Poirier, *Creep of crystals*, 1985.
- [27] C. Herring, Diffusional Viscosity of a Polycrystalline Solid, *J. Appl. Phys.* 21 (1950) 437–445. <https://doi.org/10.1063/1.1699681>.
- [28] F.R.N. Nabarro, *Report of conference on solids*, 1948.

- [29] R.. Coble, A model for boundary diffusion controlled creep in polycrystalline materials, *J. Appl. Phys.* 34 (1963). <https://doi.org/10.1063/1.1702656>.
- [30] J. Weertman, Theory of steady-state creep based on dislocation climb, *Journal Appl. Phys.* 26 (1995). <https://doi.org/10.1063/1.1721875>.
- [31] W.D. Nix, B. Ilschner, Mechanisms Controlling Creep of Single Phase Metals and Alloys, in: P. HAASEN, V. GEROLD, G. KOSTORZ (Eds.), *Strength Met. Alloy.*, Pergamon, 1979: pp. 1503–1530. <https://doi.org/https://doi.org/10.1016/B978-1-4832-8412-5.50243-5>.
- [32] S.F. Exell, D.H. Warrington, Sub-grain boundary migration in aluminium, *Philos. Mag. A J. Theor. Exp. Appl. Phys.* 26 (1972) 1121–1136. <https://doi.org/10.1080/14786437208227368>.
- [33] O.. Sherby, R.. Klundt, A.. Miller, Flow stress, subgrain size and subgrain stability at elevated temperature, *Metall. Trans. A.* 8A (1977) 843–580.
- [34] S.. Robinson, O.. Sherby, Mechanical behavior of polycrystalline tungsten at elevated temperature, *Acta Metall.* 17 (1969) 109–125.
- [35] A.M. Gervais, J.T. Norton, N.J. Grant, SUBGRAIN FORMATION IN HIGH-PURITY ALUMINUM DURING CREEP AT HIGH TEMPERATURES, *Trans. Metall. Soc. AIME.* 197 (1953) 1166.
- [36] C. Ahlquist, W.. Nix, A technique for measuring mean internal stress during high temperature creep, *Scr. Metall.* 3 (1969) 679–682.
- [37] R. Horiuchi, M. Otsuka, Mechanism of High Temperature Creep of Aluminum-Magnesium Solid Solution Alloys, *Trans. Japan Inst. Met.* 13 (1972) 284–293. <https://doi.org/10.2320/matertrans1960.13.284>.
- [38] J.J. Jonas, C.M. Sellars, W.J.M. Tegart, Strength and structure under hot-working conditions, *Metall. Rev.* 14 (1969) 1–24. <https://doi.org/10.1179/mtlr.1969.14.1.1>.
- [39] A.. Cottrell, M.A. Jaswon, Distribution of solute atoms round a slow dislocation, in: *R. Soc. London. Ser. A. Math. Phys. Sci.*, 1949: pp. 104–114.

- [40] T.G. Langdon, J. Wadsworth, Summary and topics of ICSAM-91, in: S. Hori, M. Tokizane, N. Furushiro (Eds.), *Superplast. Adv. Mater.*, The Japan Society for Research on Superplasticity, Osaka, Japan, 1991: p. 847.
- [41] A. Ball, M.M. Hutchison, Superplasticity in the Aluminium–Zinc Eutectoid, *Met. Sci. J.* 3 (1969) 1–7. <https://doi.org/10.1179/msc.1969.3.1.1>.
- [42] M. F. Ashby, R. A. Verrall, Diffusion-accommodated flow and superplasticity, *Acta Metall.* 21 (1973) 149–163. [https://doi.org/10.1016/0001-6160\(73\)90057-6](https://doi.org/10.1016/0001-6160(73)90057-6).
- [43] D. Lee, Structural changes during the superplastic deformation, *Metall. Trans.* 1 (1970) 309–311. <https://doi.org/10.1007/BF02819282>.
- [44] J. Harper, J.. Dorn, Viscous creep of aluminum near its melting temperature, *Acta Metall.* 5 (1957).
- [45] W. Blum, P. Eisenlohr, Dislocation mechanics of creep, 511 (2009) 7–13. <https://doi.org/10.1016/j.msea.2008.04.110>.
- [46] M.F. Ashby, A first report on deformation mechanism maps, *Acta Metall.* 20 (1972) 887–897.
- [47] H.J. Frost, M.F. Ashby, *Deformation-Mechanism Maps, The Plasticity and Creep of Metals and Ceramics*, 1982.
- [48] H. Hosokawa, H. Iwasaki, T. Mori, M. Mabuchi, T. Tagata, K. Higashi, Effects of Si on deformation behavior and cavitation of coarse-grained Al-4.5Mg alloys exhibiting large elongation, *Acta Mater.* 47 (1999) 1859–1867. [https://doi.org/10.1016/S1359-6454\(99\)00047-6](https://doi.org/10.1016/S1359-6454(99)00047-6).
- [49] R. Raj, M.F. Ashby, Intergranular fracture at elevated temperature, *Acta Metall.* 23 (1975) 653–666. [https://doi.org/10.1016/0001-6160\(75\)90047-4](https://doi.org/10.1016/0001-6160(75)90047-4).
- [50] L.E. Murr, *Interfacial Phenomena in Metals and Alloys*, Addison-Wesley Publishing Company, 1975.
- [51] A.H. Chokshi, A.K. Mukherjee, An analysis of cavity nucleation in superplasticity, *Acta Metall.* 37 (1989) 3007–3017.

[https://doi.org/10.1016/0001-6160\(89\)90337-4](https://doi.org/10.1016/0001-6160(89)90337-4).

- [52] A. Needleman, J.R. Rice, Plastic Creep Flow Effects in the Diffusive Cavitation of Grain Boundaries., *Acta Metall.* 28 (1980) 1315–1332. [https://doi.org/10.1016/0001-6160\(80\)90001-2](https://doi.org/10.1016/0001-6160(80)90001-2).
- [53] M.H. Yoo, H. Trinkaus, Crack and cavity nucleation at interfaces during creep, *Metall. Trans. A.* 14 (1983) 547–561. <https://doi.org/10.1007/BF02643772>.
- [54] C.W. Chen, E. Machlin, On a mechanism of high temperature intercrystalline cracking, *J. Od Met.* (1957) 829–835.
- [55] R.D. Gifkins, A Mechanism for the formation of intergranular cracks when boundary sliding occurs, *Acta Metall.* 4 (1956) 98–99.
- [56] B.F. Dyson, Constraints on diffusional cavity growth rates, *Met. Sci.* 10 (1976) 349–353. <https://doi.org/10.1179/030634576790431417>.
- [57] T.G. Nieh, W.D. Nix, A comparison of the dimple spacing on intergranular creep fracture surfaces with the slip band spacing for copper, *Scr. Metall.* 14 (1980) 365–368. [https://doi.org/10.1016/0036-9748\(80\)90360-9](https://doi.org/10.1016/0036-9748(80)90360-9).
- [58] D. Hull, D.E. Rimmer, The growth of grain- boundary voids under stress, *Philos. Mag.* 4 (1959) 673–687. <https://doi.org/10.1080/14786435908243264>.
- [59] W. Beere, M. Speight, Creep cavitation by vacancy diffusion in plastically deforming solid, *Met. Sci.* 12 (1978) 172–176. <https://doi.org/10.1179/msc.1978.12.4.172>.
- [60] J.R. Rice, Constraints on the diffusive cavitation of isolated grain boundary facets in creeping polycrystals, *Acta Metall.* 29 (1980) 675–681.
- [61] R. Raj, H.M. Shih, H.H. Johnson, CORRECTION TO: INTERGRANULAR FRACTURE AT ELEVATED TEMPERATURE, *Scr. Metall.* 11 (1977) 839–842.
- [62] J. Hancock, Creep cavitation without a vacancy flux, *Met. Sci.* 10 (1976) 319–325. <https://doi.org/10.1179/msc.1976.10.9.319>.
- [63] M.J. Stowell, Cavity growth in superplastic alloys, *Met. Sci.* 14 (1980) 267–272. <https://doi.org/10.1179/030634580790426373>.

- [64] I.W. Chen, Cavity growth on a sliding grain boundary, *Metall. Trans. A.* 14 (1983) 2289–2293. <https://doi.org/10.1007/BF02663303>.
- [65] H. Riedel, *Fracture of high temperature*, 1987.
- [66] A.H. Chokshi, T.G. Langdon, A model for diffusional cavity growth in superplasticity, *Acta Metall.* 35 (1987) 1089–1101. [https://doi.org/10.1016/0001-6160\(87\)90056-3](https://doi.org/10.1016/0001-6160(87)90056-3).
- [67] J.R. Rice, Constraints on the diffusive cavitation of isolated grain boundary facets in creeping polycrystals, *Acta Metall.* 29 (1980) 675–681.
- [68] G.. Long, P.R. Jemian, J.. Weertman, D.R. Black, H.E. Burdette, R. Spal, High-Resolution Small-Angle X-ray Scattering Camera for Anomalous Scattering, *J. Applied Crystallogr.* (1991) 30–37. <https://doi.org/10.1107/S0021889890009256>.
- [69] W.E. Luecke, S.M. Wiederhorn, B.J. Hockey, R.F. Krause Jr, G.. Long, Cavitation contributes substantially to tensile creep in silicon nitride, *J. Am. Ceram. Soc.* 78 (1995) 2085–2096.
- [70] P.J. Bouchard, F. Fiori, W. Treimer, Characterisation of creep cavitation damage in a stainless steel pressure vessel using SANS, *Appl. Phys. A Mater. Sci. Process. A* 74 (2002) S1689–S1691.
- [71] P.J. Bouchard, P.J. Withers, S.A. McDonald, R.K. Heenan, Quantification of creep cavitation damage around a crack in a stainless steel pressure vessel, *Acta Mater.* 52 (2004) 23–34. <https://doi.org/10.1016/j.actamat.2003.08.022>.
- [72] F. Fiori, G. Albertini, E. Girardin, A. Giuliani, A. Manescu, F. Rustichelli, Neutron and synchrotron radiation non-destructive methods for the characterisation of materials for different applications, *J. Alloys Compd.* 382 (2004) 39–45. <https://doi.org/10.1016/j.jallcom.2004.05.071>.
- [73] D.A. Woodford, A parametric approach to creep damage, *Met. Sci. J.* 3 (1969) 50–53. <https://doi.org/10.1179/msc.1969.3.1.50>.
- [74] D.A. Woodford, Density changes during creep in nickel, *Met. Sci. J.* 3 (1969) 234–240. <https://doi.org/10.1179/msc.1969.3.1.234>.

- [75] D.A. Miller, T.G. Langdon, An analysis of cavity growth during superplasticity, *Metall. Trans. A.* 10 (1979) 1869–1874. <https://doi.org/10.1007/BF02811731>.
- [76] X. Du, J. Zhu, Y. Kim, Microstructural characterization of creep cavitation in a fully-lamellar TiAl alloy, 9 (2001) 137–146.
- [77] G. Eggeler, J.C. Earthman, N. Nilsvang, MICROSTRUCTURAL STUDY OF CREEP RUPTURE IN A 12 % CHROMIUM FERRITIC STEEL, 37 (1989) 49–60.
- [78] L. Salvo, P. Cloetens, E. Maire, S. Zabler, J.J. Blandin, J.Y. Buffière, W. Ludwig, E. Boller, D. Bellet, C. Josserond, X-ray micro-tomography: an attractive characterization technique in materials science, *Nucl. Instruments Methods Phys.* 200 (2003) 273–286.
- [79] J.Y. Buffière, E. Maire, P. Cloetens, G. Lormand, R. Fougères, Characterization of internal damage in a MMCp using X-ray synchrotron phase contrast microtomography, *Acta Mater.* 47 (1999) 1613–1625. [https://doi.org/10.1016/S1359-6454\(99\)00024-5](https://doi.org/10.1016/S1359-6454(99)00024-5).
- [80] T.L. Burnett, R. Geurts, H. Jazaeri, S.M. Northover, S.A. McDonald, S.J. Haigh, P.J. Bouchard, P.J. Withers, Multiscale 3D analysis of creep cavities in AISI type 316 stainless steel, *Mater. Sci. Technol.* 31 (2015) 522–534. <https://doi.org/10.1179/1743284714Y.0000000639>.
- [81] E.N. Landis, D.T. Keane, X-ray microtomography, *Mater. Charact.* 61 (2010) 1305–1316. <https://doi.org/10.1016/j.matchar.2010.09.012>.
- [82] B.P. Flannery, W.G. Roberge, Observational strategies for three-dimensional synchrotron microtomography, *J. Appl. Phys.* 4668 (1998) 1–8. <https://doi.org/10.1063/1.339016>.
- [83] O. Betz, U. Wegst, D. Weide, M. Heethoff, L. Helfen, W.-K. Lee, P. Cloetens, Imaging applications of synchrotron X-ray phase-contrast microtomography in biological morphology and biomaterials science., *J. Microsc.* 227 (2007) 51–71. <https://doi.org/10.1111/j.1365-2818.2007.01785.x>.
- [84] P. Cloetens, W. Ludwig, J. Baruchel, D. Van Dyck, J. Van Landuyt, J.P.

- Guigay, M. Schlenker, Holotomography: Quantitative phase tomography with micrometer resolution using hard synchrotron radiation x rays, *Appl. Phys. Lett.* 75 (1999) 2912. <https://doi.org/10.1063/1.125225>.
- [85] H.F.T.E. F.R.S., LXXVI. Facts relating to optical science. No. IV, London, Edinburgh, Dublin Philos. Mag. J. Sci. 9 (1836) 401–407. <https://doi.org/10.1080/14786443608649032>.
- [86] W.K. Epting, J. Gelb, S. Litster, Resolving the three-dimensional microstructure of polymer electrolyte fuel cell electrodes using nanometer-scale X-ray computed tomography, *Adv. Funct. Mater.* 22 (2012) 555–560. <https://doi.org/10.1002/adfm.201101525>.
- [87] J.A. Dunlop, S. Wirth, D. Penney, A. Mcneil, R.S. Bradley, P.J. Withers, R.F. Preziosi, A minute fossil phoretic mite recovered by phase-contrast X-ray computed tomography, (2012) 457–460.
- [88] C.F. Martin, C. Josserond, L. Salvo, J.J. Blandin, P. Cloetens, E. Boller, Characterization by X-ray micro-tomography of cavity coalescence during superplastic deformation, *Scr. Mater.* 42 (2000) 375–381. [https://doi.org/10.1016/S1359-6462\(99\)00355-3](https://doi.org/10.1016/S1359-6462(99)00355-3).
- [89] P. Lhuissier, A. Villanueva Fernandez, L. Salvo, J.J. Blandin, High Temperature Deformation and Associated 3D Characterisation of Damage in Magnesium Alloys, *Mater. Sci. Forum.* 706–709 (2012) 1128–1133. <https://doi.org/10.4028/www.scientific.net/MSF.706-709.1128>.
- [90] H.M.M.A. Rashed, J.D. Robson, P.S. Bate, B. Davis, Application of X-ray microtomography to analysis of cavitation in AZ61 magnesium alloy during hot deformation, *Mater. Sci. Eng. A.* 528 (2011) 2610–2619. <https://doi.org/10.1016/j.msea.2010.11.083>.
- [91] F. Sket, A. Isaac, K. Dzieciol, G. Sauthoff, A. Borbély, A.R. Pyzalla, In situ tomographic investigation of brass during high-temperature creep, *Scr. Mater.* 59 (2008) 558–561. <https://doi.org/10.1016/j.scriptamat.2008.05.006>.
- [92] E. Maire, V. Carmona, J. Courbon, W. Ludwig, Fast X-ray tomography and acoustic emission study of damage in metals during continuous tensile tests,

- Acta Mater. 55 (2007) 6806–6815.
<https://doi.org/10.1016/j.actamat.2007.08.043>.
- [93] H. Fang, C.D. Versteyleen, S. Zhang, Y. Yang, P. Cloetens, D. Ngan-Tillard, E. Brück, S. van der Zwaag, N.H. van Dijk, Autonomous filling of creep cavities in Fe-Au alloys studied by synchrotron X-ray nano-tomography, *Acta Mater.* 121 (2016) 352–364. <https://doi.org/10.1016/j.actamat.2016.09.023>.
- [94] J. Villanova, R. Daudin, P. Lhuissier, D. Jauffrès, S. Lou, C.L. Martin, S. Labouré, R. Tucoulou, G. Martínez-Criado, L. Salvo, Fast in situ 3D nanoimaging: a new tool for dynamic characterization in materials science, *Mater. Today* 20 (2017) 354–359. <https://doi.org/10.1016/j.mattod.2017.06.001>.
- [95] A.H. Chokshi, The development of cavity growth maps for superplastic materials, *J. Mater. Sci.* 21 (1986) 2073–2082. <https://doi.org/10.1007/BF00547949>.
- [96] M. Arai, T. Ogata, A. Nitta, Continuous observation of cavity growth and coalescence by creep fatigue tests in SEM, *JSME Int. J.* 39 (1996).
- [97] A. Isaac, K. Dzieciol, F. Sket, A. Borbely, In-Situ microtomographic characterization of single-cavity growth during high-temperature creep of leaded brass, *Metall. Mater. Trans. A.* 42A (2011) 3022–3030. <https://doi.org/10.1007/s11661-011-0781-1>.
- [98] D. Kurumlu, E.J. Payton, M.L. Young, M. Schöbel, G. Requena, G. Eggeler, High-temperature strength and damage evolution in short fiber reinforced aluminum alloys studied by miniature creep testing and synchrotron microtomography, *Acta Mater.* 60 (2012) 67–78. <https://doi.org/10.1016/j.actamat.2011.09.022>.
- [99] K.S. Cheong, K.J. Stevens, Y. Suzuki, K. Uesugi, A. Takeuchi, The effects of microstructure on creep behaviour-A study through synchrotron X-ray tomography, *Mater. Sci. Eng. A.* 513–514 (2009) 222–227. <https://doi.org/10.1016/j.msea.2009.02.021>.
- [100] R.B. Figueiredo, S. Terzi, T.G. Langdon, Using X-ray microtomography to

- evaluate cavity formation in a superplastic magnesium alloy processed by equal-channel angular pressing, *Acta Mater.* 58 (2010) 5737–5748. <https://doi.org/10.1016/j.actamat.2010.06.049>.
- [101] P. Lhuissier, L. Salvo, J.J. Blandin, Parameters Controlling High Temperature Deformability of Wrought Magnesium Alloys, *Mater. Sci. Forum.* 783–786 (2014) 352–357. <https://doi.org/10.4028/www.scientific.net/msf.783-786.352>.
- [102] T.J.A. Slater, R.S. Bradley, G. Bertali, R. Geurts, S.M. Northover, M.G. Burke, S.J. Haigh, T.L. Burnett, P.J. Withers, Multiscale correlative tomography: An investigation of creep cavitation in 316 stainless steel, *Sci. Rep.* 7 (2017) 1–10. <https://doi.org/10.1038/s41598-017-06976-5>.
- [103] A. Pyzalla, B. Camin, T. Buslaps, M. Di Michiel, H. Kaminski, A. Kottar, A. Pernack, W. Reimers, Simultaneous tomography and diffraction analysis of creep damage, *Science* (80-.). 308 (2005) 92–95. <https://doi.org/10.1126/science.1106778>.
- [104] R. Boissière, J.J. Blandin, L. Salvo, Damage Development During Superplasticity of Light Alloys, *J. Eng. Mater. Technol.* 130 (2008) 021014. <https://doi.org/10.1115/1.2884335>.
- [105] H. Toda, Z.A. Bin Shamsudin, K. Shimizu, K. Uesugi, A. Takeuchi, Y. Suzuki, M. Nakazawa, Y. Aoki, M. Kobayashi, Cavitation during high-temperature deformation in Al-Mg alloys, *Acta Mater.* 61 (2013) 2403–2413. <https://doi.org/10.1016/j.actamat.2013.01.012>.
- [106] J.-B. Graverend, J. Adrien, J. Cormier, Ex-situ X-ray tomography characterization of porosity during high-temperature creep in a Ni-based single-crystal superalloy: Toward understanding what is damage, *Mater. Sci. Eng. A.* 695 (2017) 367–378.
- [107] Z. Asghar, G. Requena, H.P. Degischer, P. Cloetens, Three-dimensional study of Ni aluminides in an AlSi12 alloy by means of light optical and synchrotron microtomography, *Acta Mater.* 57 (2009) 4125–4132. <https://doi.org/10.1016/j.actamat.2009.05.010>.
- [108] A.A. Wahab, C.R. Hutchinson, M. V. Kral, A three-dimensional characterization

- of creep void formation in hydrogen reformer tubes, *Scr. Mater.* 55 (2006) 69–73. <https://doi.org/10.1016/j.scriptamat.2006.02.045>.
- [109] L.-Y. Wang, Z.-M. Song, L. Xue-Mei, G.-P. Zhang, 3D X-ray tomography characterization of creep cavities in small-punch tested 316 stainless steels, *Mater. Sci. Eng. A.* 724 (2018) 69–74.
- [110] E. Maire, V. Carmona, J. Courbon, W. Ludwig, Fast X-ray tomography and acoustic emission study of damage in metals during continuous tensile tests, *Acta Mater.* 55 (2007) 6806–6815. <https://doi.org/10.1016/j.actamat.2007.08.043>.
- [111] P. Lhuissier, M. Scheel, L. Salvo, M. Di Michiel, J.J. Blandin, Continuous characterization by X-ray microtomography of damage during high-temperature deformation of magnesium alloy, *Scr. Mater.* 69 (2013) 85–88. <https://doi.org/10.1016/j.scriptamat.2013.03.001>.
- [112] A. Isaac, F. Sket, W. Reimers, B. Camin, G. Sauthoff, A.R. Pyzalla, In situ 3D quantification of the evolution of creep cavity size, shape, and spatial orientation using synchrotron X-ray tomography, *Mater. Sci. Eng. A.* 478 (2008) 108–118. <https://doi.org/10.1016/j.msea.2007.05.108>.
- [113] G.C. Requena, P. Degischer, E.D. Marks, E. Boller, Microtomographic study of the evolution of microstructure during creep of an AlSi12CuMgNi alloy reinforced with Al₂O₃ short fibres, *Mater. Sci. Eng. A.* 487 (2008) 99–107. <https://doi.org/10.1016/j.msea.2007.10.016>.
- [114] T. Dessolier, Effet de la température sur les hétérogénéités de déformation plastique dans les alliages de magnésium Effect of the temperature on the heterogeneities of deformation in magnesium alloys. PhD thesis, Université Grenoble Alpes, 2018.
- [115] D.L. Yin, K.F. Zhang, G.F. Wang, W.B. Han, Superplasticity and cavitation in AZ31 Mg alloy at elevated temperatures, *Mater. Lett.* 59 (2005) 1714–1718. <https://doi.org/10.1016/j.matlet.2005.01.053>.
- [116] G. Martinez-Criado, J. Villanova, R. Tucoulou, D. Salomon, J.P. Suuronen, S. Laboure, C. Guilloud, V. Valls, R. Barrett, E. Gagliardini, Y. Dabin, R. Baker, S.

- Bohic, C. Cohen, J. Morse, ID16B: A hard X-ray nanoprobe beamline at the ESRF for nano-analysis, *J. Synchrotron Radiat.* 23 (2016) 344–352. <https://doi.org/10.1107/S1600577515019839>.
- [117] J. Villanova, R. Kumar, R. Daudin, P. Lhuissier, D. Jauffrès, L. Christophe, R. Tucoulou, S. Labouré, G. Martinez-criado, L. Salvo, Fast In Situ Nanotomography at ESRF, *Microsc. Microanal.* 24 (2018) 450–451. <https://doi.org/10.1017/S1431927618014496>.
- [118] R. Kumar, J. Villanova, P. Lhuissier, L. Salvo, In situ nanotomography study of creep cavities in Al-3.6-Cu alloy, *Acta Mater.* 166 (2019) 18–27. <https://doi.org/10.1016/j.actamat.2018.12.020>.
- [119] D. Paganin, *Coherent X-Ray Optics*, Oxford University Press, Oxford, 2006.
- [120] D. Paganin, S.C. Mayo, T.E. Gureyev, P.R. Miller, S.W. Wilkins, Simultaneous phase and amplitude extraction from a single defocused image of a homogeneous object, *J. Microsc.* 206 (2002) 33–40. <https://doi.org/10.1046/j.1365-2818.2002.01010.x>.
- [121] M. Langer, A. Pacureanu, H. Suhonen, Q. Grimal, P. Cloetens, F. Peyrin, X-Ray Phase Nanotomography Resolves the 3D Human Bone Ultrastructure, *PLoS One.* 7 (2012) 1–7. <https://doi.org/10.1371/journal.pone.0035691>.
- [122] L. Weber, Iterative tomographic X-Ray phase reconstruction. PhD thesis, INSA Lyon, 2016. <http://theses.insa-lyon.fr/publication/2016LYSEI085/these.pdf>.
- [123] J.W. Eaton, *GNU Octave Manuals*, 1997. <http://www.gnu.org/software/octave/doc/interpreter/>.
- [124] M.S. Del Río, R.J. Dejus, XOP 2.1 -A New Version of the X-ray Optics Software Toolkit, in: *AIP Conf. Proc.*, 2004: pp. 784–787. <https://doi.org/10.1063/1.1757913>.
- [125] A. Mirone, E. Brun, E. Guillard, P. Tafforeau, J. Kieffer, The PyHST2 hybrid distributed code for high speed tomographic reconstruction with iterative reconstruction and a priori knowledge capabilities, *Nucl. Instruments Methods Phys. Res. Sect. B Beam Interact. with Mater. Atoms.* 324 (2014) 41–48.

<https://doi.org/10.1016/j.nimb.2013.09.030>.

- [126] A. Lyckegaard, G. Johnson, P. Tafforeau, Correction of Ring Artifacts in X-ray Tomographic Images, *Int. J. Tomogr. Simul.* 18 (2011) 1–9. <http://www.ceser.in/ceserp/index.php/ijts/article/view/1164>.
- [127] F.P. Vidal, J.M. Létang, G. Peix, P. Cloetens, Investigation of artefact sources in synchrotron microtomography via virtual X-ray imaging, *Nucl. Instruments Methods Phys. Res. Sect. B Beam Interact. with Mater. Atoms.* 234 (2005) 333–348. <https://doi.org/10.1016/j.nimb.2005.02.003>.
- [128] B. Münch, P. Trtik, F. Marone, M. Stampanoni, Stripe and ring artifact removal with combined wavelet-Fourier filtering, *EMPA Act.* 17 (2009) 34–35. <https://doi.org/10.1364/OE.17.008567>.
- [129] C. Harris, M. Stephens, A combined corner and edge detector, in: *Alvey Vis. Conf.*, 1988. <https://doi.org/10.5244/C.2.23>.
- [130] T.W. Ridler, S. Calvard, Picture Thresholding Using an Iterative Slection Method, *IEEE Trans. Syst. Man Cybern.* 8 (1978) 630–632. <https://doi.org/10.1109/TSMC.1978.4310039>.
- [131] W. Rasband, T. Ferreira, *ImageJ User Guide User Guide ImageJ*, (2012) 198. <https://imagej.nih.gov/ij/docs/guide/user-guide.pdf>.
- [132] K.U. Barthel, Mean Shift Filter, (2007). <https://imagej.nih.gov/ij/plugins/mean-shift.html>.
- [133] I. Sobel, An isotropic 3×3 gradient operator,” in *Machine Vision for Three-Dimensional Scenes*, Academic Press, New York, NY, USA, 1990.
- [134] W. Lorensen, H. Cline, Marching cubes: A high resolution 3D surface construction algorithm, *Comput. Graph. (ACM)*. 21 (1987) 163.
- [135] Cast3M, (n.d.). <http://www-cast3m.cea.fr/index.php>.
- [136] P.W. Bridgman, *Studies in Large Plastic Flow and Fracture*, McGraw-Hill, New York, 1952.
- [137] J. Troufflard, G. Requena, S. Thuillier, É. Maire, Ductile Damage in Tension

- and Bending for DP980 Steel Sheets, *Key Eng. Mater.* 554–557 (2013) 110–117. <https://doi.org/10.4028/www.scientific.net/kem.554-557.110>.
- [138] A. Hosokawa, D.S. Wilkinson, J. Kang, E. Maire, Effect of triaxiality on void growth and coalescence in model materials investigated by X-ray tomography, *Acta Mater.* 60 (2012) 2829–2839. <https://doi.org/10.1016/j.actamat.2012.01.048>.
- [139] S. Goyal, K. Laha, A.K. Bhaduri, Response of Triaxial State of Stress to Creep Rupture Life and Ductility of 316 LN Austenitic Stainless Steel, *J. Mater. Eng. Perform.* 26 (2017) 752–763. <https://doi.org/10.1007/s11665-016-2492-7>.
- [140] D.E.J. Talbot, Effects of Hydrogen in Aluminium, Magnesium, Copper, and Their Alloys, *Int. Metall. Rev.* 20 (1975) 166–184. <https://doi.org/10.1179/imt1r.1975.20.1.166>.
- [141] D.R. Poirier, K. Yeum, A.L. Maples, A thermodynamic prediction for microporosity formation in aluminum-rich Al-Cu alloys, *Metall. Trans. A.* 18 (1987) 1979–1987. <https://doi.org/10.1007/BF02647028>.
- [142] T.S. Lundy, J.F. Murdock, Diffusion of Al²⁶ and Mn⁵⁴ in Aluminum, *J. Appl. Phys.* 33 (1962) 1671–1673. <https://doi.org/10.1063/1.1728808>.
- [143] X.G. Jiang, J.C. Earthman, F.A. Mohamed, Cavitation and cavity-induced fracture during superplastic deformation, *J. Mater. Sci.* 29 (1994) 5499–5514. <https://doi.org/10.1007/BF00349941>.
- [144] R. Boissiere, Effect de la temperature sur les capacites de mise en formw d'alliages de magnesium corroyes. PhD thesis, Institute polytechnique de grenoble, 2008.
- [145] J. Pilling, N. Ridley, Effect of hydrostatic pressure on cavitation in superplastic aluminium alloys, *Acta Metall.* 34 (1986) 669–679. [https://doi.org/10.1016/0001-6160\(86\)90182-3](https://doi.org/10.1016/0001-6160(86)90182-3).
- [146] T.-J. Chuang, K.I. Kagawa, J.R. Rice, L.B. Sillss, Overview Models for Diffusive Cavitation of Grain Interfaces, *Acta Mater.* 27 (1978) 265–284.
- [147] H.J. Frost, M.F. Ashby, Deformation-mechanism Maps: The Plasticity and

Creep of Metals and Ceramic, 1982.

- [148] L. Vitos, A. V. Ruban, H.L. Skriver, J. Kollar, The surface energy of metals, *Surf. Sci.* 411 (1998) 186–202. [https://doi.org/10.1016/0040-6090\(72\)90412-9](https://doi.org/10.1016/0040-6090(72)90412-9).
- [149] I.G. Jones, R.B. Crossland, Grain boundary diffusion creep in magnesium, *Met. Sci.* 11 (1977) 504–508.
- [150] A. Varloteaux, J.J. Blandin, M. Suéry, Control of cavitation during superplastic forming of high strength aluminium alloys, *Mater. Sci. Technol. (United Kingdom)*. 5 (1989) 1109–1117. <https://doi.org/10.1179/mst.1989.5.11.1109>.
- [151] J.W. Goodman, *Introduction to Fourier Optics*, 2005.
- [152] M. Hubert, *Durability of solid oxide cells: Modelling, an experimental and Characterization, investigation based on synchrotron X-ray nano-tomography*, 2016. <https://doi.org/10.1515/GREEN.2011.015>.